

**Applications of Site-directed Spin Labeling Electron Paramagnetic Resonance to
Studying the Structure, Dynamics and Interactions of Membrane Proteins**

Daniel Marlay Freed
Manassas, Virginia

B.S., University of North Carolina Wilmington, 2006

A Dissertation presented to the Graduate Faculty
of the University of Virginia in Candidacy for the Degree of
Doctor of Philosophy

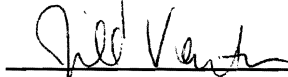
Department of Chemistry

University of Virginia
May 2012











ABSTRACT

Site-directed spin labeling (SDSL) electron paramagnetic resonance (EPR) is especially well-suited for the notoriously difficult analysis of membrane proteins, and offers numerous important advantages compared to more traditionally used techniques. Of these, arguably the most important is the ability to study membrane proteins in a more physiologically relevant environment. The first part of the following work describes the use of SDSL-EPR in conjunction with X-ray crystallography to study the substrate-induced unfolding of the Ton box motif in BtuB, the *Escherichia coli* outer membrane TonB-dependent corrinoid transporter. The data indicate that, compared to when BtuB is reconstituted in lipid bilayers, the Ton box equilibrium is shifted towards the folded state by 3 kcal/mol in BtuB crystals, with equal contributions attributed to both the crystal lattice and osmolytes in the crystallization buffer.

Although these results fortify the notion that SDSL-EPR is a valuable tool for studying membrane proteins, a better understanding of spin label energetics—within the context of the local protein environment—is essential for the unambiguous interpretation of EPR spectra and the use of long-range distance restraints obtained from spin labels. Towards that end, the molecular origins of EPR spectra from hydrocarbon-exposed sites on BtuB were examined using various EPR techniques combined with X-ray crystallography and quantitative modeling. Collectively, the data indicate that at such sites, spin label configuration and dynamics are influenced by the solvation environment

at the protein-hydrocarbon interface, and that this environment modulates weak interactions of the spin label with the protein surface.

Finally, substrate-mediated transmembrane signaling by active membrane transporters and their interaction with the energy-coupling protein TonB was examined. The effects of substrate, transport-defective Ton box mutations and a competing substrate for BtuB on the affinity of the interaction were characterized. Furthermore, the structure of TonB in solution and bound to the transporters was examined using SDSL-EPR, and from this collective body of data a transport mechanism is proposed that accounts for the findings. The results presented have important implications for the design of novel antibiotics that interfere with key intermolecular interactions made by TonB.

TABLE OF CONTENTS

Abstract	ii
Table of Contents	iv
List of Figures	ix
List of Tables	xi
Abbreviations	xii
Acknowledgements	xvi

Chapter 1: Introduction

1.1	Preface.....	1
1.2	Membrane Proteins: Importance and Challenges.....	3
1.3	Introduction to Site-directed Spin Labeling.....	5
	1.3.1 The Labeling Reaction and Practical Considerations.....	5
	1.3.2 Capabilities of Site-directed Spin Labeling EPR.....	7
1.4	TonB-dependent Transport.....	12
	1.4.1 Significance.....	12
	1.4.2 The Gram-negative Bacterial Cell Envelope.....	14

1.4.3	TonB-dependent Transport: The Proteins Involved.....	19
1.4.4	Parasitization of the Outer Membrane Transporters by Colicins.....	32
1.4.5	Remaining Questions.....	36
1.5	References.....	41

Chapter 2: Site-directed Spin Labeling Electron Paramagnetic Resonance

2.1	Basic Electron Paramagnetic Resonance Theory.....	59
2.1.1	The Zeeman Interaction.....	59
2.1.2	Nitroxide Hyperfine Interactions.....	62
2.1.3	Spectral Anisotropy.....	66
2.2	Nitroxide Lineshape.....	69
2.2.1	Non-relaxation Effects.....	71
2.2.2	Relaxation Effects.....	72
2.2.3	The Rigid Limit.....	78
2.2.4	The Isotropic Limit.....	79
2.2.5	The Intermediate Motional Regime and the Microscopic Order, Macroscopic Disorder Model.....	80

2.2.6	Processes in Proteins that affect Lineshape at X-band.....	89
2.3	Probing Conformational Exchange with Saturation Recovery.....	93
2.4	Double Electron-Electron Resonance.....	97
2.4.1	Introduction to Pulsed EPR.....	99
2.4.2	The DEER Experiment.....	102
2.4.3	Practical Considerations.....	105
2.5	References.....	108

Chapter 3: Conformational Exchange in a Membrane Transport Protein is Altered in Protein Crystals

3.1	Introduction.....	112
3.2	Results.....	117
3.3	Discussion.....	125
3.4	Methods.....	128
3.5	References.....	131

Chapter 4: Molecular Origin of Electron Paramagnetic Resonance Lineshapes on β -barrel Membrane Proteins: The Local Solvation Environment Modulates Spin Label Configuration

4.1	Introduction.....	140
4.2	Results.....	144
4.3	Discussion.....	167
4.4	Methods.....	172
4.5	References.....	176

Chapter 5: Differential Transmembrane Signaling through BtuB by Competing Substrates

5.1	Introduction.....	182
5.2	Results.....	186
5.3	Discussion.....	190
5.4	Methods.....	192
5.5	References.....	194

Chapter 6: Characterization of the Interaction between TonB and the Outer Membrane Transporters that it Energizes

6.1	Introduction.....	198
6.2	Results.....	202
6.3	Discussion.....	216
6.4	Methods.....	225
6.5	References.....	232

Chapter 7: Concluding Thoughts and Future Directions.....241

LIST OF FIGURES

Figure 1.2.1	The growth of membrane protein structural biology.....	4
Figure 1.3.1	Spin-labeling reaction scheme.....	7
Figure 1.4.1	Antibiotic resistance timeline.....	13
Figure 1.4.2	Comparison of gram-positive and gram-negative bacterial membranes...15	
Figure 1.4.3	The proteins involved in TonB-dependent transport.....	21
Figure 1.4.4	TonB structural plasticity.....	25
Figure 1.4.5	TonB-dependent transporter structure.....	27
Figure 1.4.6	Substrate-induced unfolding of the Ton box.....	29
Figure 1.4.7	Interaction of Colicin E3R with BtuB.....	35
Figure 2.1.1	The Zeeman interaction.....	62
Figure 2.1.2	The nitrogen hyperfine interaction.....	65
Figure 2.1.3	The nitroxide magnetic frame.....	66
Figure 2.1.4	Effect of magnetic anisotropy on the EPR spectrum.....	70
Figure 2.2.1	Dynamic regimes of nitroxide motion.....	79
Figure 2.2.2	MOMD coordinate systems.....	83
Figure 2.2.3	Processes in proteins that affect X-band lineshape.....	90
Figure 2.2.4	Timescales of protein dynamics.....	92
Figure 2.4.1	The DEER pulse sequence.....	102
Figure 3.1.1	Substrate-induced unfolding of the Ton box.....	115
Figure 3.2.1	EPR spectra for BtuB V10R1.....	118
Figure 3.2.2	Crystal structure of BtuB V10R1.....	121
Figure 3.2.3	Comparison of BtuB V10R1 EPR spectra in different environments....	124
Figure 4.1.1	Hydrocarbon-exposed EPR lineshapes from BtuB.....	141

Figure 4.2.1	Crystal structure of BtuB T156R1.....	146
Figure 4.2.2	Comparison of BtuB T156R1 and wild-type structures.....	148
Figure 4.2.3	Bilayer and crystalline BtuB T156R1 EPR spectra.....	150
Figure 4.2.4	Rotational diffusion tensor frame for the T156R1 fast component.....	151
Figure 4.2.5	T156R1 EPR spectra with neighboring mutations.....	153
Figure 4.2.6	Modeling of the {t, t} rotamer.....	155
Figure 4.2.7	Effects of hydrocarbon thickness on T156R1 lineshape.....	157
Figure 4.2.8	Saturation recovery data for T156R1.....	161
Figure 4.2.9	Effect of dioxane on the T156R1 EPR spectrum.....	162
Figure 4.2.10	Crystal structure of BtuB W371R1.....	163
Figure 4.2.11	G170R1 EPR spectra with neighboring mutations.....	166
Figure 5.1.1	Modulation of BtuB Ton box equilibrium by competing substrates.....	185
Figure 5.1.2	BtuB ion pair.....	186
Figure 5.2.1	BtuB V10R1 EPR spectra with R14/D316 mutations.....	188
Figure 5.2.2	Two-mutant thermodynamic cycle analysis.....	190
Figure 6.1.1	The TonB-dependent transporters in this study.....	202
Figure 6.2.1	TonB binding data for BtuB and FhuA.....	204
Figure 6.2.2	TonB binding data for FecA.....	207
Figure 6.2.3	TonB binding data for BtuB L8P and V10P.....	208
Figure 6.2.4	TonB binding data for ColE3R-liganded BtuB.....	210
Figure 6.2.5	TonB construct-dependent structural plasticity.....	211
Figure 6.2.6	TonB DEER data.....	213
Figure 6.3.1	Proposed revisions to the “membrane surveillance” model.....	225

LIST OF TABLES

Table 3.1.1	Examples of biological osmolyte systems.....	113
Table 3.2.1	Data collection and refinement statistics for BtuB V10R1.....	120
Table 3.2.2	Summary of R1 side-chain dihedral angles and rotamer designations....	123
Table 4.2.1	Data collection and refinement stats for BtuB T156R1 and W371R1....	147
Table 4.2.2	Summary of R1 side-chain dihedral angles and rotamer designations....	147
Table 4.2.3	Dynamic parameters from the MOMD fits.....	152
Table 6.2.1	Parameters from TonB binding data.....	205
Table 6.2.2	The TonB DEER distances support the intertwined dimer.....	214

ABBREVIATIONS

AC	Alternating current
ATP	Adenosine triphosphate
B ₁₂	Vitamin B ₁₂ (same as cyanocobalamin)
CM	Cytoplasmic membrane
CNCbl	Cyanocobalamin (same as vitamin B ₁₂)
ColE3R	Colicin E3 receptor-binding domain
CW	Continuous-wave
Da	Dalton
DC	Direct current
DEER	Double electron-electron resonance
DiErPC	1,2-dierucoyl- <i>sn</i> -glycero-3-phosphocholine
DMPC	1,2-dimyristoyl- <i>sn</i> -glycero-3-phosphocholine
<i>E.coli</i>	<i>Escherichia coli</i>
EPR	Electron paramagnetic resonance
FeChr	Ferrichrome
FeCit	Ferric citrate
FRET	Förster resonance energy transfer
G	Gauss
GHz	Giga-Hertz
HB	Hydrogen-bonded neighbor
kcal	Kilo-calorie
kDa	Kilo-dalton
k _{ex}	Rate constant for conformational exchange

kHz	Kilo-Hertz
K_M	Michaelis constant for Michaelis-Menten enzyme kinetics
LPS	Lipopolysaccharide
mol	mole
MOMD	Microscopic order macroscopic disorder
MP	Membrane protein
MRSA	Methicillin-resistant <i>Staphylococcus aureus</i>
MTSL	1-oxyl-2,2,5,5-tetramethyl-3-pyrroline-3-methyl methanethiosulfonate
NHB	Non-hydrogen-bonded neighbor
NMR	Nuclear magnetic resonance
OG	Octyl glucoside
OM	Outer membrane
PDB	Protein Data Bank
PEG	Polyethylene glycol
PG	Peptidoglycan
pI	Isoelectric point
PMF	Proton motive force
POPC	1-palmitoyl-2-oleoyl- <i>sn</i> -glycero-3-phosphocholine
SDSL	Site-directed spin labeling
SPR	Surface plasmon resonance
SR	Saturation recovery
TBDT	TonB-dependent transport/transporter
TMD	Transmembrane domain

T_1	Spin-lattice relaxation time
T_2	Spin-spin relaxation time
T_M	Phase memory time
τ_R	Rotational correlation time of the spin label
V_{\max}	Maximum rate for Michaelis-Menten enzyme kinetics

Amino Acids

<i>Single-Letter</i>	<i>Full Name</i>	<i>Abbreviation</i>
A	Alanine	Ala
R	Arginine	Arg
N	Asparagine	Asn
D	Aspartic Acid	Asp
C	Cysteine	Cys
Q	Glutamine	Gln
E	Glutamic Acid	Glu
G	Glycine	Gly
H	Histidine	His
I	Isoleucine	Ile
L	Leucine	Leu
K	Lysine	Lys
M	Methionine	Met
F	Phenylalanine	Phe
P	Proline	Pro

S	Serine	Ser
T	Threonine	Thr
W	Tryptophan	Trp
Y	Tyrosine	Tyr
V	Valine	Val

ACKNOWLEDGEMENTS

This document symbolizes an exciting transition in my life, and represents six years of effort during which I have learned a great deal. As such, I feel that it is appropriate at this time to thank the many people who have supported me or contributed to my development as a scientist and as a person. First, and most importantly, I must acknowledge the support that my family has given me, not only throughout graduate school, but throughout my entire life thus far.

Mom, you have always been excited and interested to hear about the newest developments in lab, even though most of this stuff is like a foreign language to you (just like the daily activities of a paralegal or book-keeper are alien concepts to me). You and Dad have provided a huge amount of support in various ways, just as you have my entire life. Dad, it amazes me how quickly you understand the details of my projects. It's fun to talk to you about my work, and if I've inherited even a small portion of your brainpower, then I haven't quite figured out how to use it yet. I cannot understate how thankful that I am for everything that both of you have done for me, and I sincerely hope that I can grow into a fraction of the person that the both of you are. Julia, you have been a supportive and protective big sister—I've especially noticed in recent years that you've taken the helm of the kid clan—and I hope that my research can one day make as big of an impact on the world as your work does. Just remember who won that ping-pong game in the basement years ago. Zach, you motivate me. You might be the smartest one in the family, and I hope that you never forget what fuels you, and that you have a big brother that you can count on. And last but not least, Chelsey—thanks for being so supportive

and understanding throughout this entire process, and for willing to rearrange your life to make things work out between us. I love all of you.

I have been extremely fortunate in that I've been exposed to some wonderful mentors and minds over the last several years. I want to thank Dr. Paulo Almeida and Dr. Antje Pokorny for igniting my interest in cell membranes and patiently tutoring me as an undergraduate researcher. Without that experience, I'm not sure where I would have ended up—but I might have missed out on a wonderful education here at UVA. To my official mentor, Dr. Dave Cafiso, thank you for giving me an opportunity to learn in your lab. I'd like to thank you in particular for being patient with me as I continue to develop as a scientist (euphemism for struggle), answering my dumb questions without judgement, and for always having an open door policy. I have to extend a big thank you for not giving up on me after I performed poorly during candidacy exams, and I hope that you now believe that the right decision was made in passing me. I hope that we continue to stay in touch in the future. I have to thank my first in-lab mentor here at UVA, Dr. Steve Lukasik. Steve, thanks for being so patient, passionate, and willing to help, even after you left the lab for bigger and better ventures. I also learned an incredible amount from Dr. Peter Horanyi. Peter, I will always be thankful for your willingness to teach me about crystallography and molecular biology, and your commitment to helping me even if it meant getting out of bed and coming in to lab in the middle of the night. I must also thank Dr. Michael Wiener and Dr. Bob Nakamoto for being unofficial secondary advisors. I have learned a lot from you both, and really enjoy our conversations about TonB-dependent transport. I also would like to thank each of my committee members for

taking the time out of your busy schedules to perform the required duties of a dissertation defense referee. And finally, I'd like to thank all of my current and past lab mates; every one of you brought unique knowledge to the table from which I've learned a lot. Our daily discussions were hugely helpful to my learning and development. This dissertation is dedicated to all of the aforementioned people, and to future Cafiso lab members—part of the aim of this work was to explain, in an intuitive manner, concepts that I found difficult, and I hope that this work is able to assist future students in their learning process.

CHAPTER 1

Introduction

1.1 Preface

The work presented here describes both advances in the development and advantages in the use of site-directed spin labeling electron paramagnetic resonance (SDSL-EPR) as a tool for studying membrane protein structure and dynamics, and also provides an example of its application towards elucidating important mechanistic details regarding the TonB-dependent transport (TBDT) of essential nutrients across the outer membrane of Gram-negative bacteria.

Although the use of spin labels for EPR studies has long been recognized as a valuable tool for studying protein structure and dynamics,¹ its widespread use did not become practical until the advent of the polymerase chain reaction and site-directed mutagenesis in the early 1980s. Professor Wayne Hubbell was the first investigator to combine site-directed mutagenesis with spin labeling,^{2,3} recognizing that the ability to introduce spin labels at any desired position within a protein would revolutionize the field of EPR. The first study correlating EPR spectra with protein structure and dynamics was published in 1996,⁴ and during the intervening 15 years several publications have enhanced our understanding of the correlation between EPR lineshape and local protein structure and dynamics. Additionally, advances in technology have led to the

development of pulse EPR instrumentation, which has helped diversify the EPR tool box to include experiments capable of extracting important parameters and electronic spin interactions that are not accessible through the use of more traditional EPR techniques.

SDSL-EPR is a burgeoning field that is poised to offer valuable information on protein structure and dynamics, especially when combined in a multidisciplinary approach. Membrane proteins, whose analysis is notoriously difficult, have been shown to be particularly amenable for investigation by SDSL-EPR, and this methodology should continue to be increasingly useful in the future as the state of the technique matures.

The following work is organized into seven chapters. The initial introductory chapter will outline general background information regarding the importance of studying membrane protein structure and dynamics, the SDSL-EPR technique and its application to membrane proteins, and finally, TBDT, an active transport process in Gram-negative bacteria that is facilitated by a network of membrane proteins. The second chapter will provide detailed EPR theory, discuss EPR lineshapes from nitroxide spin labels, and outline the EPR techniques that will be discussed in this dissertation. The third chapter provides an example of the utility of SDSL-EPR in studying protein structure and dynamics under physiologically relevant conditions, and the fourth chapter describes work that has advanced our understanding of spin label configurations and EPR lineshapes from membrane proteins. The fifth and sixth chapters describe the use of SDSL-EPR, within a multidisciplinary approach, for uncovering mechanistic details of TBDT. Finally, the seventh chapter summarizes the new findings presented in this work and provides insight into future directions that should be considered.

1.2 Membrane Proteins: Importance and Challenges

Since the introduction of the Fluid Mosaic Model by Singer and Nicholson in 1972,⁵ our understanding of cellular membranes has advanced considerably. It is now widely accepted that the cell membrane is a very dynamic and heterogeneous environment, consisting of compositional biases and various regions of functional specialization that are critical for the maintenance of cellular homeostasis.⁶ In fact, the lipids that comprise the cell membrane can themselves function as second messengers,⁷ and their concentration and distribution in the membrane can affect processes such as signal transduction, membrane trafficking, and membrane protein function.^{8,9} Likewise, the resident proteins of the cell membrane are responsible for numerous crucial functions such as the uptake of nutrients, export of waste, negotiation of the membrane potential, and the transmission of signals in and out of their host cell.¹⁰ As such, membrane proteins constitute roughly 30% of the expressed sequences in an organism's genome,¹¹ and their deregulation or dysfunction is implicated in many diseases and afflictions—over half of prescription pharmaceuticals currently on the market are thought to target membrane proteins.^{12,13}

The advancement of basic science and structure-based drug design depends heavily on knowledge of the three-dimensional architecture of membrane proteins at atomic resolution, and on elucidation of the conformational dynamics, in terms of amplitude and frequency, that bridge protein structure and function. Thus far, limitations

in technology and difficulties in the expression and purification of membrane proteins has largely precluded the high-resolution structural study of these high-value targets—less than 1% of the unique protein structures in the Protein Data Bank (PDB) are of membrane proteins (Figure 1.2.1).^{14,15}

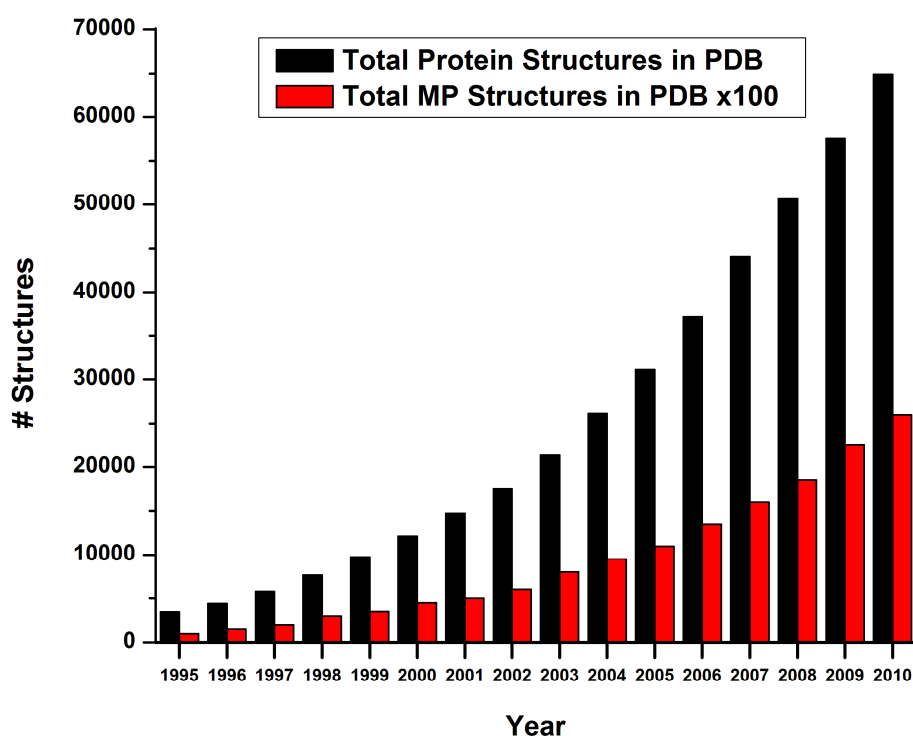


Figure 1.2.1. The growth of membrane protein structural biology. The determination of membrane protein structures has lagged far behind in the overall exponential growth of structural proteomics. Shown are the number of total protein structures in the PDB (black) and total unique membrane protein (MP) structures multiplied by a factor of one hundred in the PDB (red), between the years of 1995 and 2010.^{14,15}

Encouragingly, recent advancements in molecular biology have made important contributions towards the successful recombinant production of milligram quantities of protein in various host organisms, and their subsequent purification in monodisperse and

stable form.^{16,17} Likewise, recent technological innovations have spurred growth and excitement in the field of membrane protein structural biology. The development of synchrotron radiation sources, crystallization robots, seleno-methionine derivatization, and cryo-freezing have made X-ray crystallography studies more efficient, less time-consuming and less protein expensive. Additionally, new developments in probe and magnet technology and the introduction of methods such as transverse relaxation optimized spectroscopy have extended the barriers of nuclear magnetic resonance (NMR) spectroscopy as a tool for structure determination.¹³ Despite these recent promising advancements, obtaining high-resolution membrane protein structures still remains difficult, and traditionally implemented techniques such as NMR and X-ray crystallography suffer from several fundamental limitations that constrain the scope of their application.

Solution NMR can offer valuable insight into protein structure and dynamics, but limited sensitivity and molecular mass restrictions nonetheless exclude most membrane proteins from analysis using this technique. Furthermore, in most cases NMR experiments on membrane proteins are performed in detergent micelles, rather than in lipid bilayers. Quite often the optimal experimental detergent system does not accurately mimic the native membrane, and the resulting differences in physicochemical properties between the native bilayer and the experimental micellar environment can alter the structure or conformational sampling of a macromolecule.¹⁸⁻²² This is also a problem in X-ray crystallography, in which the vast majority of endeavors aim to utilize detergent systems that confer crystallizability or diffractability, rather than mimicry of the native

membrane. Moreover, the crystal lattice hardly resembles a physiologically relevant milieu, and there are examples in the literature regarding the modulation of protein function by the crystalline environment.²³

For these reasons, new techniques are desperately needed for the analysis of membrane protein structure and dynamics. SDSL-EPR is an emerging technique that is well-suited to complement NMR and X-ray crystallography, because it circumvents many of the limiting factors that constrain the applicability of these methodologies with respect to membrane proteins. The continuing development of SDSL-EPR should prove to be an important addition to a currently limited arsenal of techniques for studying membrane protein structure and dynamics.

1.3 Introduction to Site-directed Spin Labeling

1.3.1 The Labeling Reaction and Practical Considerations. In EPR spectroscopy, which will be discussed in much more detail in Chapter 2, transitions are induced between the energy levels of a paramagnetic system under the influence of an external magnetic field. Before the advent of site-directed spin labeling, the use of EPR in protein biochemistry was generally limited to intrinsically paramagnetic metalloproteins and enzymes that utilize or produce free radicals. SDSL renders any protein of interest paramagnetic by the site-specific attachment of a probe that possesses a stable unpaired electron. Typically, the method involves a combination of site-directed cysteine mutagenesis and chemical labeling, generally with a thiol-specific

methanethiosulfonate spin label (MTSL), to generate a disulfide-bonded paramagnetic side-chain designated as R1 (Figure 1.3.1). The unpaired electron, which gives rise to the EPR signal, is primarily localized in the 2p-orbital of the spin label's nitrogen atom.

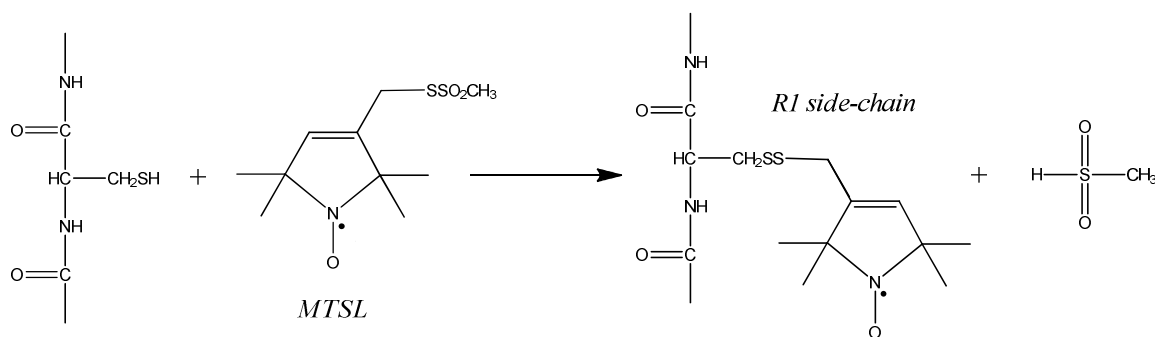


Figure 1.3.1. Spin-labeling reaction scheme. Using site-directed mutagenesis, a cysteine residue is introduced into the protein of interest. The paramagnetic spin-labeled side-chain R1 is produced by chemical modification of the cysteine with a methanethiosulfonate label.

A few factors must be taken into consideration before using this technique. First, it is better that the protein of interest has no endogenous non-disulfide-bonded cysteines. In such cases, these cysteines may be themselves mutated to alternate residues such as serine, leucine, or alanine; such an endeavor should be followed by verification of mutant protein fold and function. Alternative options include reversible metal protection²⁴ or the use of unnatural amino acid chemistry.²⁵ Similarly, it should be demonstrated that the spin label has no affinity for the protein within the context of a cysteine-less background. Additionally, in theory, the unique nature of the paramagnetic spin label allows the experimenter to probe local features of the protein at any site of interest. However, great care must be taken to avoid the introduction of cysteine mutations or spin label

placements that disrupt the native fold, stability or function of the protein. The R1 side-chain is similar in size to a tryptophan amino acid residue, and in most cases the level of perturbation due to its introduction into proteins is small.^{4,26,27}

1.3.2 Capabilities of Site-directed Spin Labeling EPR. Proteins are inherently dynamic and structurally heterogeneous.²⁸ As such, the two important factors relevant to a protein's function include the ensemble of structures attainable in solution, and the dynamics—in terms of amplitude and frequency—that underlie structural interconversion. SDSL-EPR offers the capability to study both protein structure and dynamics, although structural data is generally of lower resolution than that obtained from X-ray crystallography or NMR. However, this does not relegate SDSL-EPR to proteins of unknown structure; exchange processes between structural substates may be analyzed under physiological conditions, oligomerization events may be studied in detail, and models of membrane protein orientation in the lipid bilayer may be determined. For example, SDSL-EPR has been the method of choice in seminal papers that have described the mechanisms of potassium channel activation and gating,²⁹⁻³¹ elucidated alternating-access transport mechanisms,^{32,33} determined substrate-dependent conformational transitions in membrane transport proteins,^{34,35} and described the organization of exotoxins in membranes.³⁶

For proteins that are spin-labeled with the R1 side-chain, the unpaired electron is localized at the end of a long, flexible chain containing five rotatable bonds. Local structural features or conformational exchange that influences the motion of the unpaired electron will affect the EPR lineshape. In particular, the motion of the spin label—and

thus the EPR spectrum—is sensitive to the local primary and secondary structure, tertiary interactions, and dynamics of the protein backbone.³⁷ For example, the EPR spectrum of a spin-labeled α -helix will look different than that from a solvent-exposed spin label on a flexible loop or a spin label in tertiary contact. In fact, functionally relevant conformational changes can even be monitored in real time, as has been done for proteins such as bacteriorhodopsin, colicin E1 and the TonB-dependent transporter FepA.³⁸⁻⁴² Furthermore, metastable excited conformational substates can be accessed and studied by high-pressure EPR.⁴³ And in some cases, information regarding polarity, proticity and the overall Brownian rotational diffusion of the protein may also be acquired using standard continuous-wave techniques.⁴⁴

For membrane proteins, SDSL-EPR may also be used to determine membrane depth and solvent accessibility. Differential collisions between the spin label and secondary paramagnetic species of extremely dissimilar hydrophobicities will yield unique collision parameters. This data can subsequently be interpreted in terms of protein secondary structure and depth within the membrane, identification of tertiary contact interfaces, helix tilt and orientation with respect to the bilayer normal.^{31,45} SDSL-EPR has been used to determine the depth and orientation of proteins such as bacteriorhodopsin,⁴⁵ the TonB-dependent transporter BtuB,⁴⁶ and the diphtheria T toxin³⁶ in lipid bilayers.

By measuring the dipolar coupling between two spin labels, important distance information may be acquired. Various continuous-wave and pulse EPR methods may be used to determine interspin distances from 8 to 80 Å and the distribution of these

distances about their average value, yielding important structural and dynamical data.^{47,48}

The careful measurement of several distances allows for the implementation of constraints for the determination of protein structure and conformational changes associated with function. For example, studies utilizing distance constraints between spin labels have described detailed alternating access mechanisms for the lipid flippase MsbA³² and the sugar/H⁺ symporter LacY,³³ substrate-dependent conformational dynamics of the sodium-coupled leucine transporter LeuT³⁴ and the TonB-dependent vitamin B₁₂ transporter BtuB,⁴⁹ and conformational changes associated with G-protein coupled receptor signaling.^{50,51}

Therefore, given a sufficiently large set of spin-labeled mutants, a comprehensive and valuable set of structural and dynamical data may be obtained for membrane proteins. Indeed, SDSL-EPR has many advantages compared to other structural and spectroscopic techniques used for studying membrane protein structure and dynamics. For example, SDSL-EPR is very sensitive—only tens of picomoles of protein are required for a decent signal. Therefore, this methodology is less protein expensive and allows the experimenter to circumvent common difficulties related to the expression and purification of sufficient quantities of membrane protein often required for structural studies. As will be discussed in more detail in Chapter 2, the typically used frequencies in SDSL-EPR experiments allow for the characterization of protein dynamics on relatively fast timescales, such that nearly all functionally relevant conformational changes are accessible using this technique. Perhaps most importantly, SDSL-EPR can be used to study membrane proteins at room temperature and under physiologically

relevant conditions. Experiments may be carried out in lipid bilayers, or in some cases, the native membrane. An example of the utility of studying membrane proteins under more physiologically relevant conditions, and a cautionary tale regarding the interpretation of structural dynamics obtained from X-ray crystallography, is provided in Chapter 3. Another key advantage is that the spin label is relatively small compared to fluorescent probes, and is usually unperturbative to protein structure. Moreover, when measuring distances, SDSL-EPR does not experience the orientational problem that is encountered for Förster resonance energy transfer (FRET), and there is no need for complementary donor and acceptor probes. Finally, due to the exclusivity of the spin label's paramagnetism, there are no molecular weight limitations, which is a problem that precludes most membrane proteins and protein complexes from NMR analysis. In this work, Chapters 5 and 6 provide examples of the use of SDSL-EPR for studying the association of bacterial membrane transport proteins with their globular protein binding partners that collectively function in TonB-dependent transport.

All of these advantages make SDSL-EPR a great technique for providing information that is complementary to or inaccessible by more traditionally used methods such as NMR and X-ray crystallography. However, the ultimate utility of SDSL-EPR as a tool for studying protein structure and dynamics will hinge on our ability to better understand the energetics of the spin label. Knowledge of the likely spin label configurations, the environmental factors that influence such configurations and the kinetics of their interconversion is crucial to the unambiguous interpretation of EPR spectra and the successful use of spin labels for long-range distance constraints. In this

dissertation, Chapter 4 discusses advancements towards this goal for membrane proteins. Although more work must be done in this area, thus far SDSL-EPR has proven to be a valuable tool for studying membrane protein structure and dynamics.

1.4 TonB-dependent Transport

1.4.1 Significance. Pathogenic bacteria have long presented a major public health concern. Bacterial infections are the cause of potentially fatal conditions such as pneumonia and sepsis, and furthermore, the success of surgical procedures, transplantations, cancer chemotherapy, and care for the critically ill depend on evasion of bacterial infection.⁵² Huge progress was initially made when Florey and Chain figured out how to isolate penicillin from Sir Alexander Fleming's mold in 1940, and the subsequent wide-scale production of antibiotics increased the average life expectancy by eight years (Figure 1.4.1).⁵³ Almost 20 years later, around the same time that second generation antibiotics were introduced, methicillin-resistant *Staphylococcus aureus* (MRSA) emerged. Since the 1960s, variants of older drugs have been introduced, but no antibiotic with a novel mode of action has hit the market.^{53,54} During this intervening time, the pharmaceutical industry has essentially been playing a game of one-upmanship with bacteria, which are masters of evolution and continue to gain resistance to antibiotic therapies. Thus, the antibiotic field has effectively come full circle, and the continuing emergence of multidrug-resistant pathogenic bacteria is now a major public health concern.

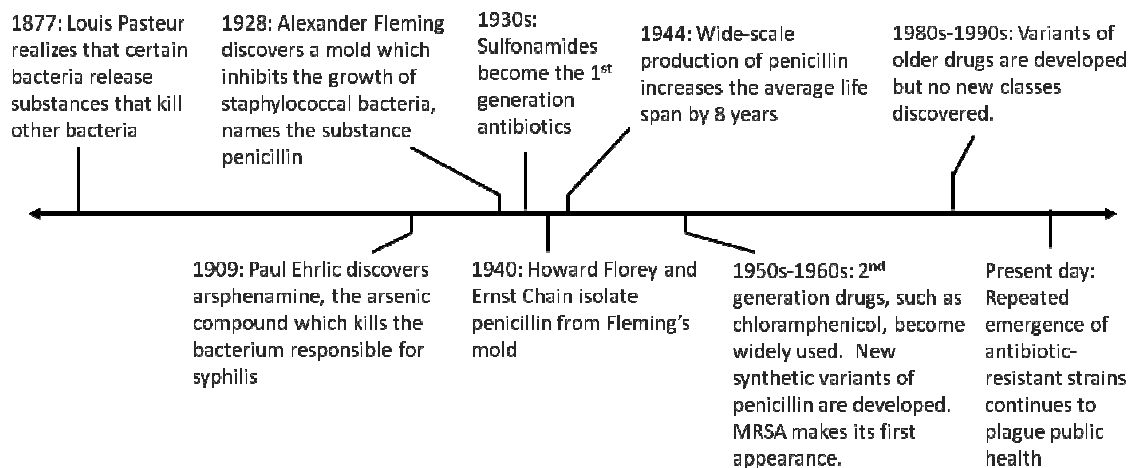


Figure 1.4.1. Antibiotic timeline. The introduction of first-generation antibiotics in the 1930s and penicillin in the 1940s increased the average life expectancy by eight years. Since then, variants of older drugs have been developed but no new classes of drugs have been introduced. Antibiotic resistance has thus become a huge public health issue.

The Centers for Disease Control and Prevention estimated in 2002 that at least 90,000 deaths per year in the United States could be attributed to bacterial infections, and more than half of these deaths resulted from antibiotic-resistant bacteria.⁵⁴ Indeed, the estimated annual market for antibiotics is the third largest amongst all drugs at about \$25 billion, with roughly one-fifth of that expenditure resulting from antibiotic-resistant bacteria.⁵³ As the resistance problem continues to proliferate, pharmaceutical companies are having little success in the development of drugs with a novel mode of action.

Gram-negative bacteria such as *Escherichia coli* pose an especially difficult challenge due to their additional cell membrane; the efficacy of most antibiotics that target Gram-negative bacteria thus requires penetration of both membranes. Even in cases where the diffusion of the antibiotic is only slowed by the additional membrane, the bacteria are able to easily neutralize small amounts of antibiotic rather than being

exposed to the large concentrations of drug in the extracellular milieu. Moreover, Gram-negative bacteria can activate pumps or modulate the activity of channels or transporters that antibiotics utilize for entry into the cell.⁵⁴ Therefore, high levels of resistance are easily established. For all of the aforementioned reasons, new antibiotics that function by means of a novel mode of action are desperately needed.

A potential target for new antibiotics is the TonB-dependent transport system. Gram-negative bacteria utilize this important network of membrane proteins for the active transport of essential nutrients into the cell, and furthermore, proper functioning is essential for virulence. Elucidation of the inner workings of this system may shed light on new molecular targets for novel antibiotics that can be directed against Gram-negative bacteria. Because this system is dependent on a complex interplay between several membrane proteins, it is also perfect for analysis by SDSL-EPR.

1.4.2 The Gram-negative Bacterial Cell Envelope. All bacteria create a peptidoglycan (PG) cell wall that confers structural rigidity and protects the cell from osmotic lysis. Gram-negative bacteria are unique in that they possess an additional outer membrane (OM) outside of this peptidoglycan layer that separates the cytoplasmic membrane (CM) and OM by a ~15-20 nm⁵⁵ aqueous space called the periplasm, which contains numerous proteins involved in processes such as intermembrane communication, transport, and cell envelope remodeling (Figure 1.4.2).⁵⁶ The main function of the OM is to serve as an enhanced permeability barrier against an often inhospitable environment. For example, the OM confers resistance to numerous host defense factors that are toxic to their Gram-positive cousins, such as lysozyme, β -lysin,

and several leukocyte proteins.⁵⁶ In Gram-negative enterobacteria such as *E.coli* and *Salmonella*, the OM offers fortification from the action of bile salts and digestive enzymes that would otherwise lead to cell lysis.⁵⁷ Furthermore, the outer leaflet of the OM is rich in lipopolysaccharide (LPS), which renders the bacterium's surface relatively hydrophilic and allows evasion from phagocytosis, certain mechanisms of complement resistance, and other immune responses through dynamic variation of the LPS surface antigen composition.⁵⁸ Most importantly from a public health perspective, the OM provides resiliency against many antibiotics that are effective against other bacteria.

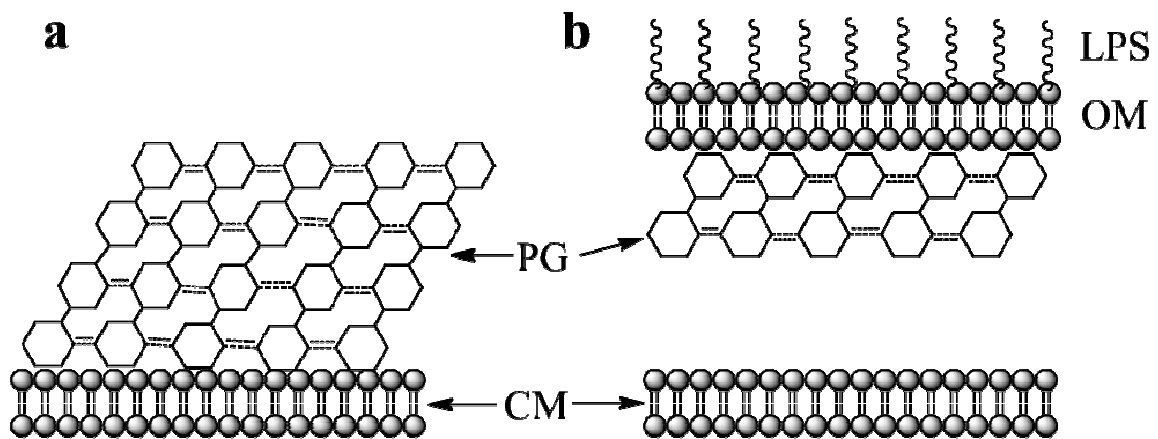


Figure 1.4.2. Comparison of Gram-positive and Gram-negative bacterial membranes. Gram-positive bacteria (a) have a single cell membrane and a thick peptidoglycan (PG) cell wall coating the cytoplasmic membrane (CM). The Gram-negative bacterial cell envelope (b) contains two cell membranes separated by about 15-20 nm; the intervening aqueous space is called the periplasm. The outer membrane (OM) sits atop a thin layer of PG, and its outer leaflet is rich in lipopolysaccharide (LPS). Lipoprotein, which decorates the inner leaflet of the OM, and in some cases links the OM to the PG, is omitted from this figure.

Although the phospholipid composition of the CM and the OM are generally very similar,^{59,60} the outer leaflet of the OM is enriched in lipid A, which is the hydrophobic anchor of LPS. This membrane-associated portion of LPS is usually comprised of six saturated fatty acid chains linked to a glucosamine disaccharide backbone. These long, saturated acyl chains maintain the outer leaflet of the OM in a gel-like phase state, which makes the OM a very effective permeability barrier to small, hydrophobic solutes.⁶¹ The disaccharide backbone of LPS molecules is highly negatively charged, and can bind various divalent cations that, in turn, affect LPS structure and aggregation.⁶² The core polysaccharide structure, along with independently synthesized O-antigen subunits, is linked to the C6 carbon of a glucosamine residue and extends away from the plane of the OM.

Due to the presence and required functions of the OM, the peptidoglycan cell wall of Gram-negative bacteria (7-8 nm) is much thinner than that of Gram-positive bacteria (20-80 nm). PG is a polymer consisting of both sugars and amino acids; alternating β -(1,4) linked residues of *N*-acetylglucosamine and *N*-acetylmuramic acid form long chains that are cross-linked to adjacent chains by tetrapeptide-derivatized *N*-acetylmuramic acid residues. Tetrapeptides on adjacent *N*-acetylmuramic acid residues are fused by the enzyme transpeptidase, forming a three-dimensional PG network that confers structural rigidity to the cell. In Gram-negative bacteria, the OM is anchored to the PG in several areas by the Lpp lipoprotein, a very abundant protein for which roughly one-third of the population is covalently bound to the PG through the amino group of its C-terminal lysine.⁶³ At the N-terminus, lipoproteins contain a cysteine whose peptide amino group

is substituted with a fatty acid residue via an amide linkage.⁶⁴ It is assumed that the main role of the lipoprotein is to stabilize the association between the OM and PG; mutants devoid of lipoprotein are viable, but have unstable cell walls characterized by the release of OM vesicles and periplasmic enzymes.⁶⁵

Presumably due to both functional considerations and folding logistics, all of the OM proteins in Gram-negative bacteria are of β -barrel structure, possessing between 8-22 transmembrane strands.⁶⁶ OmpA, an eight-stranded β -barrel with a globular C-terminal domain that binds the PG, is a major protein constituent of the OM and is thought to contribute to cell morphology.⁶⁷ Another primary protein constituent of the OM are the porins, which are 16-stranded β -barrels that trimerize to create pores that allow for the non-specific passage of hydrophilic molecules smaller than 600 Daltons (Da) across the OM and into the periplasm.^{68,69} Since the diffusion is passive, it occurs along the concentration gradient of the diffusive molecule and can be described by Fick's first law of diffusion, $V = P \times A \times \Delta c$, where V is the rate of diffusion, P is the permeability coefficient of the membrane with respect to the diffusive solute, A is the area of the membrane, and Δc is the concentration gradient across the membrane.⁵⁶ Nevertheless, the periplasmic concentration of many micronutrients is quite low, as evidenced by the presence of active transport systems in the CM.

E.coli produces predominantly three porins—OmpF, OmpC, and PhoE,⁷⁰ which tightly associate with the LPS extracellularly and the PG periplasmically.⁵⁶ Although these proteins form non-specific trimeric channels as mentioned above, the unique nature of inward-facing residues amongst the porins influences the permeability coefficient, and

thus the likelihood of diffusion for a given solute. For example, OmpF and OmpC generally prefer cations, with OmpF forming a slightly larger channel, while PhoE prefers anions. Thus, depending on the environment, the bacterium can modulate the expression of certain porins. For example, during periods of phosphate starvation the expression of PhoE will be upregulated. Similarly, the expression of OmpF is down-regulated in the presence of antibiotics or bile acids, since these compounds diffuse through the larger OmpF channel easier.⁷⁰

For the uptake of nutrients into the cell, the relationship between the rate of diffusion across the OM, V , and the V_{\max} of the active cytoplasmic transport system is important. For example, if V becomes appreciably lower than V_{\max} , in which case diffusion across the OM is nearly completely limiting, then the active transport system in the CM will not be able to function near its maximum potential. This could be a problem for larger, more hydrophobic, or negatively charged molecules such as lactose and maltose, which under normal conditions diffuse relatively slowly through the porins, yet are targeted by high V_{\max} transport systems in the CM.⁵⁶ For this reason, the active transport system for lactose in the CM has an unusually high K_M to prevent the wasteful expenditure of energy.⁵⁶ Furthermore, the OM also contains numerous proteins involved in specific facilitated diffusion (e.g. LamB for maltose and maltodextrins).

The influx of micronutrients and export of small molecule waste products is an essential process, as evidenced by the fact that proteins make up nearly half of the mass of the OM. However, a major consequence of limited OM permeability is that there is no source of energy for the active processes that occur there, such as the transport of

essential nutrients that are too large to diffuse through the porins. The production of adenosine triphosphate (ATP) would be a futile process, since it is small enough to diffuse through the porins. Likewise, electrochemical gradients, such as that which drives the production of ATP in the CM, cannot be established due to the OM permeability. Gram-negative bacteria circumvent this apparent conundrum by producing OM transport proteins that scavenge their cognate substrates with high affinity and specificity, and couple to the protonmotive force (PMF) across the CM via the proteins TonB, ExbD, and ExbB. This extremely complex process, termed TonB-dependent transport (TBDT), is responsible for the transport of various forms of chelated iron and corrinoids across the OM, and is essential for virulence in pathogenic Gram-negative bacteria.

1.4.3 TonB-dependent Transport: The Proteins Involved. Nutrients such as vitamin B₁₂ and various iron siderophore complexes are too large, and often too scarce, to effectively diffuse through porins in the OM. For the uptake of these essential nutrients, Gram-negative bacteria produce and secrete specific, high affinity active transporters to the OM. The lack of an energy source at the OM adds complexity; the energy required for transport is extracted from the PMF of the CM via TonB and accessory proteins ExbB and ExbD. The orchestrated interaction of proteins in the TonB system is critical for survival of the bacterium. Although a similar transperiplasmic system mediated in part by TolQ and TolR can partially recapitulate transport in *exbBD* mutants, no functional substitution between TonB and TolA, the energy-coupling proteins in each respective system, has been observed.⁷¹⁻⁷³ Indeed, *tonB* mutants are defective in all energy-

requiring processes at the OM, highlighting its importance and role as the energy conduit. The TBDT system is highly conserved and even extended amongst Gram-negative species; whereas *E.coli* contains one TonB-dependent system, *Xanthomonas* contains six homologous TonB-dependent systems (unless otherwise stated, components of the *E.coli* TonB-dependent system will be referred to henceforth).⁷⁴ Evidence is emerging that TonB can also function in the uptake of nickel and various carbohydrates, substantiating the notion that bacteria depend on this system for multiple important processes and can use it to adapt to their environment.⁷⁵ Furthermore, TBDT proteins are the target of numerous bacteriophages and toxic proteins called colicins that are secreted by and directed against certain strains of *E.coli*. Typically, after TonB associates with a cognate OM transporter and drives nutrient translocation across the OM, the substrate associates with a soluble periplasmic binding protein which shuttles the nutrient to an ATP-binding cassette transporter for transport across the CM and into the cytosol.

The CM components of TBDT include integral membrane proteins ExbB, ExbD and TonB (Figure 1.4.3). ExbB and ExbD appear to have roles in harvesting the PMF and in driving cyclical energy-dependent conformational changes in TonB during transport.^{76,77} Although the stoichiometry of the active complex is unknown, the cellular ratio of these proteins is roughly 1 TonB:2 ExbD:7 ExbB over a wide range of growth conditions.⁷⁸ The complete, full-length structures for each of these proteins are yet to be ascertained, but their overall topologies have been determined by several groups.⁷⁹⁻⁸¹ ExbB is a 244-residue protein containing three alpha helical transmembrane domains, with the majority of the protein occupying the cytoplasm (Figure 1.4.3). In the CM

complex, the association of ExbB with the TonB transmembrane domain is required for PMF-dependent conformational changes in TonB.⁷⁶ Moreover, mutations in the cytoplasmic ExbB C-terminus have been shown to prevent a PMF-dependent interaction between the periplasmic domains of TonB and ExbD, demonstrating the importance of transmembrane signal transduction across the CM.⁸² ExbB has also been shown to assume a protective role of newly synthesized TonB in the cytoplasm.⁸³ Although ExbB is obviously important for TonB stability and conformational cycling, the precise role of ExbB during transport remains unknown.

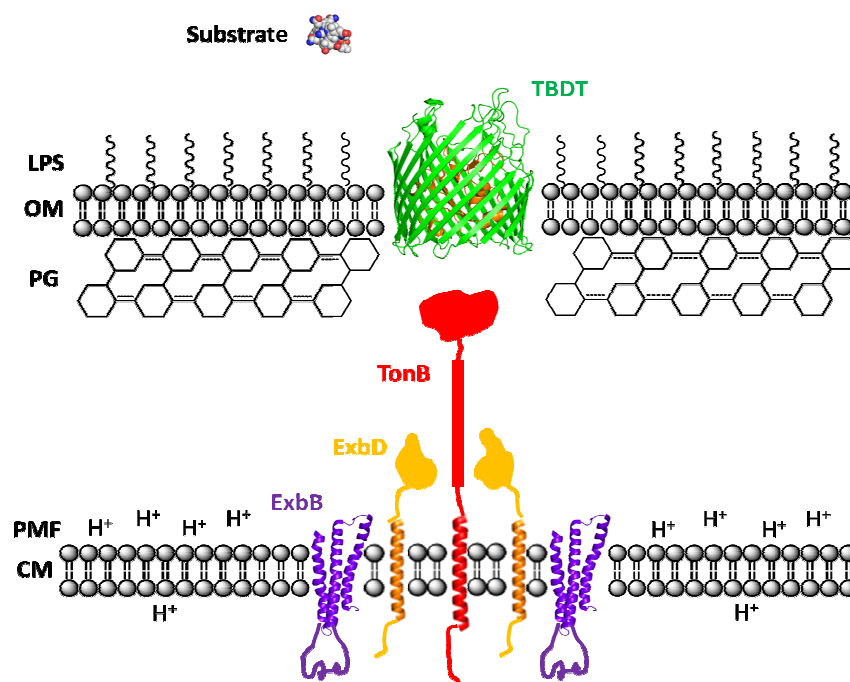


Figure 1.4.3. The Proteins Involved in TonB-dependent Transport. In the CM, ExbB and ExbD utilize the energy of the PMF to drive conformational changes in TonB. The exact stoichiometry of this complex is not known, and may vary during transport cycles. TonB can span the periplasm through its rigid polyproline motif (red rectangle) and associate with TBDTs through interactions with the extended Ton box and periplasmic turns. TonB then presumably drives conformational changes in the pore-occluding luminal domain (orange) of the TBDT through a currently unknown transport mechanism. The representations of ExbB, ExbD and TonB are renderings based on predicted topologies; the TBDT structure is of BtuB, which was solved by X-ray crystallography (1NQH).⁸⁴

ExbD is a 141-residue integral CM protein possessing globular periplasmic and single-pass transmembrane domains (Figure 1.4.3). As mentioned above, a PMF- and ExbB-dependent interaction between the ExbD and TonB periplasmic domains has been characterized—several ExbD residues between amino acids 92-113 can disulfide cross-link with TonB residue A150C *in vivo*.^{77,85} It is thought that this PMF-dependent interaction is responsible for facilitating one of the two TonB conformational transitions that occur during transport cycles, as will be discussed in more detail below. Proper association of the ExbD and TonB transmembrane domains is also required for the PMF-dependent interaction between their periplasmic domains; ExbD D25N or TonB H20A mutations prevent this interaction.⁷⁷ Furthermore, the same ExbD residues that mediate interactions with the TonB periplasmic domain also form a homodimerization interface in the absence of PMF and TonB, suggesting a possible role of ExbD homodimerization in preventing unproductive transport-relevant interactions with TonB in the absence of PMF.⁸⁵ However, there is evidence of a PMF-independent—but ExbB-dependent—association between the ExbD and TonB periplasmic domains outside of the aforementioned regions, as judged by resistance to degradation by proteinase K.⁸⁶ The relevance of this interaction is not known, but perhaps during the initial assembly of TonB into a functional CM complex, ExbB helps orient the complex for efficient PMF-dependent conformational changes in TonB that are mediated between different regions in the ExbD and TonB periplasmic domains.

TonB is a 239-residue integral CM protein possessing several functional domains (Figure 1.4.3). Residues 1-32 constitute the cytoplasmic tail region and transmembrane

domain, of which residues S16 and H20 are essential both for PMF-dependent conformational cycling and transport.⁸⁷ The spacing between these two residues is also important; each of the other residues in the transmembrane domain can be substituted with alanine without significant loss of activity. The inactivity of TonB H20A mutant is not due to lack of a protonatable side-chain, as the non-protonatable H20N mutation maintains full TonB activity.⁸⁸ Therefore, it is likely that TonB responds to variations in PMF indirectly, via ExbD and/or ExbB.

Separated from the transmembrane domain by a short linker is a proline-rich section comprising residues 66-102; the middle of this region is defined by a (EP)₆ and (KP)₆ segment. Unlike the transmembrane domain, the polyproline domain can be deleted from TonB without significant loss in activity unless the periplasm is osmotically expanded.⁸⁹ EPR-based distance measurements between spin labels in the isolated polyproline segment indicate that it exists as an extended polyproline II-like conformation of sufficient length to span the periplasm.⁹⁰ It is therefore thought that the sole purpose of this segment is to confer structural rigidity to TonB so that it can easily traverse the periplasm and associate with the OM.

Another flexible linker joins the polyproline region to the highly basic C-terminal globular domain (pI = 10.8), which consists of residues ~150-239. This region is required for association with the OM transport proteins. The YP motif, consisting of residues 163 and 164, is very highly conserved amongst TonB orthologs. In crystal structures of the TonB C-terminal domain in complex with two different TBDTs, Y163 appears to participate in recognition and/or binding to the OM transport proteins.^{91,92}

Seven functionally important, but not irreplaceable, residues have also been identified in the TonB C-terminal domain.⁹³⁻⁹⁵ These amino acids—Y163, G186, F180, F202, W213, Y215 and F230—showed differential sensitivities to various colicins and phages, and in their ability to transport ferrichrome.⁹⁴ Thus, it was proposed that these residues are important for discriminating amongst the many transporters that TonB binds.

As with ExbB and ExbD, the structure of full-length TonB is not known. However, several structures of the TonB C-terminal domain have been determined by both NMR and X-ray crystallography, and construct-dependent structural plasticity is evident (Figure 1.4.4). TonB constructs longer than residue ~155 are monomeric in solution and structurally similar, even when bound to cognate TBDTs.^{91,92,96,97} In contrast, TonB constructs shorter than residue ~155 yield strand-exchanged intertwined dimeric structures.^{98,99} TonB is known to undergo two PMF- and ExbB/D-dependent conformational transitions *in vivo*,^{76,86} and at least one of these conformers is known to be a PMF-dependent dimer,^{93,100} lending potential physiological credibility to both sets of TonB C-terminal domain structures. Furthermore, it is of interest that the length-dependence of TonB constructs on dimerization seems to originate somewhere in the proximity of residue 155, which is also near the site of the PMF-dependent interaction between TonB and ExbD that is thought to drive conformational changes in TonB. Consistent with this idea, disulfide cross-linked TonB dimers were unable to form *in vivo* upon the deletion of 9 and 11 residues centered on TonB Q160.¹⁰¹

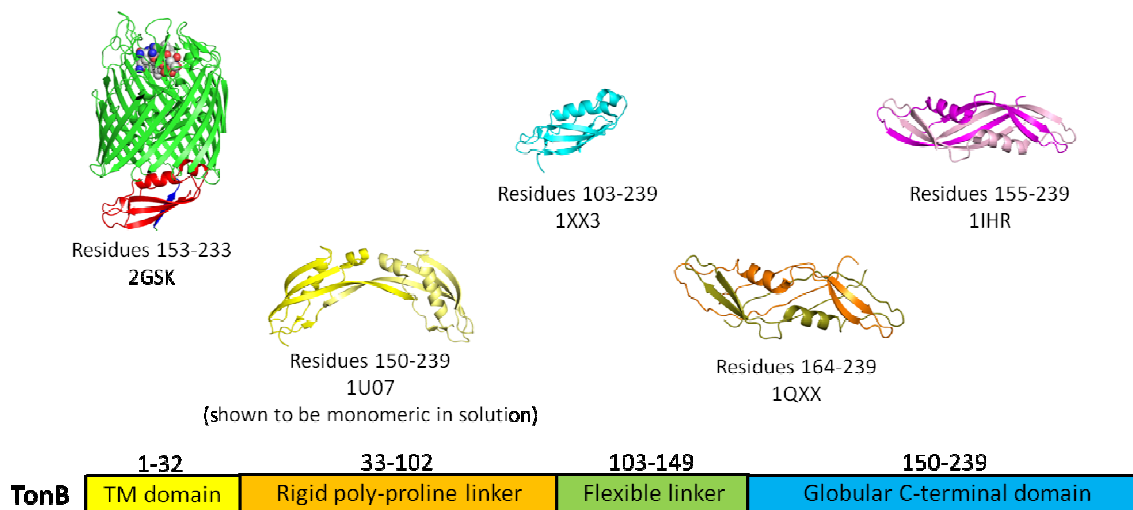


Figure 1.4.4. TonB Structural Plasticity. The length of TonB construct apparently influences TonB dimerization. TonB constructs longer than residue ~155 are all monomeric in solution and of similar structure (structure 1U07 was shown to be monomeric in solution, and each protomer within the crystallographic dimer is very similar to the other two monomeric structures), and constructs shorter than residue ~155 are strand-exchanged, intertwined dimers. Structure 2GSK is the TonB:BtuB complex.

Based on evidence from *in vivo* disulfide cross-linking and sucrose density gradient fractionation, it has been proposed that the dimeric conformation of TonB occurs early in the transport cycle, before high-affinity association with the OM transporters⁹³. Interestingly, the TonB C-terminal domain shares sequence homology with several *E.coli* PG-binding proteins, and the intertwined dimeric conformation of TonB determined by X-ray crystallography shares structural homology with the *E.coli* PG-binding LysM domain, with conserved solvent-exposed residues on TonB mapping to the LysM PG-binding site.¹⁰² Furthermore, in the same study the C-terminal region of TonB was shown to bind PG experimentally. These results led to speculation that the function of dimerized TonB might be to span the periplasm and systematically survey the underside of the PG for OM transporters. However, it has also been reported that the intertwined

dimeric conformation of TonB determined by X-ray crystallography does not faithfully represent the dimerized TonB conformation that occurs *in vivo*.⁹⁵ It is indeed possible that overexpression, crystallization, the lack of a functional transmembrane domain, or absence of interactions with ExbB and ExbD may affect the conformation of TonB in a manner that is not physiologically relevant. On the other hand, this conclusion was based on sparse and somewhat ambiguous *in vivo* disulfide cross-linking data, the pattern of which could be reflective of conformational intermediates or encounter complexes assumed during TonB structural cycling rather than stable conformations. These disparate results, combined with conflicting biochemical data (that is also dependent on TonB construct size; discussed in more detail below) regarding the affinity and stoichiometry of the interaction between TonB and its cognate transporters, warrant further examination in the future.

The TonB-dependent transporters that reside in the OM are all large, multi-domain proteins that are structurally very similar.¹⁰³ Structures for five of the seven TBDTs in *E.coli* have been determined at atomic resolution, in addition to seven unique TBDT structures from other Gram-negative bacteria. The canonical TBDT structure includes a 22-stranded β -barrel whose strands are connected by short periplasmic turns and long extracellular loops (Figure 1.4.5). Since a 22-stranded barrel creates a large hole in the OM, these proteins also contain a pore-occluding globular luminal domain at the N-terminus that restricts passage of solutes and water. In *E.coli*, the ferric citrate transporter FecA possesses an additional globular extension at the extreme N-terminus that functions in the substrate-dependent transcriptional up-regulation of proteins on the

ferric citrate import operon (Figure 1.4.5).¹⁰⁴ Together with the long extracellular loops, the pore-occluding luminal domain confers substrate-binding specificity extracellularly, and specificity for TonB periplasmically. The presence of the pore-occluding luminal domain clearly suggests that currently unknown conformational changes must occur within the transporter, most likely potentiated by TonB, in order for substrate to pass through the OM into the periplasm.

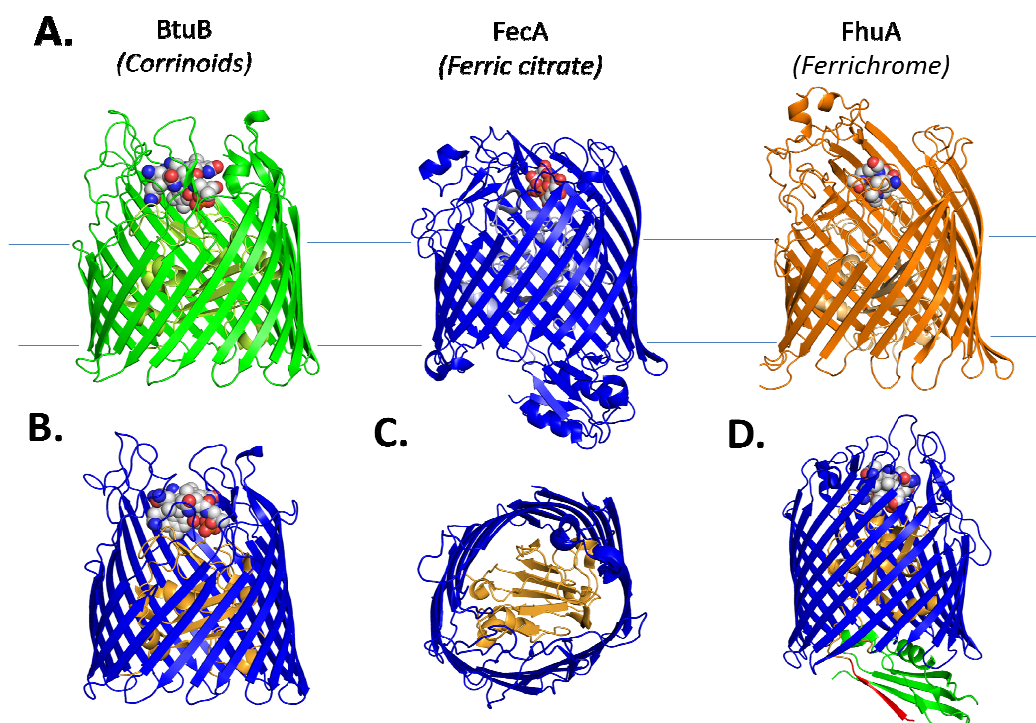


Figure 1.4.5. TonB-dependent Transporter Structure. (A) The structures of three of the seven TBDTs from *E. coli*: BtuB, which transports vitamin B₁₂ and other corrinoids (1NQH); FecA, the ferric citrate transporter (1KMP, with the N-terminal signaling domain aligned from FpvA, 2W16); and FhuA, the ferrichrome transporter (1BY5). These proteins are very similar structurally, all containing 22 transmembrane β -strands that are connected by long extracellular loops and short periplasmic turns. An N-terminal globular luminal domain restricts passage through the pore created by the large barrel. (B) The luminal domain of BtuB is colored orange for easier viewing, and (C) is shown from an extracellular perspective. (D) The structure of BtuB in complex with the C-terminal domain of TonB (2GSK). TonB is shown in green, and the BtuB Ton box is colored in red.

At the periplasmic face of the luminal domain is a highly conserved motif called the “Ton box” (consensus sequence: DTLVVTA). Recently published crystal structures of the TonB C-terminal domain in complex with BtuB (the *E.coli* vitamin B₁₂ transporter)⁹¹ and FhuA (the *E.coli* ferrichrome transporter)⁹² confirmed years of biochemical and bacteriological data that had long implicated the Ton box as the TonB-binding epitope. In these structures, TonB associates with the transporter through a β -strand exchange mechanism involving the TonB C-terminal domain and the Ton box of the TBDT (Figure 1.4.5). Current models of TBDT function involve, in part, a transmembrane allosteric event wherein extracellular substrate binding shifts the Ton box conformational equilibrium on the periplasmic side of the transporter, presumably facilitating interactions with TonB, which would then drive conformational changes in the luminal domain that lead to substrate translocation. The crux of this model is based on SDSL-EPR data wherein the Ton box undergoes a substrate-induced order-to-disorder transition and unfolds by up to 20-30 Å into the periplasm (Figure 1.4.6).^{35,49,105,106} This notion is supported by *in vivo* cross-linking data in which substrate-loaded BtuB,¹⁰⁷ FecA,¹⁰⁸ and FhuA¹⁰⁹ all show increased cross-linking with TonB compared to their apo counterparts.

Then again, the simplistic interpretation of this model was challenged after more thorough *in vitro* analyses. Although the substrate-induced shift in the Ton box conformational equilibrium is spectroscopically evident in BtuB, substrate-induced order-to-disorder changes in EPR spectra from the FecA Ton box are less apparent, and the

FhuA Ton box was determined to be constitutively unfolded.¹¹⁰ However, it is possible that detergents used during FhuA purification affected the Ton box configuration; certain detergents are indeed known to modulate Ton box energetics in BtuB.¹⁸ Furthermore, as will be discussed in more detail in Chapter 3, the substrate-induced unfolding of the Ton box is not apparent in TBDT crystal structures, although this apparent discrepancy has been attributed to impositions of the crystal lattice and solutes used in the crystallization buffers.^{27,111-113} Certainly, the nature and importance of substrate-induced modulation of Ton box configurations requires further detailed analysis.

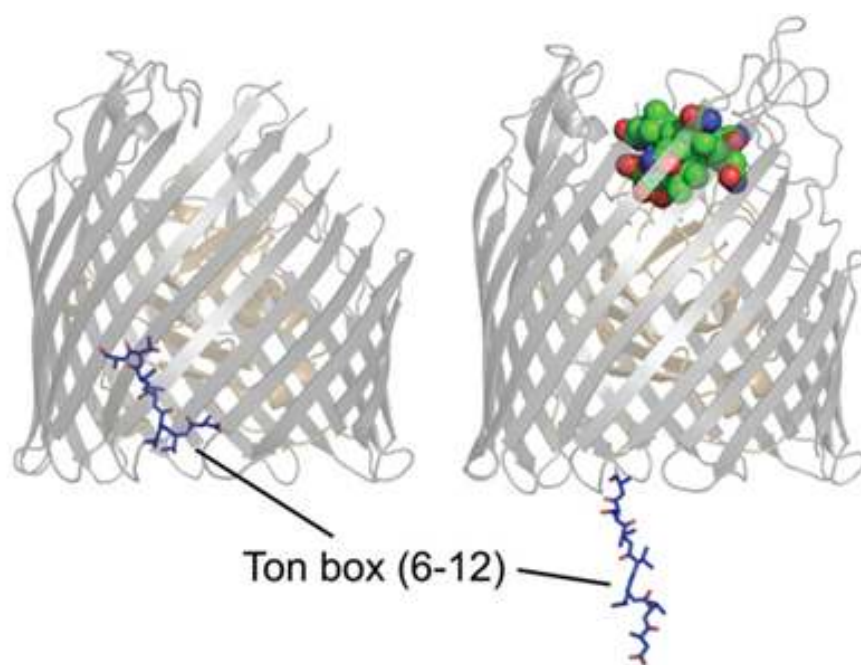


Figure 1.4.6. Substrate-Induced Unfolding of the Ton Box. The BtuB Ton box (residues 6-12) has been shown to undergo a substrate-induced shift in conformational equilibrium in which the Ton box unfolds by about 20-30 Å into the periplasm upon substrate binding. Figure modified from Freed et al.²⁷

Despite the level of sequence conservation, TonB-dependent functions are only weakly sensitive to Ton box mutations. A systematic mutational analysis of the BtuB Ton box (residues 6-12) revealed that proline mutations to positions 8 and 10, and a glycine mutation to position 10, were the only substitutions that dramatically interfered with TonB-dependent functions *in vivo*.^{114,115} These mutations did not abrogate association of BtuB with TonB, but were rather found to dramatically affect the pattern of disulfide cross-linking between the BtuB Ton box and TonB. Collectively, the data indicated that the TonB-transporter interaction is highly geometrically and orientationally specific, rather than dependent on specific side-chain or peptide backbone interactions. Interestingly, the L8P and V10P mutations were also shown to unfold the Ton box in a substrate-independent manner, indicating that proper backbone geometry is likely more important than the equilibrium distribution of Ton box conformations.¹¹⁶

The TBDTs share several conserved features in addition to the Ton box. Structure-based sequence alignments of the known TBDT structures from *E.coli* have revealed that most conservation occurs in the luminal domain, which contains nine highly conserved sequence motifs, whereas the barrel residues are poorly conserved in sequence overall, with an asymmetric distribution of conserved residues occurring between β -strands 9-18.¹¹⁷ This result implies that residues within the luminal domain are probably more important for TonB action, whereas functional barrel residues are more likely to be substrate-specific and relevant to signal transduction. Such a conclusion would not be surprising, considering that the obvious structural rearrangements which must occur for transport lie within the luminal domain—a region that also contains the Ton box. Two of

the most highly conserved sequences in TBDTs are the PGV and IRG motifs.¹¹⁷ Both motifs are located near the substrate-binding site in the luminal domain and are locked into position through multiple hydrogen bonds and electrostatic interactions with adjacent charge clusters. Although the specific role of these structural motifs is unclear, multiple studies have shown that mutagenesis of these motifs affects TBDT function.¹¹⁸⁻¹²⁰

FecA and FhuA contain a motif called the “switch helix” in the luminal domain just upstream of the Ton box, which in the crystal structures is observed to unwind upon substrate binding, moving the Ton box by as much as 20 Å. The lack of a switch helix in other TBDTs does not appear to affect substrate-induced transmembrane signaling, and removal of the FhuA switch helix resulted in only a small reduction in transport activity.¹¹⁸ Conserved charged residues in BtuB, R14 in the luminal domain and D316 on the barrel, were recently shown to play a surrogate role for the switch helix by mediating the Ton box equilibrium.¹⁰⁵ Another conserved interaction occurs between the β -cantilever and latch motifs. The β -cantilever comprises extracellular loops 7 and 8, which fold inward towards the barrel lumen, breaking the regular pattern of inter-strand hydrogen bonding between β -strands 12 and 13 near the extracellular end of the barrel. The β -cantilever bears a striking resemblance to porin selectivity filters, and interacts with the latch motif, which is located in the luminal domain and is itself surrounded by several conserved residues.¹¹⁷ The function of these motifs is currently not known. Due to the inherent difficulties in reconstituting the functional TonB-dependent system, trapping transient or excited conformational states, and viewing allostery conveyed

through a rigid β -barrel, a more comprehensive structural understanding of signaling and transport remains unknown.

1.4.4 Parasitization of the Outer Membrane Transporters by Colicins. As was mentioned earlier, the TBDTs are targeted by several exogenous toxic agents, such as colicins. The colicins are bacteriocidal proteins that are secreted by, and against, certain strains of *E.coli*. These proteins hijack TBDTs for entry into the periplasm, after which they either form pores in the CM or are transported into the cytosol where various enzymatic activities lead to cell death.¹²¹ Colicins are multifaceted proteins comprised of a central receptor-binding domain, an N-terminal translocation domain, and a C-terminal cytotoxic domain. The colicins can be binned into two major groups—group A, which uses the Tol system for OM translocation, and group B, which uses the TonB system for OM translocation.¹²¹ Similar to the transporters they parasitize, the translocation domains of group A and B colicins possess Tol and Ton boxes, respectively, to facilitate the periplasmic interactions required for transport. Although the exact mechanism of OM translocation is still poorly understood, it is clear that groups A and B are unique in this regard. However, it is generally thought that the receptor-binding domain associates with the *E.coli* cell surface through interactions with a TBDT, after which the translocation domain crosses the OM and associates with either TonB or components of the Tol system, which then results in the subsequent transport of the cytotoxic domain into the periplasm.

Whereas group A colicins typically recruit a second OM protein for translocation, most group B colicins use a single TBDT for binding and translocation. For example, the

receptor-binding domain of colicin Ia associates with Cir, which initiates interactions between the Cir Ton box and TonB. Subsequently, energy from the PMF is likely used for transit of the translocation domain across the OM into the periplasm, after which the Ton box of colicin Ia associates with TonB. Finally, it is thought that the colicin Ia-TonB interaction mediates transport of the cytotoxic domain into the periplasm.¹²¹

On the other hand, Group A colicins utilize a second OM protein such as OmpF or TolC for translocation across the OM, and might not require energy from the PMF for translocation across the OM.¹²¹ The translocation domains of group A colicins contain a Tol box, which interacts with one or more of the five components of the Tol system. Although the physiological role of the Tol system is not known, it is thought to participate in the maintenance of cell envelope integrity, LPS assembly, and cell division.¹²²⁻¹²⁴ Regardless, the Tol system shares similarities with the TonB system. As was mentioned earlier, TolQ/R can be substituted for ExbB/D and recapitulate ~10% of TonB-dependent transport activity.⁷³ Moreover, like ExbB and ExbD, TolQ and TolR are embedded in the CM and use PMF to drive conformational changes in the TonB homolog, TolA, which interacts with the periplasmic TolB and OM-associated Pal proteins.¹²⁵⁻¹²⁸ Different group A colicins use various subsets of the Tol system to gain entry into the periplasm; for example, colicin E1 uses TolA/Q, whereas colicin E3 requires TolA/B/Q/R.¹²¹

Of the group A proteins, colicins A and E1-E9 target the *E.coli* vitamin B₁₂ transporter, BtuB. Colicin E3 hijacks BtuB, recruits OmpF for translocation into the periplasm, where subsequently its cytotoxic domain enters the cytosol to execute RNase

activity that leads to cell death. Colicin E3 is of particular interest because the crystal structure of the receptor-binding domain of Colicin E3 (ColE3R) in complex with BtuB was recently published, revealing several interesting aspects of the interaction (Figure 1.4.7).¹²⁹ Most obviously, it is apparent that ColE3R binds BtuB competitively with vitamin B₁₂, which is consistent with the observation that the isolated receptor-binding domain from colicin E9 inhibits cell growth of vitamin B₁₂-dependent cells.¹³⁰ Whereas 13 BtuB residues are used to bind vitamin B₁₂, the binding interface between BtuB and ColE3R is much more extensive, involving 29 residues of BtuB and 27 residues of ColE3R. The vitamin B₁₂ and ColE3R binding interfaces share five BtuB residues—Y229, N276, T289, R497, and Y579—each of which are on extracellular loops (Figure 1.4.7).

The fact that these two ligands bind competitively was not surprising, given the finding that colicin E3 requires the Tol system for OM translocation, whereas vitamin B₁₂ is dependent on TonB recruitment for transport, presumably through the substrate-induced unfolding of the Ton box that was discussed earlier. Furthermore, a closer look at the ColE3R-BtuB structure reveals that electron density is clearly resolvable for the N-terminal residues S4 and P5, which are disordered in the apo BtuB structure.^{84,129} This raised the intriguing possibility that colicin E3 not only binds competitively with vitamin B₁₂, but also stabilizes the folded conformation of the BtuB Ton box in an apparent shielding mechanism from TonB. This result was later confirmed by SDSL-EPR; ColE3R was found to competitively bind with vitamin B₁₂ and refold the Ton box, even in the presence of certain detergents or transport-defective mutations that are known to

unfold the Ton box.¹³¹ Future studies will be required for delineation and comparison of the signaling pathways used by ColE3R and vitamin B₁₂, which both bind BtuB extracellularly, but transduce opposite signals across the OM, presumably for the selective recruitment of TonB or components of the Tol network.

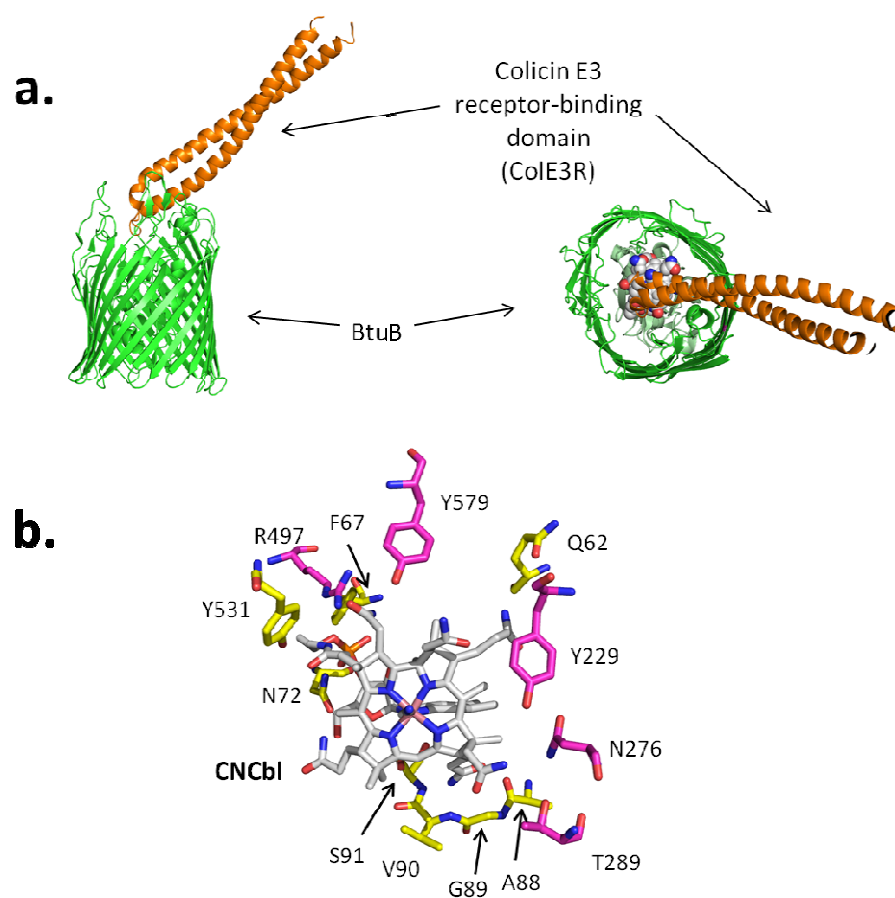


Figure 1.4.7. Interaction of Colicin E3R with BtuB. (a) The coiled-coil α -helical receptor-binding domain of colicin E3 binds BtuB primarily with a loop at the apex between helices. The binding site partially overlaps with vitamin B₁₂. (b) The BtuB residues that bind vitamin B₁₂. Residues that also bind ColE3R are colored purple.

1.4.5 Remaining Questions. Despite over 45 years of research in the field, several key questions regarding the TonB-dependent transport mechanism remain unresolved. At the CM, it is not known which components of the CM complex harvest the energy of the PMF. It has been suggested that TonB responds indirectly to changes in PMF;⁸⁸ therefore ExbB, ExbD, or both must be involved in this regard. Recently, ExbD was proposed to be a likely candidate due to the requirement of protonatable residue D25 for the mediation of PMF-dependent conformational changes in TonB.⁸⁶ High-resolution structures of the CM protein transmembrane domains could provide valuable insight towards elucidation of the proton translocation pathway. The mechanism by which the PMF is harnessed, and the amount of energy that is tapped, certainly warrant further analysis.

Another key question involves how the PMF is used by ExbD and/or ExbB to energize TonB; specifically, how many steps in the transport cycle require energy, at what points during the transport cycle does energization occur, and what is the structural basis of TonB energization? It is thought that the PMF-dependent periplasmic interaction between ExbD and TonB drives conformational changes in the C-terminal domain of TonB, but the nature of these conformational changes is vague. Since TonB is known to exist as a dimer at some point during transport—and data from the Postle group suggests that the dimeric conformation occurs early in the transport cycle—it has been proposed that the PMF is used to assemble TonB into a dimerized conformation preceding transport. Consistent with this idea, a “propeller” model of transport has been introduced.^{74,98} In this model, intertwined dimeric TonB associates with the TBDT, and

the PMF is used by ExbB and ExbD to drive a rotary motion in TonB that mechanically drives conformational changes in the TBDT luminal domain for substrate passage. This model was an attractive possibility due to the known homology between ExbB/ExbD and the MotA/MotB components of the flagellar motor, but fails to account for a stator about which the rotor must turn in order to transduce mechanical force. The “membrane surveillance” model also accounts for a PMF-dependent TonB dimer preceding the transport step.¹⁰² In this model, the PG-binding ability of the intertwined TonB dimer allows it to scan the underside of the PG for TBDTs, turning a three-dimensional search into an efficient and directed two-dimensional one. Further supporting this model, it is known that both FepA (the *E.coli* ferric enterobactin transporter) and OmpF (which associates with BtuB in the OM) interact with the PG.¹⁰² More work is required to elucidate the conformational landscape available to TonB, especially with respect to oligomerization in full-length or near full-length constructs.

Characterization of the interaction between TonB and its cognate TBDTS has yielded disparate results and requires further analysis. *In vivo* cross-linking studies have demonstrated that substrate binding increases the amount of TBDT cross-linking with TonB, indicating that the substrate-induced unfolding of the Ton box into the periplasm likely increases the affinity of the interaction.¹⁰⁷⁻¹⁰⁹ However, quantitative *in vitro* binding studies have given different results. Surface plasmon resonance (SPR) experiments using a soluble *Pseudomonas aeruginosa* TonB fragment lacking only the CM transmembrane domain demonstrated that interactions between TonB and the *Pseudomonas* pyoverdine transporter FpvA have apparent affinities in the low

micromolar range, and that the affinities are not affected by substrate binding.¹³² Ton box energetics may have been skewed by the choice of membrane mimetic, or perhaps the system was otherwise not reconstituted in a manner that accurately reflects the endogenous environment at the OM. Other alternative mechanisms may also be responsible for this unexpected result. The SPR results with FpvA were comparable with isothermal titration calorimetry data from the homologous HasB system in *Serratia marcescens*, where it has been shown that the affinities between HasB and the heme transporter HasR, and also TonB and HasR, are not modulated by substrate binding as a result of entropy-enthalpy compensation.¹³³ In *E.coli*, data is limited to SPR and analytical ultracentrifugation investigations on FhuA with various TonB fragments. These results from the Coulton group are quite variable and sometimes contradicting, spanning a broad range of affinities (~5 nM – 1 μM) that were positively, negatively, or not at all affected by substrate binding, depending on the TonB construct and SPR sensor chip used.¹³⁴⁻¹³⁶ However, the authors' overall interpretation seemed to suggest that, through multiple kinetic steps, TonB forms a 2:1 complex with FhuA, with the formation of this complex and high-affinity binding requiring the TonB polyproline segment and substrate. Based on this interpretation, the TonB dimer would form at a later step in the transport cycle, upon association with the transporter in the OM. The conclusion that two TonB molecules are required to drive transport per TBDT seems unlikely, given the severely limiting amount of TonB in the cell compared to the other components of the TonB system. A more comprehensive quantitative analysis regarding the affinity of TonB for the TBDTs using alternate methods is required to verify or dispel these results.

At the OM, the nature of conformational changes in the luminal domain that allow substrate passage through the lumen of the barrel remain unknown. Some groups have proposed a “ball-and-chain” mechanical pulling model for transport, whereby TonB action is used to dislodge the entire globular luminal domain from inside of the barrel. In one such study, the substrate-dependent susceptibility of luminal domain cysteine mutants to fluorescein labeling *in vivo* was proposed to reflect this mechanism.¹³⁷ However, this conclusion was based on paltry and somewhat ambiguous results, and the authors did not consider alternative mechanisms that might also explain the data. Other groups have proposed that the luminal domain may be partially removed from the barrel, simply undergo conformational rearrangements within the barrel, or a combination of both. For example, a steered molecular dynamics simulation using the TonB-BtuB crystal structure indicated that TonB was capable of transmitting sufficient force to BtuB to partially unfold the luminal domain, through a small yet strong contact interface.¹³⁸ However, in this simulation approximately 20 nm of luminal domain unfolding was required to accommodate passage of vitamin B₁₂ through the BtuB barrel. Since the OM and CM are separated by a periplasmic distance of 15-20 nm, it seems likely that this “pulling” model would require a significant lateral element of pulling force, a situation that requires further experimental support.

A detailed understanding of the substrate-induced signaling pathway through TBDTs remains elusive. Recently however, two key charged residues in BtuB were found to be important modulators of the Ton box equilibrium—R14, which is two residues removed from the Ton box, and D316 on the barrel. In the BtuB crystal

structures, the R14 rotamer changes when substrate binds, largely disengaging from the electrostatic interaction with D316.⁸⁴ A two-mutant thermodynamic cycle coupled with SDSL-EPR not only demonstrated that the R14A/D316A mutation unfolded the Ton box, but it was shown that the interaction energy between these residues was approximately equal to the substrate-induced shift in the Ton box equilibrium.¹⁰⁵ Another interesting study used evolution-based statistical coupling analysis to identify residues in FecA that underlie substrate-dependent transcriptional regulation.¹³⁹ It is likely that allostery conveyed long distances through rigid β -barrels is facilitated by low-amplitude correlated motions and involves subtle changes to amino acid rotamers or modifications to the hydrogen bonding network.¹⁴⁰ Identification of signaling components used by ColE3R may yield additional insight into the complexity, or simplicity, of transmembrane signaling through β -barrel membrane proteins. More such mutagenesis studies, perhaps using the detailed structure-based sequence alignments of TBDTs as a guide,¹¹⁷ are necessary to delineate the signaling pathway.

In this dissertation, Chapter 5 will compare components of the transmembrane signaling pathways utilized by ColE3R and vitamin B₁₂. In Chapter 6, the structural and biochemical characterization of the interaction of TonB with three of its cognate transporters will be described, emphasizing the role of the Ton box, substrate, and ColE3R on the interaction. From this data, advancements to our understanding of the transport mechanism will also be discussed.

1.5 References

1. Stone, T.J., Buckman, T., Nordio, P.L. & McConnell, H.M. Spin-labeled biomolecules. *Proceedings of the National Academy of Sciences of the United States of America* **54**, 1010-7 (1965).
2. Todd, A.P., Cong, J.P., Levinthal, F., Levinthal, C. & Hubbell, W.L. Site-Directed Mutagenesis of Colicin-E1 Provides Specific Attachment Sites for Spin Labels Whose Spectra Are Sensitive to Local Conformation. *Proteins-Structure Function and Genetics* **6**, 294-305 (1989).
3. Altenbach, C., Flitsch, S.L., Khorana, H.G. & Hubbell, W.L. Structural Studies on Transmembrane Proteins .2. Spin Labeling of Bacteriorhodopsin Mutants at Unique Cysteines. *Biochemistry* **28**, 7806-7812 (1989).
4. McHaourab, H.S., Lietzow, M.A., Hideg, K. & Hubbell, W.L. Motion of spin-labeled side chains in T4 lysozyme. Correlation with protein structure and dynamics. *Biochemistry* **35**, 7692-704 (1996).
5. Singer, S.J. & Nicolson, G.L. The fluid mosaic model of the structure of cell membranes. *Science* **175**, 720-31 (1972).
6. Engelman, D.M. Membranes are more mosaic than fluid. *Nature* **438**, 578-580 (2005).
7. Spiegel, S., Foster, D. & Kolesnick, R. Signal transduction through lipid second messengers. *Current Opinion in Cell Biology* **8**, 159-167 (1996).
8. Simons, K. & Ikonen, E. Functional rafts in cell membranes. *Nature* **387**, 569-572 (1997).

9. Maxfield, F.R. & Tabas, I. Role of cholesterol and lipid organization in disease. *Nature* **438**, 612-621 (2005).
10. Columbus, L., Nakamoto, R.K. and Cafiso, D.S. Membrane Proteins: Properties. in *Wiley Encyclopedia of Chemical Biology* 1-10 (2008).
11. Wallin, E. & von Heijne, G. Genome-wide analysis of integral membrane proteins from eubacterial, archaean, and eukaryotic organisms. *Protein Science* **7**, 1029-1038 (1998).
12. Klabunde, T. & Hessler, G. Drug design strategies for targeting G-protein-coupled receptors. *Chembiochem* **3**, 929-944 (2002).
13. Russell, R.B. & Eggleston, D.S. New roles for structure in biology and drug discovery - Foreword. *Nature structural biology* **7**, 928-930 (2000).
14. Berman, H.M., Westbrook, J., Feng, Z., Gilliland, G., Bhat, T.N., Weissig, H., Shindyalov, I.N., and Bourne, P.E. The Protein Data Bank. *Nucleic acids research* **28**, 235-242 (2000).
15. White, S.H. <http://blanco.biomol.uci.edu/>.
16. Tate, C.G. & Stevens, R.C. Growth and excitement in membrane protein structural biology. *Current opinion in structural biology* **20**, 399-400 (2010).
17. Bill, R.M. et al. Overcoming barriers to membrane protein structure determination. *Nature Biotechnology* **29**, 335-340 (2011).
18. Fanucci, G.E., Lee, J.Y. & Cafiso, D.S. Membrane mimetic environments alter the conformation of the outer membrane protein BtuB. *Journal of the American Chemical Society* **125**, 13932-3 (2003).
19. Lee, A.G. Cell biology - A greasy grip. *Nature* **438**, 569-570 (2005).

20. Lee, A.G. How lipids affect the activities of integral membrane proteins. *Biochimica Et Biophysica Acta-Biomembranes* **1666**, 62-87 (2004).
21. White, S.H., Ladokhin, A.S., Jayasinghe, S. & Hristova, K. How membranes shape protein structure. *Journal of Biological Chemistry* **276**, 32395-32398 (2001).
22. Andersen, O.S. & Koeppe, R.E. Bilayer thickness and membrane protein function: An energetic perspective. *Annual Review of Biophysics and Biomolecular Structure* **36**, 107-130 (2007).
23. Mozzarelli, A. & Rossi, G.L. Protein function in the crystal. *Annual Review of Biophysics and Biomolecular Structure* **25**, 343-365 (1996).
24. Puljung, M.C. & Zagotta, W.N. Labeling of Specific Cysteines in Proteins Using Reversible Metal Protection. *Biophysical journal* **100**, 2513-2521 (2011).
25. Fleissner, M.R. et al. Site-directed spin labeling of a genetically encoded unnatural amino acid. *Proceedings of the National Academy of Sciences of the United States of America* **106**, 21637-42 (2009).
26. Lietzow, M.A. & Hubbell, W.L. Motion of spin label side chains in cellular retinol-binding protein: correlation with structure and nearest-neighbor interactions in an antiparallel beta-sheet. *Biochemistry* **43**, 3137-51 (2004).
27. Freed, D.M., Horanyi, P.S., Wiener, M.C. & Cafiso, D.S. Conformational Exchange in a Membrane Transport Protein Is Altered in Protein Crystals. *Biophysical Journal* **99**, 1604-1610 (2010).
28. Frauenfelder, H., Sligar, S.G. & Wolynes, P.G. The Energy Landscapes and Motions of Proteins. *Science* **254**, 1598-1603 (1991).

29. Cuello, L.G., Cortes, D.M. & Perozo, E. Molecular architecture of the KvAP voltage-dependent K⁺ channel in a lipid bilayer. *Science* **306**, 491-5 (2004).
30. Perozo, E., Cortes, D.M. & Cuello, L.G. Structural rearrangements underlying K⁺-channel activation gating. *Science* **285**, 73-8 (1999).
31. Perozo, E., Cortes, D.M. & Cuello, L.G. Three-dimensional architecture and gating mechanism of a K⁺ channel studied by EPR spectroscopy. *Nature structural biology* **5**, 459-469 (1998).
32. Dong, J., Yang, G. & McHaourab, H.S. Structural basis of energy transduction in the transport cycle of MsbA. *Science* **308**, 1023-8 (2005).
33. Smirnova, I. et al. Sugar binding induces an outward facing conformation of LacY. *Proceedings of the National Academy of Sciences of the United States of America* **104**, 16504-9 (2007).
34. Claxton, D.P. et al. Ion/substrate-dependent conformational dynamics of a bacterial homolog of neurotransmitter:sodium symporters. *Nature structural & molecular biology* **17**, 822-9 (2010).
35. Merianos, H.J., Cadieux, N., Lin, C.H., Kadner, R.J. & Cafiso, D.S. Substrate-induced exposure of an energy-coupling motif of a membrane transporter. *Nature structural biology* **7**, 205-9 (2000).
36. Oh, K.J. et al. Organization of diphtheria toxin T domain in bilayers: a site-directed spin labeling study. *Science* **273**, 810-2 (1996).
37. Hubbell, W.L., Cafiso, D.S. & Altenbach, C. Identifying conformational changes with site-directed spin labeling. *Nature structural biology* **7**, 735-9 (2000).

38. Mollaaghababa, R., Steinhoff, H.J., Hubbell, W.L. & Khorana, H.G. Time-resolved site-directed spin-labeling studies of bacteriorhodopsin: Loop-specific conformational changes in M. *Biochemistry* **39**, 1120-1127 (2000).
39. Steinhoff, H.J. et al. Time-Resolved Detection of Structural-Changes during the Photocycle of Spin-Labeled Bacteriorhodopsin. *Science* **266**, 105-107 (1994).
40. Farahbakhsh, Z.T., Hideg, K. & Hubbell, W.L. Photoactivated Conformational-Changes in Rhodopsin - a Time-Resolved Spin-Label Study. *Science* **262**, 1416-1419 (1993).
41. Shin, Y.K., Levinthal, C., Levinthal, F. & Hubbell, W.L. Colicin-E1 Binding to Membranes - Time-Resolved Studies of Spin-Labeled Mutants. *Science* **259**, 960-963 (1993).
42. Jiang, X.Q. et al. Ligand-specific opening of a gated-porin channel in the outer membrane of living bacteria. *Science* **276**, 1261-1264 (1997).
43. McCoy, J. & Hubbell, W.L. High-pressure EPR reveals conformational equilibria and volumetric properties of spin-labeled proteins. *Proceedings of the National Academy of Sciences of the United States of America* **108**, 1331-6 (2011).
44. Hemminga, M.A., Berliner, L.J. (ed.) *ESR Spectroscopy in Membrane Biophysics*, (Springer, New York, NY, 2007).
45. Altenbach, C., Greenhalgh, D.A., Khorana, H.G. & Hubbell, W.L. A Collision Gradient-Method to Determine the Immersion Depth of Nitroxides in Lipid Bilayers - Application to Spin-Labeled Mutants of Bacteriorhodopsin. *Proceedings of the National Academy of Sciences of the United States of America* **91**, 1667-1671 (1994).

46. Ellena, J.F., Lackowicz, P., Montgomery, H. & Cafiso, D.S. Membrane Thickness Varies Around the Circumference of the Transmembrane Protein BtuB. *Biophysical journal* **100**, 1280-7 (2011).
47. Altenbach, C., Oh, K.J., Trabanino, R.J., Hideg, K. & Hubbell, W.L. Estimation of inter-residue distances in spin labeled proteins at physiological temperatures: Experimental strategies and practical limitations. *Biochemistry* **40**, 15471-15482 (2001).
48. Pannier, M., Veit, S., Godt, A., Jeschke, G. & Spiess, H.W. Dead-time free measurement of dipole-dipole interactions between electron spins. *Journal of magnetic resonance* **142**, 331-340 (2000).
49. Xu, Q., Ellena, J.F., Kim, M. & Cafiso, D.S. Substrate-dependent unfolding of the energy coupling motif of a membrane transport protein determined by double electron-electron resonance. *Biochemistry* **45**, 10847-54 (2006).
50. Van Eps, N. et al. Interaction of a G protein with an activated receptor opens the interdomain interface in the alpha subunit. *Proceedings of the National Academy of Sciences of the United States of America* **108**, 9420-4 (2011).
51. Altenbach, C., Kusnetzow, A.K., Ernst, O.P., Hofmann, K.P. & Hubbell, W.L. High-resolution distance mapping in rhodopsin reveals the pattern of helix movement due to activation. *Proceedings of the National Academy of Sciences of the United States of America* **105**, 7439-44 (2008).
52. Arias, C.A. & Murray, B.E. Antibiotic-resistant bugs in the 21st century--a clinical super-challenge. *The New England journal of medicine* **360**, 439-43 (2009).

53. Kardar, S.S. Antibiotic Resistance: New Approaches to a Historical Problem. in *ActionBioscience, Org.* (American Institute of Biological Sciences, 2005).
54. Taubes, G. The bacteria fight back. *Science* **321**, 356-61 (2008).
55. Graham, L.L., Harris, R., Villiger, W. & Beveridge, T.J. Freeze-substitution of gram-negative eubacteria: general cell morphology and envelope profiles. *Journal of Bacteriology* **173**, 1623-33 (1991).
56. Nikaido, H. & Vaara, M. Molecular-Basis of Bacterial Outer-Membrane Permeability. *Microbiological Reviews* **49**, 1-32 (1985).
57. Nikaido, H. & Nakae, T. The outer membrane of Gram-negative bacteria. *Advances in microbial physiology* **20**, 163-250 (1979).
58. Makela, P.H., Bradley, D.J., Brandis, H., Frank, M.M., Hahn, H., Henkel, W., Jann, K., Marse, S.A., Robbins, J.B., Rosenstreich, L., Smith, H., Timmis, K., Tomasz, A., Turner, M.J., & Wiley, D.C. Evasion of host defenses group report. in *The molecular basis of microbial pathogenicity* (ed. Smith, H., Skehel, J.J., & Turner, M.J.) (Verlag Chemie GmbH, Weinheim, Federal Republic of Germany, 1980).
59. Lugtenberg, E.J.J. & Peters, R. Distribution of Lipids in Cytoplasmic and Outer Membranes of Escherichia-Coli-K12. *Biochimica et biophysica acta* **441**, 38-47 (1976).
60. Osborn, M.J., Gander, J.E., Parisi, E. & Carson, J. Mechanism of assembly of the outer membrane of Salmonella typhimurium. Isolation and characterization of cytoplasmic and outer membrane. *The Journal of biological chemistry* **247**, 3962-72 (1972).

61. Plesiat, P. & Nikaido, H. Outer membranes of gram-negative bacteria are permeable to steroid probes. *Molecular Microbiology* **6**, 1323-33 (1992).
62. Galanos, C. & Luderitz, O. Electrodialysis of lipopolysaccharides and their conversion to uniform salt forms. *European journal of biochemistry / FEBS* **54**, 603-10 (1975).
63. Inouye, M., Shaw, J. & Shen, C. The assembly of a structural lipoprotein in the envelope of Escherichia coli. *The Journal of biological chemistry* **247**, 8154-9 (1972).
64. Braun, V. Covalent lipoprotein from the outer membrane of Escherichia coli. *Biochimica et biophysica acta* **415**, 335-77 (1975).
65. Hirota, Y., Suzuki, H., Nishimura, Y. & Yasuda, S. On the process of cellular division in Escherichia coli: a mutant of E. coli lacking a murein-lipoprotein. *Proceedings of the National Academy of Sciences of the United States of America* **74**, 1417-20 (1977).
66. Wimley, W.C. The versatile beta-barrel membrane protein. *Current opinion in structural biology* **13**, 404-11 (2003).
67. Sonntag, I., Schwarz, H., Hirota, Y. & Henning, U. Cell envelope and shape of Escherichia coli: multiple mutants missing the outer membrane lipoprotein and other major outer membrane proteins. *Journal of Bacteriology* **136**, 280-5 (1978).
68. Decad, G.M. & Nikaido, H. Outer membrane of gram-negative bacteria. XII. Molecular-sieving function of cell wall. *Journal of Bacteriology* **128**, 325-36 (1976).

69. Nakae, T. & Nikaido, H. Outer membrane as a diffusion barrier in *Salmonella typhimurium*. Penetration of oligo- and polysaccharides into isolated outer membrane vesicles and cells with degraded peptidoglycan layer. *The Journal of biological chemistry* **250**, 7359-65 (1975).
70. Nikaido, H. Molecular basis of bacterial outer membrane permeability revisited. *Microbiology and molecular biology reviews : MMBR* **67**, 593-656 (2003).
71. Eick-Helmerich, K. & Braun, V. Import of biopolymers into *Escherichia coli*: nucleotide sequences of the *exbB* and *exbD* genes are homologous to those of the *tolQ* and *tolR* genes, respectively. *Journal of Bacteriology* **171**, 5117-26 (1989).
72. Bradbeer, C. The proton motive force drives the outer membrane transport of cobalamin in *Escherichia coli*. *Journal of Bacteriology* **175**, 3146-50 (1993).
73. Brinkman, K.K. & Larsen, R.A. Interactions of the energy transducer TonB with noncognate energy-harvesting complexes. *Journal of Bacteriology* **190**, 421-427 (2008).
74. Postle, K. & Kadner, R.J. Touch and go: tying TonB to transport. *Molecular Microbiology* **49**, 869-882 (2003).
75. Schauer, K., Rodionov, D.A. & de Reuse, H. New substrates for TonB-dependent transport: do we only see the 'tip of the iceberg'? *Trends in biochemical sciences* **33**, 330-338 (2008).
76. Larsen, R.A., Thomas, M.G. & Postle, K. Protonmotive force, ExbB and ligand-bound FepA drive conformational changes in TonB. *Molecular Microbiology* **31**, 1809-1824 (1999).

77. Ollis, A.A., Manning, M., Held, K.G. & Postle, K. Cytoplasmic membrane protonmotive force energizes periplasmic interactions between ExbD and TonB. *Molecular Microbiology* **73**, 466-481 (2009).
78. Higgs, P.I., Larsen, R.A. & Postle, K. Quantification of known components of the Escherichia coli TonB energy transduction system: TonB, ExbB, ExbD and FepA. *Molecular Microbiology* **44**, 271-281 (2002).
79. Kampfenkel, K. & Braun, V. Topology of the ExbB protein in the cytoplasmic membrane of Escherichia coli. *The Journal of biological chemistry* **268**, 6050-7 (1993).
80. Kampfenkel, K. & Braun, V. Membrane topology of the Escherichia coli ExbD protein. *Journal of Bacteriology* **174**, 5485-7 (1992).
81. Roof, S.K., Allard, J.D., Bertrand, K.P. & Postle, K. Analysis of Escherichia coli TonB membrane topology by use of PhoA fusions. *Journal of Bacteriology* **173**, 5554-7 (1991).
82. Jana, B., Manning, M. & Postle, K. Mutations in the ExbB Cytoplasmic Carboxy Terminus Prevent Energy-Dependent Interaction between the TonB and ExbD Periplasmic Domains. *Journal of Bacteriology* **193**, 5649-5657 (2011).
83. Karlsson, M., Hannavy, K. & Higgins, C.F. ExbB acts as a chaperone-like protein to stabilize TonB in the cytoplasm. *Molecular Microbiology* **8**, 389-96 (1993).
84. Chimento, D.P., Mohanty, A.K., Kadner, R.J. & Wiener, M.C. Substrate-induced transmembrane signaling in the cobalamin transporter BtuB. *Nature structural biology* **10**, 394-401 (2003).

85. Ollis, A.A. & Postle, K. The same periplasmic ExbD residues mediate in vivo interactions between ExbD homodimers and ExbD-TonB heterodimers. *Journal of Bacteriology* **193**, 6852-63 (2011).
86. Ollis, A.A. & Postle, K. ExbD Mutants Define Initial Stages in TonB Energization. *Journal of molecular biology* (2011).
87. Larsen, R.A. & Postle, K. Conserved residues Ser(16) and His(20) and their relative positioning are essential for TonB activity, cross-linking of TonB with ExbB, and the ability of TonB to respond to proton motive force. *The Journal of biological chemistry* **276**, 8111-7 (2001).
88. Swayne, C. & Postle, K. Taking the Escherichia coli TonB transmembrane domain "offline"? Nonprotonatable Asn substitutes fully for TonB His20. *Journal of Bacteriology* **193**, 3693-701 (2011).
89. Larsen, R.A., Wood, G.E. & Postle, K. The conserved proline-rich motif is not essential for energy transduction by Escherichia coli TonB protein. *Molecular Microbiology* **10**, 943-53 (1993).
90. Kohler, S.D., Weber, A., Howard, S.P., Welte, W. & Drescher, M. The proline-rich domain of TonB possesses an extended polyproline II-like conformation of sufficient length to span the periplasm of Gram-negative bacteria. *Protein Science* **19**, 625-630 (2010).
91. Shultis, D.D., Purdy, M.D., Banchs, C.N. & Wiener, M.C. Outer membrane active transport: structure of the BtuB:TonB complex. *Science* **312**, 1396-9 (2006).
92. Pawelek, P.D. et al. Structure of TonB in complex with FhuA, E-coli outer membrane receptor. *Science* **312**, 1399-1402 (2006).

93. Ghosh, J. & Postle, K. Disulphide trapping of an in vivo energy-dependent conformation of Escherichia coli TonB protein. *Molecular Microbiology* **55**, 276-288 (2005).
94. Ghosh, J. & Postle, K. Evidence for dynamic clustering of carboxy-terminal aromatic amino acids in TonB-dependent energy transduction. *Molecular Microbiology* **51**, 203-213 (2004).
95. Postle, K., Kastead, K.A., Gresock, M.G., Ghosh, J. & Swayne, C.D. The TonB Dimeric Crystal Structures Do Not Exist In Vivo. *Mbio* **1**(2010).
96. Peacock, R.S., Weljie, A.M., Howard, S.P., Price, F.D. & Vogel, H.J. The solution structure of the C-terminal domain of TonB and interaction studies with TonB box peptides. *Journal of molecular biology* **345**, 1185-1197 (2005).
97. Koedding, J. et al. Crystal structure of a 92-residue C-terminal fragment of TonB from Escherichia coli reveals significant conformational changes compared to structures of smaller TonB fragments. *Journal of Biological Chemistry* **280**, 3022-3028 (2005).
98. Chang, C.S., Mooser, A., Pluckthun, A. & Wlodawer, A. Crystal structure of the dimeric C-terminal domain of TonB reveals a novel fold. *Journal of Biological Chemistry* **276**, 27535-27540 (2001).
99. Koedding, J. et al. Dimerization of TonB is not essential for its binding to the outer membrane siderophore receptor FhuA of Escherichia coli. *Journal of Biological Chemistry* **279**, 9978-9986 (2004).
100. Sauter, A., Howard, S.P. & Braun, V. In vivo evidence for TonB dimerization. *Journal of Bacteriology* **185**, 5747-5754 (2003).

101. Vakharia-Rao, H., Kastead, K.A., Savenkova, M.I., Bulathsinghala, C.M. & Postle, K. Deletion and substitution analysis of the Escherichia coli TonB q160 region. *Journal of Bacteriology* **189**, 4662-4670 (2007).
102. Kaserer, W.A. et al. Insight from TonB hybrid proteins into the mechanism of iron transport through the outer membrane. *Journal of Bacteriology* **190**, 4001-4016 (2008).
103. Noinaj, N., Guillier, M., Barnard, T.J. & Buchanan, S.K. TonB-dependent transporters: regulation, structure, and function. *Annual review of microbiology* **64**, 43-60 (2010).
104. Braun, V. Surface signaling: novel transcription initiation mechanism starting from the cell surface. *Archives of Microbiology* **167**, 325-31 (1997).
105. Lukasik, S.M., Ho, K.W. & Cafiso, D.S. Molecular basis for substrate-dependent transmembrane signaling in an outer-membrane transporter. *Journal of molecular biology* **370**, 807-11 (2007).
106. Fanucci, G.E. et al. Substrate-induced conformational changes of the periplasmic N-terminus of an outer-membrane transporter by site-directed spin labeling. *Biochemistry* **42**, 1391-400 (2003).
107. Cadieux, N. & Kadner, R.J. Site-directed disulfide bonding reveals an interaction site between energy-coupling protein TonB and BtuB, the outer membrane cobalamin transporter. *Proceedings of the National Academy of Sciences of the United States of America* **96**, 10673-8 (1999).

108. Ogierman, M. & Braun, V. Interactions between the outer membrane ferric citrate transporter FecA and TonB: Studies of the FecA TonB box. *Journal of Bacteriology* **185**, 1870-1885 (2003).
109. Moeck, G.S., Coulton, J.W. & Postle, K. Cell envelope signaling in *Escherichia coli*. Ligand binding to the ferrichrome-iron receptor fhua promotes interaction with the energy-transducing protein TonB. *The Journal of biological chemistry* **272**, 28391-7 (1997).
110. Kim, M., Fanucci, G.E. & Cafiso, D.S. Substrate-dependent transmembrane signaling in TonB-dependent transporters is not conserved. *Proceedings of the National Academy of Sciences of the United States of America* **104**, 11975-80 (2007).
111. Flores Jimenez, R.H., Do Cao, M.A., Kim, M. & Cafiso, D.S. Osmolytes modulate conformational exchange in solvent-exposed regions of membrane proteins. *Protein science : a publication of the Protein Society* **19**, 269-78 (2010).
112. Kim, M., Xu, Q., Fanucci, G.E. & Cafiso, D.S. Solutes modify a conformational transition in a membrane transport protein. *Biophysical journal* **90**, 2922-9 (2006).
113. Fanucci, G.E., Lee, J.Y. & Cafiso, D.S. Spectroscopic evidence that osmolytes used in crystallization buffers inhibit a conformation change in a membrane protein. *Biochemistry* **42**, 13106-12 (2003).
114. Gudmundsdottir, A., Bell, P.E., Lundrigan, M.D., Bradbeer, C. & Kadner, R.J. Point Mutations in a Conserved Region (TonB Box) of *Escherichia-Coli* Outer-

- Membrane Protein Btub Affect Vitamin-B12 Transport. *Journal of Bacteriology* **171**, 6526-6533 (1989).
115. Cadieux, N., Bradbeer, C. & Kadner, R.J. Sequence changes in the Ton box region of BtuB affect its transport activities and interaction with TonB protein. *Journal of Bacteriology* **182**, 5954-5961 (2000).
116. Cogshall, K.A., Cadieux, N., Piedmont, C., Kadner, R.J. & Cafiso, D.S. Transport-defective mutations alter the conformation of the energy-coupling motif of an outer membrane transporter. *Biochemistry* **40**, 13964-71 (2001).
117. Chimento, D.P., Kadner, R.J. & Wiener, M.C. Comparative structural analysis of TonB-dependent outer membrane transporters: implications for the transport cycle. *Proteins* **59**, 240-51 (2005).
118. Endriss, F., Braun, M., Killmann, H. & Braun, V. Mutant analysis of the Escherichia coli FhuA protein reveals sites of FhuA activity. *Journal of Bacteriology* **185**, 4683-92 (2003).
119. Barnard, T.J., Watson, M.E., Jr. & McIntosh, M.A. Mutations in the Escherichia coli receptor FepA reveal residues involved in ligand binding and transport. *Molecular Microbiology* **41**, 527-36 (2001).
120. Chakraborty, R., Lemke, E.A., Cao, Z., Klebba, P.E. & van der Helm, D. Identification and mutational studies of conserved amino acids in the outer membrane receptor protein, FepA, which affect transport but not binding of ferric-enterobactin in Escherichia coli. *Biometals : an international journal on the role of metal ions in biology, biochemistry, and medicine* **16**, 507-18 (2003).

121. Cascales, E. et al. Colicin biology. *Microbiology and Molecular Biology Reviews* **71**, 158-229 (2007).
122. Gerding, M.A., Ogata, Y., Pecora, N.D., Niki, H. & de Boer, P.A. The trans-envelope Tol-Pal complex is part of the cell division machinery and required for proper outer-membrane invagination during cell constriction in *E. coli*. *Molecular Microbiology* **63**, 1008-25 (2007).
123. Gaspar, J.A., Thomas, J.A., Marolda, C.L. & Valvano, M.A. Surface expression of O-specific lipopolysaccharide in *Escherichia coli* requires the function of the TolA protein. *Molecular Microbiology* **38**, 262-75 (2000).
124. Clavel, T., Lazzaroni, J.C., Vianney, A. & Portalier, R. Expression of the tolQRA genes of *Escherichia coli* K-12 is controlled by the RcsC sensor protein involved in capsule synthesis. *Molecular Microbiology* **19**, 19-25 (1996).
125. Kampfenkel, K. & Braun, V. Membrane topologies of the TolQ and TolR proteins of *Escherichia coli*: inactivation of TolQ by a missense mutation in the proposed first transmembrane segment. *Journal of Bacteriology* **175**, 4485-91 (1993).
126. Isnard, M., Rigal, A., Lazzaroni, J.C., Lazdunski, C. & Lloubes, R. Maturation and localization of the TolB protein required for colicin import. *Journal of Bacteriology* **176**, 6392-6 (1994).
127. Glaser-Wuttke, G., Keppner, J. & Rasched, I. Pore-forming properties of the adsorption protein of filamentous phage fd. *Biochimica et biophysica acta* **985**, 239-47 (1989).

128. Germon, P., Ray, M.C., Vianney, A. & Lazzaroni, J.C. Energy-dependent conformational change in the TolA protein of *Escherichia coli* involves its N-terminal domain, TolQ, and TolR. *Journal of Bacteriology* **183**, 4110-4 (2001).
129. Kurisu, G. et al. The structure of BtuB with bound colicin E3 R-domain implies a translocon. *Nature structural biology* **10**, 948-54 (2003).
130. Penfold, C.N. et al. A 76-residue polypeptide of colicin E9 confers receptor specificity and inhibits the growth of vitamin B12-dependent *Escherichia coli* 113/3 cells. *Molecular Microbiology* **38**, 639-49 (2000).
131. Fanucci, G.E., Cadieux, N., Kadner, R.J. & Cafiso, D.S. Competing ligands stabilize alternate conformations of the energy coupling motif of a TonB-dependent outer membrane transporter. *Proceedings of the National Academy of Sciences of the United States of America* **100**, 11382-7 (2003).
132. Adams, H., Zeder-Lutz, G., Schalk, I., Pattus, F. & Celia, H. Interaction of TonB with the outer membrane receptor FpvA of *Pseudomonas aeruginosa*. *Journal of Bacteriology* **188**, 5752-5761 (2006).
133. Lefevre, J., Delepelaire, P., Delepierre, M. & Izadi-Pruneyre, N. Modulation by substrates of the interaction between the HasR outer membrane receptor and its specific TonB-like protein, HasB. *Journal of molecular biology* **378**, 840-851 (2008).
134. Khursigara, C.M., De Crescenzo, G., Pawelek, P.D. & Coulton, J.W. Deletion of the proline-rich region of TonB disrupts formation of a 2 : 1 complex with FhuA, an outer membrane receptor of *Escherichia coli*. *Protein Science* **14**, 1266-1273 (2005).

135. Khursigara, C.M., De Crescenzo, G., Pawelek, P.D. & Coulton, J.W. Kinetic analyses reveal multiple steps in forming TonB-FhuA complexes from *Escherichia coli*. *Biochemistry* **44**, 3441-3453 (2005).
136. Khursigara, C.M., De Crescenzo, G., Pawelek, P.D. & Coulton, J.W. Enhanced binding of TonB to a ligand-loaded outer membrane receptor - Role of the oligomeric state of TonB in formation of a functional FhuA center dot TonB complex. *Journal of Biological Chemistry* **279**, 7405-7412 (2004).
137. Ma, L. et al. Evidence of ball-and-chain transport of ferric enterobactin through FepA. *Journal of Biological Chemistry* **282**, 397-406 (2007).
138. Gumbart, J., Wiener, M.C. & Tajkhorshid, E. Mechanics of force propagation in TonB-dependent outer membrane transport. *Biophysical journal* **93**, 496-504 (2007).
139. Ferguson, A.D. et al. Signal transduction pathway of TonB-dependent transporters. *Proceedings of the National Academy of Sciences of the United States of America* **104**, 513-518 (2007).
140. Luan, B.Q., Carr, R., Caffrey, M. & Aksimentiev, A. The effect of calcium on the conformation of cobalamin transporter BtuB. *Proteins-Structure Function and Bioinformatics* **78**, 1153-1162 (2010).

CHAPTER 2

Site-directed Spin Labeling Electron Paramagnetic Resonance

2.1 Basic Electron Paramagnetic Resonance Theory¹⁻⁵

Site-directed spin labeling electron paramagnetic resonance (SDSL-EPR) is a versatile spectroscopic technique that allows for the extraction of important structural and dynamical parameters from biomolecules that are not intrinsically paramagnetic. Most widely adapted to studying proteins, SDSL involves the site-specific attachment of a stably paramagnetic spin label to the protein backbone and the subsequent perturbation and analysis of spin behavior by EPR spectroscopy, generally at X-band microwave frequencies (9-10 GHz). The typical labeling reaction, practical considerations and capabilities of SDSL-EPR were discussed in the previous chapter. Here, a brief introduction to EPR theory (within the context of nitroxide spin labels) and a short description of the SDSL-EPR techniques discussed in this dissertation will be provided.

2.1.1 The Zeeman Interaction. In EPR, transitions are induced between quantized Zeeman levels of a paramagnetic system under the influence of an applied magnetic field. The Zeeman levels have discrete energies that arise from interaction of the unpaired electron spin magnetic moment $\boldsymbol{\mu}$ with the magnetic field \mathbf{H} , represented by the Hamiltonian:

$$\mathcal{H} = -\boldsymbol{\mu} \cdot \mathbf{H} \quad (2.1.1)$$

The electron spin magnetic moment is related to its spin angular momentum, \mathbf{S} , by:

$$\boldsymbol{\mu} = -g\beta\mathbf{S} \quad (2.1.2)$$

where g is called the g -factor and β is the Bohr magneton. The g -factor is a measure of the local field experienced by the electron, and is equal to 2.0023 for a free electron. If e and m represent the charge and mass of the electron, respectively, c is the speed of light, and \hbar is the reduced Planck's constant, then the Bohr magneton can be represented as:

$$\beta = |e|\hbar / 2mc \quad (2.1.3)$$

Substituting Eq. 2.1.2 into Eq. 2.1.1, the Hamiltonian becomes:

$$\mathcal{H} = g\beta\mathbf{S} \cdot \mathbf{H} \quad (2.1.4)$$

The direction of the applied magnetic field is typically modeled along the z -axis of the laboratory frame, and the corresponding Hamiltonian is:

$$\mathcal{H} = g\beta\mathbf{S}_z \cdot \mathbf{H} \quad (2.1.5)$$

where \mathbf{S}_z is the operator corresponding to the projection of the electron spin angular momentum along the field direction. The value of \mathbf{S}_z for a system with one unpaired electron is $\mathbf{S}_z = \frac{1}{2}$, and therefore the effect of the magnetic field is to produce $2(\mathbf{S}_z) + 1 = 2$ energy levels with spin quantum numbers $m_s = +\frac{1}{2}$ and $m_s = -\frac{1}{2}$. Thus, the Zeeman interaction involves precession of $\boldsymbol{\mu}$ in a parallel or anti-parallel alignment about an axis that is aligned along the magnetic field direction \mathbf{H}_z ; the $m_s = -\frac{1}{2}$ state is lower in energy and corresponds to a spin with parallel alignment of $\boldsymbol{\mu}$ about \mathbf{H}_z , whereas the $m_s = +\frac{1}{2}$ state is higher in energy and corresponds to a spin with anti-parallel alignment of $\boldsymbol{\mu}$ about

\mathbf{H}_z . Therefore with eigenvalues of $m_s = \pm 1/2$, the Zeeman levels in the presence of \mathbf{H} have energies equal to:

$$E = \pm 1/2 g\beta\mathbf{H} \quad (2.1.6)$$

and the energy difference between Zeeman levels is:

$$\Delta E_{\text{Zeeman}} = 1/2 g\beta\mathbf{H} - (-1/2 g\beta\mathbf{H}) = g\beta\mathbf{H} \quad (2.1.7)$$

According to the Bohr condition $\Delta E = h\nu$, transitions between Zeeman levels can be driven by electromagnetic radiation of frequency that satisfies the relation:

$$h\nu = g\beta\mathbf{H} = \Delta E_{\text{Zeeman}} \quad (2.1.8)$$

where the separation between Zeeman levels is linearly proportional to \mathbf{H} and ν (Figure 2.1.1). For standard continuous-wave (CW) experiments typically the microwave frequency ν is held constant while the magnetic field strength is swept, and Eq. 2.1.8 can be rearranged with respect to \mathbf{H} :

$$\mathbf{H} = h\nu / g\beta \quad (2.1.9)$$

The magnetic field \mathbf{H} can also be expressed in terms of the electron gyromagnetic ratio γ_e and the angular frequency ω_L at which $\boldsymbol{\mu}$ precesses about \mathbf{H}_z , known as the Larmor frequency:

$$\mathbf{H} = \omega_L / \gamma_e \quad (2.1.10)$$

where $\gamma_e = g\beta / \hbar$ and $\omega_L = 2\pi\nu$. Thus, as \mathbf{H} is scanned the Larmor precession frequency—and the energy difference between Zeeman levels—is eventually tuned to the energy of incident microwave radiation:

$$g\beta\mathbf{H} = \omega_L\hbar = \Delta E_{\text{Zeeman}} = h\nu \quad (2.1.11)$$

When this resonance condition is met transitions are induced between the Zeeman levels, resulting in an EPR signal.

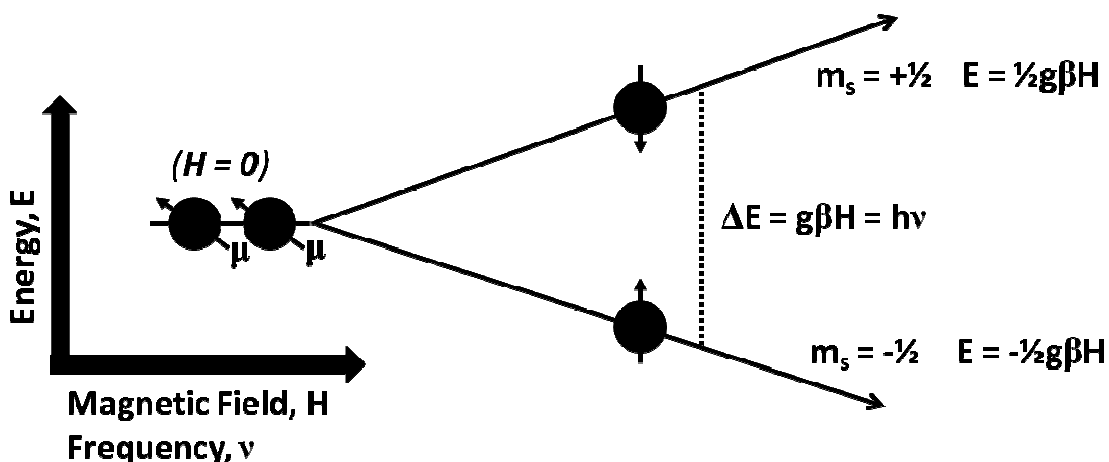


Figure 2.1.1. The Zeeman Interaction. Shown is an energy level diagram representing the linear dependence of the Zeeman interaction energies on \mathbf{H} and ν . The black balls represent electrons, and the arrows inside of the balls represent the alignments of the electron spin magnetic moment μ with a magnetic field in which the parallel alignment is up, and the anti-parallel alignment is down.

2.1.2 Nitroxide Hyperfine Interactions. The Zeeman levels are further split by hyperfine interactions between the electron magnetic moment and the magnetic moments from nearby nuclei. There are two contributions to the hyperfine interaction; the

isotropic Fermi contact interaction resulting from direct nuclear-electron contact, and the anisotropic dipole-dipole interaction. For nitroxide spin labels, hyperfine couplings typically arise from interaction of the electron magnetic moment with the nitrogen nucleus and 13 hydrogens associated with the nitroxide ring—12 of which belong to the four methyl group substituents. These hyperfine interactions modify the Zeeman energy levels because the effective magnetic field \mathbf{H}_{eff} felt by the electron magnetic moment becomes different (i.e. $\mathbf{H}_{\text{eff}} = \mathbf{H} + \mathbf{H}_{\text{local}}$); the sign and magnitude of $\mathbf{H}_{\text{local}}$ depends on the quantum spin state of the interacting nucleus and the strength of the hyperfine interaction, respectively. For example, in the anisotropic dipole-dipole interaction the electron and nuclear magnetic moments can be modeled as point dipoles since the distance \mathbf{r} between them is long relative to the dipole length (which is zero for an electron), and the interaction energy between the electron and nuclear magnetic dipoles E_{dip} can be represented as:

$$E_{\text{dip}} = \mu_{\text{N}} \mu_{\text{e}} \mathbf{r}^{-3} (3 \cos^2 \theta - 1) = -\mu_{\text{e}} \mathbf{H}_{\text{local}} \quad (2.1.12)$$

where θ is the angle between the dipolar vector and magnetic field direction \mathbf{H}_z , μ_{e} and μ_{N} are the electron and nuclear spin magnetic dipole moments, respectively. The nuclear spin magnetic moment can be expressed as:

$$\mu_{\text{N}} = g_{\text{N}} \beta_{\text{N}} \mathbf{I} \quad (2.1.13)$$

where g_{N} is the nuclear g-factor, β_{N} is the nuclear magneton, and \mathbf{I} is the nuclear spin angular momentum. Importantly, Eq. (2.1.12) indicates that the magnitude of the anisotropic hyperfine coupling depends only on the variables \mathbf{r} and θ , but not the applied

magnetic field strength \mathbf{H} . Furthermore, the $3\cos^2\theta - 1$ term indicates that the anisotropic hyperfine interaction averages to zero if the dipolar vector tumbles relative to \mathbf{H}_z sufficiently fast. The isotropic Fermi contact interaction can be represented by the Hamiltonian:

$$\mathcal{H}_{\text{iso}} = -\frac{2}{3} g_e \gamma_e \gamma_N \mu_0 \delta(\mathbf{r}_N) \mathbf{S} \cdot \mathbf{I} \quad (2.1.14)$$

where μ_0 is the vacuum permeability and $\delta(\mathbf{r}_N)$ is the delta function which extracts the spin density at the nucleus. Both the isotropic Fermi contact and the anisotropic magnetic dipole-dipole contributions are combined in the hyperfine tensor \mathbf{A} , and the complete hyperfine interaction can be represented by the Hamiltonian:

$$\mathcal{H} = \mathbf{S} \cdot \mathbf{A} \cdot \mathbf{I} \quad (2.1.15)$$

where \mathbf{S} and \mathbf{I} are the operators corresponding to the projections of the electron and nuclear spin angular momentums, respectively, along the field direction \mathbf{H}_z . By combining the hyperfine (Eq. 2.1.15) and electronic Zeeman (Eq. 2.1.5) interactions the Hamiltonian becomes:

$$\mathcal{H} = g\beta\mathbf{S}_z \cdot \mathbf{H} + \mathbf{S} \cdot \mathbf{A} \cdot \mathbf{I} \quad (2.1.16)$$

where the nuclear Zeeman term has been left out since the EPR selection rules state that electron-nuclear transitions are forbidden. As mentioned above, an important consequence of this relation is the independence of the hyperfine term from the magnetic field strength \mathbf{H} . For nitrogen $\mathbf{I} = 1$, and therefore the effect of the hyperfine interaction is to split each Zeeman level into $2(\mathbf{I}) + 1 = 3$ hyperfine levels with spin quantum

numbers $m_l = +1, 0$ and -1 (Figure 2.1.2). The nitrogen hyperfine coupling is predominantly apparent because the unpaired electron is localized in a $2p_z$ orbital on the nitrogen atom. The value of \mathbf{I} for the proton is $\mathbf{I} = \frac{1}{2}$, which further splits each energy level into $2(\mathbf{I}) + 1 = 2$ hyperfine levels with spin quantum numbers $m_l = \pm\frac{1}{2}$. However, the magnitude of the proton hyperfine splittings are exceedingly small (~ 0.2 - 0.5 G compared to ~ 5 - 37 G for nitrogen⁴), and these couplings are usually hidden within the inhomogeneous linewidth. Therefore, since the selection rules state that $m_s = \pm 1$ and $m_l = 0$, the nitrogen hyperfine interaction has the effect of creating three prominent absorbance lines in the EPR spectrum, and Eq. (2.1.8) can be amended such that the energy difference between Zeeman levels due to the nitrogen hyperfine interactions becomes:

$$\Delta E = h\nu = g\beta\mathbf{H} + \frac{1}{2}\mathbf{A}m_l \quad (2.1.17)$$

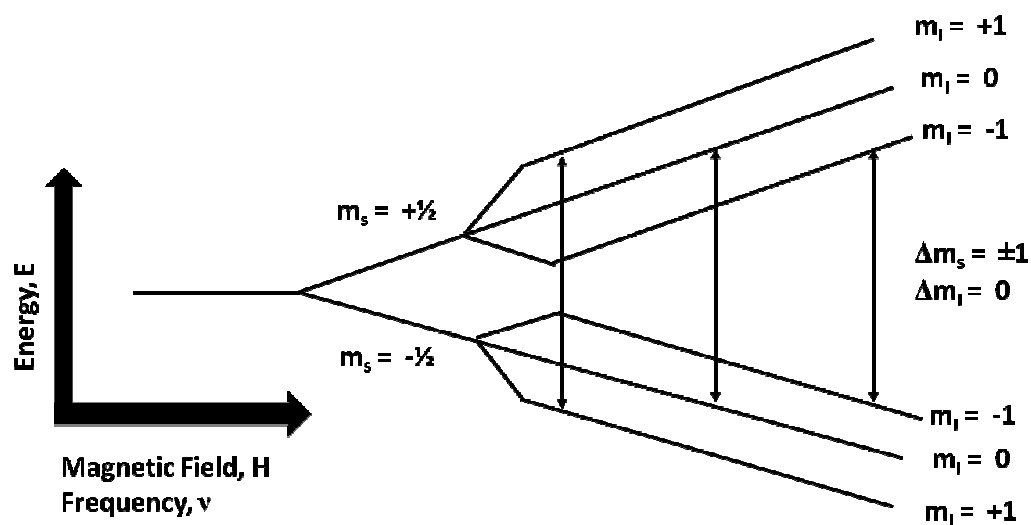


Figure 2.1.2. The Nitrogen Hyperfine Interaction. The hyperfine interaction of the electron magnetic moment with the nitrogen nuclear magnetic moment splits each Zeeman level three times for the nuclear spin quantum numbers $m_l = +1, 0$ and -1 . Selection rules state that only transitions between electronic Zeeman levels are allowed ($\Delta m_s = \pm 1$) while nuclear transitions are forbidden ($\Delta m_l = 0$).

2.1.3 Spectral Anisotropy. The Zeeman and hyperfine interactions are anisotropic, and can be described by the \mathbf{g} and \mathbf{A} tensors, respectively. Each of these 2nd rank tensors is represented by a 3×3 matrix that is diagonal in the magnetic frame (Figure 2.1.3), with principal values \mathbf{g}_{xx} , \mathbf{g}_{yy} , \mathbf{g}_{zz} and \mathbf{A}_{xx} , \mathbf{A}_{yy} , \mathbf{A}_{zz} . The anisotropy arises from a non-spherical symmetry of the Zeeman and hyperfine interactions within the $2p_z$ nitrogen orbital where the unpaired electron is localized; therefore, the magnitude of these interactions depends on their relative principal values and the orientation of the magnetic frame with respect to the direction of the applied magnetic field.

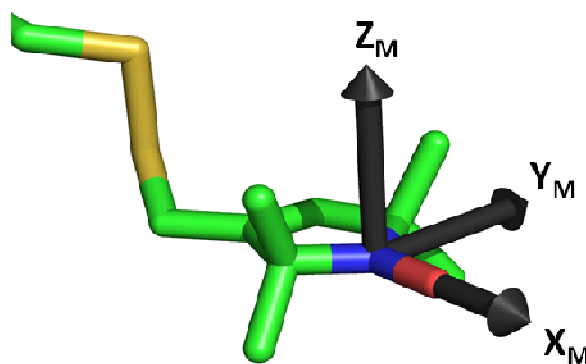


Figure 2.1.3. The Nitroxide Magnetic Frame. Shown are the principal axes of the nitroxide magnetic frame. Customarily, the x_M -axis is taken to be coincident with the N—O bond, the z_M -axis lies along the nitroxide p -orbital, and the y_M -axis is selected for a right-handed coordinate system. The magnetic frame is the principal coordinate system for the magnetic \mathbf{g} and \mathbf{A} tensors. In this coloring scheme, carbon atoms are green, nitrogen is blue, oxygen is red, sulfur is yellow, and hydrogens are not rendered.

The \mathbf{A} tensor is approximately axially symmetric (i.e. $\mathbf{A}_{zz} > \mathbf{A}_{xx} \approx \mathbf{A}_{yy}$) due to the localization of the unpaired electron in the $2p_z$ orbital of the nitrogen; since this orbital is

roughly aligned with the z_M -axis of the magnetic frame, the hyperfine coupling is much stronger when \mathbf{H} is oriented along z_M . The principal values of the \mathbf{A} tensor depend on the chemical structure of the nitroxide, and are sensitive to solvent polarity and proticity. \mathbf{A}_{zz} is the most sensitive to the solvent dielectric and hydrogen bonding with the oxygen atom. This effect arises from polarization of the N—O moiety due to the localization of the unpaired electron in the $2p_z$ orbital of the nitrogen; more polar solvents stabilize the negative charge on the oxygen and increase spin density on the nitrogen atom,^{5,6} thereby resulting in a stronger hyperfine coupling and larger \mathbf{A}_{zz} value. For the most commonly used nitroxide spin label MTSL (denoted R1 when attached to a protein) dissolved in aqueous solvent, the nominal principal values of the hyperfine tensor are $\mathbf{A}_{xx} \approx \mathbf{A}_{yy} \approx 6$ G, and $\mathbf{A}_{zz} \approx 37$ G.

As mentioned above, the g-factor for a free electron is 2.0023; however, several contributions can alter the effective magnetic moment of the electron and cause the g-factor to deviate from the free-spin value. This g-shift consists of several terms that can be derived from relativistic quantum mechanics, however the most dominant contributions arise from the spin-orbit coupling and orbital Zeeman cross terms. As with the hyperfine tensor, the \mathbf{g} tensor is approximately axially symmetric and the principal values depend on nitroxide chemical structure and are sensitive to solvent polarity and proticity. Due to its dependence on the geometrical parameters of the N—O group, the \mathbf{g}_{xx} principal value is the component most sensitive to the solvent dielectric and hydrogen bonding potential of the oxygen atom. In more polar and/or protic solvents, a lower unpaired electron density on the oxygen atom and an increased $n\pi^*$ excitation energy

results in a smaller value of \mathbf{g}_{xx} .⁵ The \mathbf{g} tensor is thus calculated as a correction to the free-electron g-value, and the magnitude of these corrections depends on the orientation of the magnetic frame with respect to \mathbf{H}_z . For the MTSL nitroxide spin label dissolved in aqueous solvent the principal g-values are nominally $\mathbf{g}_{xx} \approx 2.0089$, $\mathbf{g}_{yy} \approx 2.0061$, and $\mathbf{g}_{zz} \approx 2.0023$.

Accounting for the anisotropy in the magnetic interactions, the Hamiltonian in Eq. 2.1.16 can be expanded to:

$$\mathfrak{H}_Z = \beta(\mathbf{g}_{xx}\mathbf{S}_x\mathbf{H}_x + \mathbf{g}_{yy}\mathbf{S}_y\mathbf{H}_y + \mathbf{g}_{zz}\mathbf{S}_z\mathbf{H}_z) + \mathbf{S}_x\mathbf{A}_{xx}\mathbf{I}_x + \mathbf{S}_y\mathbf{A}_{yy}\mathbf{I}_y + \mathbf{S}_z\mathbf{A}_{zz}\mathbf{I}_z \quad (2.1.18)$$

where the subscript in bold denotes the component of each term along the x_M , y_M , or z_M axis of the magnetic frame (the external magnetic field \mathbf{H} is always taken to be in the z -direction of the laboratory frame). In terms of spectral anisotropy, Eq. (2.1.18) states that the position of absorption lines in the EPR spectrum depends on the principal tensor values and the orientation(s) of the nitroxide magnetic frame with respect to the external magnetic field.

The effect of the magnetic anisotropy on the EPR spectrum can be visualized by considering the example of spin labels trapped in a crystal lattice under the influence of an external magnetic field. Due to the approximate axial symmetry of the Zeeman and hyperfine interactions in the magnetic frame, the dependence of the \mathbf{g} and \mathbf{A} values on the angle θ between the magnetic z_M -axis and the external field \mathbf{H}_z can be represented by:

$$\mathbf{g}_{\text{eff}}(\theta) = (\mathbf{g}_{\perp}^2 \sin^2\theta + \mathbf{g}_{\parallel}^2 \cos^2\theta)^{1/2} \quad (2.1.19)$$

$$\mathbf{A}_{\text{eff}}(\theta) = (\mathbf{A}_{\perp}^2 \sin^2\theta + \mathbf{A}_{\parallel}^2 \cos^2\theta)^{1/2}$$

where the perpendicular and parallel notations represent the values of the tensor components when \mathbf{H}_z is oriented along the x_M/y_M -plane or the z_M -axis, respectively. Thus, if the crystal is oriented such that the applied magnetic field is perpendicular to the z_M -axis ($\theta = 90^\circ$), the \mathbf{g}_\perp and \mathbf{A}_\perp (\mathbf{g}_{xx} , \mathbf{A}_{xx} or \mathbf{g}_{yy} , \mathbf{A}_{yy}) terms will dominate (Figure 2.1.4). As can be seen from the X-band EPR spectra in Fig. 2.1.4, most of the \mathbf{g} -anisotropy is actually unresolved and there is a small degree of rhombicity in the \mathbf{A} and \mathbf{g} tensors (i.e. $x \neq y$). If the crystal is oriented such that the applied magnetic field is parallel to the z_M -axis ($\theta = 0^\circ$), the \mathbf{g}_\parallel and \mathbf{A}_\parallel (\mathbf{g}_{zz} and \mathbf{A}_{zz}) terms will dominate and the nitrogen hyperfine couplings become much larger. Then, if the crystal is crushed into a fine powder such that all orientations of the z_M -axis relative to the external magnetic field are represented, the $\mathbf{g}_{\text{eff}}(\theta)$ and $\mathbf{A}_{\text{eff}}(\theta)$ values are summed over θ in the EPR spectrum. At X-band frequencies (9-10 GHz) the width of the spectrum is dictated by the hyperfine anisotropy, and the total spectral anisotropy is roughly $\mathbf{A}_{zz} - \frac{1}{2}(\mathbf{A}_{xx} + \mathbf{A}_{yy}) \approx 31 \text{ G}$ (or $\sim 90 \text{ MHz}$ using the EPR conversion factor 2.83 MHz/G).

2.2 Nitroxide Lineshape^{1,2,4,6-15}

Contributions from various mechanisms affect the shape of the EPR resonance line. First, as obviously seen in Fig. 2.1.4, the CW EPR signal is not viewed as a typical absorption spectrum; rather, for instrumental reasons the EPR lineshape appears as a first-derivative spectrum. Noise from the Schottky detector diode and baseline drift from the DC electronics reduces sensitivity, complicating the scrupulous analysis of important

features in the EPR spectrum. Thus, the magnetic field is typically modulated by 1 G at 100 kHz as it is scanned, and phase sensitive detection is used to recognize signals that are amplitude-modulated at 100 kHz and in-phase with the field modulation. As a result, the amplitude of the EPR spectrum becomes proportional to the slope of the resonance signal, and is transformed into a first-derivative spectrum.

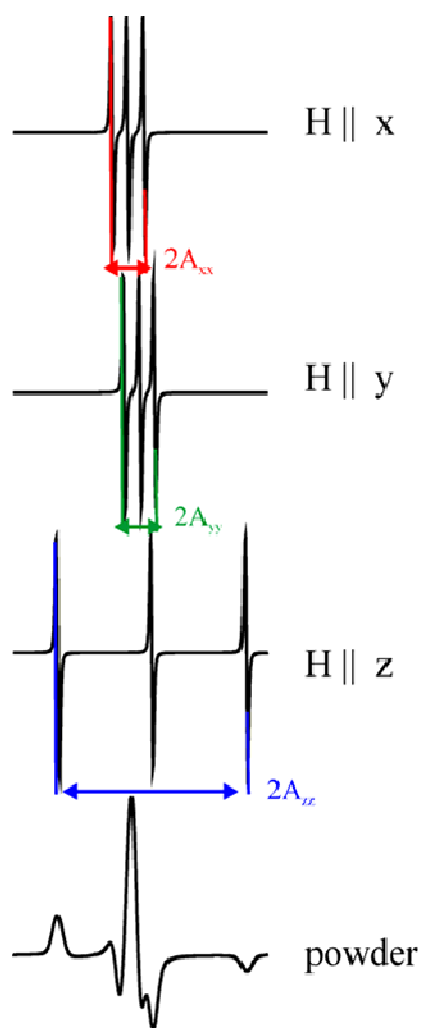


Figure 2.1.4. Effect of Magnetic Anisotropy on the EPR Spectrum. Shown is the position dependence of EPR absorbance lines on the orientation of the nitroxide magnetic frame with respect to the external magnetic field. At X-band frequencies, the anisotropy of the nitrogen hyperfine coupling dominates the lineshape, while the g -anisotropy and proton hyperfine couplings remain largely unresolved within the inhomogeneous linewidth.

The area under the EPR resonance line (the double integral of the first-derivative spectrum) is proportional to the number of unpaired spins in the sample; EPR spectra from samples with the same concentration of unpaired spins will have the same area, yet the spectra may have a very different shape or width. The width and shape of the EPR spectrum contains an abundance of information regarding the environment and behavior of the spin label. There are many mechanisms that affect EPR lineshape experimentally, and several of these will be discussed below. There are both Lorentzian and Gaussian contributions that broaden the intrinsic EPR linewidth; relaxation of the system back to equilibrium adds a Lorentzian component while various inhomogeneous effects, such as unresolved hyperfine couplings, impart a (typically) Gaussian component to the line broadening. The largest effects on the EPR spectrum arise from nitroxide motion, which variably averages the magnetic anisotropy depending on the rate and amplitude of motion.

2.2.1 Non-relaxation Effects. The intrinsic linewidth of a nitroxide varies with chemical structure; however the range is typically 0.1-0.4 G.⁴ Inhomogeneous broadening mechanisms add a non-Lorentzian (typically Gaussian) component to the linewidth, because the inhomogeneous lineshape consists of the sum of a large number of narrower homogeneously broadened lines that feel a slightly different \mathbf{H}_{eff} and thus absorb at somewhat different positions. Since the shift between each of these individual lines (called spin packets) is small, they become merged into one envelope, yielding a Gaussian profile. Inhomogeneous broadening may have several origins. If inhomogeneities in the applied magnetic field over the volume of sample exceed the

intrinsic linewidth, then the spins in various parts of the sample feel a different \mathbf{H}_{eff} and the resonance line will be broadened inhomogeneously. For nitroxides, the EPR lineshape is typically inhomogeneously broadened due to unresolved \mathbf{g} -anisotropy and proton hyperfine structure. The hyperfine splitting is ~ 0.2 G for the twelve methyl group protons and ~ 0.5 G for the nitroxide ring proton, and the intrinsic linewidth is ~ 0.1 G.⁴ However, in solution these lines are homogeneously broadened by ~ 0.1 - 0.2 G due to interactions with oxygen, and therefore the proton hyperfine couplings are not resolved. The overall Gaussian line broadening contribution from the protons is ~ 1 G.⁷

2.2.2 Relaxation Effects. The spin Hamiltonian represented by Eq. 2.1.16 demonstrates the requirement of a precise amount of energy in order to induce transitions between Zeeman levels. However when the resonance condition (Eq. 2.1.17) is met, the EPR resonance line has an intrinsic Lorentzian linewidth. This linewidth arises from interactions of the unpaired electron with its surroundings, which affects the lifetime of spin states and broadens the energy levels. In order to understand the consequences of relaxation on the EPR spectrum, and the subsequent topics in this chapter, a brief introduction to relaxation phenomena will be provided here.

The linearity of the separation between energy levels ΔE_{Zeeman} with magnetic field strength \mathbf{H} and microwave frequency ν in Eq. 2.1.8 has consequences on the populations of each energy level according to the Boltzmann distribution:

$$N_{\alpha} / N_{\beta} = e^{(g\beta\mathbf{H} / kT)} \quad (2.2.1)$$

where N_α and N_β are the populations of the $m_s = -1/2$ and $m_s = +1/2$ Zeeman levels, respectively, k is the Boltzmann constant and T is the temperature. The Boltzmann relation states that the polarization of Zeeman levels scales with the thermal energy and \mathbf{H} (and thus ν and ΔE_{Zeeman}). At thermal equilibrium, the lower energy level $m_s = -1/2$ is slightly more populated, however when the resonance condition is met transitions between Zeeman levels begin to equalize the populations. When taken off-resonance, the system relaxes back to its equilibrium Boltzmann distribution via interactions of the unpaired electron with its surroundings. The Bloch equations provide a phenomenological description of relaxation, and will be reviewed here very briefly.

In an applied magnetic field along the z -direction of the laboratory frame, an ensemble of N electron spins align such that N_α are in the $m_s = -1/2$ spin state and N_β are in the $m_s = +1/2$ spin state. If the bulk magnetic moment \mathbf{M} represents the sum of all the individual magnetic moments $\boldsymbol{\mu}$, then the component of the bulk magnetic moment along the z -direction \mathbf{M}_z can be expressed as:

$$\mathbf{M}_z = \Sigma \boldsymbol{\mu} = \gamma_e \hbar (N_\alpha - N_\beta) = \gamma_e \hbar n \quad (2.2.2)$$

where n is the population difference between spin states. At equilibrium, $\mathbf{M}_z = \mathbf{M}_0$, which is proportional to the magnetic susceptibility χ of the N spins:

$$\mathbf{M}_z = \mathbf{M}_0 = \gamma_e \hbar n = \chi \mathbf{H}_z \quad (2.2.3)$$

where the magnetic susceptibility is:

$$\chi = (N \gamma_e^2 \hbar^2 \mathbf{S}_z) / (3kT) \quad (2.2.4)$$

The spin magnetic moment $\boldsymbol{\mu}$ of the unpaired electron is related to the spin angular momentum \mathbf{S} by Eq. 2.1.2. The action of an applied magnetic field exerts a torque on the angular momentum, which causes $\boldsymbol{\mu}$ to precess about an axis that is aligned along the magnetic field \mathbf{H} at the Larmor frequency ω_L (Eq. 2.1.10). The bulk magnetic moment \mathbf{M} behaves in a similar fashion, and the rate of change of \mathbf{M} over time interval t due to this precession can be expressed as:

$$d\mathbf{M}/dt = \gamma_e(\mathbf{M} \times \mathbf{H}) \quad (2.2.5)$$

When the applied magnetic field direction is along the z-axis of the laboratory frame, Eq.2.2.5 can be decomposed and expressed in terms of the rate of change of each component of \mathbf{M} in the laboratory frame at equilibrium:

$$\begin{aligned} d\mathbf{M}_x/dt &= \omega_L \mathbf{M}_y \\ d\mathbf{M}_y/dt &= -\omega_L \mathbf{M}_x \\ d\mathbf{M}_z/dt &= 0 \end{aligned} \quad (2.2.6)$$

Now consider what happens when the system is perturbed by resonant energy. Typically an external magnetic field \mathbf{H}_z is applied in the z-direction, and a much weaker linearly polarized oscillating field \mathbf{H}' , which is a component of the microwave radiation, is applied in the xy-plane. At resonance \mathbf{H}' is precessing at the Larmor frequency, and the bulk magnetic moment begins to slowly precess about \mathbf{H}' while maintaining its rapid precession about \mathbf{H}_z . Therefore, the angle between \mathbf{M}_z and the z-axis increases and a Zeeman transition, or “spin flip”, is induced and an EPR signal is detected.

Once the perturbation is removed, the z-component of the magnetization \mathbf{M}_z will relax back to equilibrium with characteristic time constant T_1 :

$$d\mathbf{M}_z/dt = -(\mathbf{M}_z - \mathbf{M}_0) / T_1 \quad (2.2.7)$$

and the components of the magnetization in the xy-plane relax with characteristic time constant T_2 :

$$d\mathbf{M}_x/dt = -\mathbf{M}_x / T_2 \quad (2.2.8)$$

$$d\mathbf{M}_y/dt = -\mathbf{M}_y / T_2$$

Thus, the z-component of relaxation is typically called “ T_1 relaxation” and the component of relaxation in the xy-plane is generally dubbed “ T_2 relaxation” due to the time constants that characterize each mechanism. By combining the rate of change of magnetization at equilibrium due to \mathbf{H}_z and during relaxation, the Bloch equations can be written as:

$$d\mathbf{M}_x/dt = \omega_L \mathbf{M}_y - \mathbf{M}_x / T_2 \quad (2.2.9)$$

$$d\mathbf{M}_y/dt = -\omega_L \mathbf{M}_x - \mathbf{M}_y / T_2$$

$$d\mathbf{M}_z/dt = -(\mathbf{M}_z - \mathbf{M}_0) / T_1$$

The power absorbed by the sample—which determines the EPR spectrum—is related to $\mathbf{H} \cdot d\mathbf{M}/dt$ by a Lorentzian shape function; therefore, it is clear from the Bloch equations that relaxation affects the EPR lineshape.

T_1 and T_2 relaxation are more formally called “spin-lattice relaxation” and “transverse relaxation”, respectively. Spin-lattice relaxation involves the equilibration of

the bulk magnetization along the z-axis of the laboratory frame through the transfer of energy to the surroundings (lattice), and for nitroxides in solution T_1 relaxation is typically much slower than T_2 relaxation. The spin states have a finite lifetime due to relaxation, and from the Heisenberg uncertainty relation $\Delta\nu\Delta t \approx 1$ the line broadening due to spin-lattice relaxation is on the order of $(\gamma_e T_1)^{-1}$. Transverse relaxation involves the dephasing of the bulk magnetization with \mathbf{H}' in the xy-plane via interactions within the spin system; since T_2 relaxation is typically much quicker than T_1 relaxation, the contribution from transverse relaxation—on the order of $(\gamma_e T_2)^{-1}$ —determines the total linewidth.

There are many mechanisms that affect the relaxation times, and thus the EPR lineshape. For example, spin-spin interactions such as spin diffusion, Heisenberg exchange or dipolar interactions will influence the rate of transverse relaxation. Spin diffusion arises from the continuous exchange of energy throughout the system via mutual spin flip-flops, causing energy to be dissipated throughout the sample rather than being lost to the lattice. Heisenberg exchange results from direct collision between two spins whose wave functions overlap, resulting in mutual spin flip-flop. Such collisional interactions with oxygen homogeneously broadens the intrinsic lineshape, as mentioned above, such that the proton hyperfine interactions coalesce into an inhomogeneously broadened envelope. Dipolar interactions do not require orbital overlap, but instead depend on the inverse cube of the distance between interacting spins and also the angle between the dipolar vector and the applied magnetic field.

There are also inhomogeneous contributions to the transverse magnetization that vary the relative energies of the spin states, rather than their lifetimes. Particularly for echo-detected EPR spectra, instantaneous diffusion arises from a change in the local field of one spin due to the flip of a nearby dipolar-coupled spin. The change in local field causes the spin to dephase, which increases the rate of dephasing of the transverse magnetization. Spectral diffusion due to molecular motion, nuclear spin flip-flops, or electron-nuclear cross-relaxation causes the Larmor frequency of a spin packet to change over time, which initiates dephasing of the magnetization. Line broadening from spectral diffusion processes can be either Lorentzian or Gaussian, depending on how rapidly the instantaneous Larmor frequency $\omega_L(t)$ evolves throughout the distribution of frequencies that are sampled (i.e., the correlation time of the spectral diffusion process).

Perhaps the most important and obvious contribution to EPR lineshape arises from molecular motion. Motion of the nitroxide through different environments and reorientation with respect to the external magnetic field modulates the resonance frequencies and generates local fluctuating fields near the Larmor frequency that add to the oscillating microwave field \mathbf{H}' and induce relaxation. Nitroxide motion is typically characterized by a rotational correlation time, τ_R , and dynamic processes that reorient the nitroxide at frequencies that correspond to the total spectral anisotropy ($\tau_R^{-1} \approx 2\pi\Delta\nu$) will average the magnetic anisotropy (Figure 2.2.1). At X-band microwave frequencies, motional averaging of the anisotropy in the nitrogen hyperfine interaction is the primarily evident feature that is observable in the EPR spectrum, and this process is essentially analogous to the classic two-state chemical exchange process in NMR (where in this case

a distribution of resonance frequencies bounded by ω_{Azz} and $\omega_{(Axx+Ayy)/2}$ are sampled, and the exchange rate is the inverse correlation time τ_R^{-1} .¹⁴ The relation between τ_R and the spectral anisotropy leads to a finite range of spectral sensitivity to nitroxide motion; at X-band, the range of nitroxide motions that variably average the magnetic anisotropy is approximately 50 ns to 500 ps. This so-called EPR timescale gives rise to three dynamic regimes—the rigid limit, where the motion is slow ($\tau_R > \sim 50$ ns) and the spectrum is dominated by the magnetic anisotropy; the isotropic limit, where fast motion ($\tau_R < \sim 500$ ps) completely averages the anisotropies and line broadening from relaxation effects becomes negligible; and the intermediate motional regime, where the magnetic anisotropy is variably averaged and the EPR spectrum is exquisitely sensitive to small differences in the reorientational motion of the nitroxide.

2.2.3 The Rigid Limit. The static spectroscopic properties of the nitroxide are determined by the strength and geometries of the interactions amongst the assortment of magnetic moments present. This is the case in the rigid limit (Figure 2.2.1), where nitroxide motions are slower than approximately 50 ns and are therefore “frozen” on the X-band EPR timescale. Since the EPR spectrum is dictated by the anisotropy in the magnetic parameters in the rigid limit, the lineshape is very broad and appears similar to the powder spectrum in Fig. 2.1.4 (assuming an isotropic distribution of spin-labeled protein orientations in solution). According to Eq. 2.1.19, the positions of the resonance lines in the rigid limit EPR spectrum are therefore given by:

$$h\nu = \mathbf{g}_{\text{eff}}(\mathbf{0})\beta\mathbf{H} + \frac{1}{2}\mathbf{A}_{\text{eff}}(\mathbf{0})\mathbf{m}_I \quad (2.2.10)$$

and the linewidth of each resonance is on the order of the corresponding transverse relaxation time $(\gamma_e T_2)^{-1}$.

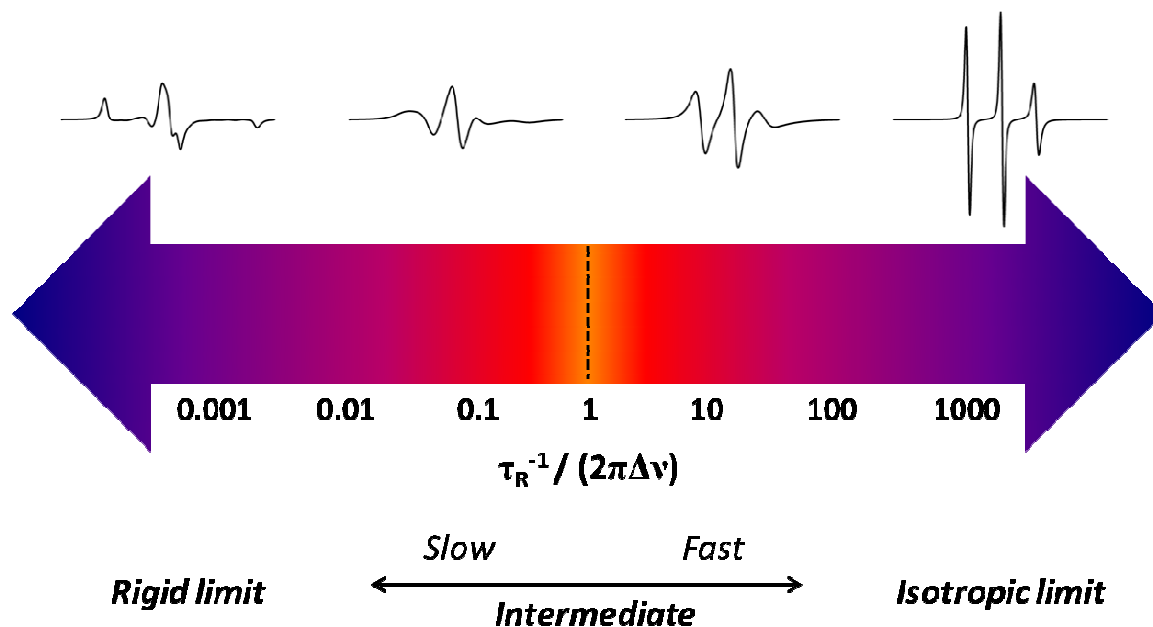


Figure 2.2.1. Dynamic Regimes of Nitroxide Motion. The relationship between the frequency of nitroxide motion (τ_R^{-1}) and the total spectral anisotropy ($2\pi\Delta\nu$) determines the sensitivity of the EPR spectrum to nitroxide motion. At X-band, the total spectral anisotropy is determined by the nitrogen hyperfine interaction (approximately 31 G, or 90 MHz using the EPR conversion factor 2.83 MHz/G), and therefore nitroxide motions between ~ 50 ns and ~ 500 ps are in the intermediate regime and average the magnetic anisotropy to various extents.

2.2.4 The Isotropic Limit. The other motional extreme is the isotropic limit, where $\tau_R^{-1} \gg 2\pi\Delta\nu$ and the anisotropic contributions to the magnetic interactions have been completely averaged out. In the isotropic limit, the EPR spectrum consists of a

series of narrow, symmetric lines of equal width (Figure 2.2.1). In this regime, the reorientational motion of the nitroxide is too fast to modulate T_2 relaxation and broaden the lines. At X-band, the isotropic limit corresponds to nitroxide motions faster than ~ 500 ps. Spectra in the isotropic limit can be simulated using time-independent effective Hamiltonian approaches that calculate effective \mathbf{A} and \mathbf{g} tensors, such as the “Wobble” model implemented by Griffith¹⁰ or the “Oscillation” model proposed by Timofeev.¹¹

2.2.5 The Intermediate Motional Regime and the Microscopic Order, Macroscopic Disorder Model. Intermediate motions give rise to complex and information-rich EPR spectra with a variable extent of motional averaging (Figure 2.2.1). In the intermediate motional regime, the EPR spectrum is extremely sensitive to small changes in the reorientational motion of the nitroxide. Within this intermediate regime, fast nitroxide motion is characterized by correlation times between ~ 0.5 ns and 2 ns, where the magnetic anisotropy is completely averaged but relaxation effects from the reorientational motion of the nitroxide broaden the linewidth. For fast nitroxide motion, the effect of τ_R on relaxation and line broadening can be determined using Redfield’s perturbation theory.¹³

A number of parameters are used to define slow nitroxide motion (between 2 ns and ~ 50 ns; Figure 2.2.1), and modeling of the corresponding EPR spectra requires a time-dependent Hamiltonian that is described by the stochastic Liouville equation of motion. Prof. Jack Freed and coworkers have developed a nitroxide motional model for the intermediate regime called the microscopic order, macroscopic disorder (MOMD)

model.^{12,15} In MOMD, the unsaturated EPR intensity as a function of frequency $I(\omega)$ may be represented in matrix element notation as:

$$I(\omega) = \langle\langle \nu | (\tilde{\Gamma} - iL) + i\omega \mathbf{1} | \nu \rangle\rangle \quad (2.2.11)$$

where $\langle\langle \nu |$ is a vector representing the observable magnetization, including the S_+ spin operator and the Boltzmann distribution function, $\tilde{\Gamma}$ is the “symmetrized” diffusion operator used to model the classical motion of the nitroxide, and L is the Liouville superoperator matrix derived from the orientation-dependent spin Hamiltonian. The matrix equation is constructed using a basis set with dimension generally in the range of 30 to 20,000 depending on the rate and amplitude of nitroxide motion and the desired spectral resolution. The basis set is constructed as a product of generalized spherical harmonics $D_{MK}^L(\alpha, \beta, \gamma)$ and the spin transition indices p and q for the electronic and nuclear spins, as described in detail in Budil *et al.*¹⁵:

$$|L, M, K, p^S, q^S, p^I, q^I\rangle \equiv |L, M, K\rangle \otimes |p^S, q^S, p^I, q^I\rangle$$

$$|L, M, K\rangle \equiv \sqrt{\frac{2L+1}{8\pi}} D_{MK}^L(\alpha, \beta, \gamma) \quad (2.2.12)$$

In the MOMD model, three coordinate frames are used to represent the microscopic motion of the nitroxide with respect to a fixed macroscopic director (Figure 2.2.2). In the molecule-fixed magnetic frame (x_M, y_M, z_M), as mentioned above z_M is taken to lie along the $2p_z$ orbital of the nitrogen, x_M coincident with the nitroxide bond axis, and y_M is selected for a right-handed coordinate system. The magnetic frame is the principal frame for the nitroxide hyperfine A- and g-tensors. The second coordinate

frame is the rotational diffusion tensor frame (x_R, y_R, z_R), which is related to the molecular frame by a z-y-z Euler rotation using the angles γ_D, β_D , and α_D , where a positive angle produces a counterclockwise rotation when viewed from the positive side of the rotating axis. For the R1 spin-labeled side-chain, the rate of nitroxide motion about each of these axes and their orientation with respect to the molecular frame indicates which dihedrals are undergoing torsional oscillations that are contributing to motional averaging in the EPR spectrum. A spherically harmonic restoring (ordering) potential may be implemented, described by the relation $U(\theta) = -\frac{1}{2}k_B T c_0^2 (3\cos^2\theta - 1)$ where c_0^2 is the scaling coefficient. Typically only the first-order term of the restoring potential is applied, which constrains the amplitude of diffusion about z_R within a cone defined by the instantaneous angle θ between z_R and the symmetry axis of the conical potential. The symmetry axis of the conical potential defines the z-axis of the third coordinate frame, the uniaxial director frame. The director frame is fixed with respect to the protein, and forms an angle ψ with respect to the external magnetic field \mathbf{H} . To get the final spectrum corresponding to an isotropic distribution of protein orientations, the spectra are summed over ψ . Finally, in addition to the explicit magnetic interactions of the electron and nuclear spins, the MOMD model allows for implementation of orientation-dependent Lorentzian and Gaussian line broadening.

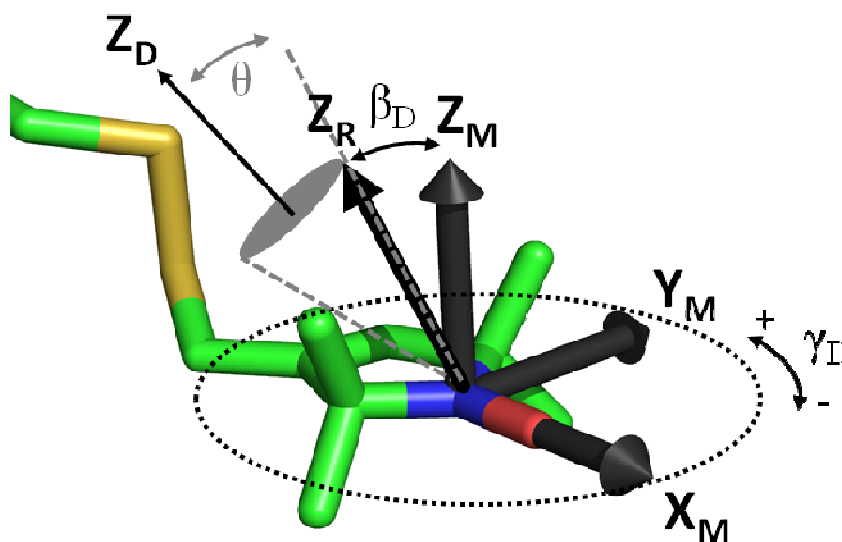


Figure 2.2.2. MOMD Coordinate Systems. Shown is the relationship between the magnetic tensor frame (x_M, y_M, z_M) the z-axis of the rotational diffusion tensor frame, z_R , and the z-axis of the uniaxial director frame, z_D . For simple z-axis anisotropic motion, the rotation about the z_M -axis by angle γ_D is followed by rotation about the new y_M' -axis by angle β_D (for clarity, β_D is shown as a negative rotation and only the z-axis of the rotational diffusion tensor is rendered). The amplitude of z_R motion may be restricted within a cone defined by the instantaneous angle θ by implementation of the first-order term of a restoring potential.

Thus, in the MOMD model nitroxide motion is characterized by the rate anisotropy (described by the rotational diffusion tensor and Euler angles) and the amplitude (described by the restoring potential) of rotational diffusion. Typically, the relationship between the ordering potential and amplitude of motion is described by an order parameter S , where $S = \frac{1}{2}(3\cos^2\theta - 1)$; therefore the value of S is positive when $0^\circ \leq \theta < 54.7^\circ$. The rotational correlation time is related to the rotational diffusion tensor by the relation $\tau_R = (6\mathbf{R})^{-1}$, where \mathbf{R} may either be the geometric mean of the principal values of the rotational diffusion tensor $(\mathbf{R}_{xx} \cdot \mathbf{R}_{yy} \cdot \mathbf{R}_{zz})^{1/3}$ or one of the principal values for

an anisotropic correlation time. It should be noted that the principal values of the \mathbf{R} tensor are typically expressed as \mathbf{R}_{jj}' , where $\mathbf{R}_{jj}' = \log_{10}(\mathbf{R}_{jj})$. Thus, MOMD fitting of experimental spectra supplies several pieces of information—the principal components of the rotational diffusion tensor, the orientation of the rotational diffusion tensor frame, the amplitude of nitroxide motion, the extent of line broadening, and for multicomponent spectra the relative populations of each component. Whereas the effect of various combinations of dynamic parameters on the EPR spectrum has been meticulously reviewed elsewhere,⁸ little discussion has been lent to practical issues and general strategies that must be considered when using MOMD. Therefore, these topics will be briefly discussed here with respect to the newly released Multicomponent software developed by Dr. Christian Altenbach for MOMD modeling.

A variety of nonlinear-least-squares-based algorithms may be used to fit a MOMD spectrum to an experimental EPR spectrum in order to extract useful information regarding intermediate nitroxide motion. The Monte Carlo approach is a robust, random sampling method that employs large step sizes across the entire parameter space, and calculates the reduced χ^2 to identify the parameter value that gives the best fit. This method is time-consuming and impractical, yet accurate and in some cases necessary when other algorithms get stuck in a local χ^2 minimum that does not produce the best fit. The Downhill Simplex algorithm is a heuristic search method that uses smaller step sizes to determine the local χ^2 optimum for each simplex, and the step size is reduced to fine-tune the fit as it reaches convergence. This method can be time-consuming depending on the initial step size and accuracy of the initial parameter guess, however the initial step

size can be defined at the user's discretion. The Downhill Simplex method is particularly useful for determination of the Euler angles that specify the location of the rotational diffusion tensor frame; typically an initial step size of 10 degrees is optimal.

The third and final minimization procedure available in Multicomponent is a modified Levenberg-Marquardt algorithm. This quasi-Newton method requires calculation of a partial derivative of the spectrum with respect to each of the nonlinear parameters for each iteration of the minimization, thus requiring small step sizes in parameter values and long computation times. However, since the partial derivative information can be used to estimate the quality of fit per iteration, the reliability and efficiency of the fit is increased by eliminating or constraining indeterminate parameters. Thus, the Levenberg-Marquardt is an efficient and accurate method for obtaining convergence, but suffers from the tendency to get stuck in local χ^2 minima that do not produce the best overall fit. In many cases, global convergence may be more efficiently reached through multi-faceted approach, such as initial minimization with the Downhill Simplex method (with a properly defined initial step size) followed by fine-tuning with the Levenberg-Marquardt algorithm.

Due to the inherent complexity of intermediate motion, modeling such spectra with the MOMD routine requires the fitting of many parameters that are often to some extent correlated, raising concerns over the uniqueness of fits. Several strategies may be implemented to reduce the number of fitting parameters and increase the number of constraints on the fitting process. Obtaining the EPR spectra at low temperatures (e.g. 200 K) freezes out contributions from nitroxide motion, effectively creating the rigid

limit condition. Fitting the rigid limit EPR spectra with Eq. 2.2.10 allows for the determination of the principal values of the magnetic \mathbf{g} and \mathbf{A} tensors, which reduces the number of MOMD fitting parameters. A more accurate calculation of the principal values of the \mathbf{g} tensor may be obtained by fitting rigid limit spectra obtained at higher microwave frequencies, where there is better resolution in the \mathbf{g} anisotropy. If the magnetic parameters are known, then only the dynamic parameters require minimization (i.e. rotational diffusion tensor, Euler angles, ordering potential, homogeneous and inhomogeneous line broadening tensors). Furthermore, if a motional model already exists which defines the typical behavior of the nitroxide spin label (e.g. weakly-ordered χ_A/χ_S model for solvent-exposed α -helical sites¹⁶), then these parameter values may be used to initially define the dynamic parameters prior to minimization.

In the absence of a preexisting motional model, the parameter search space can be constrained for simple motional modes due to the axial symmetry in the magnetic parameters. In cases where the rotational diffusion rate is fast about a single axis on the EPR timescale, solely the z-axis of the diffusion tensor may be minimized (since this is the axis about which the ordering potential is applied), in combination with the ordering potential and the Euler angles γ_D and β_D (while also constraining them between 0° and 90°). However, if the ultimate goal is to map the axis of rotation onto a crystal structure or model of the spin label to determine which dihedral(s) are contributing to motional averaging, all of the redundant values of the Euler angles must be considered in order to determine the most likely orientation of the rotational diffusion frame. For example, given z-axis rate anisotropy and Euler angles ($\gamma_D = 10^\circ$, $\beta_D = 50^\circ$), the set of equivalent

values for γ_D are $\{10^\circ, 170^\circ, 190^\circ, 350^\circ\}$ and the equivalent values of β_D are $\{50^\circ, 130^\circ, 230^\circ, 310^\circ\}$. Typically most permutations of these values will not make physical sense with respect to the orientation of the rotational diffusion tensor frame, especially when taking into consideration the EPR lineshape and the final parameters of the fit. When additional axes of rotation come into play, the rate anisotropy becomes more complicated and additional parameters must be minimized over a larger search space (although the redundancy in the Euler angles is reduced).

Many of the dynamic parameters are correlated to a various extent, depending on the nature of nitroxide motion. For example, the diffusion rates are generally correlated with the ordering potential and line broadening, and also various combinations of Euler angles depending on the rate anisotropy. The effect is to generate a range of values where modifications to one parameter value may be perfectly compensated for by alterations in the correlated parameter. Depending on the overall objective, specific correlated parameters may be fixed (i.e. not minimized) to constrain the uncertainty and number of parameters to be fit. Although the range over which concomitant variations in correlated values will nearly perfectly compensate (i.e. not change χ^2) is typically small, it is not insignificant and must be taken into consideration when comparing spectral fits. In the Multicomponent program, the extent of these correlations can be monitored throughout the fit by correlation matrices.

The number of parameters doubles when there are two spectral components in slow exchange, which introduces a significant amount of uncertainty into the fitting process. In such cases, every effort should be made to create a situation in which one

component may be eliminated in order to individually fit the components. In the circumstance where one component is in the intermediate regime and the other is in the isotropic limit, this task is easily attainable using Redfield theory to simulate and subtract the motionally narrowed component. Similarly, if one component is in the rigid limit then the spectrum can be fit and subtracted by determining the principal values of the magnetic tensors—although there may be significant error in the calculation of the A_{xx} , A_{yy} and g tensor components depending on the lineshape of the faster component. When the dynamic modes are similar and overlap significantly in the EPR spectrum, the defining features of each line are merged together and the correlation between parameters increases significantly. As will be seen in Chapter 4, the BtuB T156R1 dynamic modes are very similar, but the equilibrium distribution is affected by acyl chain length. Therefore, the goal was to reconstitute BtuB into a membrane that produces a single component (DLPC bilayers). Varying the temperature is another option; however, this includes the complicated assumption that only the equilibrium between dynamic modes and their rotational rates are modulated while all other interactions of the nitroxide with its environment remain unchanged.

Despite concerns arising from overparameterization and uniqueness of fit, when used properly the MOMD model as implemented in Multicomponent is a powerful tool for the extraction of important dynamic parameters from EPR spectra in the intermediate motional regime. The EPR spectra in this regime are remarkably sensitive to the rate, rate anisotropy and amplitude of nitroxide motion, and opportunely, various modes of

protein dynamics modulate spin label motion and variably average the X-band magnetic anisotropy.

2.2.6 Processes in Proteins that Affect Lineshape at X-band. As indicated above, processes that affect nitroxide motion on the nanosecond timescale will modulate the transverse relaxation and average the magnetic anisotropy at X-band microwave frequencies. In SDSL-EPR a nitroxide spin label, typically MTSL, is covalently attached to the protein backbone to generate the R1 side-chain. Thus, nanosecond motions of the R1 nitroxide ring relative to the external magnetic field will affect the EPR lineshape and yield important information about the structure and dynamics of the local protein environment.

There are primarily three processes in proteins that affect nanosecond-timescale nitroxide motion (Figure 2.2.3). The first process involves the overall Brownian diffusion of the protein, which is generally approximated by the Stokes-Einstein relation. In low-viscosity aqueous solvents at room temperature, the rotational diffusion of globular proteins smaller than approximately 40 kDa occurs on the nanosecond timescale. In dilute solutions the rotational diffusion is random, and therefore adds an isotropic contribution to the motional averaging. In some cases, such as for EPR-based protein-protein binding assays, it may be advantageous to extract information regarding the overall rotational diffusion of the spin-labeled protein. However, in most situations contributions to the EPR spectrum from this mechanism are undesirable, because it hides the unique contributions to the lineshape indicative of the spin label's local environment.

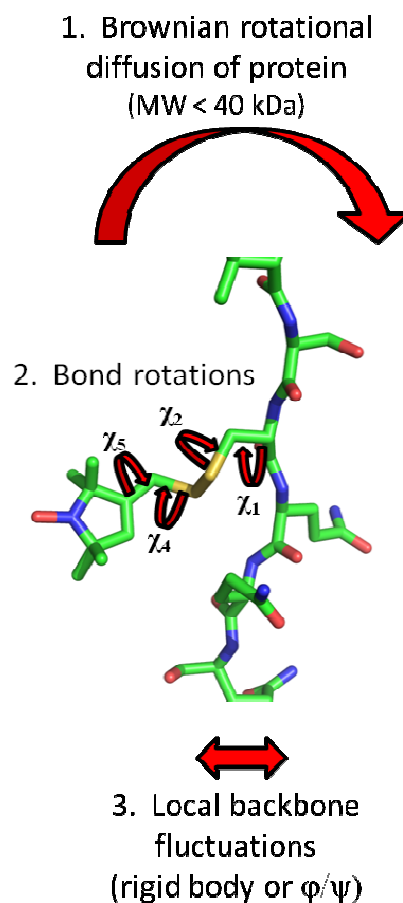


Figure 2.2.3. Processes in Proteins that Affect X-band Lineshape. Shown are the three main dynamic processes in proteins that affect the X-band EPR lineshape. For small soluble proteins, if the overall rotational diffusion occurs on the nanosecond timescale, then the magnetic anisotropy will be averaged by isotropic motion. The second process that contributes to averaging involves bond rotations of the spin label; typically torsional oscillations about amino acid side-chain dihedrals occurs on the nanosecond timescale at room temperature. Finally, high-frequency, low amplitude local backbone motions is the third process that may average the magnetic anisotropy at X-band frequencies.

The second process in proteins that contributes to motional averaging involves bond rotations of the spin label (Figure 2.2.3). Fortunately, the intrinsic rate of bond isomerization in amino acid side-chain dihedrals occurs on the nanosecond timescale at room temperature. Since the R1 spin label is similar in structure and composition to a

typical amino acid, in the absence of competing interactions or steric restrictions isomerization about R1 dihedrals also typically occurs on the nanosecond timescale. The dihedral angles χ_1 , χ_2 , χ_4 , and χ_5 can interconvert between the **m** ($-60^\circ \pm 20^\circ$), **p** ($+60^\circ \pm 20^\circ$) and **t** ($\pm 180^\circ \pm 20^\circ$) rotamers, according to the conventions of Lovell et al.,¹⁷ although isomerization about the disulfide bond χ_3 between $+90^\circ$ and -90° requires negotiation of a large activation energy barrier and generally occurs at a much slower rate.¹⁶ In essence, the nitroxide is at the end of a relatively long and flexible side-chain that can interconvert between a number of rotamers on the nanosecond timescale. Consequently, local primary, secondary or tertiary structural features of the protein that modulate nanosecond spin label dynamics will, in turn, modulate the X-band EPR spectrum. For example, the EPR spectrum of a spin-labeled α -helix will look different than that from a spin label on a flexible loop or a spin label in tertiary contact.

Backbone dynamics are the third process in proteins that affects nanosecond nitroxide motion (Figure 2.2.3). Local backbone fluctuations or ϕ/ψ oscillations that occur on the nanosecond-timescale and reorient the nitroxide with respect to the external magnetic field will motionally average the X-band EPR spectrum. Conformational exchange at the level of the protein backbone can also modulate the spectral anisotropy. While high-frequency, low-amplitude conformational exchange will directly average the anisotropic EPR lineshape, slow conformational exchange will produce a multicomponent EPR spectrum so long as each conformational substate produces different nanosecond dynamics of the nitroxide (and the exchange rate $k_{\text{ex}}^{\text{AB}} \ll \Delta\nu^{\text{AB}}$). In other words, while the conformational exchange itself is too slow to produce motional

averaging, differences in the physicochemical environment within each substate will produce multiple components undergoing slow spectral diffusion that are resolvable within the EPR spectrum.

Most protein conformational exchange is in fact slow on the X-band EPR timescale (Figure 2.2.4), as will be seen for the BtuB Ton box equilibrium in Chapter 3. In some cases, the internal dynamics of the spin label are modulated by the local environment such that multiple dynamic modes of the nitroxide are in slow exchange, as will be seen in Chapter 4. In both of the above circumstances, the exchange rate is too slow to modulate T_2 relaxation and average the corresponding lineshapes. Therefore the situation becomes ambiguous, and multicomponent EPR spectra may arise either from slow protein conformational exchange or slow spin label rotameric exchange. Fortunately, several strategies are emerging for distinguishing slow rotameric exchange from slow conformational exchange, including osmolyte perturbation,¹⁸ high-pressure EPR¹⁹ and saturation recovery.²⁰

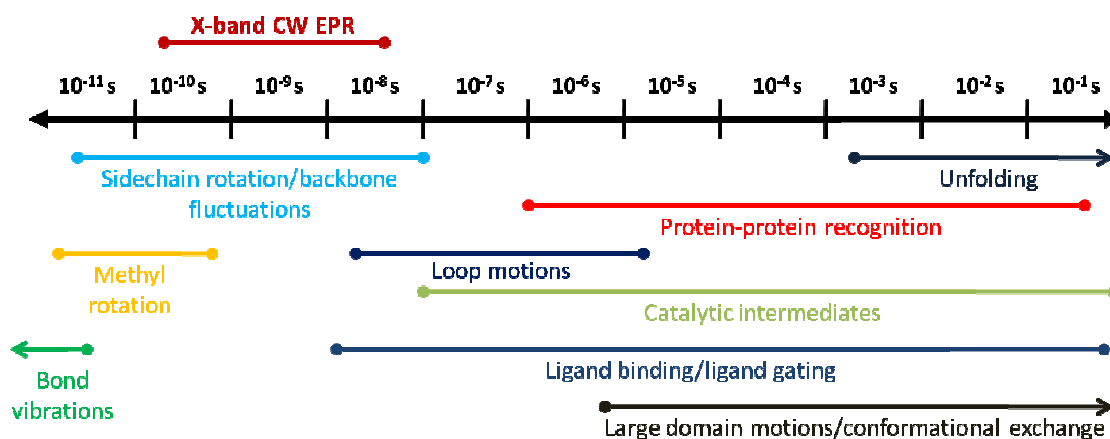


Figure 2.2.4. Timescales of Protein Dynamics. Shown is a comparison of the timescale for averaging of the X-band EPR spectrum versus the timescales of some common dynamic processes that occur in proteins.

2.3 Probing Conformational Exchange with Saturation Recovery

Some spin label rotameric exchange processes, such as isomerization about the disulfide bond, are slow on the X-band EPR timescale ($k_{\text{ex}}^{\text{AB}} \ll \Delta\nu^{\text{AB}}$). Slow rotameric exchange between chemically inequivalent environments produces multiple components in the continuous wave EPR spectrum, which are indistinguishable from protein conformational equilibria that are also slow on the X-band timescale (Figure 2.2.4). This ambiguity presents a major conundrum since the objective of the SDSL-EPR experiment is to exclusively analyze structural dynamics of the protein; in essence, the flexibility of the spin label can be both an advantage and a disadvantage.

However, the slowest side-chain rotameric exchange processes typically occur on the order of a few μs —at least an order of magnitude faster than most protein conformational exchange, which typically occurs on timescales of tens of μs or slower (Figure 2.2.4).²¹ Moreover, since exchange processes on the timescale of 1–100 μs modulate T_1 relaxation, while some spin label rotameric exchange processes are too slow to modulate the transverse relaxation and average the corresponding lineshapes, in many cases the exchange is fast enough to average the intrinsic spin-lattice relaxation times. In contrast, typical protein conformational exchange will either partially or not at all average the intrinsic T_1 s. Therefore, T_1 measurements provide a means for differentiating rotameric exchange from conformational exchange.

Saturation recovery (SR) is a pulse EPR technique developed by Prof. James Hyde and coworkers for the measurement of T_1 relaxation times at room temperature.²²⁻²⁴

In SR, a long saturating pulse is applied to the $m_I = 0$ nitrogen hyperfine line and the return of signal intensity (Boltzmann polarization) is monitored with a weak CW microwave field at the same frequency. The SR signal is detected as the exponential return of the longitudinal magnetization to equilibrium and follows the general behavior:

$$\mathbf{M}_z(\mathbf{t}) = \mathbf{M}_0(1 - e^{-\frac{t}{T_1}}) \quad (2.3.1)$$

where $\mathbf{M}_z(\mathbf{t})$ is the instantaneous longitudinal magnetization and \mathbf{M}_0 is the magnetization at equilibrium, according to Eq. 2.2.3. In addition to electron spin-lattice relaxation (characterized by the time constant T_{1e}), spectral diffusion within the $m_I = 0$ hyperfine manifold due to rotational diffusion (τ_R) and between manifolds via electron-nuclear cross-relaxation (T_{1n}) can contribute to the recovery of \mathbf{M}_z and thus the measured time constant of recovery, T_1 . Spin packets that diffuse throughout the $m_I = 0$ nitrogen hyperfine manifold amongst a distribution of frequencies broader than the bandwidth of the saturating pump pulse will affect the SR signal if τ_R is slow compared to the duration of the pulse and fast compared to T_{1e} ; spin packets that were not perturbed by the saturating pulse will diffuse into the perturbed area under observation and add a contribution to the recovery on the order of τ_R . The situation is similar for electron-nuclear cross-relaxation, where the spin packets diffuse over a large frequency range relative to the bandwidth of the pump pulse, and will thus add a contribution to the SR signal on the order of T_{1n} if the length of the pulse is shorter than T_{1n} . Typically, T_{1n} and τ_R are much shorter than T_{1e} ; therefore, saturation pulses of sufficiently long durations (> 100 ns) such that spectral diffusion due to T_{1n} and τ_R is complete within the pulse length will suppress the contributions to the SR signal from these mechanisms.

Multicomponent EPR spectra characteristic of two nitroxide dynamic modes in slow exchange are characterized by two rotational correlation times, τ_R^A and τ_R^B . Since rotational correlation times generally correlate with T_1 ,²⁰ in principle each dynamic mode will have a different intrinsic spin-lattice relaxation time, T_1^A and T_1^B . Thus, for such systems the SR signal is a function of each intrinsic relaxation time (T_1^A and T_1^B) and the exchange rate (k_{ex}^{AB}). If the exchange rate between dynamic modes is slow on the T_1 timescale:

$$k_{ex}^{AB} \ll \frac{1}{2} \left(\frac{1}{T_1^A} - \frac{1}{T_1^B} \right) \quad (2.3.2)$$

then k_{ex}^{AB} will not modulate the intrinsic spin-lattice relaxation times and the SR signal will recover to equilibrium with a bi-exponential time course characterized by two time constants equal to T_1^A and T_1^B . At the other extreme, if the exchange rate between dynamic modes is fast on the T_1 timescale:

$$k_{ex}^{AB} \gg \frac{1}{2} \left(\frac{1}{T_1^A} - \frac{1}{T_1^B} \right) \quad (2.3.3)$$

then the measured SR signal will be a single-exponential recovery with one effective time constant:

$$\mathbf{M}_z(\mathbf{t}) = \mathbf{M}_0 \left(1 - e^{-\frac{t}{T_1^{\text{eff}}}} \right) \quad (2.3.4)$$

which is a linear combination of the intrinsic T_1 relaxation times weighted by the fractional populations of each component:

$$T_1^{\text{eff}} = f^A \cdot T_1^A + (1 - f^A) \cdot T_1^B \quad (2.3.5)$$

where the fractional populations f^A and f^B can be determined from MOMD spectral fits. In the intermediate exchange regime the problem becomes underdetermined; in such situations the two exponential time constants in the SR signal become a function of the intrinsic relaxation times, the fractional population of each component, and the exchange rate. One strategy for treatment of intermediate-regime SR data involves the titration of a relaxation agent, such as molecular oxygen, that variably modulates the intrinsic T_1 of each component.²⁵ Combined with MOMD fitting to determine the fractional populations of each component, the intrinsic T_1 s and exchange rate can be determined according to the procedure described by Bridges *et al.*²⁰ This method is valid for the characterization of exchange lifetimes between approximately 1-70 μ s, a time window which has been traditionally difficult to access with solution NMR but wherein many important exchange processes in proteins exist.

Thus, SR-EPR can be used to distinguish slow rotameric exchange processes from protein conformational exchange, both of which give rise to multiple components in the CW EPR spectrum. Since rotameric exchange processes typically occur on timescales faster than several μ s, these processes will generally yield single-exponential SR signals and the slow limit of the exchange rate can be determined by Eq. 2.3.3. In order to solve Eq. 2.3.3 however, both intrinsic T_1 s must be known. Given the time constant for recovery measured by SR, one predetermined T_1 , and the fractional populations of each component determined by MOMD fitting, Eq. 2.3.5 can be used to calculate the second T_1 . Thus, in order to determine the slow limit of the exchange rate, it is a critical prerequisite that one spectral component must be isolated experimentally for the

measurement of its T_1 relaxation time with SR-EPR. Protein conformational exchange processes typically occur slower than tens of μs and will generally yield bi-exponential SR signals; for extremely slow exchange, the fast limit on the exchange rate can be determined by Eq. 2.3.2 in order to describe the exchange in a more quantitative manner.

2.4 Double Electron-Electron Resonance

One of the most powerful capabilities of SDSL-EPR involves measuring the coupling between interacting spins, which encodes information regarding interspin distances and distance distributions. A sufficiently large set of distances obtained between pairs of spin labels can provide valuable information on protein structural dynamics at a resolution of $\sim 3 \text{ \AA}$,²⁶ given the conformations of the spin labels are known. The coupling between two spins S_A and S_B is described by the Hamiltonian:

$$\mathcal{H}_{ee} = S_A \cdot \mathbf{D} \cdot S_B + \mathbf{J} \cdot S_A \cdot S_B \quad (2.4.1)$$

where \mathbf{D} is the dipole-dipole tensor and \mathbf{J} is the exchange coupling. By assuming an isotropic exchange coupling and the point-dipole approximation, the Hamiltonian can be expressed as the sum of secular and pseudosecular contributions:

$$\begin{aligned} \mathcal{H}_{\text{sec}} &= [\mathbf{J} + \omega_{AB}(1 - 3\cos^2\theta)] S_{A,z} S_{B,z} \\ \mathcal{H}_{\text{psec}} &= [\mathbf{J} - \frac{1}{2}\omega_{AB}(1 - 3\cos^2\theta)] (S_{A,x} S_{B,x} + S_{A,y} S_{B,y}) \end{aligned} \quad (2.4.2)$$

In the above expressions, θ is the angle between the spin-spin vector and the external magnetic field and ω_{AB} is the dipolar coupling frequency, given by:

$$\omega_{AB} = (\mu_0 \mathbf{g}_A \mathbf{g}_B \beta^2) / (4\pi r_{AB}^3) \quad (2.4.3)$$

where μ_0 is the vacuum permeability, \mathbf{g} represents the \mathbf{g} tensor for each spin, β is the Bohr magneton, and r_{AB} is the interspin distance. Thus, the dipolar part of the spin-spin coupling is a function of the interspin distance and the angle between the dipolar vector and external magnetic field. For distances longer than ~ 10 Å, the exchange interaction becomes negligible and the interaction is solely due to the dipole-dipole coupling between spins.³⁰

Various CW EPR techniques can measure distances shorter than ~ 25 Å; determining the exchange interaction allows for the measurement of distances between ~ 4 -8 Å,²⁷ whereas lineshape broadening due to the dipolar interaction allows measurement of distances in the ~ 8 -25 Å range.²⁸ For distances longer than ~ 25 Å, the dipolar coupling is too small to broaden the CW spectrum and is hidden in the inhomogeneous linewidth. The pulsed EPR method double electron-electron resonance (DEER) is a two-frequency echo-based technique that can extract weak dipolar couplings for the measurement of distances in the range of ~ 17 -80 Å.²⁹ In DEER, spectral diffusion of spin packets at one frequency is induced at successive time intervals via reversal of the dipolar contribution from coupled spins at the second frequency. Reversal of the dipolar contribution affects the angular rate ω_A of the spins at the first frequency, which eliminates the ability of these spins to be subsequently refocused by the final echo. Conveniently, for distances longer than ~ 15 Å the resulting DEER signal depends only on the secular contribution to the spin coupling Hamiltonian,³⁰ and its intensity is modulated based on the cosine of the dipolar frequency. In this section, a brief

introduction to pulsed EPR will precede a more detailed description of the DEER experiment, which will be followed by a few practical considerations.

2.4.1 Introduction to Pulsed EPR. In order to understand pulsed EPR, first the difference between CW and Fourier transform techniques must be realized. These techniques can be compared by using an (oversimplified) analogy which relates them to musical instruments, where the sample is a guitar which is continuously playing a unique chord, and the magnet is a piano. For CW techniques, the magnet successively plays each key on the piano, detecting resonances between the frequencies in the guitar chord and frequencies of the piano notes along the way. An alternative approach is to strike each key on the piano (magnet) at the same time and Fourier transform the resulting sound to obtain the frequency spectrum of the guitar (sample); this is called the multiplex advantage and is fundamental to pulsed magnetic resonance experiments. In pulsed EPR a short and intense microwave pulse is applied consisting of a finite bandwidth of frequencies, the signals coming from the sample are digitized and Fourier transformed to obtain the EPR spectrum in the frequency domain.

While \mathbf{H} is the static magnetic field used to establish the equilibrium condition, an additional weaker microwave field \mathbf{H}' is required to detect resonances. Both \mathbf{H}' and the detection coils must lie in the xy plane so that magnetic effects from the sample after perturbation from equilibrium are not masked by the much stronger field \mathbf{H} . Thus, only transverse magnetization will give a signal, and the duration over which a signal can be acquired depends on both homogeneous (T_2) and inhomogeneous contributions to the effective transverse relaxation. The heart of pulsed EPR experiments lies in the

manipulation of the magnetization by \mathbf{H}' pulses that have specific tip angles, and the subsequent detection of the magnetic behavior during its return to equilibrium. Microwave pulses are often named by their tip angles, and the most commonly employed tip angles are $\pi/2$ (90 degrees) and π (180 degrees). A $\pi/2$ pulse will tip the magnetization into the xy plane, whereas a π pulse inverts the net magnetization vector by 180 degrees into the $-z$ -axis. Upon application of a $\pi/2$ pulse, the magnetization is coherent and rotating in the xy plane at the Larmor frequency. However, because the electron spins interact with their surroundings, the transverse magnetization will decay away and return to equilibrium through relaxation processes after the pulse ends. During this event, the magnetization loses phase coherence and each spin packet precesses in the xy plane with different angular frequencies. This process is called free-induction decay (FID), and it generates detectable currents in resonator that encode the frequency-domain EPR spectrum.

Immediately after the pulse is turned off, relaxation effects begin and the signal starts to disappear. Therefore, signal acquisition would ideally commence immediately after the pulse is turned off; however, the spectrometer cannot acquire the signal directly after the microwave pulse because the nW-range receiver would be damaged by power on the order of 1 kW from the pulse (and the signal would be masked anyway). Thus, there is a lag between the end of the pulse and when the signal can be measured; this is called dead time and is typically ~ 80 ns, depending on the quality factor, or Q , of the resonator.

The decay of the FID in an inhomogeneously broadened spectrum is dominated by the inhomogeneous effects, i.e. the dephasing of spin packets of different frequencies. While homogeneous dephasing due to relaxation results in random and irreversible events, dephasing of the magnetization due to inhomogeneous effects is reversible and static (no net energy is lost). Because the nitroxide EPR spectrum is inhomogeneously broadened, the remaining transverse magnetization (i.e. the EPR signal) can be resurrected after the FID has begun by application of an additional pulse that produces an “echo”. The development of echo techniques as pioneered by Erwin Hahn in 1950³¹ has revolutionized the field of pulsed magnetic resonance. The simplest and most common echo, termed a Hahn echo, involves a $\pi/2$ pulse followed by a π pulse; if the second pulse is applied at a time t after dephasing begins, then the echo maximum will occur at time t after the second pulse. This second pulse produces a signal after the dead time, and the echo shape resembles two back-to-back FIDs.

Echoes work by refocusing the magnetization and resurrecting a signal after dephasing and relaxation processes have begun. When the magnetization initially dephases there will be faster moving spin packets and slower moving spin packets, depending on their relative frequencies (i.e. $\omega_0 \pm \Delta\omega$). Upon application of the π pulse, the magnetization is inverted 180 degrees yet the spin packets rotate with the same speed and in the same direction relative to the coherent magnetization ω_0 . Now, instead of moving away from the slower spin packets, the faster moving spin packets move towards the slower spin packets and the magnetization eventually refocuses into an echo. The time constant for echo decay is called the phase memory time T_M ; many processes

contribute to T_M , such as spin-spin relaxation, spectral diffusion, spin diffusion, and instantaneous diffusion.

2.4.2 The DEER Experiment. Dead time-free four-pulse DEER is a two-frequency technique in which the modulation of echo intensity from one spin population is monitored while the inversion pulse timing of a second spin population is varied (Figure 2.4.1).

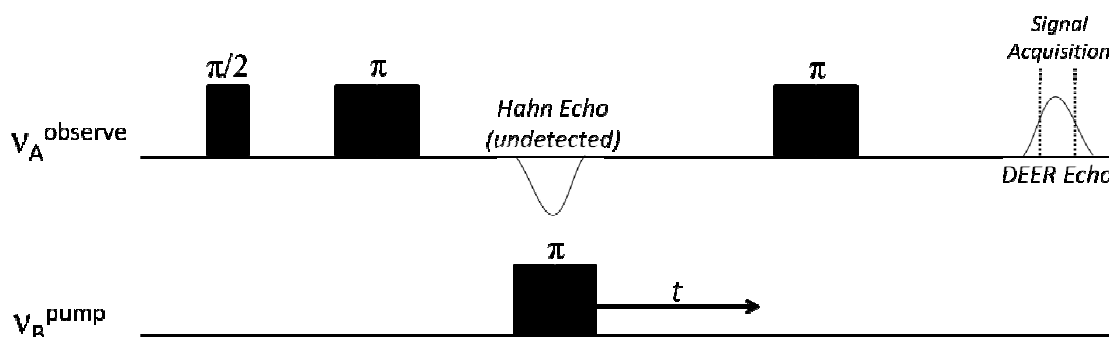


Figure 2.4.1. The DEER Pulse Sequence. Shown is the four-pulse DEER sequence. An inversion pump pulse at frequency “B” reverses the sign of the dipolar coupling felt by coupled “A” spins, which affects ω_A and thus their subsequent ability to be refocused by the final “A” π -pulse. The extent to which ω_A is affected is a function of the dipolar interaction and the timing of the “B” pump pulse. Therefore, by varying the time at which the “B” inversion pulse is applied, the detected echo intensity will be modulated as a function of the dipolar interaction.

The observe pulse is typically centered on the maximum of the low-field hyperfine manifold and is denoted frequency “A”, while the pump pulse is generally centered on the maximum of the central hyperfine manifold and is called frequency “B”. The timing of the three “A” pulses remains constant, however the “B” inversion pulse is typically

applied at a time slightly before the first undetected Hahn echo, and the timing of its application is varied over several repetitions of the DEER pulse sequence. For each repetition, subsequent to the pump pulse a refocusing inversion pulse is applied at frequency “A” and the echo intensity is determined.

During the four-pulse DEER experiment, an initial $\pi/2$ pulse at frequency “A” tips the corresponding magnetization into the xy plane. The “A” spins precess at frequency ω_A , and after the pulse ends, relaxation and inhomogeneous effects (e.g. magnetic field inhomogeneities and different resonance fields) dephase the spins such that each spin packet precesses at a specific frequency $\omega_A \pm \Delta\omega$. One of the contributions to $\Delta\omega$ stems from the dipolar interaction, which adds or subtracts to the angular frequency a value of $\pm \frac{1}{2}\omega_{AB}$, depending on the quantum state of the coupled “B” spin. The subsequent π -pulse at frequency “A” reverses the dephasing and refocuses the “A” spins to ω_A , resulting in an undetected Hahn echo. Once the spins again begin to dephase, the dipolar frequency is extracted by the application of an inversion pump pulse to the “B” spins, which changes the dipolar contribution experienced by the “A” spins from $+\frac{1}{2}\omega_{AB}$ to $-\frac{1}{2}\omega_{AB}$, and vice versa. The change of the dipolar contribution changes the angular rate of the dipolar-coupled “A” spin packets, which therefore do not refocus to ω_A with the correct timing upon application of the final π -pulse applied at frequency “A”. Importantly, the resulting echo intensity is modulated as a function of both the dipolar frequency ω_{AB} and the phase lag acquired by the “A” spins, which depends on the pump pulse timing at frequency “B”.⁹ The DEER signal intensity as a function of pump pulse timing can be expressed as:

$$I(t) = I_0 \cos(\omega_{AB}(\tau - t)) \quad (2.4.4)$$

where $I(t)$ is the intramolecular contribution to the signal, neglecting intermolecular background interactions; I_0 is the initial echo intensity in the absence of any modulation of the dipolar interaction (when there is no dipolar coupling, the echo intensity will not be modulated); τ is the timing between the first two “A” frequency $\pi/2$ and π pulses; t is the timing of the “B” frequency pump pulse; and ω_{AB} is the dipolar coupling frequency between spins “A” and “B”, given by Eq. 2.4.3. Thus, the distance between two spins is encoded as a cosine function in the DEER signal. Often there is a distribution of distances about an average value, and the information regarding the width of the distance distribution is encoded in the amplitude of signal oscillation after the initial decay; large distance distributions yield a more dampened oscillation. Therefore, DEER data from doubly spin-labeled proteins gives valuable information regarding protein conformation and structural heterogeneity within conformational substates. However, an exponential background contribution to the signal due to intermolecular interactions between spins must be subtracted,⁹ and this contribution can be expressed by:

$$I(t)_{inter} = e^{-k C f_b |\tau - t|} \quad (2.4.5)$$

where C is the concentration of “A” spins that are interacting intermolecularly, f_b is the fraction of “B” spins excited by the pump pulse, and k is given by:

$$k = (8\pi^2 \beta^2 \mathbf{g}_A \mathbf{g}_B) \cdot (9 \cdot 3^{1/2} \cdot \hbar) \quad (2.4.6)$$

The background contribution is highly dependent on the sample concentration, and is affected by processes such as instantaneous diffusion.

2.4.3 Practical Considerations. The optimization of experimental conditions depends on many factors, and only a few important ones will be discussed here: temperature, concentration, delay times, and data analysis. The signal-to-noise ratio (S/N) varies with temperature due to the temperature dependence of the spin transitions and relaxation times. The polarization of spin transitions is a Boltzmann distribution of level populations (Eq. 2.2.1), which is inversely proportional to temperature. In addition, relaxation becomes slower at lower temperatures, so one may think that performing the DEER experiment under the lowest attainable temperature would be ideal. However, after a certain point the gain in S/N due to optimal polarization and phase memory times is overcompensated for by the loss in S/N due to a long spin-lattice relaxation time. This is because T_1 determines the repetition rate of our experiment, and for a given measurement time the S/N increases with the square root of the number of repetitions. Usually the optimal temperature for the DEER experiment is within the range of 50-65 K, however these temperatures require the use of expensive helium as a cryogen instead of nitrogen. Consequently, nitrogen is usually used at a regulated temperature of 80 K unless the relaxation times remain undesirably quick and lower temperatures are required.

The signal amplitude increases with concentration up to a certain point where instantaneous diffusion dominates the phase memory time and the transverse magnetization decays at an appreciably high rate. When refocusing with π -pulses, instantaneous diffusion owes an additional exponential decaying factor to the echo. Assuming a reasonably high labeling efficiency, sufficient S/N can be realized in DEER

experiments of doubly-labeled proteins with a concentration of 100 μM at X-band frequencies, and concentrations higher than 300 μM should be avoided.

The dipolar frequency is inversely proportional to the cube of the interspin distance; therefore long distances yield DEER echoes with low frequency oscillations. Generally the average distance can be determined from the initial decay of the cosine function; however, in order to accurately characterize the distance distribution in such circumstances, the pump pulse at frequency “B” must be swept over a longer time interval. However, the phase memory time of the “A” spins limits the delay time that can be allotted between the second and third observer π -pulses (dipolar evolution time); once the transverse magnetization has completely dephased such that there is no M_{xy} , the “A” spins cannot be refocused. For this reason, in order to accurately determine longer distance distributions, the T_M must be sufficiently long. For membrane proteins T_M is often on the order of 1-2 μs at 80 K, which limits the accuracy of the measurement to 5 \AA for distributions centered around distances of 35 \AA , and distributions about longer distances will be ill-defined.³⁰ Further uncertainties up to ~ 15 \AA may be introduced into the measured distances and distance distributions if the spin label rotamer distribution is not known.

Computing the distance distribution from the Fourier transform of the time-domain signal (i.e. the Pake pattern) is an ill-posed problem.³⁰ Small distortions in the DEER signal or Pake spectrum due to noise or deviations from the ideal Pake spectrum due to orientation selection can have large effects on the distance distribution. For this reason, mathematical algorithms must be applied that stabilize the solution against noise-

induced artifacts by requiring a certain smoothness of the distance distribution. Tikhonov regularization³² is the most widely used approach in science and engineering to solve this ill-posed problem. In this approach, the smoothing is applied in such a way that allows for a compromise between the minimization of the mean square deviation of the theoretical and experimental form factors, and the minimization of the roughness. This compromise is defined by the minimization of the following target function:

$$G_{\alpha}(P) = \rho + \alpha\eta \quad (2.4.7)$$

where ρ is the mean square deviation between the theoretical and experimental form factors, η is the roughness, and α is the regularization parameter. The optimal regularization parameter α minimizes the target function, and is found by the “L-curve criterion”—a parametric plot of $\log\eta(\alpha)$ vs. $\log\rho(\alpha)$ where the optimum α corresponds to the elbow of the L-shaped curve. Tikhonov regularization involves a compromise, and if distance distributions involve both broad and narrow components, then it may not be the best approach. In these cases, more accurate distance distributions can be obtained by the superposition of several Gaussian peaks. Although there are many improvements that must be made in terms of the reliable interpretation of data, the four-pulse DEER experiment is in principle a powerful method for measuring intramolecular distances and distance distributions.

2.5 References

1. Nordio, P.L. General Magnetic Resonance Theory. in *Spin Labeling: Theory and Applications* (ed. Berliner, L.J.) (Academic Press, New York, 1976).
2. Poole Jr., C.P. *Electron Spin Resonance: A Comprehensive Treatise on Experimental Techniques*, (John Wiley & Sons, 1982).
3. Wertz, J.E. & Bolton, J.R. *Electron Spin Resonance: Elementary Theory and Practical Applications*, (McGraw-Hill, 1972).
4. Robinson, B.H., Mailer, C. & Reese, A.W. Linewidth analysis of spin labels in liquids. I. Theory and data analysis. *Journal of magnetic resonance* **138**, 199-209 (1999).
5. Owenius, R., Engstrom, M., Lindgren, M. & Huber, M. Influence of solvent polarity and hydrogen bonding on the EPR parameters of a nitroxide spin label studied by 9-GHz and 95-GHz EPR spectroscopy and DFT calculations. *Journal of Physical Chemistry A* **105**, 10967-10977 (2001).
6. Stone, T.J., Buckman, T., Nordio, P.L. & McConnell, H.M. Spin-labeled biomolecules. *Proceedings of the National Academy of Sciences of the United States of America* **54**, 1010-7 (1965).
7. Bales, B.L. Inhomogeneously Broadened Spin-Label Spectra. in *Biological Magnetic Resonance: Spin Labeling Theory and Applications*, Vol. 8 (eds. Berliner, L.J. & Reuben, J.) (Plenum Press, New York, 1989).
8. Columbus, L. Ph.D. Thesis. University of California, Los Angeles (2001).

9. Hemminga, M.A., Berliner, L.J. (ed.) *ESR Spectroscopy in Membrane Biophysics*, (Springer, New York, NY, 2007).
10. Griffith, O.H. & Jost, P.C. Lipid spin labels in biological membranes. in *Spin Labeling Theory and Applications* (ed. Berliner, L.J.) (Academic Press, New York, 1976).
11. Timofeev, V.P. & Tsetlin, V.I. Analysis of Mobility of Protein Side-Chains by Spin Label Technique. *Biophysics of Structure and Mechanism* **10**, 93-108 (1983).
12. Freed, J.H. Theory of slow tumbling ESR spectra for nitroxides. in *Spin Labeling Theory and Applications* (ed. Berliner, L.J.) (Academic Press, New York, 1976).
13. Redfield, A.G. On the theory of relaxation processes. *Adv. Magn. Reson.* **1**, 1-32 (1965).
14. Fajer, P.G. Electron Spin Resonance spectroscopy labeling in peptide and protein analysis. in *Encyclopedia of Analytical Chemistry* (ed. Meyers, R.A.) 5725-5761 (John Wiley & Sons, Ltd, Chichester, 2000).
15. Budil, D.E., Lee, S., Saxena, S. & Freed, J.H. Nonlinear-least-squares analysis of slow-motion EPR spectra in one and two dimensions using a modified Levenberg-Marquardt algorithm. *Journal of Magnetic Resonance Series A* **120**, 155-189 (1996).
16. Columbus, L., Kalai, T., Jeko, J., Hideg, K. & Hubbell, W.L. Molecular motion of spin labeled side chains in alpha-helices: analysis by variation of side chain structure. *Biochemistry* **40**, 3828-46 (2001).

17. Lovell, S.C., Word, J.M., Richardson, J.S. & Richardson, D.C. The penultimate rotamer library. *Proteins* **40**, 389-408 (2000).
18. Lopez, C.J., Fleissner, M.R., Guo, Z., Kusnetzow, A.K. & Hubbell, W.L. Osmolyte perturbation reveals conformational equilibria in spin-labeled proteins. *Protein science : a publication of the Protein Society* **18**, 1637-52 (2009).
19. McCoy, J. & Hubbell, W.L. High-pressure EPR reveals conformational equilibria and volumetric properties of spin-labeled proteins. *Proceedings of the National Academy of Sciences of the United States of America* **108**, 1331-6 (2011).
20. Bridges, M.D., Hideg, K. & Hubbell, W.L. Resolving Conformational and Rotameric Exchange in Spin-Labeled Proteins Using Saturation Recovery EPR. *Applied magnetic resonance* **37**, 363 (2010).
21. Henzler-Wildman, K. & Kern, D. Dynamic personalities of proteins. *Nature* **450**, 964-72 (2007).
22. Percival, P.W. & Hyde, J.S. Pulsed Epr Spectrometer .2. *Review of Scientific Instruments* **46**, 1522-1529 (1975).
23. Huisjen, M. & Hyde, J.S. Saturation Recovery Measurements of Electron Spin-Lattice Relaxation-Times of Free-Radicals in Solution. *Journal of Chemical Physics* **60**, 1682-1683 (1974).
24. Huisjen, M. & Hyde, J.S. Pulsed Epr Spectrometer. *Review of Scientific Instruments* **45**, 669-675 (1974).
25. Kawasaki, K., Yin, J.J., Subczynski, W.K., Hyde, J.S. & Kusumi, A. Pulse EPR detection of lipid exchange between protein-rich raft and bulk domains in the

- membrane: methodology development and its application to studies of influenza viral membrane. *Biophysical journal* **80**, 738-48 (2001).
26. Sale, K., Song, L., Liu, Y.S., Perozo, E. & Fajer, P. Explicit treatment of spin labels in modeling of distance constraints from dipolar EPR and DEER. *Journal of the American Chemical Society* **127**, 9334-5 (2005).
 27. Miick, S.M., Martinez, G.V., Fiori, W.R., Todd, A.P. & Millhauser, G.L. Short alanine-based peptides may form 3(10)-helices and not alpha-helices in aqueous solution. *Nature* **359**, 653-5 (1992).
 28. Rabenstein, M.D. & Shin, Y.K. Determination of the distance between two spin labels attached to a macromolecule. *Proceedings of the National Academy of Sciences of the United States of America* **92**, 8239-43 (1995).
 29. Pannier, M., Veit, S., Godt, A., Jeschke, G. & Spiess, H.W. Dead-time free measurement of dipole-dipole interactions between electron spins. *Journal of magnetic resonance* **142**, 331-340 (2000).
 30. Jeschke, G. & Polyhach, Y. Distance measurements on spin-labelled biomacromolecules by pulsed electron paramagnetic resonance. *Physical chemistry chemical physics : PCCP* **9**, 1895-910 (2007).
 31. Hahn, E.L. Spin echoes. *Physical Review* **80**, 580-594 (1950).
 32. Tikhonov, A.N. & Arsenin, V.Y. *Solutions of ill-posed problems.*, (Wiley, New York, 1977).

CHAPTER 3

Conformational Exchange in a Membrane Transport Protein is Altered in Protein Crystals¹

3.1 Introduction

Proteins are inherently dynamic and structurally heterogeneous. They exhibit collective and uncoupled motions over a wide range of timescales,^{2,3} and may assume numerous discrete structural substates that are in equilibrium. Conformational entropy on the fast timescale involves the sampling of multiple energetically and structurally similar substates that are separated by energy barriers of less than 1 kT. This entropy and local frustration provide lubrication for the larger-amplitude conformational changes that are intimately tied to functional processes such as enzymatic activity and allosteric regulation.⁴⁻⁶

Since the hydrophobic effect largely underlies protein folding energetics, dynamic changes to the protein fold during function are often accompanied by a reorganization of water and differences in hydration at the protein-solvent interface. It has long been known that several organisms have evolved specialized osmolyte systems to maintain viability during periods of environmental water stress, and these osmolytes operate by both lowering the activity of water and modulating its solvent properties to stabilize protein function (Table 3.1.1).⁷ The action of these osmolytes may either stabilize (e.g.

polyols, sucrose) or destabilize (e.g. urea) protein structure, depending on the nature of chemical potential perturbation of the osmolyte solution by the protein within the interacting region (the interacting region can be defined as the volume over which the protein exerts a thermodynamic influence on solution components).⁸⁻¹¹ In essence, if the protein perturbs the chemical potential within the interacting region, the system must respond by changing the chemical potential by an equal but opposite amount in order to return to chemical equilibrium. This response involves an adjustment in the concentration of water within the interacting region; effectively, the favorability of protein solvation is modified.¹² In these cases, the change in relative energies of protein-protein versus protein-solvent interactions results in the concomitant modulation of protein conformational equilibria that involve changes in hydration within the interacting region. Under extreme circumstances, osmolytes may either completely denature or precipitate proteins. However, under the right conditions, the effect of stabilizing osmolytes may be exploited to nucleate aqueous protein solutions into crystals for high-resolution structural studies.

Organism	Environment	Osmolyte systems
Unicellular marine algae	~2-4 M NaCl	Glycerol, Sucrose
Eubacteria	1 M NaCl	Glutamic acid, Proline
Freeze-tolerant insects	T < 0°C	Glycerol, Sorbitol
Desert spadefoot toad	Dessication	Urea

Table 3.1.1. Examples of Biological Osmolyte Systems. Shown are a few examples of osmolyte systems that have evolved in order to maintain protein stability during periods of environmental water stress.

Thus, there are indications that protein crystallization and the stabilizing osmolytes used for crystallization can alter protein dynamics and conformational sampling. Experiments employing precipitants or osmolytes commonly used in protein crystallization demonstrate that these solutes may have a significant effect on exchange between long-lived conformational substates; for example, osmolytes have been found to alter conformational substates involved in enzymatic activity,^{13,14} chaperone function,¹⁵ and ion conduction.¹⁶ Forces within the crystal lattice that arise from its unique physical properties or protein-protein contacts may also modulate protein dynamics. Molecular dynamics simulations indicate that the crystal lattice may affect conformational sampling in both soluble¹⁷⁻¹⁹ and membrane²⁰ proteins, and various spectroscopic approaches have experimentally demonstrated an insidious effect of the crystal lattice on the thermodynamics and kinetics of conformational exchange in several proteins.²¹

In BtuB, the outer membrane (OM) *Escherichia coli* vitamin B₁₂ (cyanocobalamin, CNCbl) transporter, SDSL-EPR has been used to investigate the dynamics and structural transitions in an N-terminal energy coupling segment termed the Ton box.²² The Ton box couples BtuB to TonB, which provides the energy required for transport.^{23,24} SDSL-EPR provides strong evidence that the Ton box undergoes a CNCbl-dependent unfolding (Figure 3.1.1).^{25,26} This event moves the Ton box 20-30 Å into the periplasmic space, where it may act as a trigger to initiate BtuB-TonB interactions.²⁷ In contrast, the Ton box remains folded within the transporter in crystal structures of BtuB both in the presence and absence of substrate. While there are small shifts in the

conformation of the Ton box upon substrate binding, no evidence is seen for the substrate-dependent unfolding observed spectroscopically.²⁸

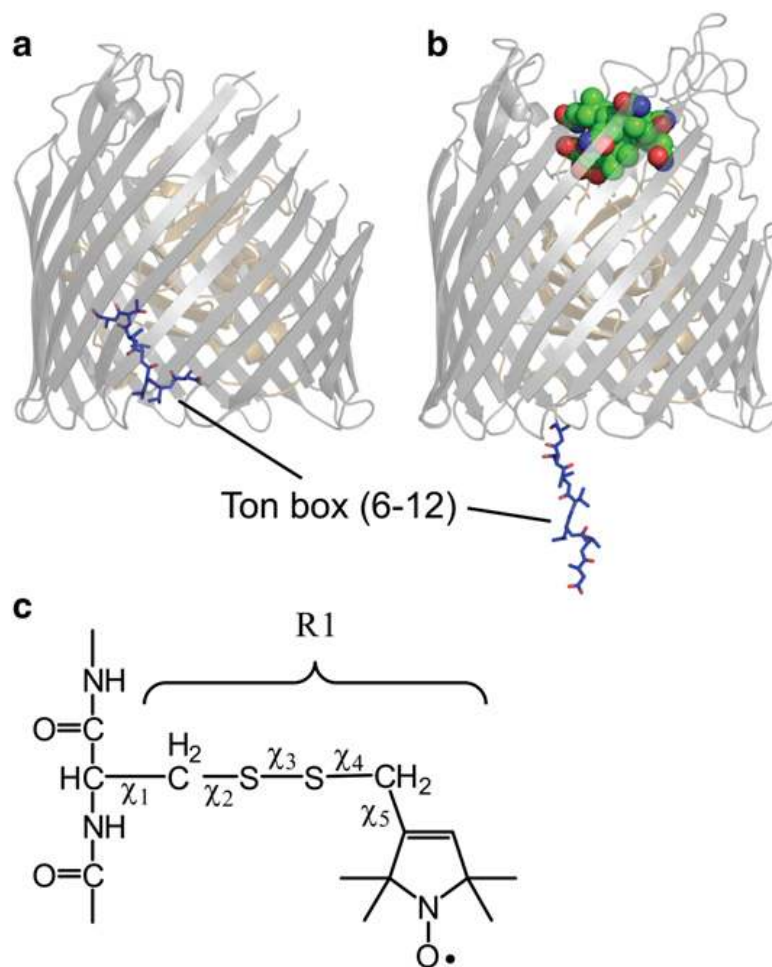


Figure 3.1.1. Substrate-Induced Unfolding of the Ton box. BtuB in the (a) apo form where the Ton box position is highlighted (PDB ID: 1NQE). (b) CNCbl-bound form of BtuB showing the state of the Ton box as determined by EPR spectra and pulse EPR distance measurements (based upon PDB ID 1NQH and spectroscopic restraints obtained for the Ton box in bilayers).²⁷ This unfolding event places the Ton box as much as 30 Å into the periplasmic space. (c) The structure of the spin-labeled R1 side-chain and dihedral angles that define the rotamers of R1. Figure from Freed et al.¹

The discrepancy between the spectroscopic and crystallographic result might have several origins. EPR spectroscopy of membrane-associated BtuB demonstrates that there is an equilibrium between folded and unfolded substates of the Ton box, and that this equilibrium is shifted toward the more folded state by the osmolytes used in BtuB crystallization.²⁹⁻³¹ Stabilizing osmolytes such as polyethylene glycols (PEGs) are believed to be excluded from hydrated protein surfaces,^{10,11} thereby reducing protein solubility. As a result, the presence of PEGs will favor conformational substates that are less hydrated.^{9,13,32} The packing of the protein within the crystal lattice might also account for the difference between the spectroscopic and crystallographic result. Although protein-protein contacts within the unit cell should not interfere sterically with the unfolding of the Ton box, the contributions that the lattice might make to the Ton box equilibrium are not known.

To determine how the Ton box equilibrium is modified within the protein crystal compared to the bilayer state, a spin-labeled mutant of BtuB was generated where the nitroxide side-chain R1 (Figure 3.1.1c) was incorporated into the Ton box at position 10. EPR spectroscopy was combined with X-ray diffraction and structure determination on the same protein crystals. The EPR spectra obtained from the protein crystal indicate that the substrate-dependent Ton box transition is blocked. This spectroscopic result is consistent with crystal structures of BtuB V10R1, which indicate that the Ton box remains folded and the R1 side-chain is buried with and without substrate. By comparing EPR spectra of BtuB V10R1 in bilayers with spectra from the protein crystal, the standard free energy change ($\Delta\Delta G^\circ$) induced by the crystal environment on the Ton box

conformational equilibrium was determined, and the energetic contributions made by osmolytes and the crystal lattice was dissected.

3.2 Results

The Ton box Exhibits a Substrate-dependent Unfolding in Bilayers but Not in Protein Crystals

The spin label at position 10 was chosen for these experiments for two reasons. First, the incorporation of R1 at some sites may perturb the Ton box fold; however, the incorporation of R1 at position 10 does not appear to be highly disruptive.²⁶ Second, the spectra from BtuB V10R1 are particularly good at revealing different conformational substates of the Ton box, and these states are easily quantified from the EPR spectra of V10R1.

Shown in Fig.3.2.1a are EPR spectra for BtuB V10R1 with and without substrate in POPC lipid bilayers. Spectra for BtuB V10R1 in bilayers have been reported previously,²⁶ and in the absence of substrate the spectrum is dominated by a broad component resulting from an immobile spin-labeled side-chain that is near the rigid limit of nitroxide motion at X-band ($\tau_R \approx 30\text{-}50$ ns). This broad component results from a spin label that is in strong tertiary contact with other side-chains in BtuB. In the presence of substrate, the spectrum changes dramatically and is dominated by a narrow high-amplitude component arising from a motionally averaged nitroxide attached to a disordered backbone segment. A careful examination of the EPR lineshapes in Fig.3.2.1a

indicates that in each case (with and without substrate), both immobile and mobile components can be distinguished. These components represent the folded and unfolded substates of the Ton box in equilibrium,³³ and the populations of these substates may be estimated from the EPR spectra using spectral subtraction (see Methods). This estimate shows that in the presence of substrate, ~50% of the Ton box is unfolded, and the standard free energy difference (ΔG°) between these two states is approximately zero.

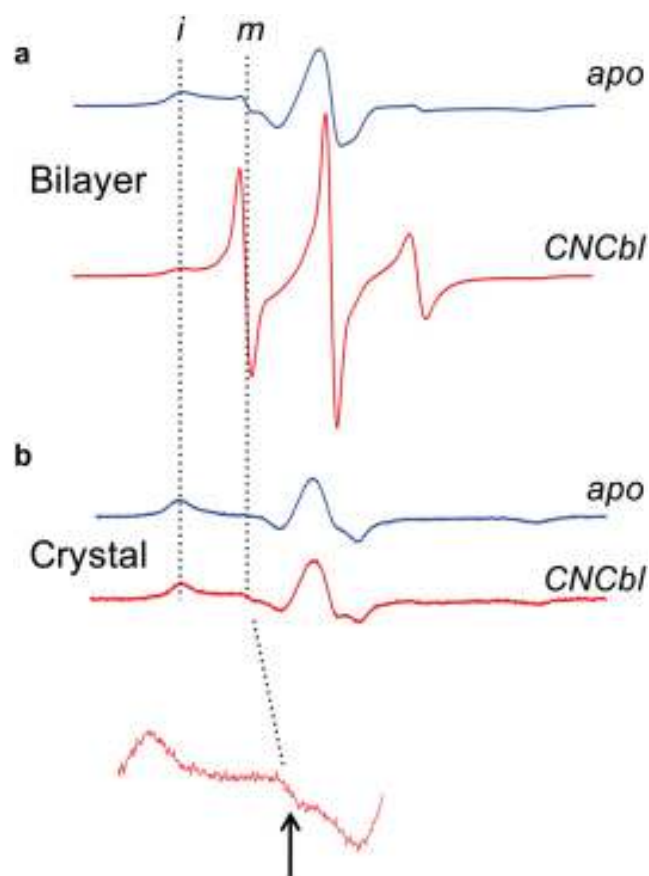


Figure 3.2.1. EPR Spectra for BtuB V10R1. The EPR spectra for V10R1 without (blue traces) and with (red traces) substrate when BtuB is incorporated into (a) POPC lipid bilayers, or (b) in the protein crystal. The inset below is a 10x vertical expansion showing a small signal from unfolded Ton box. The dashed vertical lines indicate the positions of signals resulting from an immobilized (*i*) and mobile (*m*) nitroxide side-chain, corresponding to the folded and unfolded Ton box, respectively. Figure from Freed et al.¹

Figure 3.2.1*b* shows an analogous pair of spectra obtained for BtuB V10R1 in protein crystals suspended in cryo buffer (see Methods), with and without substrate. In the protein crystal, each spectrum reflects a nitroxide near the rigid limit of motion at X-band. The substrate-induced transition, which is clearly seen in bilayers (Figure 3.2.1*a*), is absent. A careful examination of the EPR spectrum for crystallized btuB in the presence of CNCbl (Figure 3.2.1*b*) reveals a very minor mobile component (arrow in Figure 3.2.1*b*). This component matches the lineshape obtained for BtuB V10R1 in the unfolded state and appears to represent a small fraction of unfolded Ton box in the presence of substrate. Quantitation of this minor component by spectral subtraction indicates that it represents < 0.5% of the total spin signal from V10R1, and that the folded form of the Ton box is stabilized by at least 3 kcal/mol for BtuB bound to substrate in the protein crystal. Because the energy difference between the folded and unfolded states of the Ton box is close to zero in bilayers, the free energy difference between these two protein substates is altered ($\Delta\Delta G^0$) by ~ 3 kcal/mol for BtuB V10R1 in the protein crystal.

Structures from Crystals of BtuB V10R1 Show No Evidence for a Substrate-dependent Unfolding

Protein crystals of BtuB V10R1 in both the absence and presence of substrate diffracted to 2.4 Å and refinement details are given in Table 3.2.1. In both cases, the Ton box is resolved and folded within the protein interior, and several extracellular loops

become resolved in the presence of ligand, as seen previously for wild-type BtuB.²⁸ Fig.3.2.2 *a* and *b* display periplasmic views of BtuB V10R1, where the position of V10R1 in the protein interior as well as the configuration of the Ton box is shown. The label is sitting at the bottom of a pocket facing the periplasmic surface; and as expected, it is interacting with a number of side-chains, including R219 and R255. As a result, conversion between label rotamers should be highly restricted, consistent with the rigid limit spectra seen by EPR in Fig.3.2.1.

Structure	BtuB V10R1 apo	BtuB V10R1 +Ca ²⁺ B12
Data Collection		
Beamline	APS-22ID	APS-22ID
Wavelength (Å)	1.000	1.000
Temperature (K)	90	90
Reflections observed	311,539	294,094
Unique reflections	32,472	32,358
Resolution range (Å) ^a	50-2.40 (2.49-2.40)	50-2.45 (2.54-2.45)
Space group	P3 ₁ 21	P3 ₁ 21
R _{sym} (%)	9.1 (38.3)	12.1 (45.8)
Redundancy	9.6	9.1
Refinement		
Resolution range (Å)	44.1-2.44 (2.50-2.44)	44.0-2.44 (2.51-2.44)
Reflections used	30,769	30,642
Completeness (%)	97.6 (79.3)	96.6 (67.3)
R _{cryst} (%) ^b	22.1	22.9
R _{free} (%) ^c	24.8	27.5
RMS Deviations		
Bond lengths (Å)	0.021	0.019
Bond angles (°)	1.839	2.037
Number of Atoms		
Protein	4605	4865
Water	113	79
Other	C8E4 (7), Mg (4)	CNCbl (1), Ca ²⁺ (3), C8E4 (6)
PDB Accession Code	3M8B	3M8D

Table 3.2.1. Data Collection and Refinement Statistics for BtuB V10R1. ^a Highest resolution shell data shown in parenthesis. ^b $R_{cryst} = \sum ||F_{obs}| - |F_{calc}|| / \sum |F_{obs}|$, where F_{obs} and F_{calc} are the observed and calculated structure factor amplitudes, respectively. ^c R_{free} is R_{cryst} calculated using 5% of the data which is randomly chosen and omitted from the refinement.

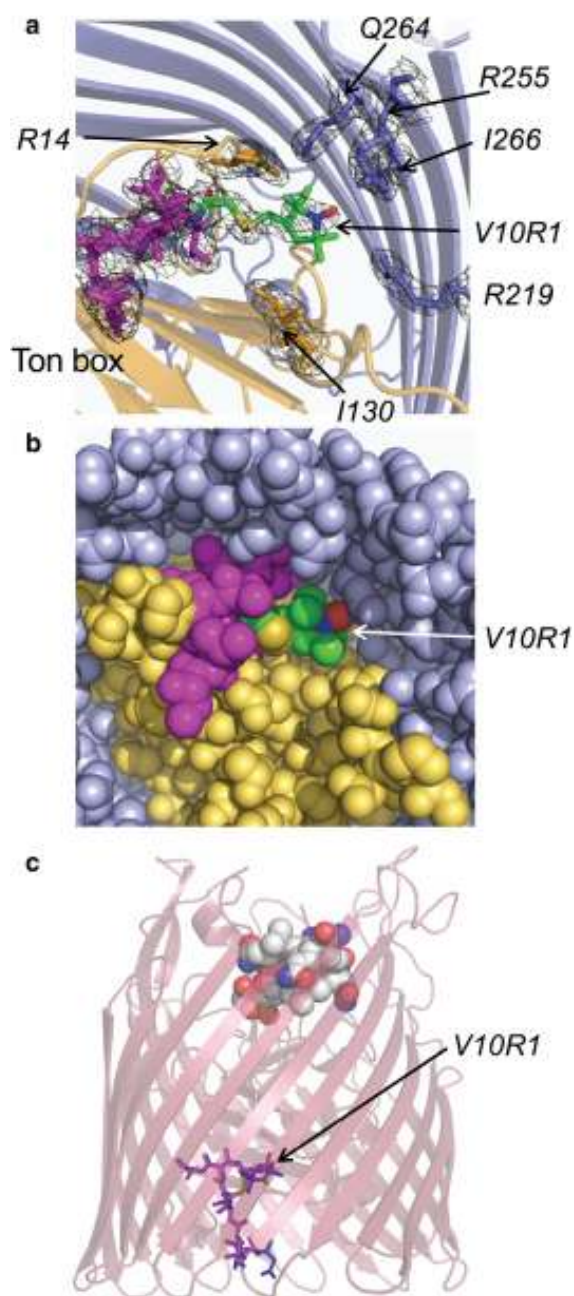


Figure 3.2.2. Crystal Structure of BtuB V10R1. (a) Periplasmic view of the structure and 2F_o-F_c electron density (contoured at 1σ) showing the placement of the spin-labeled side-chain V10R1 and residues that closely interact with the label in the apo form (PDB ID 3M8B). Shown in magenta is the backbone of the Ton box, and the N-terminal luminal domain is colored beige. (b) Periplasmic view of BtuB V10R1 similar to that shown in panel *a*, except with van der Waals surfaces rendered for all atoms. The spin label is at the base of a periplasmic pocket and is in close tertiary contact with a number of atoms. (c) A comparison of the Ton box of BtuB V10R1 with and without substrate. A side view of the crystal structure of the Ca²⁺/CNCbl-bound form of BtuB V10R1 (PDB ID 3M8D) is shown with the Ton box in magenta aligned with the Ton box of the apo form of BtuB V10R1, shown in blue. From Freed et al.¹

The angles for χ_1 and χ_2 (Figure 3.1.1c) for R1 typically assume a limited set of rotameric states on protein surfaces, where the rotamers allow for an interaction between S_δ and $H-C_\alpha$.³⁴ Here, V10R1 is found to have χ_1 and χ_2 angles of 56° and 69° in the apo form and 49° and 60° in the CNCbl-bound form, which are both in a {p, p} configuration using the conventions of Lovell et al.³⁵ The entire set of spin label dihedral angles for V10R1 is given in Table 3.2.2. The S_δ — $H-C_\alpha$ distance for the R1 side-chain is ~ 4.5 Å, which is longer than that typically seen for R1 on helix surface sites. Although this rotamer is energetically allowed, it has not previously been observed in crystal structures,³⁴ presumably due to the sterically restricted environment surrounding V10R1.

Mutant	Rotamer	χ_1	χ_2	χ_3	χ_4	χ_5
V10R1 apo	{p,p}	56	69	83	67	67
V10R1 Ca ²⁺ B ₁₂	{p,p}	49	60	70	93	46

Table 3.2.2. Summary of R1 Side-chain Dihedral Angles and Rotamer Designations. The dihedral angles for the spin-labeled side-chain are listed for BtuB V10R1 in the apo and Ca²⁺B₁₂-bound forms.

Figure 3.2.2c compares the Ton box for the V10R1 mutant with and without CNCbl. The R1 side-chain and the Ton box to which it is attached remain folded into the protein interior upon the addition of substrate, consistent with a lack of change in the EPR spectra shown in Fig.3.2.1b for the protein crystal. Substrate addition to BtuB V10R1 produces a change in the position of residue 7, as seen previously for the wild-

type protein.²⁸ However, residue 6, which is resolved in the wild-type structure, is not resolved for BtuB V10R1 once substrate is bound.

Both the Crystal Lattice and Osmolytes Shift the Equilibrium between Ton box Substates

To determine whether the crystal lattice makes a contribution to the free energy change when bilayer and crystal forms of BtuB are compared, EPR spectra from V10R1 were compared for the protein crystal and the protein solubilized into the cryo buffer. The two spectra for CNCbl-bound BtuB V10R1 are compared in Figure 3.2.3 *a* and *b*, and are clearly different. In particular, the spectrum from solubilized protein (Figure 3.2.3*b*) yields a mobile component with much higher amplitude than that for the protein crystal (Figure 3.2.3*a*). This mobile signal has a lineshape identical to that seen for the unfolded state in the bilayer (Figure 3.2.1*a*). Quantitation of the two components in this spectrum indicates that the mobile population makes up $\sim 8 \pm 2\%$ of the total spins. This fraction of unfolded Ton box corresponds to a change in free energy ($\Delta\Delta G^\circ$ for this transition relative to the bilayer reconstituted BtuB) of $\sim 1.5 \pm 0.2$ kcal/mol, indicating that the osmolytes and the crystal lattice make roughly equal contributions to the change in conformational energy that is seen in the protein crystal.

The lineshapes for the immobilized component in the absence of substrate for the bilayer-reconstituted and crystalline BtuB V10R1 are shown in Figure 3.2.3 *c* and *d*, respectively. In this case the mobile component was subtracted from the bilayer-reconstituted spectrum in Fig.3.2.1*a* to yield the immobile component only. Both of

these lineshapes result from immobilized spin labels near the rigid limit of nitroxide motion. However, the hyperfine extrema in Fig.3.2.3c are not as distinct as in Fig.3.2.3d, and components representing the g-tensor anisotropy in the central ($m_1 = 0$) resonance line of BtuB V10R1 are better resolved in the protein crystal (Figure 3.2.3d). This difference provides an indication that additional motional modes are available for V10R1 in the bilayer environment.

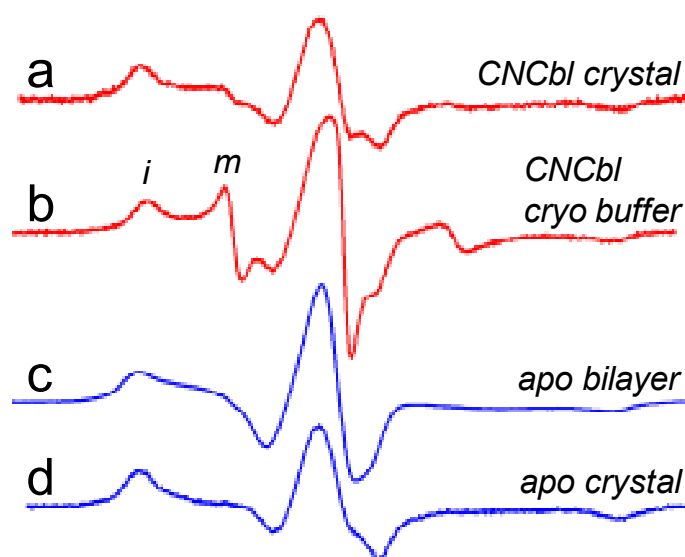


Figure 3.2.3. Comparison of BtuB V10R1 EPR Spectra in Different Environments. EPR spectra from BtuB V10R1 with bound substrate in (a) the protein crystal, (b) in the crystallization buffer at a protein concentration too dilute to form crystals, and in the apo state in (c) POPC lipid bilayers and (d) the protein crystal. The symbols *i* and *m* indicate immobilized and mobile components in the spectra for panel b. The small mobile component has been subtracted from the spectrum in panel c. Figure from Freed et al.¹

3.3 Discussion

In this work, SDSL-EPR was used to examine a conformational equilibrium in the *E.coli* outer membrane transporter, BtuB, both in lipid bilayers and in protein crystals. The results indicate that the equilibrium between folded and unfolded forms of the Ton box is shifted by ~ 3 kcal/mol when the protein is taken from the bilayer phase to the *in surfo* crystalline phase. This has the effect of stabilizing the folded form of the Ton box in the protein crystal, and it provides an explanation for the observation that the Ton box is resolved both in the absence and presence of substrate in crystal structures,²⁸ but is seen to unfold in lipid bilayers. It should be emphasized that protein crystallography does not provide an incorrect structure for BtuB. Rather, the conditions of the protein crystal alter the equilibrium distribution of conformational substates, compared to the distribution found by SDSL-EPR, to favor the more compact and ordered conformer.

Osmolytes, such as PEGs, are well known to modify protein behavior,³⁶ and previous work has demonstrated that osmolytes stabilize a folded form of the Ton box²⁹⁻³¹ and more compact, less hydrated conformations of the extracellular ligand-binding loops in BtuB.³⁷ The data obtained here indicate that the osmolytes and the crystal lattice contribute almost equally to the energy change seen in the Ton box equilibrium. While the action of PEGs and other osmolytes is reasonably well understood, it is not presently known how the protein lattice in the crystal couples to the Ton box equilibrium and stabilizes its folded form in BtuB. The Ton box is greater than 17 Å from sites of crystal contact, and superposition of the wild-type BtuB coordinates from the TonB-BtuB crystal structure³⁸ (where TonB was added before crystallization and associates with the

unfolded Ton box) onto the BtuB V10R1 structure indicates that the unfolded Ton box would not contact BtuB symmetry partners. Previous work has shown that there is an interaction between charged residues near the Ton box and the BtuB β -barrel,³³ and that eliminating this interaction unfolds the Ton box. Conceivably, a change in the dynamics or structure of the BtuB β -barrel when the protein is in the crystal lattice might alter the energy of this interaction and account for the effect of the lattice upon the Ton box. Computational studies indicate that correlated motions within proteins are expected to promote signal transduction,³⁹ in one such simulation, binding of calcium ions to the BtuB extracellular loops was found to enhance correlated motions in BtuB,⁴⁰ supporting a possible role of this mechanism in BtuB transmembrane signaling. Thus, it is possible that lattice vibrational modes interfere with the correlated motions in BtuB that are important for signal transduction. Alternatively, protein-protein contacts within the crystal lattice might exist directly at a site of signal transduction, or could indirectly dampen local motions that are important for signaling. Although the mechanism by which the crystal lattice affects conformational equilibria is presently not known, there are examples in the literature describing an insidious effect of the lattice on protein structural dynamics,^{41,42} kinetics,^{43,44} and allostery.⁴⁵ In this study, the energetic contribution made by the crystal lattice on an important conformational equilibrium has been quantified for the first time.

The field of membrane protein structural biology is far from mature, and it is expected that the effects seen here on protein conformational sampling apply to a wider range of membrane proteins. Solution NMR can provide high-resolution structural data

on membrane proteins in micelles, allowing comparisons to be made with structures obtained by X-ray diffraction in the crystal lattice. NMR spectroscopy is often found to resolve portions of proteins that are not seen by crystallography,⁴⁶ presumably because NMR is better at examining structures that are inherently dynamic. In outer membrane porins such as OmpA, the strands of the β -barrel are shorter in the NMR-derived structures than in the crystal structures;⁴⁷ however, it is not clear whether this difference is a result of crystallization conditions or the micellar environment used for NMR. Even in a reconstituted bilayer, which is a much better approximation of the native environment compared to the crystal lattice, protein conformational sampling may be modulated relative to the native environment.⁴⁸⁻⁵¹ However, many of these effects appear to be due to the fraction of acidic lipids selected for the reconstitution, which in turn control local ion concentrations and pH. As for BtuB, the Ton box equilibrium does not appear to be modulated by lipid composition (Q. Xu and D.S. Cafiso, unpublished); this equilibrium is maintained within a range of lipid bilayers as well as intact outer membrane preparations.²⁵

Changes in the equilibrium distribution of protein conformational substates are thought to underlie protein signaling events⁵² and allostery.⁵³ Because of its fast timescale and ability to study proteins in a more physiologically relevant environment, EPR spectroscopy is better equipped to detect these conformational substates and to measure conformational equilibria in proteins compared to X-ray crystallography or solution NMR. In BtuB, SDSL-EPR demonstrates that both the folded and unfolded states of the Ton box are sampled and that substrate binding shifts the equilibrium to the

more disordered state. Furthermore, colicin E3, which is also a ligand for BtuB, shifts the Ton box equilibrium to favor the folded, ordered state of the Ton box.⁵⁴ These are precisely the types of changes that are proposed to underlie protein signaling, and in the present case, they may function to regulate coupling between BtuB and TonB.

3.4 Methods

Mutagenesis, Expression, and Purification. The V10C mutation was introduced into *btuB* using a QuikChange site-directed mutagenesis kit (Stratagene, La Jolla, CA), and was subsequently verified by nucleotide sequencing. Expression and purification of BtuB for the formation of protein crystals was performed as described previously,^{28,55} and BtuB was reconstituted into lipid bilayers by following a procedure described elsewhere.⁵⁶

Spin Labeling. For spin labeling, the first round of purification was paused before initiation of the salt gradient. The Q-Sepharose slurry (Amersham, Piscataway, NJ) bound with BtuB was transferred to a conical tube and reacted with 1 mL of 45 mM S-(1-oxy-2,2,5,6-tetramethylpyrroline-3-methyl)methanethiosulfonate (MTSL; Toronto Research Chemicals, Ontario, Canada) for 4 h at room temperature.

Crystallization and Crystallographic Data Collection. Purified BtuB (11 mg/mL in 30 mM Tris pH 8.0, 20 mM C₈E₄) was crystallized by mixing 1 μ L of BtuB and 1 μ L of reservoir buffer in an EasyXtal hanging-drop tray (Qiagen, Germantown, MD), containing 200 μ L of total reservoir buffer for each crystallization condition, and

followed by incubation at 290 K. The reservoir buffer consisted of 200-500 mM magnesium acetate, 5.0-7.5% PEG3350, and 20 mM Bis Tris at pH 6.6. Crystals were visible after 1-2 days, and grew to ~200 μm in the longest dimension after 1-2 weeks. For crystals to be incubated with substrate, 1 μL of soaking buffer (150 mM calcium chloride, 2.5% PEG3350, 20 mM Bis Tris at pH 6.6, and 10 mM C_8E_4) was added to each well, followed by incubation overnight. The crystals were subsequently transferred into soaking buffer containing 1 mM cyanocobalamin and 20% glycerol, and allowed to incubate for at least 4 h. For x-ray diffraction, apo and $\text{Ca}^{2+}\text{B}_{12}$ -soaked crystals were transferred to cryo buffer (150 mM magnesium acetate or calcium chloride, 2.5% PEG3350, 20 mM Bis Tris at pH 6.6, 10 mM C_8E_4 , and 20% glycerol) for 1-2 min before loop-mounting and cryocooling by insertion into liquid nitrogen. Diffraction data were taken at 90 K at the 22-ID beamline at the Advanced Photon Source (Argonne National Laboratory, Argonne, IL). See Table 3.2.1 for more details.

Structure Determination. Indexing, integration, and scaling of the diffraction data was performed using HKL2000.⁵⁷ The structures were solved with the Phaser⁵⁸ maximum likelihood molecular replacement method, using PDB depositions 1NQE and 1NQH²⁸ as search models for the apo and substrate-bound data, respectively. To reduce model bias, residue V10 was deleted from the apo search model, and the entire Ton box was deleted from the substrate-bound search model. Model building was done in COOT,⁵⁹ and unrestrained TLS refinement⁶⁰ was performed using Refmac⁶¹ and PHENIX was used to refine the occupancy of the spin label.⁶² The spin-labeled residue V10R1 was manually built in COOT. Anomalous difference Fourier maps were

calculated to accurately position bound cobalt and calcium using Sfall and fast-Fourier transform.⁶³ Completed structures were evaluated and validated with MolProbity.⁶⁴

Electron Paramagnetic Resonance. Apo- and substrate-soaked crystals were incubated for at least 4 h in cryo buffer and soaking buffer (with 1 mM cyanocobalamin and 20% glycerol), respectively. Crystals were then transferred to a 0.60 mm ID x 0.84 mm OD round capillary with a syringe for EPR spectroscopy, which was performed on an X-band Bruker EMX spectrometer (Bruker Biospin, Billerica, MA) equipped with a dielectric resonator. All EPR spectra were recorded with a 100 G magnetic field sweep at 2.0 mW incident power and at a temperature of 298 K. The phasing, normalization, and subtraction of EPR spectra was performed using LabVIEW software provided by Dr. Christian Altenbach (University of California, Los Angeles, CA).

To determine the free energies and free energy changes between Ton box substates, the population of each Ton box conformation was determined by spectral subtraction and quantification of the spectral components as described previously.³⁰ For BtuB V10R1, the EPR spectra are linear combinations of the spectra resulting from the folded and unfolded Ton box conformations. As a result, the fraction of spins in each population may be estimated by determining the contribution that each conformation makes to the total spectrum. The label at position 10 was chosen for these measurements because EPR spectra for V10R1 yield dramatically different lineshapes for the folded and unfolded forms of the Ton box. As a result, it is easy to simulate both the folded and unfolded lineshape. In this case, the mobile lineshape was simulated using Redfield theory⁶⁵ and subtracted from the composite spectrum until the lineshape corresponding to

the purely folded Ton box conformation was obtained. Double integration of the first derivative EPR spectrum yields a value that is proportional to the number of spins, and was used to estimate the populations of folded and unfolded Ton box.

3.5 References

1. Freed, D.M., Horanyi, P.S., Wiener, M.C. & Cafiso, D.S. Conformational Exchange in a Membrane Transport Protein Is Altered in Protein Crystals. *Biophysical Journal* **99**, 1604-1610 (2010).
2. Frauenfelder, H., Sligar, S.G. & Wolynes, P.G. The Energy Landscapes and Motions of Proteins. *Science* **254**, 1598-1603 (1991).
3. Henzler-Wildman, K. & Kern, D. Dynamic personalities of proteins. *Nature* **450**, 964-72 (2007).
4. Henzler-Wildman, K.A. et al. A hierarchy of timescales in protein dynamics is linked to enzyme catalysis. *Nature* **450**, 913-U27 (2007).
5. Bahar, I., Chennubhotla, C. & Tobi, D. Intrinsic dynamics of enzymes in the unbound state and, relation to allosteric regulation. *Current opinion in structural biology* **17**, 633-640 (2007).
6. Swain, J.F. & Gierasch, L.M. The changing landscape of protein allostery. *Current opinion in structural biology* **16**, 102-108 (2006).
7. Yancey, P.H., Clark, M.E., Hand, S.C., Bowlus, R.D. & Somero, G.N. Living with water stress: evolution of osmolyte systems. *Science* **217**, 1214-22 (1982).

8. Timasheff, S.N. Protein-solvent preferential interactions, protein hydration, and the modulation of biochemical reactions by solvent components. *Proceedings of the National Academy of Sciences of the United States of America* **99**, 9721-6 (2002).
9. Timasheff, S.N. Protein hydration, thermodynamic binding, and preferential hydration. *Biochemistry* **41**, 13473-13482 (2002).
10. Arakawa, T. & Timasheff, S.N. The Stabilization of Proteins by Osmolytes. *Biophysical journal* **47**, 411-414 (1985).
11. Arakawa, T. & Timasheff, S.N. Mechanism of Poly(Ethylene Glycol) Interaction with Proteins. *Biochemistry* **24**, 6756-6762 (1985).
12. Bolen, D.W. Effects of naturally occurring osmolytes on protein stability and solubility: issues important in protein crystallization. *Methods* **34**, 312-22 (2004).
13. Colombo, M.F., Rau, D.C. & Parsegian, V.A. Protein Solvation in Allosteric Regulation - a Water Effect on Hemoglobin. *Science* **256**, 655-659 (1992).
14. Parsegian, V.A., Rand, R.P. & Rau, D.C. Macromolecules and water: Probing with osmotic stress. *Energetics of Biological Macromolecules* **259**, 43-94 (1995).
15. Street, T.O., Krukenberg, K.A., Rosgen, J., Bolen, D.W. & Agard, D.A. Osmolyte-induced conformational changes in the Hsp90 molecular chaperone. *Protein science : a publication of the Protein Society* **19**, 57-65 (2010).
16. Vodyanoy, I., Bezrukov, S.M. & Parsegian, V.A. Probing Alamethicin Channels with Water-Soluble Polymers - Size-Modulated Osmotic Action. *Biophysical journal* **65**, 2097-2105 (1993).

17. Walser, R., Hunenberger, P.H. & van Gunsteren, W.F. Molecular dynamics simulations of a double unit cell in a protein crystal: Volume relaxation at constant pressure and correlation of motions between the two unit cells. *Proteins-Structure Function and Bioinformatics* **48**, 327-340 (2002).
18. Walser, R., Hunenberger, P.H. & van Gunsteren, W.F. Comparison of different schemes to treat long-range electrostatic interactions in molecular dynamics simulations of a protein crystal. *Proteins-Structure Function and Bioinformatics* **43**, 509-519 (2001).
19. Meinhold, L. & Smith, J.C. Fluctuations and correlations in crystalline protein dynamics: A simulation analysis of Staphylococcal nuclease. *Biophysical journal* **88**, 2554-2563 (2005).
20. Bond, P.J., Faraldo-Gomez, J.D., Deol, S.S. & Sansom, M.S.P. Membrane protein dynamics and detergent interactions within a crystal: A simulation study of OmpA. *Proceedings of the National Academy of Sciences of the United States of America* **103**, 9518-9523 (2006).
21. Mozzarelli, A. & Rossi, G.L. Protein function in the crystal. *Annual Review of Biophysics and Biomolecular Structure* **25**, 343-365 (1996).
22. Kim, M., Fanucci, G.E. & Cafiso, D.S. Substrate-dependent transmembrane signaling in TonB-dependent transporters is not conserved. *Proceedings of the National Academy of Sciences of the United States of America* **104**, 11975-80 (2007).
23. Postle, K. & Kadner, R.J. Touch and go: tying TonB to transport. *Molecular Microbiology* **49**, 869-882 (2003).

24. Wiener, M.C. TonB-dependent outer membrane transport: going for Baroque? *Current opinion in structural biology* **15**, 394-400 (2005).
25. Merianos, H.J., Cadieux, N., Lin, C.H., Kadner, R.J. & Cafiso, D.S. Substrate-induced exposure of an energy-coupling motif of a membrane transporter. *Nature structural biology* **7**, 205-9 (2000).
26. Fanucci, G.E. et al. Substrate-induced conformational changes of the periplasmic N-terminus of an outer-membrane transporter by site-directed spin labeling. *Biochemistry* **42**, 1391-400 (2003).
27. Xu, Q., Ellena, J.F., Kim, M. & Cafiso, D.S. Substrate-dependent unfolding of the energy coupling motif of a membrane transport protein determined by double electron-electron resonance. *Biochemistry* **45**, 10847-54 (2006).
28. Chimento, D.P., Mohanty, A.K., Kadner, R.J. & Wiener, M.C. Substrate-induced transmembrane signaling in the cobalamin transporter BtuB. *Nature structural biology* **10**, 394-401 (2003).
29. Fanucci, G.E., Lee, J.Y. & Cafiso, D.S. Spectroscopic evidence that osmolytes used in crystallization buffers inhibit a conformation change in a membrane protein. *Biochemistry* **42**, 13106-12 (2003).
30. Kim, M., Xu, Q., Fanucci, G.E. & Cafiso, D.S. Solutes modify a conformational transition in a membrane transport protein. *Biophysical journal* **90**, 2922-9 (2006).
31. Flores Jimenez, R.H., Do Cao, M.A., Kim, M. & Cafiso, D.S. Osmolytes modulate conformational exchange in solvent-exposed regions of membrane proteins. *Protein science : a publication of the Protein Society* **19**, 269-78 (2010).

32. Zimmerberg, J., Bezanilla, F. & Parsegian, V.A. Solute Inaccessible Aqueous Volume Changes during Opening of the Potassium Channel of the Squid Giant-Axon. *Biophysical journal* **57**, 1049-1064 (1990).
33. Lukasik, S.M., Ho, K.W. & Cafiso, D.S. Molecular basis for substrate-dependent transmembrane signaling in an outer-membrane transporter. *Journal of molecular biology* **370**, 807-11 (2007).
34. Fleissner, M.R., Cascio, D. & Hubbell, W.L. Structural origin of weakly ordered nitroxide motion in spin-labeled proteins. *Protein science : a publication of the Protein Society* **18**, 893-908 (2009).
35. Lovell, S.C., Word, J.M., Richardson, J.S. & Richardson, D.C. The penultimate rotamer library. *Proteins* **40**, 389-408 (2000).
36. Auton, M., Bolen, D.W. & Rosgen, J. Structural thermodynamics of protein preferential solvation: Osmolyte solvation of proteins, aminoacids, and peptides. *Proteins-Structure Function and Bioinformatics* **73**, 802-813 (2008).
37. Kim, M., Xu, Q., Murray, D. & Cafiso, D.S. Solutes alter the conformation of the ligand binding loops in outer membrane transporters. *Biochemistry* **47**, 670-9 (2008).
38. Shultis, D.D., Purdy, M.D., Banchs, C.N. & Wiener, M.C. Outer membrane active transport: structure of the BtuB:TonB complex. *Science* **312**, 1396-9 (2006).
39. Chennubhotla, C. & Bahar, I. Signal propagation in proteins and relation to equilibrium fluctuations. *Plos Computational Biology* **3**, 1716-1726 (2007).

40. Luan, B.Q., Carr, R., Caffrey, M. & Aksimentiev, A. The effect of calcium on the conformation of cobalamin transporter BtuB. *Proteins-Structure Function and Bioinformatics* **78**, 1153-1162 (2010).
41. Pedersen, T.G. et al. A nuclear magnetic resonance study of the hydrogen-exchange behaviour of lysozyme in crystals and solution. *Journal of molecular biology* **218**, 413-26 (1991).
42. Gallagher, W., Tao, F. & Woodward, C. Comparison of hydrogen exchange rates for bovine pancreatic trypsin inhibitor in crystals and in solution. *Biochemistry* **31**, 4673-80 (1992).
43. Efremov, R., Gordeliy, V.I., Heberle, J. & Buldt, G. Time-resolved microspectroscopy on a single crystal of bacteriorhodopsin reveals lattice-induced differences in the photocycle kinetics. *Biophysical journal* **91**, 1441-1451 (2006).
44. Zhu, L., Sage, J.T., Rigos, A.A., Morikis, D. & Champion, P.M. Conformational interconversion in protein crystals. *Journal of molecular biology* **224**, 207-15 (1992).
45. Paoli, M., Liddington, R., Tame, J., Wilkinson, A. & Dodson, G. Crystal structure of T state haemoglobin with oxygen bound at all four haems. *Journal of molecular biology* **256**, 775-792 (1996).
46. Zhou, Y.P. et al. NMR solution structure of the integral membrane enzyme DsbB: Functional insights into DsbB-catalyzed disulfide bond formation. *Molecular Cell* **31**, 896-908 (2008).
47. Tamm, L.K., Abildgaard, F., Arora, A., Blad, H. & Bushweller, J.H. Structure, dynamics and function of the outer membrane protein A (OmpA) and influenza

- hemagglutinin fusion domain in detergent micelles by solution NMR. *Febs Letters* **555**, 139-143 (2003).
48. Brown, M.F. Modulation of Rhodopsin Function by Properties of the Membrane Bilayer. *Chemistry and Physics of Lipids* **73**, 159-180 (1994).
 49. Turnheim, K., Gruber, J., Wachter, C. & Ruiz-Gutierrez, V. Membrane phospholipid composition affects function of potassium channels from rabbit colon epithelium. *American Journal of Physiology-Cell Physiology* **277**, C83-C90 (1999).
 50. Baenziger, J.E. et al. Lipid composition alters drug action at the nicotinic acetylcholine receptor. *Molecular Pharmacology* **73**, 880-890 (2008).
 51. Charalambous, K., Miller, D., Curnow, P. & Booth, P.J. Lipid bilayer composition influences small multidrug transporters. *BMC biochemistry* **9**, 31 (2008).
 52. Smock, R.G. & Gierasch, L.M. Sending Signals Dynamically. *Science* **324**, 198-203 (2009).
 53. Hilser, V.J. An Ensemble View of Allostery. *Science* **327**, 653-654 (2010).
 54. Fanucci, G.E., Cadieux, N., Kadner, R.J. & Cafiso, D.S. Competing ligands stabilize alternate conformations of the energy coupling motif of a TonB-dependent outer membrane transporter. *Proceedings of the National Academy of Sciences of the United States of America* **100**, 11382-7 (2003).
 55. Chimento, D.P., Mohanty, A.K., Kadner, R.J. & Wiener, M.C. Crystallization and initial X-ray diffraction of BtuB, the integral membrane cobalamin transporter of

- Escherichia coli. *Acta crystallographica. Section D, Biological crystallography* **59**, 509-11 (2003).
56. Fanucci, G.E., Cadieux, N., Piedmont, C.A., Kadner, R.J. & Cafiso, D.S. Structure and dynamics of the beta-barrel of the membrane transporter BtuB by site-directed spin labeling. *Biochemistry* **41**, 11543-51 (2002).
57. Otwinowski, Z. & Minor, W. Processing of X-ray diffraction data collected in oscillation mode. *Macromolecular Crystallography, Pt A* **276**, 307-326 (1997).
58. McCoy, A.J. et al. Phaser crystallographic software. *Journal of Applied Crystallography* **40**, 658-674 (2007).
59. Emsley, P. & Cowtan, K. Coot: model-building tools for molecular graphics. *Acta Crystallographica Section D-Biological Crystallography* **60**, 2126-2132 (2004).
60. Winn, M.D., Isupov, M.N. & Murshudov, G.N. Use of TLS parameters to model anisotropic displacements in macromolecular refinement. *Acta Crystallographica Section D-Biological Crystallography* **57**, 122-133 (2001).
61. Murshudov, G.N., Vagin, A.A. & Dodson, E.J. Refinement of macromolecular structures by the maximum-likelihood method. *Acta Crystallographica Section D-Biological Crystallography* **53**, 240-255 (1997).
62. Adams, P.D. et al. PHENIX: building new software for automated crystallographic structure determination. *Acta Crystallographica Section D-Biological Crystallography* **58**, 1948-1954 (2002).
63. Potterton, E., Briggs, P., Turkenburg, M. & Dodson, E. A graphical user interface to the CCP4 program suite. *Acta Crystallographica Section D-Biological Crystallography* **59**, 1131-1137 (2003).

64. Davis, I.W. et al. MolProbity: all-atom contacts and structure validation for proteins and nucleic acids. *Nucleic acids research* **35**, W375-83 (2007).
65. Stone, T.J., Buckman, T., Nordio, P.L. & McConnell, H.M. Spin-labeled biomolecules. *Proceedings of the National Academy of Sciences of the United States of America* **54**, 1010-7 (1965).

CHAPTER 4

Molecular Origin of Electron Paramagnetic Resonance Lineshapes on β -barrel Membrane Proteins: The Local Solvation Environment Modulates Spin Label Configuration¹

4.1 Introduction

Spin labels have proven to be powerful tools for probing protein structure and dynamics. In the EPR-based technique SDSL, a spin-labeled side-chain is used to probe the local structure and dynamics at the labeled site and to provide distance restraints between pairs of labeled side-chains.²⁻⁵ This approach is particularly valuable in the case of large protein complexes or membrane proteins, where other approaches may have limited utility. Spin labels have also been used extensively to refine structures using high-resolution NMR, where paramagnetic enhancements of nuclear relaxation provide long-range distance restraints between nuclei and spin-labeled side-chains.^{6,7} Although there are several approaches that can be used to covalently attach spin labels to proteins, the ease of attachment based upon cysteine chemistry has made the methanethiosulfonate-derivatized side-chain R1 the most popular spin-labeled side-chain for protein labeling (Figure 4.1.1*a*).

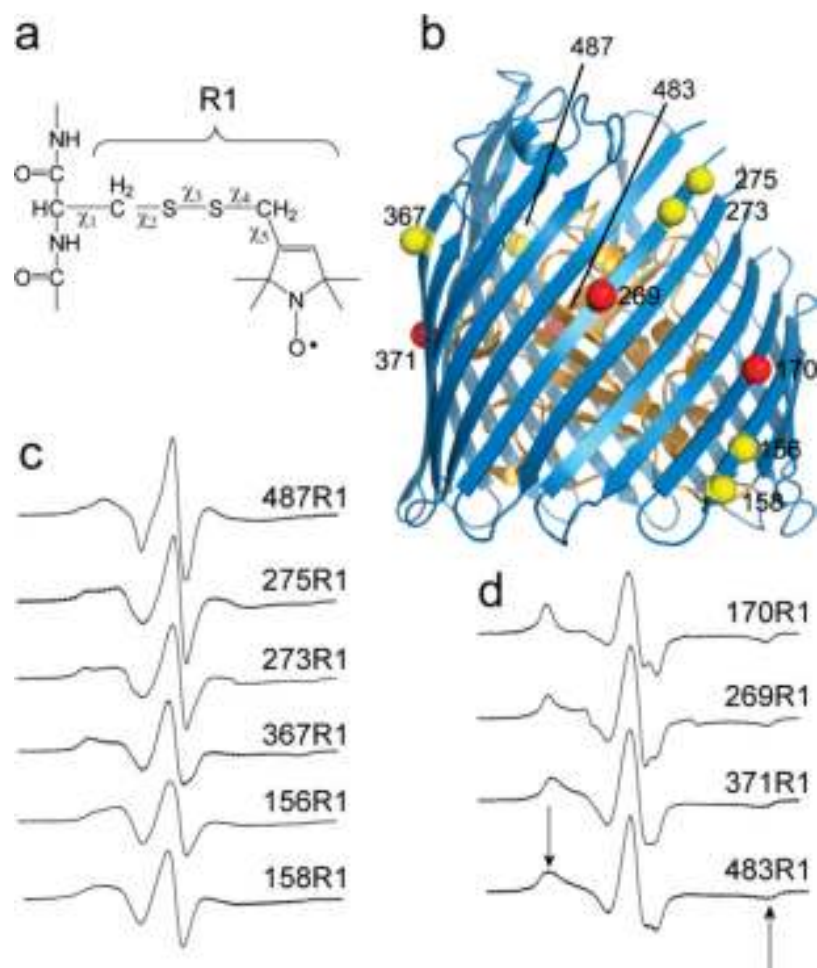


Figure 4.1.1. Hydrocarbon-exposed EPR Lineshapes from BtuB. (a) Model for the spin-labeled side-chain R1 obtained by derivatization with an MTSL spin label. Five rotatable bonds link the R1 spin label to the protein backbone, but motions that average the nitroxide magnetic interactions are often dominated by motion about χ_4 and χ_5 (see the text). (b) Model of BtuB (PDB entry 1NQH⁸) showing the position of ten $C\alpha$ atoms that have been spin-labeled with R1. Previous work⁹ indicates that when reconstituted into POPC bilayers, sites near the aqueous solvent interface (c) tend to yield EPR spectra that are multicomponent (yellow spheres) but sites in the membrane interior (d) yield EPR spectra that are near the rigid limit (red spheres). All spectra are 100 G scans and are normalized to equivalent spin numbers, except the amplitudes of the spectra in panel d are scaled by a factor of 1.5. The arrows in panel d indicated the positions of the hyperfine extrema in the EPR spectrum, which are not averaged in the rigid-limit spectra. Figure from Freed et al.¹

A crucial aspect of interpreting EPR spectra and long-range distances from spin-labeled sites is knowledge of the configuration of the label side-chain. The configuration

of the R1 side-chain at labeled sites has been determined experimentally by examining the modes of motion that modulate the EPR spectrum,^{10,11} and by crystallography on model proteins such as T4 lysozyme.¹²⁻¹⁵ These studies have largely examined aqueous-exposed α -helical sites, where the internal motion of the spin label is known to be dominated by dynamics about the fourth and fifth dihedral angles that link the label to the protein backbone (see Figure 4.1.1*a*). In most cases, label motion at these sites is not strongly influenced by neighboring residues, and differences in EPR spectra at such sites largely reflect differences in protein backbone dynamics on the nanosecond timescale.^{10,16} Moreover, the preferred rotameric states of the spin label side-chain are strongly influenced by a weak attractive interaction between the distal sulfur atom and the backbone C $_{\alpha}$ proton.

Information about the motion and configuration of the spin label at hydrocarbon-exposed sites in membrane proteins is more limited. Two structures were recently reported for the R1 side-chain at helix surface sites in LeuT,¹⁷ and this study suggests that unlike soluble proteins, at hydrocarbon-exposed sites the R1 label tends to make interactions with the protein surface. Until now, no structures of the R1 label at the surfaces of β -sheets in either membrane proteins or soluble proteins have been reported, making the accurate interpretation of EPR lineshapes and modeling of distance restraints obtained from spin labels at these sites difficult. The environment surrounding R1 should be more sterically restricted on the surface of a β -sheet compared to that of an α -helix; indeed, work on the soluble β -sheet cellular retinol-binding protein using mutagenesis coupled with SDSL-EPR demonstrated that R1 motion is strongly affected by the identity

of nearest-neighbor residues, and that highly ordered states result from β -branched residues (such as valine and isoleucine) at the non-hydrogen-bonded neighbor position.¹⁸ In the case of the β -barrel membrane protein BtuB (Figure 4.1.1*b*), the spectra also appear to be modulated by the neighboring residues;¹⁹ however, there is no consistent pattern of label motion and EPR lineshape that can be correlated with the local steric environment. For example, the EPR spectrum of BtuB W371R1 is near the rigid limit on the X-band timescale (Figure 4.1.1*d*), yet its nearest-neighbor residues consist of two threonines, one alanine, and one glycine. In contrast, the EPR lineshape of BtuB Y275R1 results from R1 having an intermediate rate of motion (Figure 4.1.1*c*), yet its nearest-neighbor residues consist of two lysines, one tyrosine, and one leucine. Moreover, the EPR spectra at some sites in BtuB are strongly influenced by lipid acyl chain length, an observation that suggests that the spin label might be reporting on protein backbone dynamics or protein shape that is modulated by membrane thickness.¹⁹

In this work, the crystal structures for two spin-labeled sites on the hydrocarbon-facing surface of BtuB were determined, and the motion of the R1 side-chain was examined as a function of both the neighboring side-chain identity and the local solvent environment. Labels at the β -barrel surface of BtuB do not assume the same rotameric states that are typically seen on solvent-exposed helical sites, and their motion is strongly influenced by interactions that are made with the protein surface. At position 156 in BtuB, which lies close to the solvent interface, two motional components are present in the EPR spectrum, which are a result of exchange between rotameric states of the spin label. In addition, the equilibrium between these states is strongly modulated by the lipid

environment. At position 170, which is in the bilayer interior, the EPR spectrum indicates that the spin label is immobilized, and this immobilization is independent of lipid environment and neighboring residue identity. The BtuB W371R1 crystal structure suggests that immobilization at sites in the bilayer interior is due to interactions of the spin label with the protein surface, consistent with what was recently reported for LeuT.¹⁷ Collectively, the results indicate that R1 motion and its interactions with the protein surface are highly dependent upon solvation at the labeled site. These results are important for correctly interpreting EPR lineshapes from β -barrel membrane proteins, probing the environment at the protein-lipid interface, and determining structures and structural changes when spin labels are used as long-range probes of interspin distances.

4.2 Results

In this work, the *E.coli* outer membrane protein BtuB was used to examine the molecular basis of R1 spin label motion at hydrocarbon-exposed sites on β -barrel membrane proteins. Shown in Fig.4.1.1 are EPR spectra obtained for several sites on BtuB that have been labeled with R1^{9,19} and reconstituted into POPC bilayers. The EPR spectra from the outer surface of BtuB are quite variable but can be divided into two general groups: spectra that are clearly multicomponent, indicating the R1 exhibits at least two types of motion (Figure 4.1.1c), and spectra that are dominated by a component due to a slowly moving nitroxide, where the hyperfine anisotropy is not averaged (Figure 4.1.1d). Although there are exceptions, the multicomponent spectra arise more

frequently from residues in the aqueous phase or near the aqueous solvent interface, while the strongly immobilized spectra originate almost exclusively from spin-labeled sites buried in the membrane hydrocarbon.

Structural Model of T156R1 from X-ray Crystallography

BtuB T156R1 is at a site near the aqueous solvent interface that exhibits a multicomponent EPR spectrum (Figure 4.1.1c). To investigate the origin of these dynamic modes, BtuB T156R1 was crystallized and the structure was determined at 90 K (Figure 4.2.1). The BtuB crystals diffracted to a resolution of 2.6 Å, and the resulting structure was refined to an R_{free} of 25.39%; the complete data collection and refinement statistics are listed in Table 4.2.1.

Clear electron density is observable for the entire R1 side chain, allowing for determination of the χ_1 - χ_5 dihedral angles (Table 4.2.2). The first two dihedral angles, χ_1 and χ_2 , are in a {t,m} rotamer using the conventions of Lovell et al.²⁰ This rotamer has been observed previously for R1 at solvent-exposed helical sites, but it is the least frequent of the three rotamers that are seen.²¹ Because of the large absolute value of χ_2 (-83°), the S_δ - HC_α stabilizing interaction that is frequently seen in spin-labeled α -helical structures is absent ($d = 4.2$ Å). Instead, the R1 side-chain appears to be stabilized by other interactions with the protein backbone, including S_δ - N_{i+1} and S_δ - $O=C$ interactions ($d = 3.5$ Å). These interatomic distances are consistent with the other {t,m} rotamers reported in the literature^{13,14} and may be important R1-backbone interactions

that stabilize the spin label in this configuration. In two recently published structures of R1 at hydrocarbon-exposed helical sites,¹⁷ R1 assumes the {m,m} rotamer (the most common rotamer at helical sites) and is found to fold back onto the protein surface. In contrast, the 156R1 side-chain projects away from the protein backbone where the nitroxide ring is localized in a hydrophobic pocket formed by residues Q158, L160, V166, and L168.

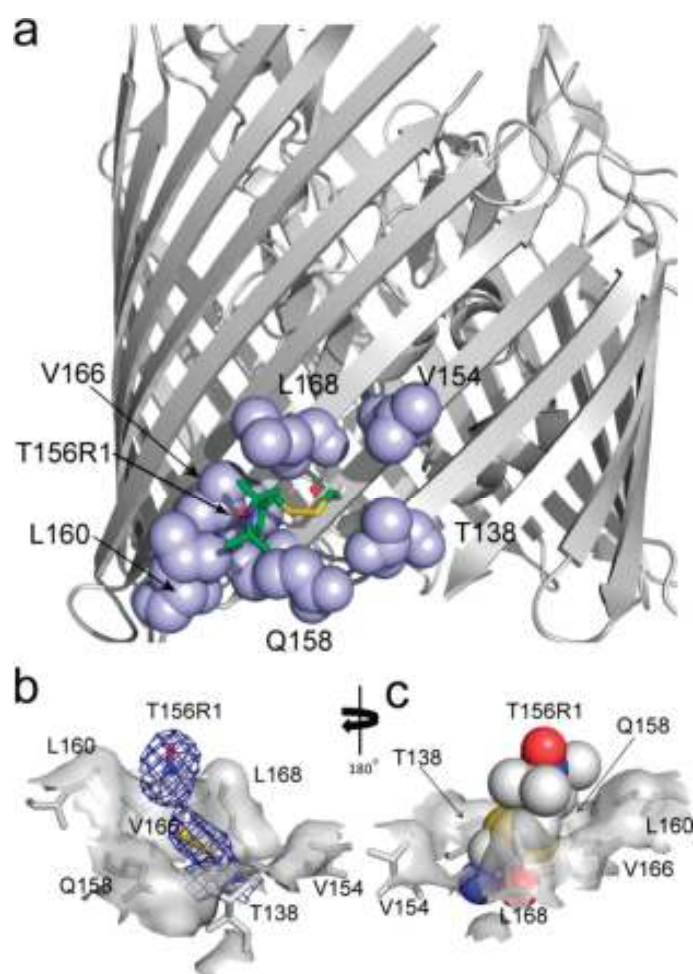


Figure 4.2.1. Crystal Structure of BtuB T156R1. (a) X-ray crystal structure (90 K) of BtuB T156R1 (PDB entry 3RGM) determined at 2.6 Å showing the R1 side-chain (stick representation) and the positions of the nearest-neighbor residues (in CPK rendering). (b and c) Alternate views of the site around T156R1, with the van der Waals surface colored gray. In panel b, the 2F_o-F_c electron density is shown as blue mesh contoured at 1σ. Data collection and refinement statistics are listed in Table 4.2.1. From Freed et al.¹

Structure:	BtuB T156R1	BtuB W371R1
Data Collection		
Beamline	APS-22ID	APS-22BM
Wavelength (Å)	1.000	1.000
Temperature (K)	90	90
Reflections observed	224,348	266,642
Unique reflections	27,492	37,950
Resolution range (Å) ^a	50-2.60 (2.64-2.60)	50-2.30 (2.38-2.30)
Space group	P3 ₁ 21	P3 ₁ 21
Cell dimensions	a = b = 81.6Å, c = 227.7Å $\alpha = \beta = 90^\circ, \gamma = 120^\circ$	a = b = 81.7Å, c = 227.1Å $\alpha = \beta = 90^\circ, \gamma = 120^\circ$
R _{sym} (%)	6.2 (48.1)	10.5 (32.5)
Redundancy	8.2	7.0
Refinement		
Resolution range (Å)	44.3-2.60 (2.67-2.60)	33.4-2.30 (2.36-2.30)
Reflections used	26,070	35,973
Completeness (%)	98.3 (82.7)	95.2 (74.0)
R _{cryst} (%) ^b	21.32	22.16
R _{free} (%) ^c	25.39	24.98
RMS Deviations		
Bond lengths (Å)	0.020	0.023
Bond angles (°)	1.817	1.953
Number of Atoms		
Protein	4535	4612
Water	86	130
Other	C8E4 (6), Mg (11)	C8E4 (7), Mg (3)
PDB Accession Code	3RGM	3RGN

Table 4.2.1. Data Collection and Refinement Statistics for BtuB T156R1 and W371R1. ^a Highest resolution shell data shown in parenthesis. ^b $R_{\text{cryst}} = \sum ||F_{\text{obs}}| - |F_{\text{calc}}|| / \sum |F_{\text{obs}}|$, where F_{obs} and F_{calc} are the observed and calculated structure factor amplitudes, respectively. ^c R_{free} is R_{cryst} calculated using 5% of the data which is randomly chosen and omitted from the refinement.

Mutant	Rotamer	χ_1	χ_2	χ_3	χ_4	χ_5
T156R1	{t,m}	176	-83	-94	-82	-30
W371R1	{p,p}	47	78	64	113	130

Table 4.2.2. Summary of R1 side-chain dihedral angles and rotamer designations. The dihedral angles for the spin-labeled side-chain are listed for BtuB T156R1 and W371R1.

The substitution of R1 at position 156 did not perturb BtuB structure. The all-atom pairwise root-mean-square deviation compared to the wild-type apo structure⁸ is 0.21 Å; however, small changes in the local side-chain rotamer distribution are evident in neighboring residues. The largest change occurs for residue $i + 2$, Q158, where the first rotatable bond isomerizes, moving the ϵ -nitrogen approximately 3 Å from its position in the wild-type protein (Figure 4.2.2). Compared to the wild-type structure, the L160 conformer is also altered in the spin-labeled structure as is the L168 side-chain (Figure 4.2.2).

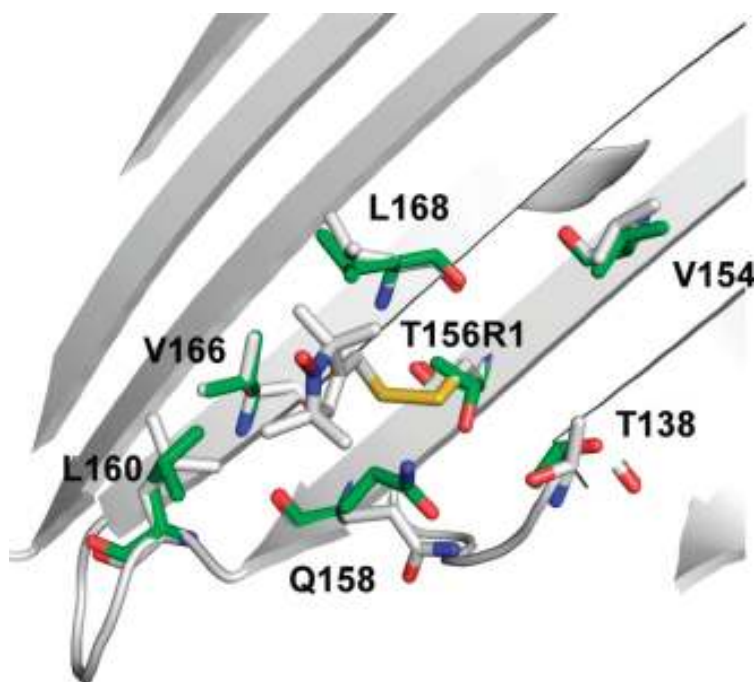


Figure 4.2.2. Comparison of BtuB T156R1 and Wild-type Structures. BtuB t156R1 crystal structure superposed on the wild-type coordinates (PDB entry 1NQE). BtuB T156R1 nearest-neighbor residues are rendered as sticks and colored gray, whereas the same residues from the wild-type structure are colored green. The Q158, L160 and L168 rotamers are altered upon introduction of R1 at position 156. From Freed et al.¹

EPR Spectra and the Crystal Structure Suggest a Mode of Motion for BtuB T156R1

Shown in Fig.4.2.3 are EPR spectra of BtuB T156R1 reconstituted into POPC bilayers and in the protein crystal at room temperature. The POPC spectrum can be simulated using the MOMD model (see Methods) assuming that the spin label undergoes two modes of motion: a relatively fast (1.7 ns) anisotropic motion about the z-axis of the diffusion tensor, and a slower anisotropic x-axis motion (see Table 4.2.3). The room temperature EPR spectrum obtained from *in surfo* crystals of BtuB T156R1 is different and can be simulated by a single component undergoing relatively fast z-axis motion (1.7 ns), similar to the fast component seen for the POPC sample. The EPR spectrum of BtuB T156R1 in crystallization buffer is identical to the crystalline spectrum, and lowering the temperature of this sample did not induce the appearance of a second slow component in the EPR spectrum, such as that seen in the POPC spectrum (data not shown). As a result, it is likely that the label conformer observed in the crystal structure (the {t,m} rotamer) gives rise to the EPR spectrum of the crystal at room temperature (and the fast component seen in the POPC spectrum). This assignment is consistent with the MOMD fit. From this fit, the Euler angles for the fast component can be used to plot the rotational diffusion tensor frame onto the 156R1 crystal structure (Figure 4.2.4). Within the context of this model, the orientation of the z-axis is roughly in a direction that would be the average of the direction for the fourth and fifth bonds linking the spin label to the protein backbone, indicating that 156R1 is executing rapid rotation about the χ_4 and χ_5 bonds. Rotameric conversion about χ_1 - χ_3 is unlikely to be rapid on the X-band EPR

timescale, and motional averaging of the nitroxide magnetic interactions about χ_4 and χ_5 is consistent with previous studies of R1 in T4 lysozyme.¹¹

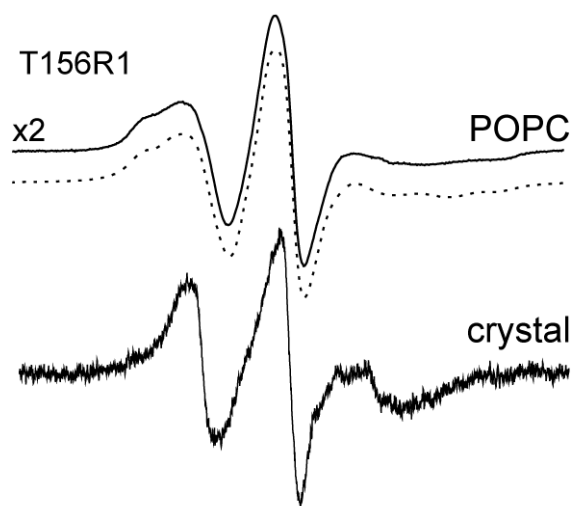


Figure 4.2.3. Bilayer and Crystalline BtuB T156R1 EPR Spectra. EPR spectra of BtuB T156R1 reconstituted into POPC bilayers (top) and a sample of ~20-30 intact protein crystals suspended in crystallization buffer (bottom). The dashed line represents the fit to the POPC spectrum (see Table 4.2.3 for the fit parameters). The room temperature crystalline EPR spectrum consists of a single component undergoing fast rotational diffusion of the X-band EPR timescale; the rate and anisotropy of the motion are similar to those of T156R1 in DLPC bilayers. All spectra are 100 G scans. From Freed et al.¹

Mutagenesis of Neighboring Residues is Consistent with the Motional Model for T156R1

For β -sheet protein structure, a residue may interact with hydrogen-bonded (HB) and non-hydrogen-bonded (NHB) neighbors, and with residues at positions $i \pm 2$. In general, these interactions are dependent on the side-chain configuration and on the local

β -strand twist and tilt.²² To test the model presented in Fig.4.2.4, EPR spectra of BtuB T156R1 with single amino acid mutations made to each of the neighboring residues was obtained. The EPR spectra are shown in Fig.4.2.5, and MOMD fits to the spectra are listed in Table 4.2.3.

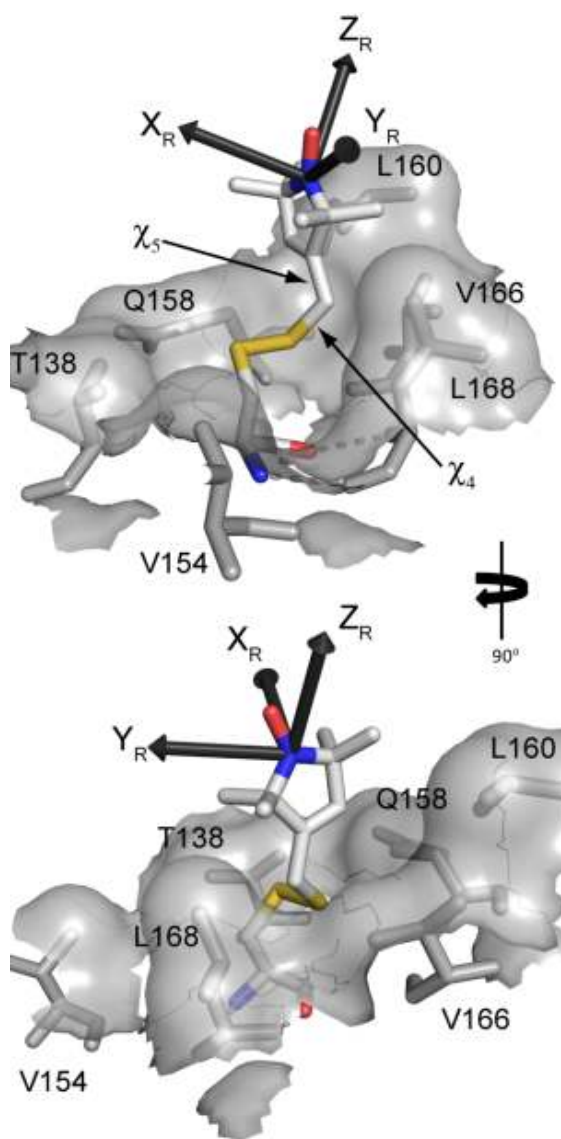


Figure 4.2.4. Rotational Diffusion Tensor Frame for the T156R1 Fast Component. The rotational diffusion tensor frame for the fast component is shown plotted onto the T156R1 crystal structure. Since motional averaging is primarily occurring about the z-axis, the spin label appears to be executing rapid rotation about the χ_4 and χ_5 bonds. From Freed et al.¹

Mutant	Comp.	%	$\tau(x)$ (ns)	$\tau(y)$ (ns)	$\tau(z)$ (ns)	α	β	γ
T156R1 DLPC	2	100	-	11	1.7	-23	65	-26
T156R1 DMPC	1	22	4.3	-	-	0	0	11
	2	78	-	12	2.1	-23	63	-26
T156R1 POPC	1	26	14	-	-	0	0	17
	2	74	-	20	1.7	-24	58	-18
T156R1 DiErPC	1	59	7.6	-	-	0	0	31
	2	41	17	-	2.4	-36	50	-13
T156R1/T138A	1	27	6.9	-	-	0	0	20
	2	73	-	13	2.3	-28	63	-17
T156R1/T138Q	1	49	11	-	-	0	0	22
	2	51	-	18	1.7	-34	54	-11
T156R1/T138W	1	31	4.6	-	-	0	0	13
	2	69	-	-	1.1	0	65	-31
T156R1/L168A	1	21	6.1	-	-	0	0	28
	2	79	-	13	2.7	-23	65	-27
T156R1/L168V	1	33	9.0	-	-	0	0	23
	2	67	-	13	2.4	-28	62	-22
T156R1/L168W	1	65	7.8	-	-	0	0	34
	2	35	-	-	0.96	0	55	0
T156R1/V154A	1	52	3.1	-	-	0	0	20
	2	48	-	12	3.0	-29	65	-31
T156R1/V154Q	1	64	5.4	-	-	0	39	11
	2	36	-	-	0.56	0	54	-40
T156R1/Q158A	1	39	4.6	-	-	0	0	21
	2	61	4.7	-	16	52	37	-10
T156R1/Q158N	1	50	6.2	-	-	0	0	25
	2	50	8.4	-	5.4	45	45	-2
T156R1/L160A	1	35	8.0	-	-	0	0	24
	2	65	-	13	3.2	-31	62	-19

Table 4.2.3. Dynamic Parameters from the MOMD fits. The slow component is described as component 1, whereas the fast component is labeled as component 2. The slow component was fit with intermediate to slow x-axis anisotropic motion. In most cases, the majority of motional averaging in the fast spectral component was due to fast z-axis anisotropic motion. The dashes represent anisotropic correlation times from the fits that were slower than the timescale for averaging at X-band ($\tau > \sim 50$ ns). In these cases, to reduce the number of parameters, the correlation times were arbitrarily set to 167 ns ($R = 6.0$) for the remainder of the fit and thus are not reported.

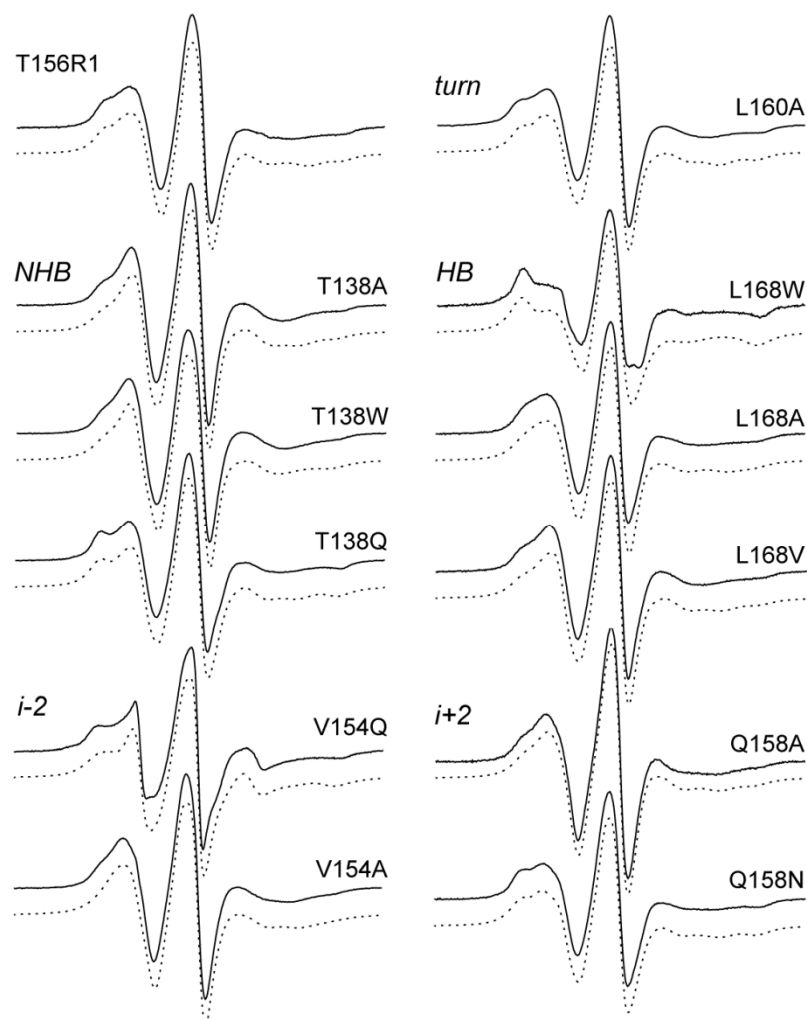


Figure 4.2.5. T156R1 EPR Spectra with Neighboring Mutations. EPR spectra of BtuB T156R1 reconstituted into POPC vesicles with 11 mutations made to T156R1 neighbors. These spectra include those from mutations to the $i \pm 2$ residues (V154 and Q158), the hydrogen-bonded (L168) and non-hydrogen-bonded (T138) neighbors, and residue L160, which is on a periplasmic turn and forms the apex of a hydrophobic pocket near 156R1. The dashed lines below each spectrum represent the MOMD simulations for each spectrum (see Table 4.2.3 for the parameters used to generate each simulated spectrum). All spectra are 100 G scans. From Freed et al.¹

All the spectra shown in Fig.4.2.5 result from multiple motional components and require two modes of motion to be reasonably simulated by the MOMD model. In some cases, the lineshapes of T156R1 are not strongly affected by mutations to neighboring

residues, although in many cases, these mutations shift the relative populations of the fast and slow components in the EPR spectrum of T156R1. Substitutions at the HB neighbor, L168, have the strongest effects, and increased steric size at this site increases the fraction of the slow component in the EPR spectrum. As seen in Fig.4.2.5 and Table 4.2.3, the L168W substitution produces a large change and inverts the populations to strongly favor the slow component. The larger side-chain at position 168 is expected to sterically interfere with the position of T156R1 in the {t,m} rotamer, and may force R1 to favor an alternate rotamer of χ_1 and/or χ_2 that yields the slow spectral component.

The $i + 2$ residue Q158 lies close to the label disulfide, and as discussed above, Q158 is the only residue that assumes a significantly different rotamer in the T156R1 crystal structure compared to the wild-type BtuB structure. Mutations at residue 158 affect the axes and rates of rotation for the fast component, and the rates of motion for the slow component. Smaller side-chains at position 158 result in faster motional rates for the slow component and slower diffusion about the z-axis for the fast component. Additionally, the fraction of label giving rise to the slow component increases for Q158N and Q158A compared to that of the wild-type residue.

As discussed below, the likely source of the slow component is an alternate label rotamer, which differs from that found in the crystal structure. The rotameric state that gives rise to the slow component in these EPR spectra is not known, but the {t,t} and {m,m} rotamers are energetically reasonable,^{21,23} would only require the negotiation of one kinetic barrier, and appear to be allowed within the local side-chain environment around T156R1. Of these possibilities, the {t,t} configuration seems like the more

realistic candidate since modeling of this rotamer in the T156R1 crystal structure supports the mutagenesis data well, and interacts closely but does not clash with any neighboring residues (Figure 4.2.6). Although the {m,m} rotamer is the most common configuration observed at helical sites, in this configuration the distal sulfur would clash with residue T138. While it is possible that the neighboring rotamer distribution could change to accommodate the {m,m} rotamer, there is no experimental evidence to support this notion and thus the {t,t} rotamer will be discussed as a likely alternate rotamer.

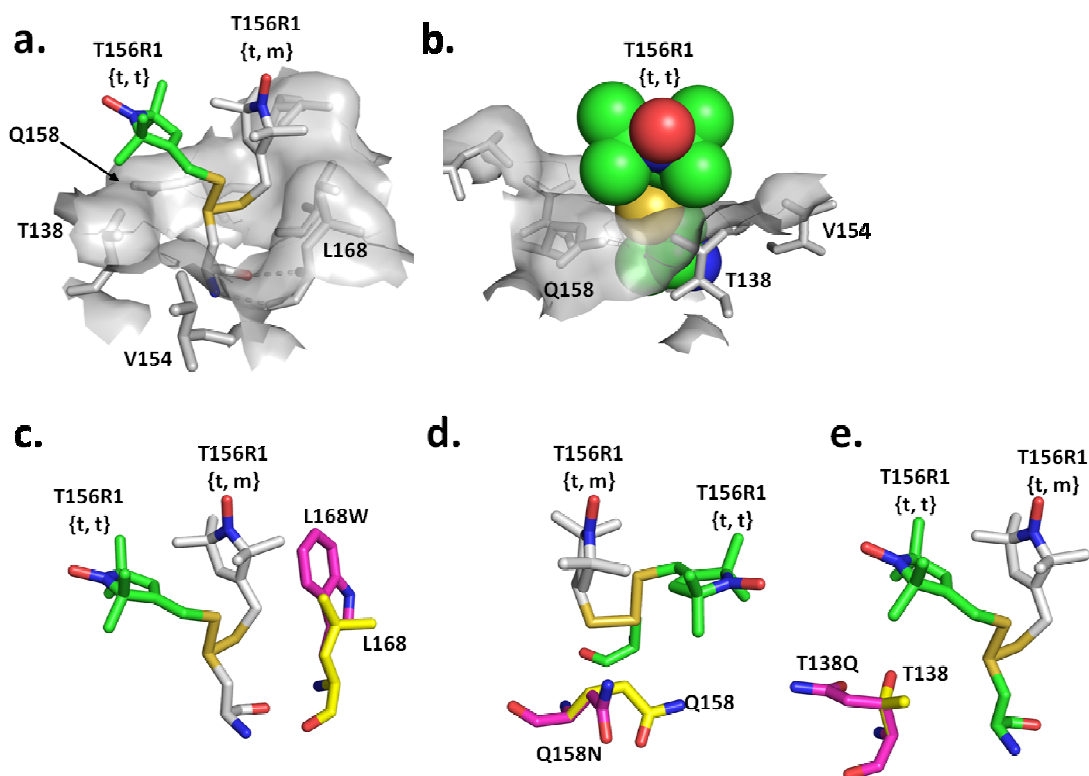


Figure 4.2.6. Modeling of the {t,t} Rotamer. Modeling of the {t,t} rotamer in the BtuB T156R1 crystal structure only requires adjustment of one dihedral angle (χ_2) and appears to be sterically allowed. (a) Comparison of the {t,m} and proposed {t,t} rotamers. (b) The {t,t} rotamer, shown in CPK format, would interact with neighboring residues Q158 and T138. (c - e) The mutations that increase the population of the slow component in the 156R1 spectrum (most likely sterically allowed rotamers²⁴ shown in purple) are consistent with an alternate rotamer in the {t,t} configuration (shown in green).

In the {t,t} configuration, the MOMD fits suggest that R1 would be oscillating primarily about the γ_5 bond, which is consistent with its modeled orientation with respect to neighboring residues in the 156R1 crystal structure. Furthermore, in this conformation R1 would interact more closely with residues T138 and Q158, which could account for effects of these mutations on the EPR lineshapes of T156R1 (Figure 4.2.6). For example, the introduction of tryptophan at position 168 might clash with the {t,m} rotamer, and therefore R1 could favor the {t,t} configuration instead (Figure 4.2.6c). Moreover, the interaction between R1 and the NHB neighbor T138 is not strong in the {t,m} state, and while two mutations do not change the motion of the label, the T138Q mutation increases the population of the slow component. This is consistent with modeling of the {t,t} configuration indicating this rotamer might be favored with glutamine rather than threonine at position 138 (Figure 4.2.6e). However, it is not known how mutations at V154 would affect either of these rotamers, since the closest contact is 5.9 Å between a V154 side-chain methyl group and the 156R1 C $_{\beta}$ and remains unchanged in both the {t,m} and {t,t} R1 rotamers.

Bilayer Thickness Shifts Dynamic Modes of the BtuB T156R1 Spin Label

Previous work demonstrated that the 156R1 EPR lineshape was sensitive to hydrocarbon thickness.¹⁹ Specifically, it was found that thinner membranes resulted in an increased level of motional averaging of 156R1, but that R1 motion was not strongly affected by the phase state of the surrounding lipid. It was proposed that R1 does not

interact strongly with annular lipids but that it might report changes in the structure or dynamics of the β -barrel in response to a hydrophobic mismatch. Shown in Fig.4.2.7 are EPR spectra of BtuB T156R1 in lipid bilayers of four different thicknesses, all in the liquid crystalline state, as well as simulations of these spectra using the MOMD model (see Table 4.2.3 for parameters).

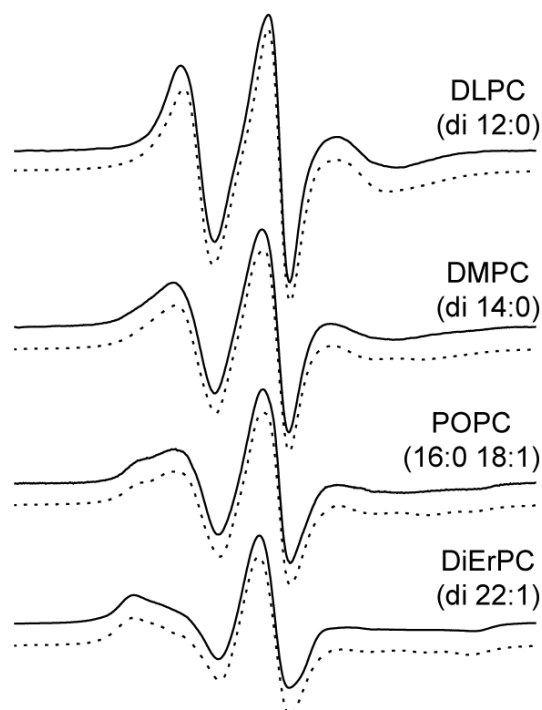


Figure 4.2.7. Effects of Hydrocarbon Thickness on T156R1 Lineshape. Comparison of T156R1 EPR spectra at 25°C that are reconstituted into lipid bilayers of increasing hydrocarbon thickness. The hydrocarbon thicknesses, determined previously,^{25,26} are approximately 19.5, 25.0, 27.1, and 43.4 nm for DLPC, DMPC, POPC, and DiErPC bilayers, respectively. The EPR lineshapes are shown as solid traces, and the MOMD fits are shown as dashed lines below each spectrum. The DLPC spectrum could be fit with a single component, and the population of a second slow component increases with bilayer thickness (see Table 4.2.3 for MOMD parameters). These spectra were reported elsewhere but did not include the MOMD simulations.¹⁹ Figure from Freed et al.¹

In DLPC (di 12:0) bilayers, 156R1 is a single-component spectrum; the MOMD fits suggest that the spin label is undergoing rapid oscillations about the χ_4 and χ_5 bonds (1.7 ns). This spectrum is identical to the crystalline 156R1 EPR spectrum, in which BtuB was crystallized from a C_8E_4 micellar solution. For the DMPC (di 14:0) spectrum, this fast component is essentially unchanged, but an additional component having an intermediate motion (4.3 ns) about the x-axis of the molecular frame ($\gamma_D = 11$; $\beta_D = 0$) is present. With increasing bilayer thickness, the population of the slow component increases and reaches 59% of the total spin population in DiErPC bilayers (di 22:1). Although no pattern can be seen in the rotational rates of the slow component as a function of bilayer thickness, the axes of rotation change slightly with thicker membranes. These results suggest that changes in membrane thickness primarily affect an equilibrium between two dynamic modes of T156R1, which appear to represent different rotameric states (supporting evidence below). The fast correlation time $\tau(z)$ that makes the most significant contribution to the motional averaging of T156R1 remains essentially constant with membrane thickness, suggesting that membrane thickness does not affect lineshape directly through changes in nanosecond backbone fluctuations as previously suggested.¹⁹

Structural Origins of the Slow Dynamic Mode of T156R1

Some R1 rotameric exchange processes, such as isomerization about the disulfide, are slow on the X-band EPR timescale ($\tau_R > \sim 50$ ns).¹¹ Slow rotameric exchange can

produce multiple components in the continuous wave EPR spectrum which are indistinguishable from protein conformational equilibria that are also slow on the X-band timescale. However, because protein conformational change is typically at least one order of magnitude slower than rotameric exchange and is also slow on the nitroxide T_1 relaxation timescale, T_1 measurements can be used to differentiate rotameric exchange from conformational exchange.²⁷

To determine the origin of the multicomponent lineshape, BtuB T156R1 was reconstituted into DLPC, POPC, and DiErPC bilayers and saturation recovery EPR was used to measure the T_1 relaxation time of each sample. As seen in Fig.4.2.8, each of the signals recovered to equilibrium with a single exponential time course. The curves could be fit to the expression $M_z(t) = M_0(1 - e^{-\frac{t}{T_1}})$, yielding a single exponential fit and one apparent T_1 value. Because the T156R1 spectra in POPC and DiErPC have two motional components, the single exponential recovery indicates that the exchange rate between dynamic modes is fast on the T_1 timescale: $k_{exAB} \gg \frac{1}{2}(\frac{1}{T_{1A}} - \frac{1}{T_{1B}})$, where T_{1A} and T_{1B} represent the intrinsic spin-lattice relaxation times of the individual motional modes.

The lower limit on the rate of exchange between the two motional modes of T156R1 could be estimated from the individual values of T_{1A} and T_{1B} . The MOMD fits (Table 4.2.3) indicate that the fast dynamic mode remains relatively unchanged with membrane thickness. If it is assumed that the T_1 relaxation time for the fast component thus remains constant, then the value of T_{1A} from the DLPC saturation recovery data can be taken to be that of the fast component in each spectrum, and T_{1B} can be estimated

using the MOMD populations of each component (the measured saturation recovery signal should be a linear combination of T_1^A and T_1^B , e.g. for POPC, $(0.74)(723 \text{ ns}) + (0.26)(T_{1B}) = 1.90 \mu\text{s}$). Using this approach, the saturation recovery data indicate that in POPC bilayers the exchange rate is faster than 596 kHz and in DiErPC bilayers the exchange rate is faster than 557 kHz. These correspond to interconversion times of 1.68 and 1.80 μs , respectively. Because most conformational exchange occurs no faster than tens of microseconds,²⁸ the two components in the T156R1 spectra are likely the result of label rotameric exchange.

As indicated above, a likely alternate configuration for T156R1 is the {t,t} rotamer. Moreover, it is likely that the slow component in the EPR spectrum results from the interaction of the label in this rotamer with the hydrophobic surface of the protein. Dioxane has been used to probe weak interactions between R1 and protein surfaces,¹⁴ and it might be expected to alter T156R1 lineshapes by modulating the interaction of the label with the protein surface. Shown in Fig.4.2.9 are EPR spectra that result from titration of dioxane into BtuB T156R1 reconstituted into bilayers. For the POPC sample, dioxane increases the population of the 156R1 fast component as well as the correlation time of the slow component (MOMD fits not shown), suggesting that dioxane competes with the spin label for the surface of the protein and weakens the interaction between R1 and the protein surface. Interestingly, in DiErPC bilayers, dioxane has no effect at concentrations up to 10% (v/v) but solubilizes the liposomes above this threshold, as reported previously.²⁹ It is not clear why the behavior in DiErPC is different, but this result could

indicate that the R1 side-chain interacts more strongly with the protein surface in these membranes and is not effectively displaced by dioxane.

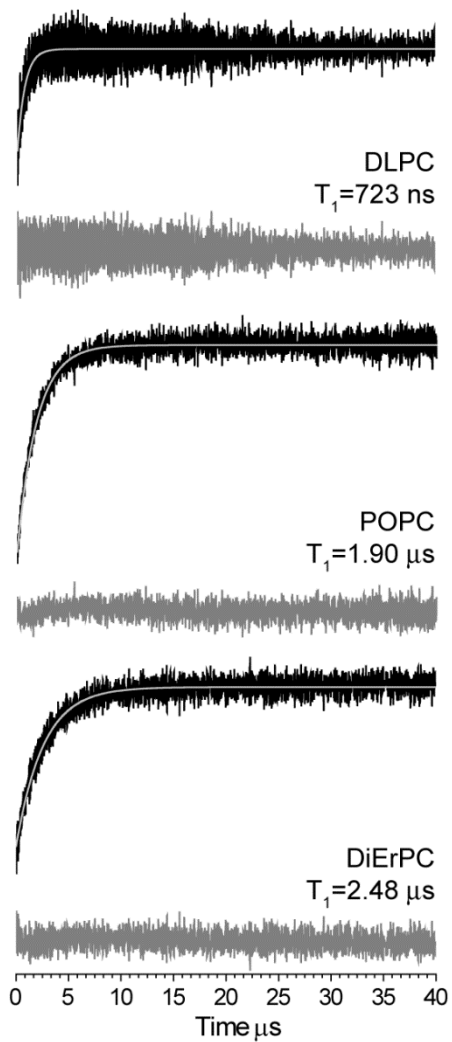


Figure 4.2.8. Saturation Recovery Data for T156R1. Saturation recovery data (black traces) for BtuB T156R1 reconstituted into DLPC (top), POPC (middle), and DiErPC (bottom) bilayers. Each signal could be fit with a single exponential recovery function (white trace), and the average T_1 values of three measurements are given. The residual to the fit is colored gray. The first ~ 100 data points representing the instrumental defense pulse were omitted from the fits and figures. Figure from Freed et al.¹

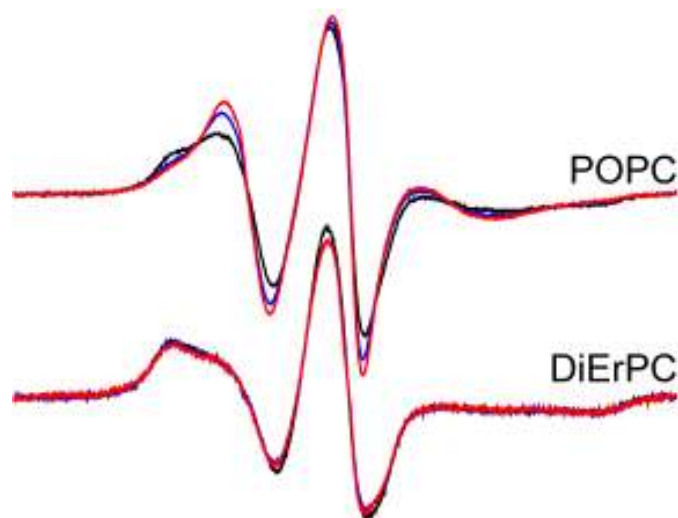


Figure 4.2.9. Effect of Dioxane on the T156R1 EPR Spectrum. Spectra are shown in the absence of dioxane (black) and in the presence of 5% (v/v) (blue) and 10% (red) dioxane. In POPC bilayers, dioxane increases the population of the fast component, consistent with the proposal that the slow label conformer results from an interaction of the label with a hydrophobic pocket on the protein surface. In DiErPC bilayers, dioxane does not affect the rotameric equilibrium, presumably because this interaction is much stronger in thicker lipid bilayers.

Structural Model of W371R1 from X-ray Crystallography

Residue W371R1 is located deep in the membrane bilayer and exhibits an EPR spectrum near the rigid limit (Figure 4.1.1); however, its nearest-neighbor residues consist of a glycine, an alanine, and two threonines. To determine why R1 is highly immobilized at this site, the structure of 371R1 was determined at 90 K. The crystals diffracted to 2.3 Å, and the resulting structure was refined to an R_{free} of 24.98%; the complete data collection and refinement statistics are listed in Table 4.2.1. As seen for 156R1, electron density for the entire R1 side-chain is resolved (Figure 4.2.10), and χ_1

and χ_2 are in a {p,p} rotamer (Table 4.2.2). This R1 rotamer has been reported only once in the literature,³⁰ for a label in a sterically constrained environment in tertiary contact.

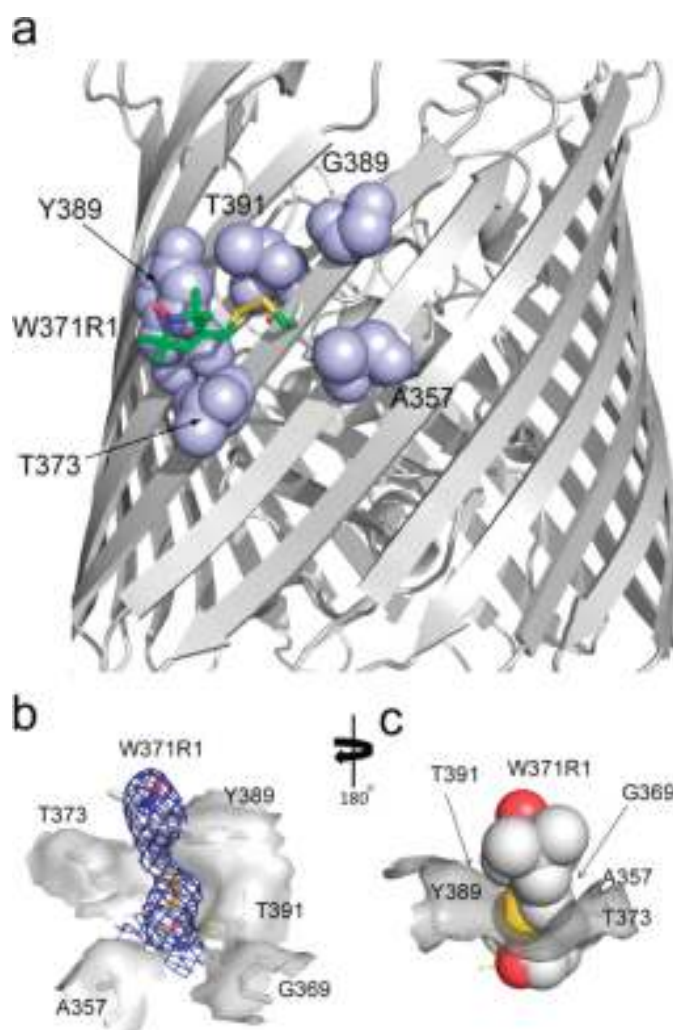


Figure 4.2.10. Crystal Structure of BtuB W371R1. (a) X-ray crystal structure (90 K) of BtuB W371R1 (PDB entry 3RGN) determined at 2.3 Å showing the R1 side-chain as sticks and the positions of the nearest-neighbor residues in CPK rendering. (b and c) Alternate views of the site around W371R1, with the van der Waals surface colored gray. W371R1 sits in a pocket formed by residues T373 and Y389. In panel b, the 2F_o-F_c electron density is shown as blue mesh contoured at 1σ. Data collection and refinement statistics are listed in Table 4.2.1. Figure from Freed et al.¹

The W371R1 mutation does not affect BtuB structure; the all-atom pairwise root-mean-square deviation compared to the wild-type apo structure⁸ is 0.22 Å, and the neighboring side-chain rotamers are all unperturbed. It should be noted that residue 371 is near a BtuB crystal contact site on a neighboring β-strand; however, W371R1 does not contact the BtuB symmetry partner, and the rotameric state of R1 does not appear to be affected by this proximity. As seen for T156R1, the S_{δ} — HC_{α} stabilizing interaction found at many spin-labeled α-helical sites is absent ($d = 4.5$ Å). Instead, 371R1 may be stabilized internally by S_{δ} — N_{i+1} ($d = 3.6$ Å) and S_{δ} — $O=C$ (3.0 Å) interactions similar to that of the 156R1 side chain. The spin label sits in a pocket formed by Y389 and T373; a methyl group on the nitroxide ring interacts with the Y389 $C_{\epsilon}2-H$ ($d_{H-H} = 2.2$ Å), the R1 S_{δ} atom interacts with Y389 $C_{\delta}2-H$ and $C_{\epsilon}2-H$ ($d_{S-H} = 3.2$ Å) and the R1 $C_{\epsilon}-H$ group may interact with O_{γ} of T373 ($d_{H-O} = 3.0$ Å). In other BtuB structures, W371 sits in this same pocket on the protein surface. Because of the increased level of strand twist, there is limited interstrand hydrogen-bonding between the N-terminal end of strand 12 and the C-terminal end of strand 13. Nevertheless, this does not result in any measurable increase in backbone dynamics since the 371R1 lineshape is near the rigid limit. Although a considerable amount of strand tilt on β-strand 13 points the side-chains towards 371R1, the increased strand twist places the C_{α} of the HB neighbor T391 about 2 Å below the C_{α} of 371R1, decreasing the chances of a strong interaction between 371R1 and its hydrogen-bonded neighbor regardless of residue identity.

The configuration of W371R1 in this structural model is consistent with the broad spectrum that is obtained at room temperature. This model suggests that R1 at this

deeply buried hydrophobic site interacts with a pocket on the protein surface formed by neighboring side-chains. This site does not present a sterically restrictive environment to the R1 side-chain, and the interaction of R1 with this pocket must be sufficiently strong to immobilize the nitroxide on the nanosecond timescale. Unfortunately, a room temperature crystalline EPR data could not be collected because there were not enough crystals to produce a signal. Unlike the spin label at site 156, W371R1 is not sensitive to hydrocarbon thickness, perhaps because it is more deeply buried in the bilayer (data not shown).

EPR Spectra of G170R1 are Insensitive to Local Side-Chain Substitutions and Hydrocarbon Thickness

Residue G170R1 is located at a site buried in the membrane interior that also yields a rigid-limit EPR spectrum; however, it is surrounded by a more sterically restrained environment than W371R1. At this site, we mutated surrounding residues to alanine to determine whether specific side-chain interactions with G170R1 might be important for immobilization of the spin label. The resulting EPR lineshapes are shown in Fig.4.2.11. The results indicate that the motion of G170R1 is only very weakly dependent on the identity of nearest-neighbor residues. Tyrosine, a residue that has been shown to interact with and stabilize the nitroxide ring,¹⁵ is the $i + 2$ neighbor of G170R1. However, exchanging the tyrosine at residue 172 with an alanine did not significantly affect EPR lineshape; in fact, there was a minor decrease in the peak-to-peak amplitude,

indicating additional immobilization of R1. The peak-to-peak amplitude of the central line also slightly decreases when residue $i - 2$ is mutated to alanine, indicating a further immobilization of the spin label when the local steric environment decreases on the same β -strand as R1. For all of the mutants, small changes in g -anisotropy can be seen in the central line, which may reflect changes in local side-chain polarity. Furthermore, in contrast to the spectra from T156R1, the EPR lineshape from G170R1 is not dependent upon lipid composition. These results suggest that G170R1 is not being immobilized by specific interactions made with neighboring residues; in other words, at this deeply buried site, R1 can form strong interactions with the protein surface irrespective of the identity of the neighboring side-chain.

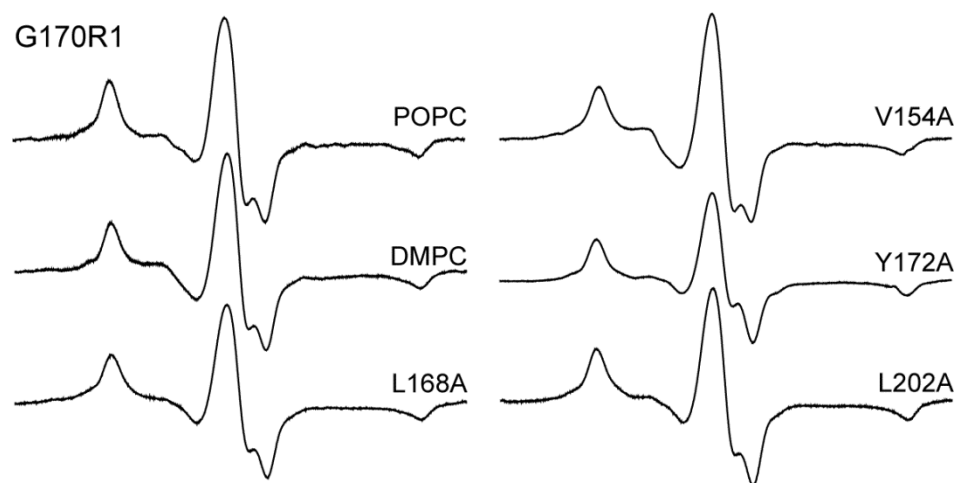


Figure 4.2.11. G170R1 EPR Spectra with Neighboring Mutations. EPR spectra of BtuB G170R1 reconstituted into POPC and DMPC bilayers, and spectra in POPC bilayers from four single alanine mutations surrounding G170R1. These spectra include those from mutations to the $i \pm 2$ residues (Y172 and L168) and the HB (V154) and NHB (L202) neighbors. No effect of hydrocarbon thickness was observed over a broad range of membrane thicknesses (only POPC and DMPC data shown).

4.3 Discussion

The ultimate utility of SDSL-EPR as a tool for studying protein structure and dynamics hinges on our ability to better understand spin label structure and dynamics. Thus far, studies aimed at characterizing spin label energetics have focused almost exclusively on soluble proteins. At aqueous solvent-exposed helical sites, in most cases the spin-labeled side-chain R1 does not make strong interactions with neighboring residues;^{12,13,16} however, the disulfide linkage interacts with the protein backbone, and differences in EPR spectra are usually dominated by differences in backbone dynamics.^{10,31} On β -sheet proteins facing an aqueous medium, EPR spectroscopy indicates that the R1 side-chain interacts strongly with neighboring residues, and the motion of the label is strongly modulated by the identity of the HB and NHB neighbors.¹⁸ For spin labels in a hydrophobic environment, such as the surface of a membrane protein, the work presented here indicates that the R1 nitroxide ring makes interactions with hydrophobic pockets on the protein surface, and that the label-protein interaction is sensitive to the solvation environment.

A recent analysis on the structures of R1 at helix surface sites in LeuT first reported that R1 is more likely to interact with the protein surface at protein-hydrocarbon interfaces compared to protein-aqueous interfaces.¹⁷ The work presented here is consistent with this result and with the general finding that side chain rotamers that face the hydrocarbon in transmembrane proteins (either α -helical or β -barrel) are different versus those in soluble proteins.³² The data presented here indicate that T156R1, W371R1, and G170R1 interact with hydrophobic pockets formed by side-chains on the

β -barrel surface of BtuB. In the case of W371R1, the room temperature EPR spectrum is highly immobilized, even though the site is not sterically restrictive. The crystal structure of BtuB W371R1 indicates that this immobilization is due to the interaction of the nitroxide ring with a pocket formed by Y389 and T373. A common configuration for R1 at helical surface sites is the {m,m} or {t,p} rotamer for χ_1 and χ_2 ; however, at position 371 on the BtuB β -barrel, the R1 side-chain is in a {p,p} rotamer, which has been observed only once at a sterically hindered site.³⁰ It is likely that this rotamer is being dictated by interactions of the R1 side-chain with the pocket formed by Y389 and T373, but since there is a chance that R1 configuration at this site might be affected by its proximity to a crystal contact site, more work is required to verify rotamer propensities at deeply buried sites on β -barrel membrane proteins.

The G170R1 mutagenesis data further indicate that R1 labels buried in the membrane interior are immobilized by interactions with the protein surface, and not by interactions with specific neighboring side-chains. In the case of T156R1, the {t,m} conformer observed in the crystal structure projects away from the protein backbone and towards the solvent interface. The interaction of the spin label with the protein surface at this site appears to be weaker and modulated by the solvation environment.

Several other observations support the idea that a hydrophobic environment promotes interactions of the R1 side-chain with the protein surface. As indicated above, strongly immobilized EPR spectra on the surface of BtuB arise almost exclusively from labels positioned in the membrane hydrocarbon, while multicomponent spectra appear to be more prevalent at interfacial sites. Although sites on the positively curved surface of

BtuB are less sterically constrained than sites on cellular retinol-binding protein, a soluble β -sheet protein, the EPR spectra from cellular retinol-binding protein¹⁸ exhibit more motional averaging than spectra from the hydrocarbon surface of BtuB. Interactions of R1 with the protein surface will become more important if interactions with the surrounding solvent are less favorable, and this may be the case at the protein-hydrocarbon interface. Spin labels on BtuB were previously shown to be insensitive to the phase state of the bulk lipid,¹⁹ which is consistent with the finding here that R1 tends to interact with the protein surface at the protein-hydrocarbon interface. Moreover, in an accompanying study on the β -barrel protein OmpA reconstituted into various detergent micelles was consistent with this hypothesis, and indicated that sites with less aqueous solvent penetration yield more motionally restricted EPR spectra and shorter interspin distances measured across the β -barrel.³³

The work presented here provides an explanation for the dramatic sensitivity of the EPR spectrum at position 156 to lipid chain length. Membrane thickness modulates two rotameric states of R1 at this site, which give rise to fast and slow components in the EPR spectrum. Conceivably, the sensitivity of 156R1 to membrane thickness might arise from a modulation of local acyl chain packing or variation of water penetration at this site. Amino acid side-chain rotamer conformations have, in fact, been shown to be responsive to alterations in the polarity gradient along the protein surface.³² Similar to the thinnest bilayer formed from DLPC lipids, BtuB T156R1 in the C₈E₄ detergent system produces only a single fast component in the EPR spectrum (see Figure 4.2.3). It

is likely that the local polarity or degree of water penetration at this site is much greater in the detergent or short chain lipid.

In a previous study, it was noted that three other outward-facing sites on β -strand 2 are sensitive to lipid thickness.¹⁹ The spectra at these sites (positions 150, 152, and 154) also result from two motional components, and lipid composition appears to modulate the populations of these components. As a result, the effects seen at position 156 are not limited to sites near the solvent interface. These lipid effects have not been observed elsewhere on the BtuB barrel at deeply buried hydrocarbon sites (strands 3, 7, 12, and 17), which suggests that this end of the BtuB barrel may be different than other regions of the protein.

The length of the β -strands in the barrel of BtuB and other TonB-dependent transporters is highly asymmetric around the circumference of the protein. Recent work using nitroxide depth measurements indicated that the protein-bilayer interface is also asymmetric around the circumference of BtuB, and that the region near strand 1 is highly mismatched to the hydrocarbon thickness.⁹ Conceivably, this hydrophobic mismatch might alter the optimal lipid chain packing with the protein surface, create more local defects in the bilayer, and/or alter water penetration around this surface of the protein, thereby modulating the interactions of spin labels with the protein surface. This region of BtuB (β -strands 22, 1, and 2) also has higher crystallographic B-factors in both the *in meso* and *in surfo* structures than other regions around the β -barrel.^{8,34} Although the MOMD fits of spectra from T156R1 do not suggest that nanosecond backbone dynamics are directly contributing to motional averaging of the label, it is possible that slow

backbone fluctuations around strand 2 are also altering interactions of the label with the protein surface.

In summary, the R1 spin-labeled side-chain tends to interact with the protein surface at hydrocarbon-facing sites in BtuB. In contrast to aqueous-facing sites, the mobility of R1 on the BtuB barrel and the resulting EPR spectra at these sites are influenced by the availability of binding pockets for R1 on the surface of the protein and not necessarily by steric constraints imposed by neighboring residues. Moreover, R1 is highly sensitive to the solvation environment, and at some sites, interactions of the spin label with the protein surface can be modulated by lipid acyl chain length.

The R1 side-chain is widely used as a probe for obtaining long-range distance restraints for molecular modeling, either through measurements of paramagnetic enhancements of nuclear relaxation or through measurements of electron dipole-dipole interactions. In these cases, knowledge of the likely side-chain configurations for R1 becomes a critical factor in modeling the structure with desirable resolution. Moreover, although general structural features of a protein can be easily decoded from SDSL-EPR data, the unambiguous interpretation of detailed structural and dynamical information from the EPR spectrum requires knowledge of the spin label's behavior. The work presented here indicates that the rotamers found for R1 at aqueous-exposed sites in β -barrel membrane proteins will likely be different from those found for sites facing the membrane hydrocarbon. Even in cases where R1 is not constrained by interactions with neighboring residues, it is likely to prefer rotamers that create favorable interactions with hydrophobic pockets on the protein surface at sites located within the membrane interior.

4.4 Methods

Mutagenesis, Expression, Purification, and Spin-labeling of BtuB Mutants. All mutations in BtuB were introduced into a pAG1 vector (for EPR spectroscopy) or a pET22b vector (for crystallization) using a QuikChange site-directed mutagenesis kit (Stratagene, La Jolla, CA), and the mutations were subsequently verified by nucleotide sequencing. For EPR spectroscopy of BtuB mutants, the expression, purification, spin-labeling, and reconstitution into lipid bilayers were performed following a procedure detailed previously.³⁵ All lipids were obtained from Avanti Polar Lipids (Alabaster, AL), and except where noted, all BtuB mutants were reconstituted into 1-palmitoyl-2-oleoyl-*sn*-glycero-3-phosphocholine (POPC) bilayers for EPR spectroscopy. POPC forms a fluid-phase bilayer over a broad temperature range, and as discussed elsewhere,⁹ it has a hydrocarbon thickness that is similar to that of the native outer membrane of *Escherichia coli*. For BtuB crystallization, the expression, purification and spin-labeling of BtuB were performed as described previously.^{30,36}

Crystallization and Crystallographic Data Collection. Purified BtuB (11 mg/mL in 30 mM Tris at pH 8.0 and 20 mM C₈E₄) was crystallized by mixing 1 μ L of BtuB and 1 μ L of reservoir buffer in an EasyXtal hanging drop tray (Qiagen, Germantown, MD), containing 200 μ L of total reservoir buffer for each crystallization condition, followed by incubation at 290 K. The reservoir buffer consisted of 200-550 mM magnesium acetate, 5.0-7.5% PEG3350, and 20 mM Bis Tris at pH 6.6. Crystals were visible after 1-2 days of incubation and grew to \sim 200 μ m in the longest dimension after 1-2 weeks. For X-ray diffraction, BtuB crystals were transferred to cryo buffer (150 mM magnesium acetate,

2.5% PEG3350, 20 mM Bis Tris at pH 6.6, 10 mM C_8E_4 , and 20% glycerol) for 1-2 min before loop-mounting and cryo-cooling by insertion into liquid nitrogen. Diffraction data were recorded at 90 K at the 22-ID and 22-BM beamlines at the Advanced Photon Source (Argonne National Laboratory, Argonne, IL).

Structure Determination. Indexing, integration, and scaling of the diffraction data were performed using HKL2000.³⁷ The structures were determined with the Phaser³⁸ maximum likelihood molecular replacement method, using PDB entry 1NQE⁸ as a search model. To reduce model bias, the spin-labeled residues were deleted from the search model prior to molecular replacement. Model building was conducted in COOT,²⁴ unrestrained TLS³⁹ refinement was performed using Refmac,⁴⁰ and PHENIX⁴¹ was used to refine the occupancy of the spin label. The spin-labeled residues were manually built in COOT. Completed structures were evaluated and validated with MolProbity.⁴²

EPR Spectroscopy of Spin-labeled BtuB Mutants. Room-temperature (298 K) X-band EPR spectroscopy was performed on a Bruker EMX spectrometer equipped with a dielectric resonator (Bruker Biospin, Billerica, MA) or an E-line 102 Century series spectrometer from Varian outfitted with a loop-gap resonator. Low-temperature (200 K) X-band EPR spectroscopy was performed with an E-line 102 Century series spectrometer from Varian equipped with a loop-gap resonator. For all X-band measurements, 5 μ L of approximately 100 μ M protein sample was loaded into Pyrex capillaries (0.60 mm ID x 0.84 mm OD; Fiber Optic Center, Inc., New Bedford, MA) using a syringe, and EPR spectroscopy on spin-labeled BtuB crystals was performed as described previously³⁰ (see Chapter 3). Low-temperature (200 K) Q-band EPR spectroscopy was performed on an

ELEXSYS E-500 spectrometer equipped with an ER5106 QT-W resonator (Bruker Biospin) with 5 μL of approximately 100 μM protein sample loaded with a syringe into quartz capillaries (0.60 mm ID x 0.84 mm OD, Fiber Optic Center, Inc.). All EPR spectra were recorded with either a 100 G (at 298 K) or 150-200 G (at 200 K) magnetic field sweep at 2.0 mW incident power. The phasing and normalization of EPR spectra were performed using LabVIEW provided by C. Altenbach (University of California, Los Angeles, CA).

Saturation Recovery EPR. Saturation recovery was performed on an X-band ELEXSYS E-580 spectrometer equipped with an MS-2 split-ring resonator (Bruker Biospin). The spectrometer was fitted with a Stanford Research Instruments (Sunnyvale, CA) SR445A amplifier in place of the video amplifier originally supplied with the instrument. For these measurements, 5 μL of approximately 100 μM protein sample was loaded into Pyrex capillaries (0.60 mm ID x 0.84 mm OD, Fiber Optic Center, Inc.) using a syringe. A 500 ns saturating pump pulse was applied to the center of the $m_1 = 0$ hyperfine line, and a 2 mW continuous-wave observe power was applied at the same frequency. The field was stepped on- and off-resonance by 100 G at 5 Hz to subtract any background signal. Each measurement was independently repeated three times with good reproducibility (standard deviations within 75 ns), and the average T_1 relaxation times from the three measurements are reported.

Modeling of EPR Spectra. Low-temperature (200 K) X- and Q-band EPR spectra were fit using an effective Hamiltonian rigid limit model executed in LabVIEW. From these fits, the hyperfine A and g tensor values were determined and used as constraints for

fitting the room-temperature EPR spectra with the Microscopic Order, Macroscopic Disorder (MOMD) model⁴³ implemented in the Multicomponent program developed by C. Altenbach. The following tensor values were used from spectral fitting: $g_{xx} = 2.0085$, $g_{yy} = 2.0059$, and $g_{zz} = 2.0021$; $A_{xx} = 6.5$, $A_{yy} = 5.6$, and $A_{zz} = 35.0$.

The high degree of overlap between the fast and slow components in the 156R1 spectra introduces significant uncertainty into the fitting process. To address this issue, the single component 156R1 spectrum in DLPC bilayers was initially fit, and the final parameters from this fit were used as initial input parameters for the fast component during the subsequent two component fits. Additionally, because of the correlation between rotational diffusion and local order, the spectra were fit without a restoring potential to reduce fitting time and the number of parameters. In this work, a precise motional model of R1 involving both the rate and amplitude of motion was not necessarily the objective; rather, emphasis was placed on the comparison of spectral populations and diffusion rates as a function of neighboring mutations and varying hydrocarbon thickness. In fact, better fits were obtained for the spectra presented here assuming anisotropic diffusion without a restoring potential, especially with respect to the high-field hyperfine manifold.

During fitting, the R_{xyz} tensor (diffusion tensor in Cartesian representation) was allowed to vary for each component independently. Once a good fit to the central line was established, the Euler angles were adjusted for each component, paying special attention to the quality of fit at the high-field manifold. If necessary, the R tensors were varied again; this process was iteratively repeated until a satisfactory fit was obtained. In

cases of simple z-axis anisotropic motion, only the γ_D and β_D angles were varied to constrain the number of fitting parameters. Likewise, for simple x-axis anisotropic motion, only γ_D was varied. Subsequently, the Lorentzian (and, if necessary, Gaussian) linewidths, initially set to 0 G, were allowed to vary to obtain the final fit. In some cases, the A tensor values were allowed to vary by 0.6 G if necessary to obtain the best fit. The quality of the fit was assessed using the reduced χ^2 between the experimental and theoretical spectra, as well as visually evaluating the match between prominent spectral features.

4.5 References

1. Freed, D.M., Khan, A.K., Horanyi, P.S. & Cafiso, D.S. Molecular origin of electron paramagnetic resonance line shapes on beta-barrel membrane proteins: the local solvation environment modulates spin-label configuration. *Biochemistry* **50**, 8792-803 (2011).
2. Fanucci, G.E. & Cafiso, D.S. Recent advances and applications of site-directed spin labeling. *Current opinion in structural biology* **16**, 644-53 (2006).
3. Jeschke, G. & Polyhach, Y. Distance measurements on spin-labelled biomacromolecules by pulsed electron paramagnetic resonance. *Physical chemistry chemical physics : PCCP* **9**, 1895-910 (2007).
4. Hubbell, W.L., Cafiso, D.S. & Altenbach, C. Identifying conformational changes with site-directed spin labeling. *Nature structural biology* **7**, 735-9 (2000).

5. Hubbell, W.L., Gross, A., Langen, R. & Lietzow, M.A. Recent advances in site-directed spin labeling of proteins. *Current opinion in structural biology* **8**, 649-56 (1998).
6. Clore, G.M., Tang, C. & Iwahara, J. Elucidating transient macromolecular interactions using paramagnetic relaxation enhancement. *Current opinion in structural biology* **17**, 603-16 (2007).
7. Liang, B., Bushweller, J.H. & Tamm, L.K. Site-directed parallel spin-labeling and paramagnetic relaxation enhancement in structure determination of membrane proteins by solution NMR spectroscopy. *Journal of the American Chemical Society* **128**, 4389-97 (2006).
8. Chimento, D.P., Mohanty, A.K., Kadner, R.J. & Wiener, M.C. Substrate-induced transmembrane signaling in the cobalamin transporter BtuB. *Nature structural biology* **10**, 394-401 (2003).
9. Ellena, J.F., Lackowicz, P., Montgomery, H. & Cafiso, D.S. Membrane Thickness Varies Around the Circumference of the Transmembrane Protein BtuB. *Biophysical journal* **100**, 1280-7 (2011).
10. Columbus, L. & Hubbell, W.L. Mapping backbone dynamics in solution with site-directed spin labeling: GCN4-58 bZip free and bound to DNA. *Biochemistry* **43**, 7273-87 (2004).
11. Columbus, L., Kalai, T., Jeko, J., Hideg, K. & Hubbell, W.L. Molecular motion of spin labeled side chains in alpha-helices: analysis by variation of side chain structure. *Biochemistry* **40**, 3828-46 (2001).

12. Fleissner, M.R., Cascio, D. & Hubbell, W.L. Structural origin of weakly ordered nitroxide motion in spin-labeled proteins. *Protein science : a publication of the Protein Society* **18**, 893-908 (2009).
13. Guo, Z., Cascio, D., Hideg, K. & Hubbell, W.L. Structural determinants of nitroxide motion in spin-labeled proteins: solvent-exposed sites in helix B of T4 lysozyme. *Protein science : a publication of the Protein Society* **17**, 228-39 (2008).
14. Guo, Z., Cascio, D., Hideg, K., Kalai, T. & Hubbell, W.L. Structural determinants of nitroxide motion in spin-labeled proteins: tertiary contact and solvent-inaccessible sites in helix G of T4 lysozyme. *Protein science : a publication of the Protein Society* **16**, 1069-86 (2007).
15. Langen, R., Oh, K.J., Cascio, D. & Hubbell, W.L. Crystal structures of spin labeled T4 lysozyme mutants: implications for the interpretation of EPR spectra in terms of structure. *Biochemistry* **39**, 8396-405 (2000).
16. McHaourab, H.S., Lietzow, M.A., Hideg, K. & Hubbell, W.L. Motion of spin-labeled side chains in T4 lysozyme. Correlation with protein structure and dynamics. *Biochemistry* **35**, 7692-704 (1996).
17. Kroncke, B.M., Horanyi, P.S. & Columbus, L. Structural Origins of Nitroxide Side Chain Dynamics on Membrane Protein alpha-Helical Sites. *Biochemistry* **49**, 10045-10060 (2010).
18. Lietzow, M.A. & Hubbell, W.L. Motion of spin label side chains in cellular retinol-binding protein: correlation with structure and nearest-neighbor interactions in an antiparallel beta-sheet. *Biochemistry* **43**, 3137-51 (2004).

19. Xu, Q. et al. Membrane hydrocarbon thickness modulates the dynamics of a membrane transport protein. *Biophysical journal* **95**, 2849-58 (2008).
20. Lovell, S.C., Word, J.M., Richardson, J.S. & Richardson, D.C. The penultimate rotamer library. *Proteins* **40**, 389-408 (2000).
21. Warshaviak, D.T., Serbulea, L., Houk, K.N. & Hubbell, W.L. Conformational analysis of a nitroxide side chain in an alpha-helix with density functional theory. *The journal of physical chemistry. B* **115**, 397-405 (2011).
22. Murzin, A.G., Lesk, A.M. & Chothia, C. Principles determining the structure of beta-sheet barrels in proteins. I. A theoretical analysis. *Journal of molecular biology* **236**, 1369-81 (1994).
23. Tombolato, F., Ferrarini, A. & Freed, J.H. Dynamics of the nitroxide side chain in spin-labeled proteins. *The journal of physical chemistry. B* **110**, 26248-59 (2006).
24. Emsley, P. & Cowtan, K. Coot: model-building tools for molecular graphics. *Acta Crystallographica Section D-Biological Crystallography* **60**, 2126-2132 (2004).
25. Kucerka, N., Tristram-Nagle, S. & Nagle, J.F. Structure of fully hydrated fluid phase lipid bilayers with monounsaturated chains. *The Journal of membrane biology* **208**, 193-202 (2005).
26. Lewis, B.A. & Engelman, D.M. Lipid bilayer thickness varies linearly with acyl chain length in fluid phosphatidylcholine vesicles. *Journal of molecular biology* **166**, 211-7 (1983).
27. Bridges, M.D., Hideg, K. & Hubbell, W.L. Resolving Conformational and Rotameric Exchange in Spin-Labeled Proteins Using Saturation Recovery EPR. *Applied magnetic resonance* **37**, 363 (2010).

28. Henzler-Wildman, K. & Kern, D. Dynamic personalities of proteins. *Nature* **450**, 964-72 (2007).
29. Glorio-Paulet, P. & Durst, R.A. Determination of potato glycoalkaloids using a liposome immunomigration, liquid-phase competition immunoassay. *Journal of Agricultural and Food Chemistry* **48**, 1678-1683 (2000).
30. Freed, D.M., Horanyi, P.S., Wiener, M.C. & Cafiso, D.S. Conformational Exchange in a Membrane Transport Protein Is Altered in Protein Crystals. *Biophysical Journal* **99**, 1604-1610 (2010).
31. Columbus, L. & Hubbell, W.L. A new spin on protein dynamics. *Trends in biochemical sciences* **27**, 288-95 (2002).
32. Chamberlain, A.K. & Bowie, J.U. Analysis of side-chain rotamers in transmembrane proteins. *Biophysical journal* **87**, 3460-9 (2004).
33. Jimenez, R.H., Freed, D.M. & Cafiso, D.S. Lipid and membrane mimetic environments modulate spin label side chain configuration in the outer membrane protein A. *The journal of physical chemistry. B* **115**, 14822-30 (2011).
34. Cherezov, V. et al. In meso structure of the cobalamin transporter, BtuB, at 1.95 Å resolution. *Journal of molecular biology* **364**, 716-34 (2006).
35. Fanucci, G.E., Cadieux, N., Piedmont, C.A., Kadner, R.J. & Cafiso, D.S. Structure and dynamics of the beta-barrel of the membrane transporter BtuB by site-directed spin labeling. *Biochemistry* **41**, 11543-51 (2002).
36. Chimento, D.P., Mohanty, A.K., Kadner, R.J. & Wiener, M.C. Crystallization and initial X-ray diffraction of BtuB, the integral membrane cobalamin transporter of

- Escherichia coli. *Acta crystallographica. Section D, Biological crystallography* **59**, 509-11 (2003).
37. Otwinowski, Z. & Minor, W. Processing of X-ray diffraction data collected in oscillation mode. *Macromolecular Crystallography, Pt A* **276**, 307-326 (1997).
 38. McCoy, A.J. et al. Phaser crystallographic software. *Journal of Applied Crystallography* **40**, 658-674 (2007).
 39. Winn, M.D., Isupov, M.N. & Murshudov, G.N. Use of TLS parameters to model anisotropic displacements in macromolecular refinement. *Acta Crystallographica Section D-Biological Crystallography* **57**, 122-133 (2001).
 40. Murshudov, G.N., Vagin, A.A. & Dodson, E.J. Refinement of macromolecular structures by the maximum-likelihood method. *Acta Crystallographica Section D-Biological Crystallography* **53**, 240-255 (1997).
 41. Adams, P.D. et al. PHENIX: building new software for automated crystallographic structure determination. *Acta Crystallographica Section D-Biological Crystallography* **58**, 1948-1954 (2002).
 42. Davis, I.W. et al. MolProbity: all-atom contacts and structure validation for proteins and nucleic acids. *Nucleic acids research* **35**, W375-83 (2007).
 43. Budil, D.E., Lee, S., Saxena, S. & Freed, J.H. Nonlinear-least-squares analysis of slow-motion EPR spectra in one and two dimensions using a modified Levenberg-Marquardt algorithm. *Journal of Magnetic Resonance Series A* **120**, 155-189 (1996).

CHAPTER 5

Differential Transmembrane Signaling through BtuB by Competing Substrates

5.1 Introduction

For the uptake of essential nutrients that are too large to diffuse through porins in the outer membrane (OM), Gram-negative bacteria produce and secrete active membrane transport proteins that bind their substrates with high-affinity and propel them into the periplasmic space. This process requires energy, which is a scarce commodity at the OM. Therefore, the transporters couple to the electrochemical gradient maintained by the cytoplasmic membrane (CM) through association with TonB, and its accessory CM proteins ExbB and ExbD. Hence, the TonB-dependent transport of vitamin B₁₂ (cyanocobalamin, CNCbl) and various iron siderophores is a highly complex process orchestrated between concentric membranes.

The recognition motif for TonB has been identified by structural^{1,2} and biochemical³⁻⁵ studies to be a short and conserved segment at the N-terminus of the TonB-dependent transporters (TBDTs), termed the Ton box. In the *Escherichia coli* CNCbl transport protein BtuB, SDSL-EPR data indicates that the Ton box is in conformational exchange, and that CNCbl binding shifts this equilibrium towards the unfolded state (Figure 5.1.1).^{6,7} This substrate-dependent conformational transition

results in the extension of the Ton box 20-30 Å into the periplasm,⁸ and is presumably the trigger which initiates interactions with TonB. Recently, a pair of charged residues in BtuB, R14 and D316, were found to mediate the Ton box equilibrium.⁹ In BtuB crystal structures,¹⁰ these residues point towards each other and appear to be engaged in an electrostatic interaction (Figure 5.1.2). Upon substrate binding the R14 side-chain isomerizes, increasing the distance between the charged moieties of these residues by about 3.2 Å. However, in lipid bilayers the distance change upon substrate binding is significantly larger than indicated in the crystal structure,⁸ due to differences in crystalline and membrane-associated forms of BtuB.¹¹ By monitoring the conformation of the Ton box using SDSL-EPR and employing a thermodynamic two-mutant cycle analysis, the ion pair was found to contribute ~1.8 kcal/mol to the Ton box equilibrium.⁹ Furthermore, in the presence of CNCbl the interaction between these residues was essentially eliminated (0.1 kcal/mol). The difference in these energies (1.7 kcal/mol) represents the shift in interaction energy that is produced by substrate binding, and implicates the R14/D316 ion pair as a switch that mediates substrate-dependent transmembrane signaling in BtuB.

In addition to their role in the uptake of essential nutrients, TBDTs are used as receptors for colicins. These bacteriocidal proteins are secreted by and targeted against certain strains of *E.coli*, and hijack the TBDTs to initiate the killing process. The colicins generally consist of three domains: a central receptor-binding domain, an N-terminal translocation domain, and a C-terminal cytotoxic domain that confers toxicity either through pore-forming or enzymatic activity.¹² Following association of the receptor-

binding domain with a TBDT, translocation of the latter two domains across the OM may occur via two pathways.¹³ The translocation domains of group A colicins pass through the pore of a second co-localized OM protein, usually OmpF, and subsequently use various components of the Tol system for translocation of their C-terminal killing domain. In contrast, group B colicins require energy for transport and use the TonB system to presumably traverse through the lumen of their cognate TBDT directly. Currently, the molecular details underlying colicin import are poorly understood.

Of the group A proteins, colicins A and E1-E9 target BtuB. Recent work using SDSL-EPR demonstrated that a 76-residue fragment of the colicin E3 receptor-binding domain (ColE3R) shifts the BtuB Ton box equilibrium towards the folded state by approximately 1.3 kcal/mol, opposite to the effect seen when CNCbl binds (Figure 5.1.1*d*).¹⁴ This effect was not attributed to the competitive binding of CNCbl and ColE3R for BtuB, since ColE3R was able to shift the Ton box equilibrium towards the folded state in the absence of CNCbl. Furthermore, ColE3R retained its ability to shift the conformational equilibrium in the presence of transport-defective Ton box mutations and the reconstitution of BtuB into POPC/octyl-glucoside mixed micelles, perturbations which are known to unfold the Ton box. Stabilization of the folded Ton box conformation by ColE3R is thought to prevent interactions between BtuB and TonB, since colicin E3 translocation requires interactions with components of the Tol system.

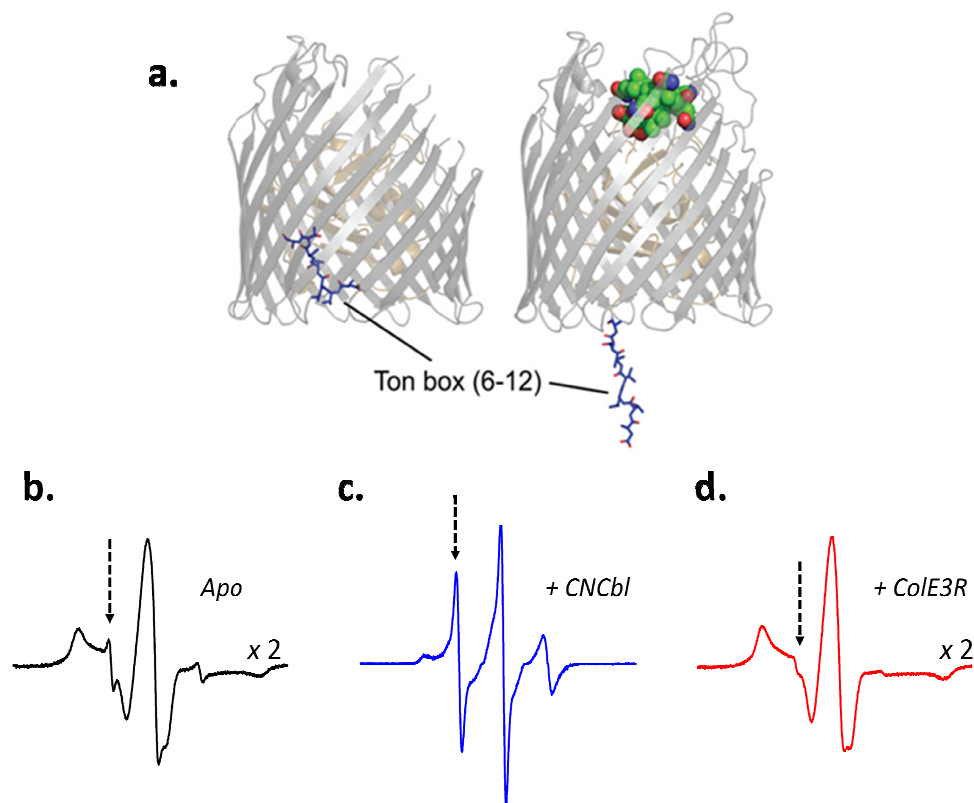


Figure 5.1.1. Modulation of the BtuB Ton box Equilibrium by Competing Substrates. (a and b) SDSL-EPR data from the spin-labeled BtuB V10R1 mutant indicates that the Ton box is in equilibrium between folded and unfolded states. The EPR spectra are linear combinations of signals arising from spin labels on the unfolded (narrow, isotropic lineshape) and folded (broad, anisotropic lineshape) forms of the Ton box, according to the proportion of each substate that is populated. The signal arising from the unfolded Ton box in (b-d) is marked with an arrow. (c) Binding of CNCbl shifts the equilibrium towards the unfolded state, whereas (d) binding of CoIE3R shifts the equilibrium towards the folded state of the Ton box. Spectra in (b) and (d) are scaled by a factor of two.

It is not known how these two ligands bind competitively to the extracellular face of BtuB, yet transduce opposite signals across the OM to the Ton box. Five of the thirteen BtuB residues that bind CNCbl also bind CoIE3R, however, there are 24 additional BtuB residues that bind CoIE3R exclusively.¹⁵ Because of the partial overlap in binding sites, transmembrane modulation of the Ton box equilibrium by CoIE3R and CNCbl may involve the same network of residues, subsets of similar residues, or

completely different signaling pathways. In the following work, a two-mutant cycle is combined with SDSL-EPR to determine the energetic contribution that the R14/D316 ion pair might make to the refolding of the Ton box by ColE3R.

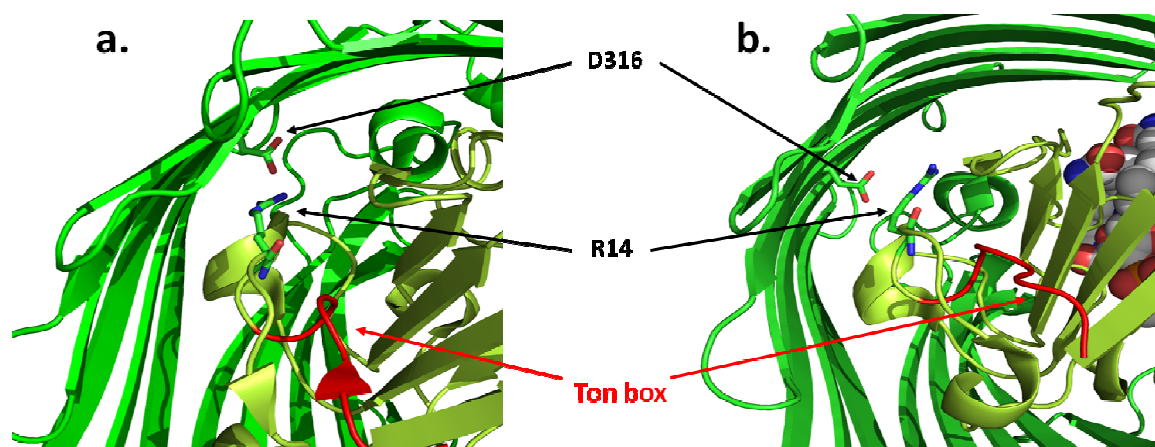


Figure 5.1.2. BtuB Ion Pair. (a) Residues R14 and D316 are closely interacting, apparently electrostatically. (b) When substrate binds BtuB, the R14 rotamer disengages from the interaction, increasing the distance between these residues by about 3.2 Å.¹⁰

5.2 Results

Two-mutant cycles can be used to study experimentally the pairwise interaction energy between two amino acid residues.^{16,17} Previously, a two-mutant cycle was combined with SDSL-EPR to investigate the role of the R14/D316 ion pair in mediating the unfolding of the Ton box in BtuB.⁹ Those results indicated that R14 and D316 are coupled by ~1.8 kcal/mol, that substrate binding largely eliminates this interaction, and that mutation of one or both of these residues to alanine unfolds the Ton box. Here, the

energetic contribution that these residues might make to refolding the Ton box by ColeE3R was examined.

BtuB was spin-labeled at position 10, because the spectra from V10R1 are particularly well-resolved with respect to the unfolded and folded forms of the Ton box.⁶ The signal arising from the folded Ton box is very broad and arises from strong immobilization of V10R1 through tertiary contacts with residues within the BtuB β -barrel,¹¹ whereas the signal from the unfolded Ton box is distinctly narrow and representative of complete motional averaging of the magnetic anisotropy. Since the lineshapes from the two states of the Ton box are drastically different, the fractions of Ton box in the folded and unfolded configurations may be easily estimated from the V10R1 spectrum.

Figure 5.2.1 shows EPR spectra from BtuB V10R1 without (gray spectra) and with (black spectra) saturating amounts of ColeE3R in the presence of single or double alanine mutations to R14 and D316. Clearly the mutations unfold the Ton box, as can be qualitatively assessed by comparing the amplitudes of the narrow, motionally averaged components in each spectrum. However, by comparing the spectra with and without ColeE3R, it is apparent that ColeE3R retains its ability to refold the Ton box even when both R14 and D316 are substituted with alanine. This indicates that additional interactions are directly involved in the ColeE3R-mediated refolding of the Ton box outside of any contribution the R14 and D316 side-chains might make.

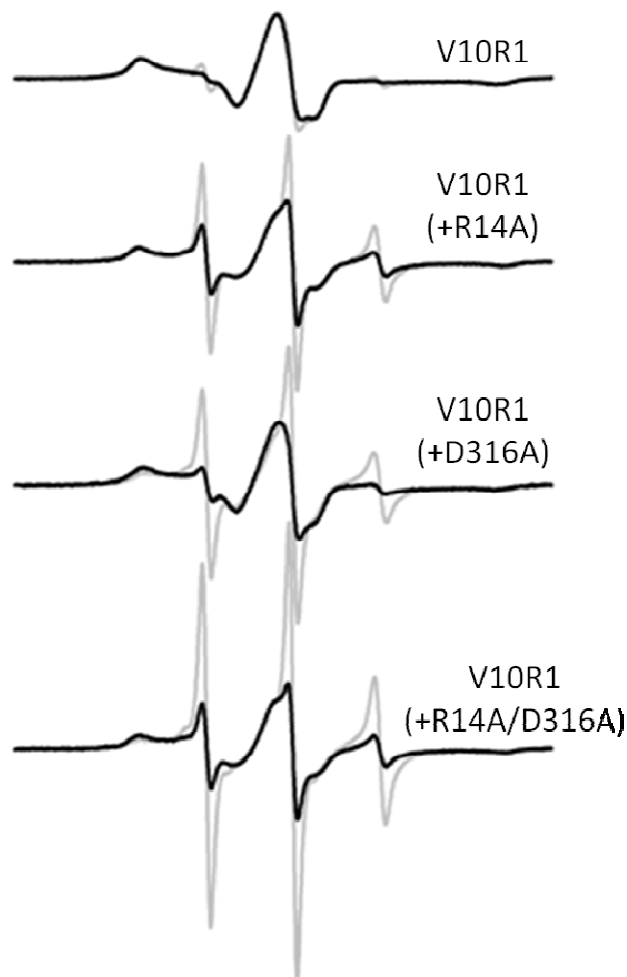


Figure 5.2.1. BtuB V10R1 EPR Spectra with R14/D316 Mutations. Shown are the EPR spectra of BtuB V10R1 with (black) and without (gray) ColE3R in the presence of single and double alanine mutations to R14 and D316. ColE3R is still able to refold the Ton box, even when both R14 and D316 are substituted with alanine.

The effect of these mutations on the Ton box equilibrium can be extracted from the EPR data by spectral subtraction. The relative populations of folded and unfolded Ton box may be estimated by simulating the mobile, isotropic component using Redfield theory¹⁸ and subtracting it from the composite EPR spectrum until the broad, anisotropic

lineshape from the folded Ton box remains. Double integration of the EPR spectrum indicates the contribution that each signal makes to the composite EPR spectrum. From the relative populations of each spectral component, the free energy difference (ΔG°) between Ton box conformational substates may be estimated, and the changes in free energies ($\Delta\Delta G^\circ$) from the alanine mutations around the two-mutant cycle can be determined.

The two-mutant cycle analysis is shown in Fig.5.2.2, along with the $\Delta\Delta G^\circ$ between each mutant. The numbers shown in red and blue were reported previously⁹ and represent the free energy changes for CNCbl-bound and apo BtuB, respectively, for comparison. Shown in green are the free energy changes for ColE3R-liganded BtuB, and as expected, the sum of the energy changes going around the cycle is roughly zero (0.03 kcal/mol). The fact that $\Delta\Delta G^\circ_1 \neq \Delta\Delta G^\circ_3$ and $\Delta\Delta G^\circ_2 \neq \Delta\Delta G^\circ_4$ indicates that there is an interaction energy between these residues, and this energy can be calculated from the sum of the parallel legs of the cycle. The interaction energy between R14 and D316 is about 1.6 kcal/mol regardless of which pair is taken; in other words, R14 and D316 contribute ~1.6 kcal/mol to the Ton box equilibrium in the presence of ColE3R. In the cycles with apo and CNCbl-bound BtuB, the interaction energies are 1.8 kcal/mol and 0.1 kcal/mol, respectively. Collectively, the data indicate that while CNCbl-binding eliminates the interaction between R14 and D316 and shifts the Ton box equilibrium towards the unfolded state,⁹ ColE3R-binding shifts the Ton box equilibrium towards the folded state, but does not substantially affect the interaction energy between these two residues (0.2 kcal/mol difference).

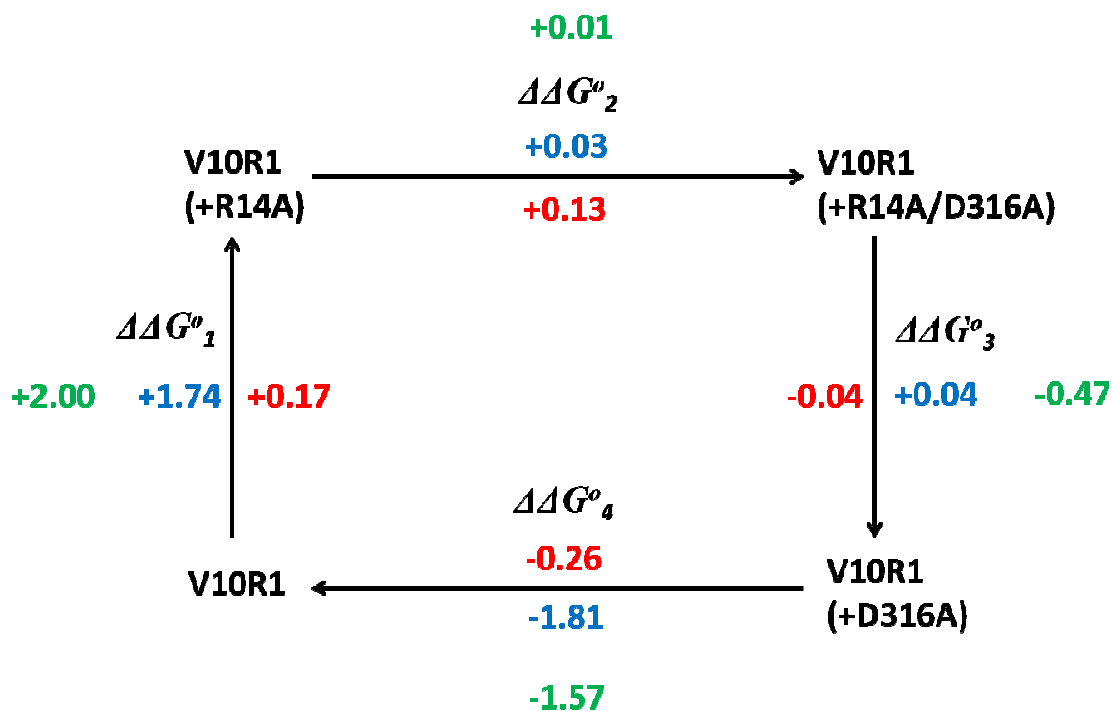


Figure 5.2.2. Two-mutant Thermodynamic Cycle Analysis. Shifts in the ΔG° of the Ton box equilibrium between the two indicated BtuB mutants. Blue numbers represent free energy changes (in kcal/mol) for apo BtuB, red numbers are for CNCbl-bound BtuB, and green numbers are the free energy changes when ColE3R is liganded to BtuB. The signal from the unfolded Ton box was fit using Redfield theory,¹⁸ and spectral subtraction was used to determine the populations of unfolded and folded Ton box.

5.3 Discussion

It has previously been shown⁹ that the pairwise interaction energy between residues R14 and D316 in BtuB is ~ 1.8 kcal/mol, and elimination of this interaction by alanine mutagenesis unfolds the Ton box. The effect of CNCbl binding is similar—the interaction is essentially eliminated,⁹ and the Ton box equilibrium is shifted towards the unfolded state by approximately the same $\Delta\Delta G^\circ$ (~ 1.3 - 2.0 kcal/mol, depending on which

Ton box residue is spin-labeled^{14,19}). Therefore, it appears that this ion pair functions as a CNCbl-dependent switch at the periplasmic terminus of the transmembrane signaling pathway that directly regulates the Ton box equilibrium in BtuB.

In this work, a two-mutant cycle analysis was combined with SDSL-EPR to determine the effect of Cole3R binding on the interaction energy between R14 and D316. It is shown that Cole3R retains its ability to refold the Ton box in the presence of alanine mutations to R14 and/or D316, and the interaction energy between these residues is relatively unchanged by the presence of Cole3R (1.6 kcal/mol). The small difference between the interaction energies measured with and without Cole3R (0.2 kcal/mol) might arise from the difficulty in estimating the small fraction of unfolded Ton box from the Cole3R-liganded BtuB V10R1 spectra. Nonetheless, the measured change in interaction energy is negligible compared to the ~1.3 kcal/mol that Cole3R contributes to refolding the Ton box,¹⁴ and this indicates that Cole3R does not use the R14 and D316 side-chains to modulate the Ton box equilibrium in BtuB. Although the two-mutant cycle cannot be used to deduce the mechanisms of pairwise interactions or how many other components might be involved in a particular pathway, it is clear that CNCbl and Cole3R elicit opposite effects on the BtuB Ton box via transmembrane signaling pathways that include, at least in part, different interactions.

The finding that Cole3R and CNCbl might signal via different pathways is not surprising given the limited amount of overlap in their extracellular binding sites;¹⁵ BtuB residues that exclusively bind each substrate may initiate the propagation of opposing signals. Alternatively, different sets of interactions may be used to fold and unfold the

Ton box. Indeed, a small component representative of folded Ton box is evident in spectra from the double mutation R14A/D316A, indicative of contributions to the Ton box equilibrium from additional interactions outside of those between the R14 and D316 side-chains. Thus, ColE3R may refold the Ton box by increasing the strength of such interactions. Due to the inherent rigidity of β -barrels, it is likely that allostery conveyed long distances through these proteins is facilitated by low-amplitude correlated motions and involves subtle changes to amino acid rotamers or modifications to the hydrogen-bonding network.²⁰ Such changes are difficult to capture and observe structurally, and the findings presented here indicate that SDSL-EPR combined with a two-mutant cycle analysis provides a useful method for identifying amino acid residues that contribute to modulation of the BtuB Ton box equilibrium by substrates.

5.4 Methods

Mutagenesis, Expression, Purification, and Spin-labeling of BtuB Mutants. All mutations in BtuB were introduced into a pAG1 vector using a QuikChange site-directed mutagenesis kit (Stratagene, La Jolla, CA), and the mutations were subsequently verified by nucleotide sequencing. For EPR spectroscopy of BtuB mutants, the expression, purification, spin-labeling, and reconstitution into 1-palmitoyl-2-oleoyl-*sn*-glycero-3-phosphocholine (POPC) lipid bilayers were performed following a procedure detailed previously.^{9,21}

Expression and Purification of ColE3R. A fragment of colicin E9 corresponding to residues 343-418 has been shown to retain receptor binding activity and has an identical amino acid sequence to the receptor binding domain of colicin E3.²² This fragment, herein referred to as ColE3R, was cloned into a pET17b vector containing a C-terminal His₆ tag. For expression, the plasmid DNA encoding ColE3R was transformed into BL21(DE3) competent *E.coli* cells. Transformed cells were cultured at 37°C, induced with 0.25 mM isopropyl β-d-thiogalactoside at OD₆₀₀=0.6-0.7, and grown 3-4 h post-induction. Cells were harvested, lysed, and ColE3R was purified using Ni²⁺ affinity chromatography and concentrated to 10 mM. Cloning, expression, and purification was consistent with procedures described in more detail elsewhere.²³

Preparation of Samples and EPR Spectroscopy. Purified BtuB V10R1, with or without the R14A and/or D316A mutations, was spin-labeled and reconstituted into POPC vesicles for a final BtuB concentration of ~100 μM. Purified ColE3R was added to a final concentration of ~3 mM and the samples were subjected to at least 5 consecutive freeze-thaw cycles to facilitate access of ColE3R to all BtuB receptors. For EPR, 5 μL of sample was loaded into Pyrex capillaries (0.60 mm ID x 0.84 mm OD; Fiber Optic Center, Inc., New Bedford, MA) using a syringe, and X-band EPR spectroscopy was performed at room-temperature (298 K) on a Bruker EMX spectrometer equipped with a dielectric resonator (Bruker Biospin, Billerica, MA). All EPR spectra were recorded with a 100 G magnetic field sweep at 2.0 mW incident power. The phasing and normalization of EPR spectra were performed using LabVIEW provided by C. Altenbach (University of California, Los Angeles, CA). To determine the free

energies and free energy changes between Ton box substates, the population of each Ton box conformation was determined by spectral subtraction and quantification of the spectral components was performed as described in Chapters 5.2 and 3.4, and elsewhere^{11,24}.

5.5 References

1. Shultis, D.D., Purdy, M.D., Banchs, C.N. & Wiener, M.C. Outer membrane active transport: structure of the BtuB:TonB complex. *Science* **312**, 1396-9 (2006).
2. Pawelek, P.D. et al. Structure of TonB in complex with FhuA, E-coli outer membrane receptor. *Science* **312**, 1399-1402 (2006).
3. Cadieux, N., Bradbeer, C. & Kadner, R.J. Sequence changes in the Ton box region of BtuB affect its transport activities and interaction with TonB protein. *Journal of Bacteriology* **182**, 5954-5961 (2000).
4. Cadieux, N. & Kadner, R.J. Site-directed disulfide bonding reveals an interaction site between energy-coupling protein TonB and BtuB, the outer membrane cobalamin transporter. *Proceedings of the National Academy of Sciences of the United States of America* **96**, 10673-8 (1999).
5. Gudmundsdottir, A., Bell, P.E., Lundrigan, M.D., Bradbeer, C. & Kadner, R.J. Point Mutations in a Conserved Region (Tonb Box) of Escherichia-Coli Outer-

- Membrane Protein BtuB Affect Vitamin-B12 Transport. *Journal of Bacteriology* **171**, 6526-6533 (1989).
6. Fanucci, G.E. et al. Substrate-induced conformational changes of the periplasmic N-terminus of an outer-membrane transporter by site-directed spin labeling. *Biochemistry* **42**, 1391-400 (2003).
 7. Merianos, H.J., Cadieux, N., Lin, C.H., Kadner, R.J. & Cafiso, D.S. Substrate-induced exposure of an energy-coupling motif of a membrane transporter. *Nature structural biology* **7**, 205-9 (2000).
 8. Xu, Q., Ellena, J.F., Kim, M. & Cafiso, D.S. Substrate-dependent unfolding of the energy coupling motif of a membrane transport protein determined by double electron-electron resonance. *Biochemistry* **45**, 10847-54 (2006).
 9. Lukasik, S.M., Ho, K.W. & Cafiso, D.S. Molecular basis for substrate-dependent transmembrane signaling in an outer-membrane transporter. *Journal of molecular biology* **370**, 807-11 (2007).
 10. Chimento, D.P., Mohanty, A.K., Kadner, R.J. & Wiener, M.C. Substrate-induced transmembrane signaling in the cobalamin transporter BtuB. *Nature structural biology* **10**, 394-401 (2003).
 11. Freed, D.M., Horanyi, P.S., Wiener, M.C. & Cafiso, D.S. Conformational Exchange in a Membrane Transport Protein Is Altered in Protein Crystals. *Biophysical Journal* **99**, 1604-1610 (2010).
 12. Cascales, E. et al. Colicin biology. *Microbiology and Molecular Biology Reviews* **71**, 158-229 (2007).

13. Lazdunski, C.J. et al. Colicin import into *Escherichia coli* cells. *Journal of Bacteriology* **180**, 4993-5002 (1998).
14. Fanucci, G.E., Cadieux, N., Kadner, R.J. & Cafiso, D.S. Competing ligands stabilize alternate conformations of the energy coupling motif of a TonB-dependent outer membrane transporter. *Proceedings of the National Academy of Sciences of the United States of America* **100**, 11382-7 (2003).
15. Kurisu, G. et al. The structure of BtuB with bound colicin E3 R-domain implies a translocon. *Nature structural biology* **10**, 948-54 (2003).
16. Ackers, G.K. & Smith, F.R. Effects of site-specific amino acid modification on protein interactions and biological function. *Annual review of biochemistry* **54**, 597-629 (1985).
17. Horovitz, A. & Fersht, A.R. Strategy for analysing the co-operativity of intramolecular interactions in peptides and proteins. *Journal of molecular biology* **214**, 613-7 (1990).
18. Stone, T.J., Buckman, T., Nordio, P.L. & McConnell, H.M. Spin-labeled biomolecules. *Proceedings of the National Academy of Sciences of the United States of America* **54**, 1010-7 (1965).
19. Fanucci, G.E., Lee, J.Y. & Cafiso, D.S. Spectroscopic evidence that osmolytes used in crystallization buffers inhibit a conformation change in a membrane protein. *Biochemistry* **42**, 13106-12 (2003).
20. Luan, B.Q., Carr, R., Caffrey, M. & Aksimentiev, A. The effect of calcium on the conformation of cobalamin transporter BtuB. *Proteins-Structure Function and Bioinformatics* **78**, 1153-1162 (2010).

21. Fanucci, G.E., Cadieux, N., Piedmont, C.A., Kadner, R.J. & Cafiso, D.S. Structure and dynamics of the beta-barrel of the membrane transporter BtuB by site-directed spin labeling. *Biochemistry* **41**, 11543-51 (2002).
22. Penfold, C.N. et al. A 76-residue polypeptide of colicin E9 confers receptor specificity and inhibits the growth of vitamin B12-dependent *Escherichia coli* 113/3 cells. *Molecular Microbiology* **38**, 639-49 (2000).
23. Cadieux, N., Phan, P.G., Cafiso, D.S. & Kadner, R.J. Differential substrate-induced signaling through the TonB-dependent transporter BtuB. *Proceedings of the National Academy of Sciences of the United States of America* **100**, 10688-93 (2003).
24. Kim, M., Xu, Q., Fanucci, G.E. & Cafiso, D.S. Solutes modify a conformational transition in a membrane transport protein. *Biophysical journal* **90**, 2922-9 (2006).

CHAPTER 6

Characterization of the Interaction between TonB and the Outer Membrane Transporters that it Energizes

6.1 Introduction

While the outer membrane (OM) of Gram-negative bacteria serves to provide an enhanced permeability barrier against an often inhospitable environment, it must also selectively facilitate the uptake of essential micronutrients into the periplasm. The TonB system circumvents this conundrum through a complex active transport process that involves coupling substrate-specific OM transport proteins to the protonmotive force (PMF) of the cytoplasmic membrane (CM) via the integral CM proteins TonB, ExbD and ExbB. Energy from the PMF is used by ExbD and ExbB to drive conformational changes in ExbD and TonB,¹⁻⁵ the latter of which can span the length of the periplasm due to its rigid polyproline motif⁶ and interact with the OM transporters via its globular C-terminal domain^{7,8} to participate in transport by means of a currently unknown mechanism. In *Escherichia coli*, this TonB-dependent energy transduction between membranes is responsible for the OM transport of vitamin B₁₂ and various forms of chelated iron, and susceptibility to a variety of colicins and bacteriophages that hijack TonB-dependent transport proteins.⁹

The TonB-dependent transporters (TBDTs) in this system are 22-stranded β -barrel membrane proteins with short periplasmic turns and long extracellular loops that participate in substrate recognition and binding at the extracellular face of the OM.¹⁰⁻¹² The transporters also possess an N-terminal pore-occluding globular domain consisting of multiple highly-conserved motifs including the Ton box,¹³ which has been shown to unfold into the periplasm upon substrate binding.¹⁴⁻¹⁷ This substrate-induced shift in conformational equilibrium is presumed to regulate interaction of the TBDTs with TonB.¹⁸⁻²⁰ Consistent with this view, crystal structures of soluble TonB fragments in complex with the *E. coli* vitamin B₁₂ transporter BtuB⁷ or *E. coli* ferrichrome transporter FhuA⁸ indicate that the unfolded Ton box engages in an interprotein β -sheet interaction with the globular C-terminal domain of TonB through a strand exchange mechanism. However, despite the level of sequence conservation, amino acid substitutions to the Ton box do not strongly affect the interaction with TonB; only proline or glycine mutations to residues 8, 9 or 10 in the BtuB Ton box are known to abrogate or greatly reduce transport.²¹ The L8P and V10P mutations have been shown to affect the BtuB Ton box configuration²² and alter the pattern of disulfide cross-linking with TonB *in vivo*.²³ Since proline and glycine are the two amino acids most likely to disrupt local secondary structure, these results indicated that the interaction of TonB with the Ton box is not dependent on specific side-chain interactions, but rather requires a specific orientation for functionality.

In addition to their role in TonB-dependent transport, the TBDTs serve as receptors for colicins, which are protein antibiotics that are both produced by and directed

against certain strains of *E.coli*. Through a mechanism that is currently not well understood, colicins bind to their cognate OM receptor and use either the Ton- or Tol-dependent system to energize translocation of their cytotoxic domains across the OM.²⁴ In many cases a second OM protein, such as OmpF, is recruited to serve as the translocation pore, adding further complexity to the system. Colicins that bind TonB-dependent receptors but use the Tol-dependent system for translocation must select for the presence of TolA over TonB at the periplasmic face of the OM. One such discriminatory mechanism may be shifting the Ton box equilibrium to stabilize the folded conformation, as has been observed for the association of the receptor-binding domain of colicin E3 (ColE3R) and BtuB.²⁵

Despite a wealth of *in vivo*, qualitative *in vitro*, and structural data, relatively little is known quantitatively regarding the interaction between TonB and its cognate OM transporters. Various methods have reported different binding affinities spanning three orders of magnitude (10^{-9} M- 10^{-6} M); furthermore, only in some cases was the affinity modulated by substrate, and the studies also revealed different binding stoichiometries.²⁶⁻
³⁰ One possible source of error may result from the choice of detergent system, which has been shown to affect the energetics of the Ton box equilibrium in BtuB.³¹ Moreover, the breadth of these investigations has also been narrow—in each case involving a single TBDT—and quantitative data for more than one TBDT endogenous to a given organism does not exist. Due to the difficulties in working with full-length TonB, each of these studies utilized a different-sized soluble TonB fragment, which has been shown to affect the oligomerization properties and structure of TonB.^{30,32-35} Although *in vivo* data

suggests that TonB cycles through several conformations,^{2,3,5,36} at least one of which is a dimer,³⁷ the role of this dimer in the transport cycle remains unknown.

In this study fluorescence anisotropy is used to measure the binding affinity of a soluble TonB fragment—lacking only the N-terminal 32 residues constituting the transmembrane domain—for three *E. coli* TBDTs reconstituted into POPC/CHAPS mixed micelles: BtuB, FhuA, and the ferric citrate transporter FecA (Figure 6.1.1). The effects of substrate, transport-defective Ton box mutations and Cole3R on the affinity of the interaction are also determined. From these results an explanation is provided that reconciles the drastic differences in previously reported binding affinities. Furthermore, the structure of TonB is examined in solution using SDSL combined with double electron-electron resonance (DEER), and it is found that the TBDTs affect TonB oligomerization in a manner opposite to what has been previously reported.^{28,29} Finally, from this body of data a transport mechanism is proposed that accounts for the findings. The results presented here have important implications for the design of novel antibiotics that interfere with TonB conformational cycling.

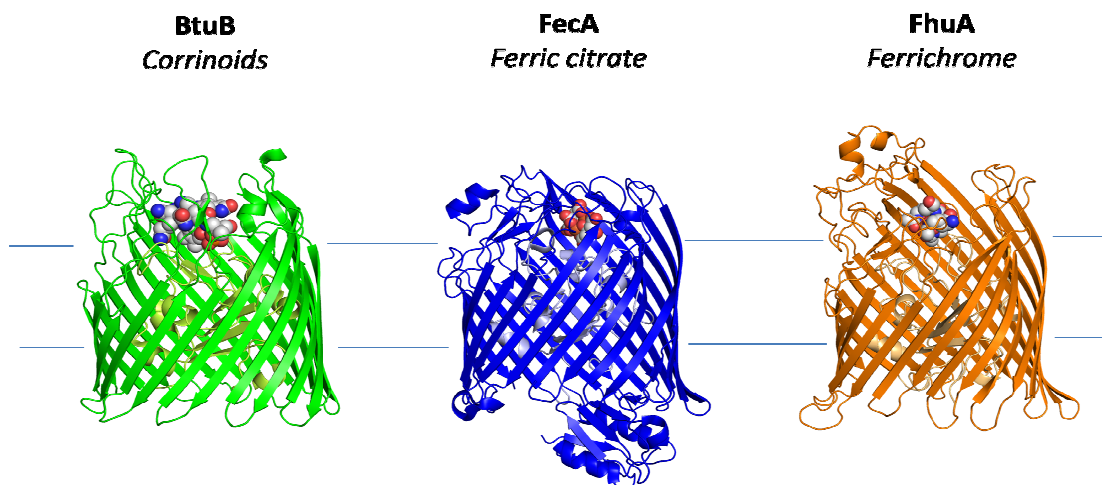


Figure 6.1.1. The TonB-dependent Transporters in this Study. The interaction will be examined between a soluble fragment of TonB and BtuB (1NQH¹²), FecA (1KMP¹⁰), and FhuA (1BY5³⁸). FecA possesses an additional N-terminal globular domain, but no structure of full-length FecA exists. Therefore, in this figure, the structure of full-length FpvA from *Pseudomonas aeruginosa* (2O5P³⁹) containing the N-terminal domain was superimposed on the FecA coordinates, and the N-terminal globular domain from FpvA is shown with the transmembrane domain from FecA.

6.2 Results

In this work, the interaction between three TBDTs and a soluble TonB fragment consisting of residues 33-239, herein referred to as TonB_{ΔTMD}, was examined using fluorescence anisotropy and SDSL-EPR. To determine the affinities of TonB_{ΔTMD} for the three TBDTs and how the interaction is modulated by various scenarios, the TonB_{ΔTMD} L194C mutant was generated for labeling with a BODIPY FL fluorescent probe. In each of the published TonB structures, this residue is at a solvent-exposed site in the TonB C-terminal domain. For each measurement, the TonB_{ΔTMD} concentration (23 nM) was held

constant while the TBDT was titrated in, and the anisotropy values were recorded until saturation was reached. The data were fit to hyperbolic binding equations, and required a Hill coefficient for a good fit in each case (see Methods). For the binding measurements, the TBDTs were reconstituted into 20:1 CHAPS:POPC mixed micelles for two reasons: first, in mixed micelles there is no directionality problem, which allows for easy access of TonB to the TBDTs. Second, whereas some detergent systems affect Ton box energetics, the CHAPS:POPC mixed micelle system does not affect the Ton box equilibrium compared to what is measured in lipid bilayers (DS Cafiso, unpublished data).

Two Modes of Binding to BtuB and FhuA Indicate TonB Conformational Heterogeneity

The results from the BtuB and FhuA titrations are shown in Fig.6.2.1. It is obvious that for each TBDT, there are two modes of TonB $_{\Delta\text{TMD}}$ binding—a high-affinity interaction ($K_D \approx 50$ nM and 70 nM for BtuB and FhuA, respectively), and a low-affinity interaction ($K_D \approx 15$ μM). The parameters extracted from fits to the data are shown in Table 6.2.1. Interestingly, the results indicate that TonB $_{\Delta\text{TMD}}$ does not require a substrate-loaded TBDT for high-affinity binding, and the addition of substrate does not significantly increase the strength of either interaction; for both BtuB and FhuA the high-affinity modes become ~ 200 - 300 cal/mol more favorable in the presence of substrate. This result appears to be inconsistent with previously published *in vivo* cross-linking data, which suggests that substrate binding increases the association of TonB with its cognate TBDTs.¹⁸⁻²⁰ This discrepancy might arise, for example, from an unfaithful

reproduction of key components or restraints that occur *in vivo*, or a smaller observed increase in affinity with substrate due to the modification of other interactions.

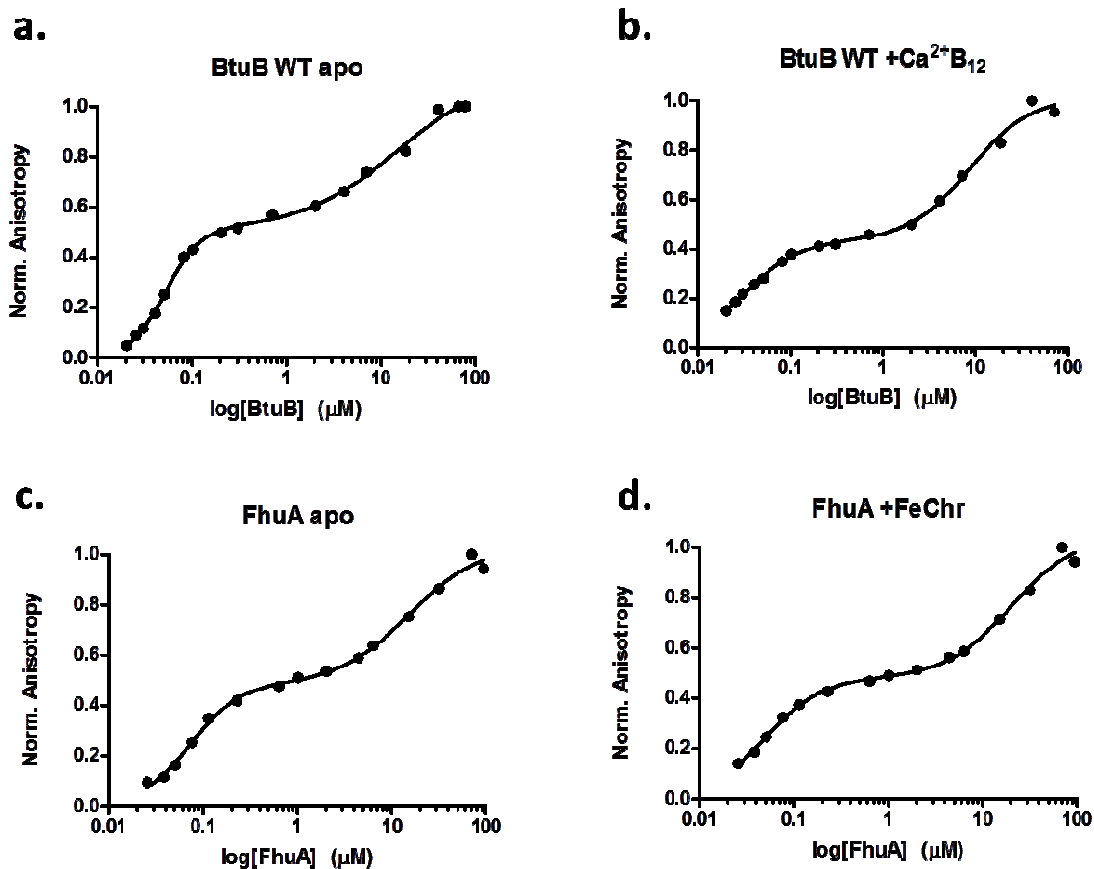


Figure 6.2.1. TonB Binding Data for BtuB and FhuA. Shown are normalized TonB_{ΔTMD} anisotropies (see Methods) as a function of wild-type BtuB (top) or FhuA (bottom) concentration, in the absence (left) and presence (right) of substrate (calcium/vitamin B₁₂ and ferrichrome, respectively). The experimental anisotropies all ranged from ~0.06-0.24. In each case, there are two modes of binding, indicative of TonB conformational heterogeneity. The parameters from the fits to the data are listed in Table 6.2.1.

Protein Ligand	<u>High-Affinity</u>				<u>Low-Affinity</u>			
	K_D	Std. Error	n	Std. Error	K_D	Std. Error	n	Std. Error
BtuB apo	52.2 nM	2.5 nM	2.4	0.2	15.1 μ M	5.0 μ M	0.86	0.2
BtuB +Ca ²⁺ B ₁₂	31.4 nM	3.2 nM	1.4	0.3	8.7 μ M	1.2 μ M	1.3	0.2
FhuA apo	72.4 nM	7.2 nM	1.6	0.2	15.2 μ M	3.0 μ M	1.2	0.3
FhuA +FeChr	49.0 nM	4.7 nM	1.4	0.2	20.1 μ M	4.1 μ M	1.3	0.3
FecA apo	---	---	---	---	7.5 μ M	1.1 μ M	1.0	0.1
FecA +FeCit	---	---	---	---	9.8 μ M	1.1 μ M	1.0	0.1
BtuB L8P apo	---	---	---	---	11.3 μ M	2.0 μ M	1.1	0.2
BtuB L8P +Ca ²⁺ B ₁₂	---	---	---	---	6.3 μ M	1.9 μ M	0.90	0.2
BtuB V10P apo	---	---	---	---	17.7 μ M	8.6 μ M	0.67	0.1
BtuB V10P +Ca ²⁺ B ₁₂	---	---	---	---	17.7 μ M	2.8 μ M	0.68	0.0
BtuB +ColE3R	---	---	---	---	1.5 μ M	0.23 μ M	1.1	0.2

Table 6.2.1. Parameters from TonB Binding Data. Shown are the affinities (as the dissociation constant, K_D) between TonB _{Δ TMD} and the TBDTs under the listed conditions, the standard errors of these affinities, the Hill coefficients used to obtain a good fit, and the standard errors in the Hill coefficients.

In principle, fluorescence anisotropy would not be capable of identifying multiple binding sites on TonB _{Δ TMD}, since its rotational diffusion would already be extremely slow upon initial association with the TBDT in the mixed micelle (the molecular mass of the TBDT:TonB _{Δ TMD} complex alone is \sim 100 kDa). Similarly, the data do not support multiple binding sites on BtuB and FhuA, since in this scenario titration of the TBDTs would result in consistent association of TonB _{Δ TMD} with the high-affinity site. Thus, the data must be accounted for by TonB conformational heterogeneity, where the populations giving rise to each affinity are in slow exchange on the experimental timescale (\sim 1-3 hrs).

The FecA N-terminal Signaling Domain Interferes with High-Affinity TonB Binding

FecA possesses an additional globular signaling domain N-terminal to the Ton box (residues 1-79). In the presence of ferric citrate, this domain relays transporter occupancy to the cytoplasmic membrane protein FecR, which then activates the cytoplasmic σ -factor FecI, thereby upregulating transcription of the ferric citrate import operon.^{40,41} The presence of this N-terminal globular domain is the only significant structural difference compared to FhuA and BtuB; therefore, titrations were performed with FecA to determine any contribution the N-terminal domain might have to the affinity with TonB $_{\Delta TMD}$.

The results from the FecA titrations are given in Fig.6.2.2 and Table 6.2.1. In contrast to BtuB and FhuA, TonB $_{\Delta TMD}$ is only able to bind FecA with an affinity in the low micromolar range (Table 6.2.1). Although there is only one resolvable affinity, the maximum anisotropy values were similar to those for BtuB and FhuA (~0.24), indicating that complete saturation of TonB $_{\Delta TMD}$ was reached. Similar to BtuB and FhuA, the addition of substrate does not modulate the affinity of TonB $_{\Delta TMD}$ for FecA. Thus, it appears that this domain interferes with high-affinity binding of TonB, and although the FecA Ton box undergoes a substrate-dependent order-to-disorder transition,¹⁴ substrate binding does not alleviate this inhibition.

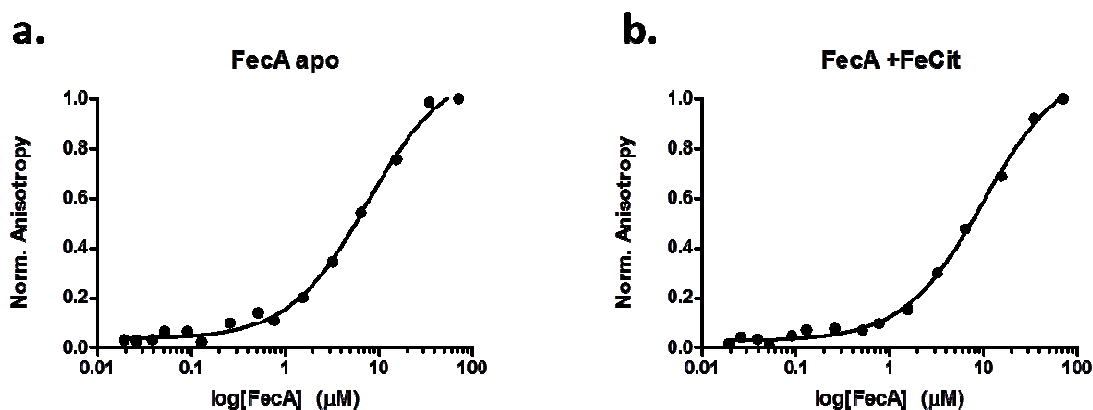


Figure 6.2.2. TonB Binding Data for FecA. Shown are normalized TonB_{ΔTMD} anisotropies (see Methods) as a function of FecA concentration, in the absence (a) and presence (b) of ferric citrate. The experimental anisotropies all ranged from ~0.06-0.24, indicating that although there is only one resolvable mode of TonB binding, all TonB is bound. The parameters from the fits to the data are listed in Table 6.2.1.

Transport-Defective Mutations in the BtuB Ton Box Interfere with High-Affinity TonB Binding

Somewhat paradoxically, transport-defective mutations unfold the BtuB Ton box²² and do not abrogate the interaction with TonB.²³ Instead, these substitutions appear to deleteriously alter a delicate and specific binding geometry between BtuB and TonB.²³ Therefore, the L8P and V10P transport-defective mutations were engineered into the BtuB Ton box to examine the effect of these substitutions on the TonB:TB_{DT} interaction. The results from these titrations are given in Fig.6.2.3 and Table 6.2.1. The results are strikingly similar to those from FecA; total saturation of TonB was reached, but both the L8P and V10P mutations interfere with the high-affinity binding mode, shifting the

affinity of this interaction into the same range as the low-affinity-binding $\text{TonB}_{\Delta\text{TMD}}$ population. Consistent with the above results, substrate does not affect the affinity of the interaction between $\text{TonB}_{\Delta\text{TMD}}$ and the transport-defective BtuB mutants.

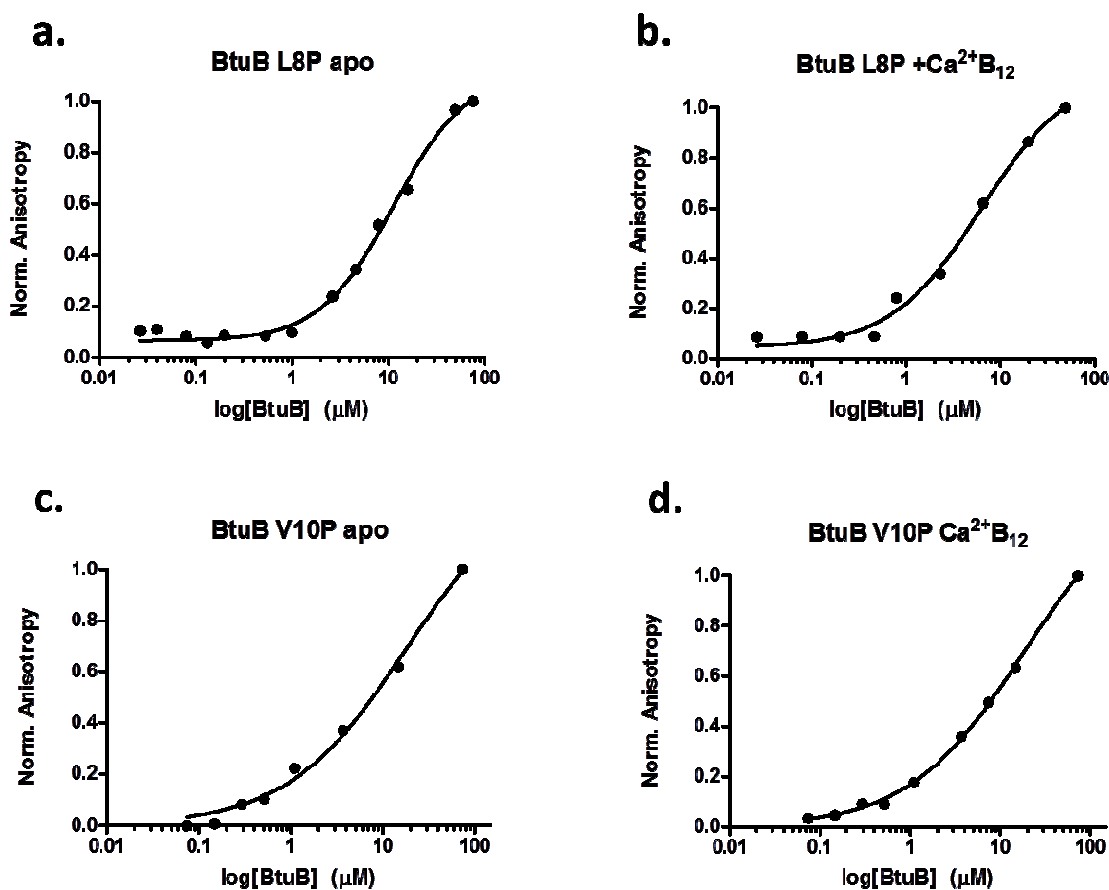


Figure 6.2.3. TonB Binding Data for BtuB L8P and V10P. Shown are normalized $\text{TonB}_{\Delta\text{TMD}}$ anisotropies (see Methods) as a function of BtuB L8P (top) or BtuB V10P (bottom) concentration, in the absence (left) and presence (right) of calcium/vitamin B_{12} . The experimental anisotropies all ranged from ~ 0.06 - 0.24 , indicating that although there is only one resolvable mode of TonB binding, all TonB is bound. The parameters from the fits to the data are listed in Table 6.2.1.

Colicin E3R Perturbs the High-Affinity Association of TonB with BtuB

The receptor-binding domain of colicin E3 associates with BtuB and refolds the Ton box.²⁵ If key components or restraints are indeed missing in the model system used here, then the addition of ColE3R might also be expected to have little effect on the affinity. To examine the effect of ColE3R on the affinity of the TonB_{ΔTMD}:BtuB interaction, BtuB was saturated with ColE3R as it was titrated into BODIPY FL-labeled TonB_{ΔTMD}. As expected, no interaction was detected between ColE3R and TonB_{ΔTMD} (data not shown). However, data from the BtuB titration in the presence of ColE3R could be fit with a monophasic hyperbolic binding equation yielding a single $K_D = 1.5 \mu\text{M}$, indicating that ColE3R-binding reduces the strength of the high-affinity interaction between BtuB and TonB_{ΔTMD} by ~ 2 kcal/mol (Figure 6.2.4, Table 6.2.1). Thus, CNCbl binding unfolds the Ton box but does not significantly increase the affinity (-0.2 kcal/mol), while ColE3R binding refolds the Ton box and significantly decreases the affinity ($+2$ kcal/mol). Since it appears that ColE3R uses different interactions to refold the Ton box (see Chapter 5), a different Ton box conformation might be stabilized by ColE3R that is less amenable to TonB_{ΔTMD} binding, in addition to the shift in equilibrium towards the folded state.

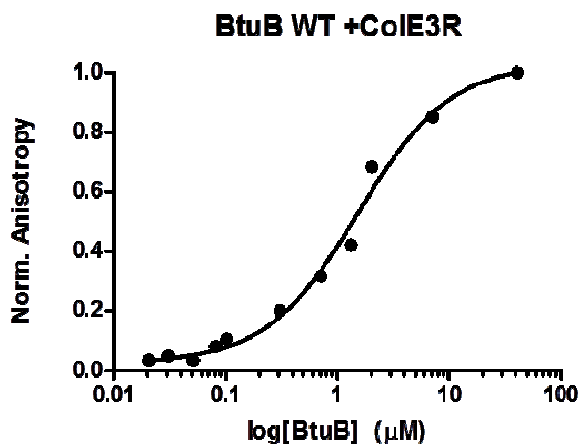


Figure 6.2.4. TonB Binding Data for ColE3R-liganded BtuB. Shown are normalized $\text{TonB}_{\Delta\text{TMD}}$ anisotropies (see Methods) as a function of wild-type BtuB concentration, in the presence of ColE3R. The experimental anisotropies all ranged from ~ 0.06 - 0.24 , indicating that although there is only one resolvable mode of TonB binding, all TonB is bound. The parameters from the fits to the data are listed in Table 6.2.1.

Structural Basis of the High-Affinity TonB:Transporter Interaction

The published structures of the TonB C-terminal domain exhibit construct-dependent conformational differences. High-resolution structures of soluble TonB fragments longer than residue ~ 155 are monomeric in solution and structurally similar, even when bound to TBDTs (Figure 6.2.5).^{7,8,32,34} However, structures of TonB fragments shorter than residue ~ 155 are intertwined, strand-exchanged dimers.^{33,35} The fluorescence anisotropy data is indicative of $\text{TonB}_{\Delta\text{TMD}}$ conformational heterogeneity, and a previous study indicated that the same TonB construct exists in dimer-monomer equilibrium.⁴² Therefore, DEER spectroscopy was used to examine the oligomerization properties and structure of $\text{TonB}_{\Delta\text{TMD}}$ in solution and bound to the TBDTs.

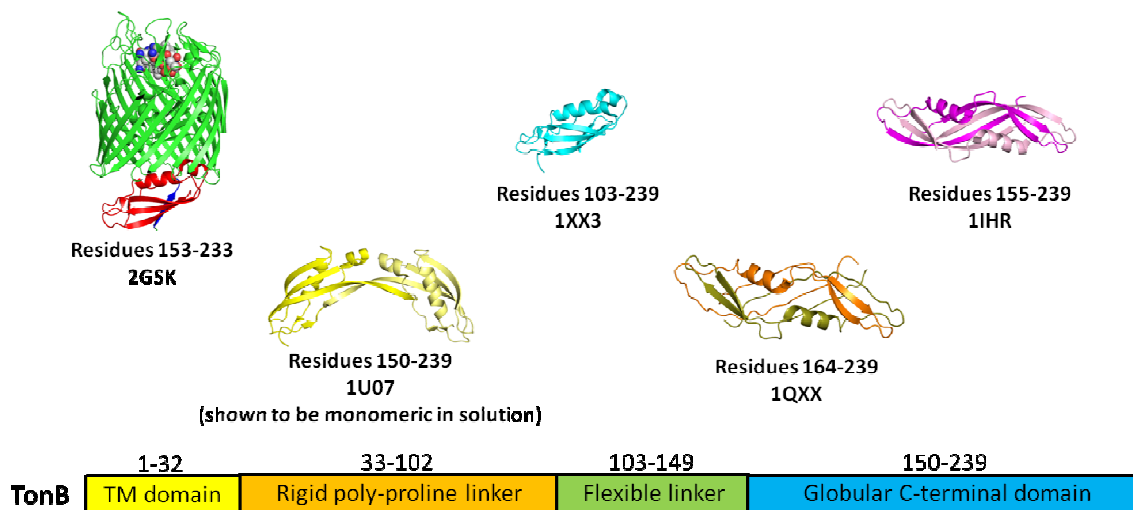


Figure 6.2.5. TonB Construct-Dependent Structural Plasticity. Structures of the TonB C-terminal domain differ in their oligomerization properties and overall structure depending on construct length. Structures longer than residue ~155 are all monomeric in solution, whereas structures shorter than residue ~155 are intertwined dimers. The captions below the structures indicate the construct length and PDB identification number.

The DEER experiment perturbs the interaction between dipolar-coupled spin labels in order to extract useful distance information.⁴³ If the nitroxide moieties of two spin labels are close enough to be dipolar-coupled ($d_{R1-R1} < 60-80 \text{ \AA}$), then the DEER signal will reveal a characteristic cosine-like modulation. In essence, the depth of the modulation depends on the number of dipolar-coupled spins, and the shape of the modulation gives information on interspin distances and their distribution about the average value.⁴⁴ Thus, if a spin label is placed on the TonB $_{\Delta\text{TMD}}$ C-terminal domain, then TonB $_{\Delta\text{TMD}}$ dimers will reveal a modulation depth and useful structural information can be discerned; however, TonB $_{\Delta\text{TMD}}$ monomers will not yield a modulation depth.

Three positions on the TonB $_{\Delta\text{TMD}}$ C-terminal domain were chosen for spin-labeling based on the relative differences in C α -C α distances amongst published TonB structures: 187, 194, and 203. These mutants were spin-labeled and purified into the same buffer system used for the binding measurements, and the DEER data is shown in Fig.6.2.6. It is clear from the modulation depths of each TonB $_{\Delta\text{TMD}}$ mutant (Figure 6.2.6*a,c,e*; black traces) that at least one conformational population of TonB $_{\Delta\text{TMD}}$ exists as a dimer in solution. There are minor contributions to the DEER data from another interspin distance, although it is unclear whether this is representative of sparsely-populated trimers, a small group of structurally different TonB $_{\Delta\text{TMD}}$ dimers, or an artifact from an imperfect fit to the data. Conceivably, this signal might arise from the second conformational population of TonB $_{\Delta\text{TMD}}$; while the relative contribution of this component to the DEER signal is small compared to the roughly equivalent contributions made to the overall change in fluorescence anisotropy, the equilibrium distribution may be shifted by the higher sample concentrations used for EPR. For clarity however, distances from the population contributing the majority of the signal will be discussed here.

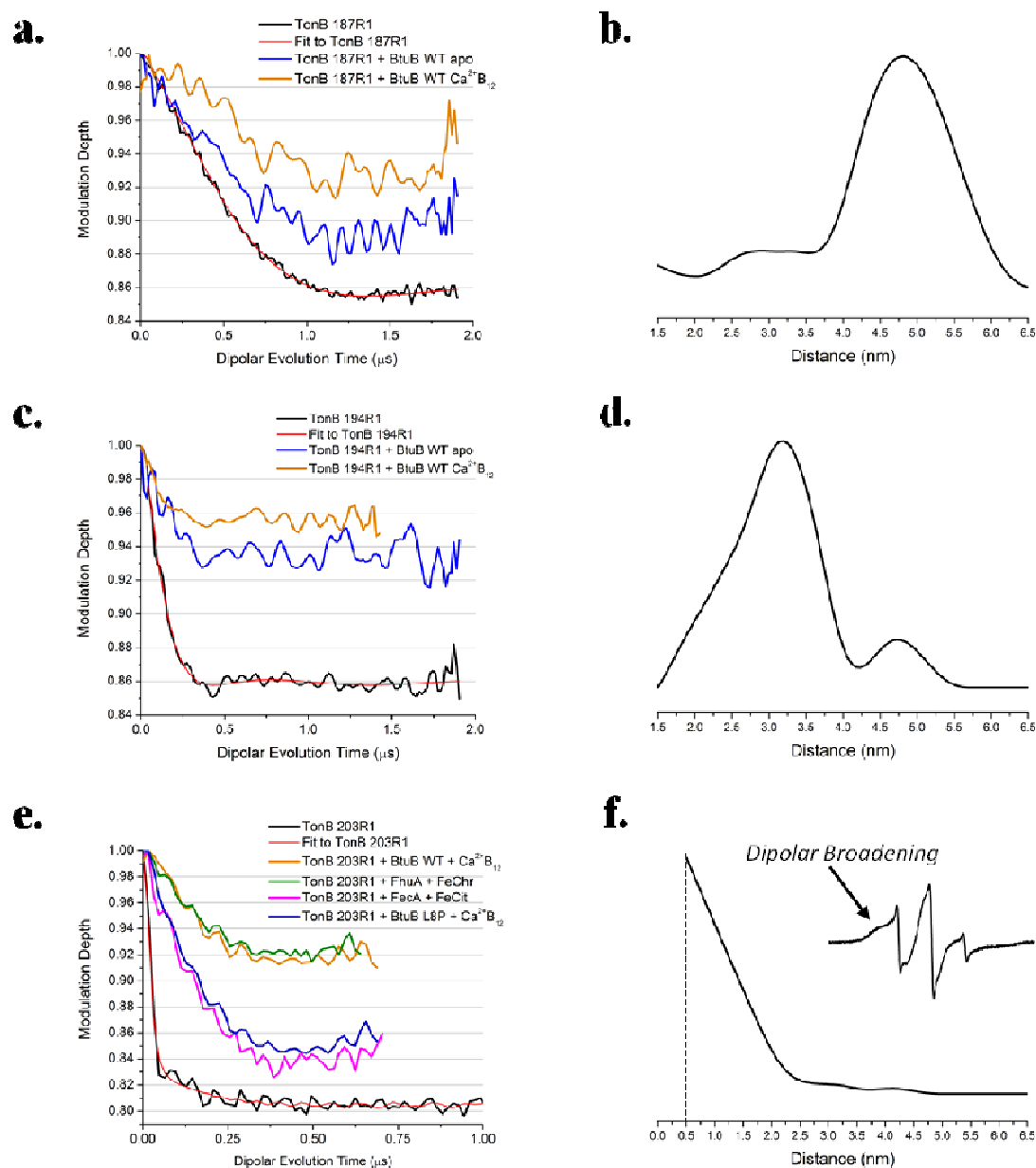


Figure 6.2.6. TonB DEER data. TonB was spin-labeled at three different locations on the C-terminal domain and distances were obtained from the DEER experiment. Shown in the left panel are the time-domain DEER signals for TonB alone and with stoichiometrically limiting amounts of TBDT, and shown in the right panel are the distances obtained from each TonB mutant alone in solution (black signals and red fits in the left panel), determined from Tikhonov regularization (see Table 6.2.2). Shown are data from (a,b) TonB 187R1, (c,d) TonB 194R1, and (e,f) TonB 203R1. The DEER data indicates that the high-affinity binding TonB conformer is a dimer, and that this dimer dissociates upon binding to the TBDTs. The steep decay in the 203R1 DEER signal and inability of the fitting algorithm to determine a good fit (boundary shown by dotted line) indicates that the interspin distance is very short. Consistent with this, the continuous-wave EPR spectrum of 203R1 (f) contains a very broad component that may be due to dipolar interactions between spin labels that are within ~ 15 Å.

The distances are shown in Table 6.2.2, and these distances are only compatible with the intertwined dimeric structures of TonB.^{33,35} There appears to be dipolar broadening in the continuous-wave EPR spectrum of TonB_{ΔTMD} 203R1 (Figure 6.2.6f, inset), which is also consistent with the intertwined dimeric structure and the distance shorter than ~15 Å measured by DEER (Table 6.2.2). Most importantly, the latter result indicates that the flash-frozen TonB_{ΔTMD} conformation during DEER experiments at 80 K appears to be similar to the room temperature structure. Attempts at modeling dimers from the TonB monomeric structures do not provide compatible solutions with the DEER distances, providing further support for a configuration similar to the intertwined dimer published previously. It should be emphasized that these distances only represent three restraints, and the actual structure of TonB_{ΔTMD} in solution may be somewhat different than the intertwined dimer seen crystallographically.

TonB Residue	DEER R1-R1 Distance; Distribution	Intertwined Dimer Cα-Cα Distance (1IHR)
187	52.4 Å; σ(r)=10.7 Å	46.0 Å
194	30.0 Å; σ(r)=5.5 Å	25.3 Å
203	< ~15 Å	11.5 Å

Table 6.2.2. The TonB DEER Distances Support the Intertwined Dimer. Shown are the nitroxide-nitroxide distances and distance distributions from the most populated signals in the DEER data, compared to the Cα-Cα distances from the strand-exchanged intertwined dimeric structure (1IHR³³). The distances line up quite nicely, supporting the existence of a TonB_{ΔTMD} structure very similar to the intertwined dimer. The DEER data gives the distance between unpaired electrons on the R1 nitroxide moiety, which might not line up precisely with distances measured from the alpha carbon. Nevertheless, the DEER distances do not match any other reported TonB structure—even if dimers are modeled from the monomeric structures.

To determine whether the TonB_{ΔTMD} dimer corresponds to the high- or low-affinity population, and what structural changes might occur upon binding to the TBDTs, the DEER experiments were repeated in the presence of stoichiometrically limiting amounts of transporter (~0.85 molar ratio) in the apo and substrate-loaded states. Unexpectedly, the modulation depth significantly decreased when BtuB was added, and even more so when BtuB was substrate-loaded (Figure 6.2.6*a,c,e*). This decrease was not attributed to the mixed micelles; this environment had no effect on the modulation depth (data not shown). The accurate measurement of distances proved difficult due to the concomitant loss of modulation depth and signal-to-noise; however, the considerable reduction of modulation depth is equally informative, and indicates that the TonB_{ΔTMD} dimer dissociates upon binding to BtuB. A more comprehensive analysis was performed on TonB_{ΔTMD} 203R1. For this mutant, addition of substrate-bound BtuB and FhuA nearly eliminated the modulation depth, however the effect was negligible with substrate-bound FecA or BtuB L8P, two proteins that did not allow high-affinity TonB_{ΔTMD} binding (Figure 6.2.6*e*). These results appear to indicate that the population of TonB_{ΔTMD} that binds the TBDTs with nanomolar affinity is a dimer, and this dimer dissociates upon interaction with the transporters. Previous surface plasmon resonance (SPR) studies have reported the inverse scenario—a 2:1 binding stoichiometry between TonB and FhuA, where two TonB monomers bind successively.^{28,29} However, this interpretation was based on complicated kinetic models that did not account for the inverse possibility, and is moreover an unlikely scenario given the cellularly limiting amount of TonB⁴⁵ and the proposal that dimerization occurs early in the transport cycle.³

6.3 Discussion

In this work, the interaction between TonB_{ΔTMD} and its cognate transporters was examined using fluorescence anisotropy and SDSL-EPR. The results indicate that TonB_{ΔTMD} is conformationally heterogeneous, with populations that bind BtuB and FhuA with affinities in the range of ~50 nM and ~15 μM. It is shown that TonB_{ΔTMD} can bind the apo transporters with high-affinity, and the strength of this interaction is not significantly increased when the transporters are substrate-loaded. In contrast, Cole3R-liganded BtuB significantly decreases the affinity of the interaction, with one apparent affinity in the micromolar range. The latter result was also observed for FecA and BtuB variants with transport-defective mutations in the Ton box. This data suggests that substrate is not required for nanomolar-affinity TonB binding, but the ability to form a geometrically specific interaction with the Ton box is. Structural characterization of TonB_{ΔTMD} using DEER spectroscopy indicates that the TonB_{ΔTMD} population that binds the TBDTs with high-affinity appears to be similar to the previously published intertwined dimeric structures, and this dimer dissociates upon interaction with the TBDTs.

A number of *in vivo*¹⁸⁻²⁰ and *in vitro*¹⁴⁻¹⁷ studies support a model where the interaction between TonB and its cognate transporters is regulated by substrate binding; however, the data presented in this work are somewhat incongruent with this model. It is possible that the minor ~0.2-0.3 kcal/mol enhancement in affinity upon substrate addition seen here is enough to increase the disulfide cross-linking between TonB and the TBDTs that is observed *in vivo*. However, it was previously demonstrated using SDSL-EPR that

substrate binding shifts the BtuB Ton box equilibrium by ~ 1.5 - 2.0 kcal/mol.^{16,25} While the measurement of apparently weaker affinities due to ligand depletion can not be ruled out, it is also possible that the affinity of TonB _{Δ TMD} for substrate-loaded transporters measured by fluorescence anisotropy appears weaker experimentally due to the modification of other interactions. For example, the extracellular loops are thought to gate the substrate-binding site in the TBDTs,^{10,46} and it is conceivable that a portion of TonB binding energy is used to help weaken the TBDT:substrate interaction to facilitate the one-way passage of substrate into the periplasm following transport. Moreover, the FhuA Ton box is known to be constitutively unfolded,¹⁴ which further indicates that the interaction between TonB and its transporters might not be as tightly regulated as was originally thought.

There are other indications that interactions with TonB may not be tightly regulated. Various results regarding the substrate-dependent modulation of the TonB:FhuA interaction have been obtained from SPR experiments, although the differences appear to be attributed to the choice of sensor chip.²⁸⁻³⁰ In another study, the *Serratia marcescens* heme transporter HasR was shown *in vitro* to modify interactions with both TonB and the TonB homolog HasB upon substrate binding via entropy-enthalpy compensation, with no net change in affinity.²⁷ Similarly, it is shown here that TonB _{Δ TMD} is able to bind BtuB and FhuA with nanomolar-affinity even in the absence of substrate. Moreover, transport-defective mutations to the BtuB Ton box greatly reduce the affinity of the interaction both in the presence and absence of substrate. These mutations have been shown to unfold the Ton box²² and dramatically affect the pattern of

disulfide cross-linking with TonB *in vivo*.²³ Collectively, these data indicate that the Ton box is crucial for high-affinity binding, but a correct binding geometry appears to be more important than the equilibrium distribution of Ton box substates.

The ColE3R-liganded BtuB and FecA binding data support this conclusion. Since it has been shown that ColE3R uses different interactions to refold the BtuB Ton box compared to those used by CNCbl to unfold the Ton box (see Chapter 5), the significant decrease in affinity seen with ColE3R might arise not merely from refolding the Ton box but from stabilization of a different Ton box geometry. Similarly, only a single micromolar affinity was seen for FecA, which is structurally unique in that it possesses an N-terminal globular signaling domain (Figure 6.1.1). The absence of a high-affinity interaction between FecA and TonB_{ΔTMD} indicates that this domain might sterically interfere with the interaction between TonB_{ΔTMD} and the FecA Ton box. Supporting this view, titrations with FpvA—a *Pseudomonas aeruginosa* FecA ortholog that also contains an N-terminal signaling domain—have demonstrated that TonB binds with an affinity in the low micromolar range that is independent of substrate.²⁶ Moreover, NMR chemical shift perturbation experiments⁴⁷ have indicated that the FecA N-terminal signaling domain likely interferes with the TonB:Ton box association. It is surprising, however, that this apparent inhibition is not alleviated when FecA is ferric citrate-bound, even though the FecA Ton box has been shown to undergo a substrate-dependent order-to-disorder transition.¹⁴ It is possible that other factors *in vivo*, such as association of the signaling domain with FecR, are required to facilitate high-affinity binding in the presence of substrate. Altogether, the above results provide an explanation for the

dramatic differences (10^{-9}M - 10^{-6}M) in affinities that have been reported between TonB and its cognate transporters;²⁶⁻³⁰ micromolar affinities can be attributed to the inability of TonB to form an ideal binding geometry with the Ton box, which can be a consequence of improper TonB structure or the presence of a TBDT N-terminal signaling domain, for example.

Two modes of binding between TonB and FhuA have previously been observed using SPR.²⁸ Based on results obtained with different TonB constructs, a two-site binding model was proposed that implicated the TonB polyproline region as the high-affinity epitope and suggested that the C-terminal domain makes the low-affinity interactions. Arguing against this interpretation, it has been shown that deletion of the polyproline segment does not affect TonB-dependent activity *in vivo*.⁴⁸ Here, the presence of two TonB $_{\Delta\text{TMD}}$ binding modes to BtuB and FhuA seen by fluorescence anisotropy rather suggests that TonB $_{\Delta\text{TMD}}$ is structurally heterogeneous, and that interconversion between these conformations requires at least several hours. DEER spectroscopy indicates that at least one of the TonB $_{\Delta\text{TMD}}$ conformations is a dimer, and dimer dissociation may be quite slow, depending on the solution conditions, expression history, fragment size, and the amount of buried surface area.⁴⁹ Furthermore, a previous study using the same expression and similar purification conditions demonstrated that the TonB $_{\Delta\text{TMD}}$ fragment exists as a mixture of dimers and monomers in solution.⁴² The proposition that TonB $_{\Delta\text{TMD}}$ is conformationally heterogeneous is not surprising, given the structural characterization of different TonB conformations,^{7,8,32-35} and indications that

TonB cycles through no less than three conformations *in vivo*,^{2,3,5,36} at least one of which is a PMF-dependent dimer.^{3,37}

There are obvious differences amongst the published TonB structures, and accordingly, the physiological relevance of each conformation has been challenged. Although it is not known whether the low-affinity interaction seen here is physiologically relevant, TonB has been shown to associate with non-receptor β -barrel proteins in the OM,⁵⁰ and the low-affinity mode may reflect interactions of this TonB $_{\Delta TMD}$ conformation with transporter β -barrel residues due to an inability to recognize the Ton box. This conformation might mimic the structure of newly synthesized TonB *in vivo* that has not yet been assembled into a functional complex with ExbB and ExbD, which would prevent unproductive interactions between the TBDTs and unenergized TonB. The DEER data indicate that the high-affinity-binding TonB $_{\Delta TMD}$ population assumes a conformation similar to the intertwined dimeric structures, which have only been observed for TonB fragments shorter than residue ~ 155 .^{33,35} A recent study proposed that this conformation of TonB does not exist *in vivo*.⁵¹ However, this conclusion was based on sparse and somewhat ambiguous disulfide cross-linking data, and positive cross-linking results between residues that are far apart in the crystal structure may represent conformational intermediates *in vivo*. Furthermore, structural homology with *E.coli* proteins that bind the peptidoglycan (PG) layer and subsequent experimental demonstration of PG-binding ability⁵² has lent credibility to the intertwined TonB dimer.

Despite their differences, it is possible that each of the high-resolution TonB structures represent physiologically relevant conformations. These structures can be

binned into two categories: those from TonB constructs longer than residue ~155 are monomeric in solution and structurally similar, even when bound to TBBDTs;^{7,8,32,34} whereas structures from constructs shorter than residue ~155 are intertwined, strand-exchanged dimers (Figure 6.2.5).^{33,35} As mentioned above, TonB cycles through several conformations *in vivo*, at least one of which is a PMF-dependent dimer. It is therefore possible that both conformations determined experimentally occur at different points in the transport cycle, and several lines of reasoning support this notion. In addition to its apparent role in affecting TonB fragment dimerization *in vitro*, the region near residue 155 makes important interactions *in vivo*. ExbD, which is known to drive conformational changes in TonB,³⁶ engages in a PMF-dependent interaction with TonB near residue 150.² Moreover, it has been shown that 9 or 11 residue deletions centered on TonB Q160 were unable to dimerize or associate with the OM *in vivo*, indicating that ExbD may play a role in the assembly of TonB dimers.⁵³ It has been proposed that TonB dimerization likely occurs at an early stage of the transport cycle,³ and the observed PG-binding ability of TonB has led to the “membrane surveillance” model, where the intertwined dimeric conformation of TonB systematically surveys the underside of the PG for TBBDTs.⁵²

The DEER data presented here indicates that a TonB_{ΔTMD} dimer is the high-affinity-binding population, demonstrates that it is structurally similar to the PG-binding intertwined dimer, and shows that the TonB_{ΔTMD} dimer dissociates upon binding to the TBBDTs. It is conceivable that the resulting monomeric form of TonB complexed to the TBBDT with high-affinity might be represented by the structures of monomeric TonB fragments bound to BtuB⁷ and FhuA⁸. Structurally, the monomeric conformation can be

produced from the dimeric conformation by movement of the α -helix about a flexible hinge that connects the α -helix with β -strand 2, “closing” the hinge so that the interaction between the α -helix and β -strand 2 occurs intramolecularly instead of intermolecularly. Computational algorithms predict this region to have significant disorder and flexibility compared to the rest of the C-terminal domain, which may facilitate conformational rearrangements.⁵⁴ The transition would also involve breaking intermolecular hydrogen bonds between β -strands 1,4' and 4,1' in each monomer, which are compensated for by the formation of new intramolecular hydrogen bonds.

Although the TonB transmembrane domain, ExbB, ExbD and PMF are required for transport-relevant TonB conformational cycling *in vivo*,^{3,5} a small amount of detectable TonB-dependent activity has been observed when TonB is overexpressed in *exbB/exbD/tolQ/tolR* mutants.⁵⁵ This result suggests that TonB can occasionally (but not efficiently) achieve the energized conformation in the absence of ExbB and ExbD, or alternatively, it is possible that some TonB molecules are initially synthesized in a transport-competent conformation that is never subsequently achieved without ExbB/ExbD. Therefore, it is possible that energy from the PMF and association with the TBDTs *in vivo* catalyzes cyclic transitions between TonB conformations (i.e. PMF-dependent dimerization and Ton box-dependent monomerization) that are separated by significant activation energy barriers. Likewise, the overexpression of TonB $_{\Delta\text{TMD}}$ in the *E.coli* cytoplasm might yield a fraction of proteins that resemble the newly synthesized conformation, but also a substantial amount of proteins that fold into an “energized”

dimeric conformation, which is stable by virtue of the barrier heights and absence of TBDTs in the cytoplasm.

Collectively, the above data support and build on the “membrane surveillance” model⁵² of TonB conformational cycling and transport (Figure 6.3.1). In this revised model, newly synthesized TonB is secreted to the CM and can interact with β -barrel proteins in the OM, albeit through low-affinity, unproductive interactions that do not involve the Ton box (Figure 6.3.1*a*). Once TonB is assembled into a functional complex (of unknown stoichiometry) with ExbB and ExbD, the PMF is used by ExbD to contact the TonB C-terminal domain near residue 155 and assemble it into an intertwined dimeric configuration. In this conformation, TonB can associate with the PG and systematically survey its underside for TBDTs (Figure 6.3.1*b*). The PG forms a network of honeycomb-like cells approximately 50 Å in diameter⁵⁶ that directly contacts the OM in various regions.⁵⁷ It is known that at least one TBDT (FepA) can directly associate with the PG, however several TBDTs are known to commonly associate with PG-binding proteins such as OmpF and OmpA.⁵² Therefore, scanning the underside of the PG layer would bestow TonB with an efficient search mechanism. Dimerized TonB might encounter a cluster of TBDTs anchored (directly or indirectly) to the PG, and recognition of a transporter through its extended Ton box facilitates dissociation of the dimer (Figure 6.3.1*c*). This scenario, where the dissociation of two TonB proteins traveling together permits concomitant interactions with two TBDTs, would be more efficient than the proposed model in which two TonB proteins bind one TBDT.²⁹ In the final step, dissolution of the TonB dimer allows for PMF-dependent ExbB/ExbD action that

initiates, via TonB, the conformational rearrangements in the TBDT luminal domain that permit substrate passage into the periplasm. Following transport, TonB is reassembled into a dimerized configuration.

The data presented here provide more comprehensive and quantitative knowledge regarding the interaction between TonB and its cognate transporters. The results support the general notion that TonB is conformationally heterogeneous, and lend potential credibility to both the intertwined dimeric and monomeric structures determined previously. The high-affinity association of TonB with its cognate transporters is highly orientation-specific, and the design of synthetic TBDT ligands that stabilize alternate Ton box geometries (similar to the effect that ColE3R might have) could function effectively as novel antibiotics. Alternative strategies could involve the design of molecules that interfere with TonB conformational cycling by, for example, targeting the PMF-dependent ExbD:TonB interaction or stabilizing the intertwined TonB dimer.

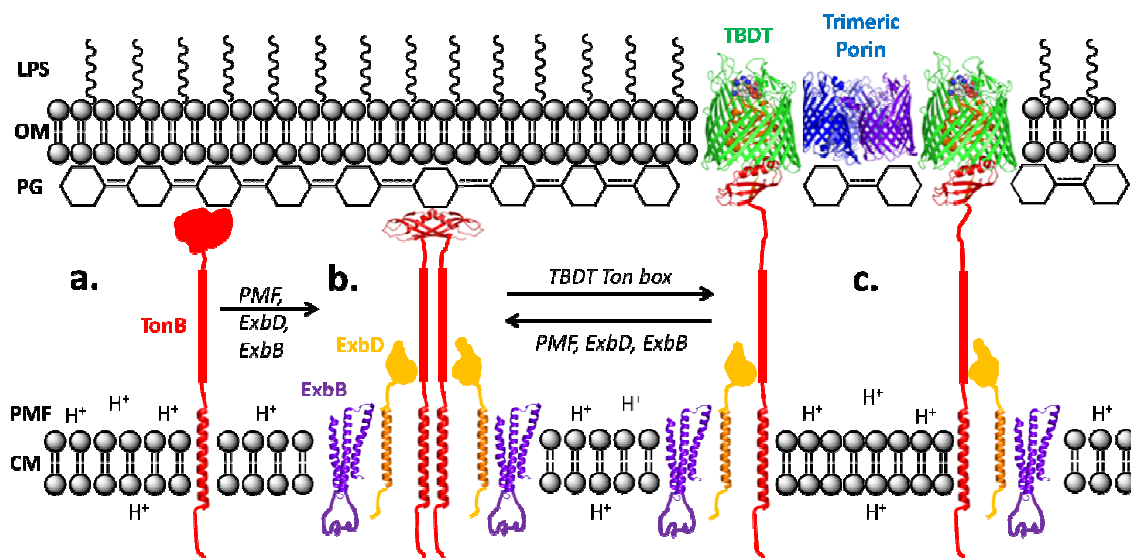


Figure 6.3.1. Proposed Revisions to the “Membrane Surveillance” Model. In this model, (a) newly synthesized TonB that has not yet associated with ExbB and ExbD can interact with the TBDTs, but through low-affinity interactions likely made with residues on the β -barrel. (b) Once TonB associates with ExbB and ExbD in a functional complex, ExbD engages in a PMF-dependent interaction with the C-terminal domain of TonB and assembles two monomers into an intertwined dimer (PDB ID 1IHR³³). In this configuration, TonB can bind the PG and systematically survey its underside for TBDTs. It is known that at least one TBDT can directly associate with the PG, but several TBDTs are known to associate with proteins that directly bind the PG, such as the trimeric porin OmpF. (c) Once TonB finds one or more TBDTs via their extended Ton box, the intertwined dimer dissociates prior to high-affinity binding (PDB ID 2GSK⁷), and this dissociation allows ExbB/ExbD/TonB to potentiate PMF-dependent conformational changes in the TBDT luminal domain to permit passage of substrate into the periplasm. Following transport, TonB is reassembled into the intertwined dimeric conformation. The transmembrane domains of TonB, ExbB, and ExbD are simply models and do not represent a known structure for these proteins.

6.4 Methods

Cloning and Mutagenesis. The DNA fragment corresponding to TonB residues 33-239 (TonB_{ΔTMD}) was PCR-amplified with primers designed to incorporate 5' *NcoI* and 3' *XhoI* sites for cloning the amplified product into pHIS-parallel1,⁵⁸ which is a pET-22b derivative containing an N-terminal His₆ tag followed by a TEV restriction site. The PCR product was digested, ligated into a pHIS-parallel1 vector that had been digested

with the same enzymes, and sequenced to verify proper insertion. All mutations were introduced into TonB and BtuB plasmid DNA using the QuickChange site-directed mutagenesis kit (Stratagene, La Jolla, CA), and subsequently verified by nucleotide sequencing. The Colicin E3R construct was prepared as described previously.⁵⁹

Protein Expression and Purification. The plasmid encoding TonB $_{\Delta TMD}$ was transformed into T7 Express lysY/I^q competent cells (New England Biolabs, Ipswich, MA), and 1 L of 2xYT media containing 100mg/L ampicillin was inoculated with 10 ml overnight preculture grown to stationary phase. Cells were cultured at 37°C, induced with 0.5 mM isopropyl β -D-thiogalactopyranoside (IPTG) at OD₆₀₀=0.7 and grown at 20°C for 5-6 hours post-induction. Cells were collected by centrifugation and resuspended in 25 mM Tris, pH 7.5, containing 1mM 4-(2-Aminoethyl) benzenesulfonyl fluoride hydrochloride (AEBSF; Thermo Fisher Scientific, Pittsburgh, PA), 0.5 mM dithiothreitol (DTT; Avantor Performance Materials, Inc., Phillipsburg, NJ), 20 U/ml aprotinin (Calbiochem, Darmstadt, Germany), and 100 μ M leupeptin (Roche Diagnostics, Indianapolis, IN). When possible, each of the following steps were carried out on ice or at 4°C, unless otherwise noted.

Cells were lysed by French pressure disruption, and the cleared supernatant was mixed at 4°C for 30 min. with 10 ml of Ni²⁺-NTA agarose resin that had been equilibrated in 25 mM Tris, pH 7.5, 300 mM NaCl, 20 mM imidazole. TonB $_{\Delta TMD}$ was eluted with 25 mM Tris, pH 7.5, 300 mM NaCl, 250 mM imidazole, and fractions containing protein were collected. In some cases, 1 mM DTT was added and allowed to react at room temperature for 30 min. to reduce disulfide bonds. The His₆ tag was cut

overnight at room temperature with 500U proTEV protease (Promega, Madison, WI) while TonB_{ΔTMD} was dialyzed against 25 mM Tris pH 7.5, 200 mM NaCl. TonB_{ΔTMD} was then buffer exchanged into 25 mM Tris pH 7.5, 100 mM NaCl and loaded onto an equilibrated HiTrap SP HP cation exchange column (GE Healthcare, Piscataway, NJ). TonB_{ΔTMD} was eluted with a gradient of 25 mM Tris pH 7.5, 1 M NaCl. Fractions containing pure TonB_{ΔTMD} were identified using SDS-PAGE, and similar to what has previously been reported,⁴² TonB_{ΔTMD} migrated to a higher apparent molecular weight (~33 kDa) on SDS-PAGE gels, presumably due to its rigid polyproline motif. The protein was buffer exchanged into 25 mM Tris pH 7.5, 128 mM NaCl and concentrated using an Amicon 3,000 MWCO membrane (Millipore, Billerica, MA).

Expression, purification and reconstitution of BtuB,⁶⁰ and FhuA and FecA,¹⁴ were performed as described previously. Reconstituted proteoliposomes were resuspended in 10 mM HEPES pH 6.5, 128 mM NaCl. After reconstitution, the 1-palmitoyl-2-oleoyl-*sn*-glycero-3-phosphocholine (POPC) concentrations were determined using a standard phosphate assay, and 3-((3-Cholamidopropyl)dimethylammonio)-1-propanesulfonate (CHAPS; Anatrace, Santa Clara, CA) was added in excess to a 20:1 molar ratio for reconstitution into mixed micelles. Although some detergents are known to unfold the BtuB Ton box,³¹ this mixed micelle system does not affect the equilibrium of the Ton box and should also allow easy access of TonB to the transporters for binding studies (DS Cafiso, unpublished data).

Expression and purification of Colicin E3R was performed as described previously,⁵⁹ except that purified ColE3R was buffer exchanged into 10 mM HEPES pH

6.5, 128 mM NaCl. All protein concentrations were measured in triplicate using the amido black assay,⁶¹ and the average concentrations were used for determination of binding affinities. The concentrations determined from amido black correlated well with those measured for the soluble proteins TonB $_{\Delta TMD}$ and ColE3R by absorbance spectroscopy at 280 nm.

Fluorescence Anisotropy and Data Analysis. For fluorescent labeling, purified TonB $_{\Delta TMD}$ L194C was concentrated to ~ 100 μM and reacted with an 8-fold molar excess of tris(2-carboxyethyl)phosphine (TCEP, Thermo Fisher Scientific, Pittsburgh, PA). Following incubation for 30 min. at room temperature, a 10-fold molar excess of BODIPY FL *N*-(2-Aminoethyl)Maleimide (Life Technologies, Grand Island, NY) at 5 mM dissolved in dimethyl sulfoxide and 25mM Tris pH 7.5 was added and allowed to react at room temperature for 2 hours. During labeling the dimethyl sulfoxide concentration was less than 5% (v/v). Excess fluorophore was removed by extensive dialysis in 25 mM Tris pH 7.5, 128 mM NaCl at 4°C. The labeling efficiency was calculated to be $\sim 75\%$ using absorbance spectroscopy and the extinction coefficient of BODIPY FL ($\sim 79,000 \text{ M}^{-1}\text{cm}^{-1}$). Although several different TonB structures alone and in complex with transporters have been reported, in all of these structures residue 194 is solvent-exposed and aimed away from potential tertiary- or membrane-contact sites.

For titrations in a total volume of 150 μl , TonB $_{\Delta TMD}$ was combined with a large excess of 10 mM Hepes pH 6.5, 128 mM NaCl, for a final TonB $_{\Delta TMD}$ concentration of 23 nM. For each titration, approximately 10-15 samples were prepared where various concentrations of BtuB, FhuA, or FecA were added at the expense of Hepes buffer. For

substrate-bound titrations, the substrate was also added at the expense of Hepes buffer. For such BtuB titrations, CaCl_2 , which increases the affinity of BtuB for vitamin B_{12} by a factor of 1000,⁶² was added to 400 μM . Vitamin B_{12} was added to 2 μM in order to minimize inner filter effects until the BtuB concentrations during the titration required larger amounts of substrate for saturation; in these cases a 1.1-fold molar excess was used. To examine the effect of ColE3R on the TonB:BtuB affinity, ColE3R was added to 750 μM . For substrate-bound FhuA titrations, 150 μM Fe^{3+} -ferrichrome was added, and for substrate-bound FecA titrations, 100 μM ferric citrate was added. In all cases, the samples were allowed to equilibrate at room temperature for at least 30 minutes before transfer into 100 μl quartz sample cells for anisotropy measurements. Despite the near transparency of the mixed micelle suspension, at high protein concentrations there were minor increases in the measured anisotropies attributed to scattering due to the small Stoke's shift of BODIPY FL. Great care was taken to verify that neither viscosity nor scattering effects influenced the measured affinities.

Fluorescence anisotropy data were collected on a Fluorolog Modular Spectrofluorometer (Horiba Scientific, Edison, NJ). The excitation and emission wavelengths were 501 nm and 515 nm, respectively, with 3 nm monochromator slit widths and an integration time of 0.1 s or 1 s, depending on the counts per second. Each data point was measured in triplicate, and the average anisotropy was recorded. Data were plotted and analyzed using GraphPad Prism software. For easy viewing, the anisotropies were normalized to the maximum and minimum data points, such that the values plotted on the y-axis would approximately equal the fraction bound. As such,

however, it should be noted that for each titration the TonB anisotropy values were ~0.06-0.07 without transporter and reached a maximum value of ~0.22-0.25 through the titration, indicating complete binding of both TonB conformational populations in each case. In cases of monophasic binding behavior, the data could not be fit to a simple hyperbola and thus were fit to the equation: $= \frac{B_{max} * x^n}{K_D^n + x^n}$. Similarly, in cases of biphasic binding behavior the data were fit to the equation: $= \frac{B_{max1} * x^{n1}}{K_{D1}^{n1} + x^{n1}} + \frac{B_{max2} * x^{n2}}{K_{D2}^{n2} + x^{n2}}$. For the titrations with FecA, BtuB L8P, and wild-type BtuB with ColE3R, an additive background contribution was applied to obtain a better fit: $y = \frac{B_{max} * x^n}{K_D^n + x^n} + Background$. Standard errors were calculated automatically by the software and are reported.

Electron Paramagnetic Resonance and Data Analysis. For spin-labeling, TonB_{ΔTMD} was concentrated to ~150 μM before ion exchange chromatography and reacted with a ten-fold molar excess of S-(2,2,5,5-tetramethyl-2,5-dihydro-1H-pyrrol-3-yl)methyl methanesulfonylthioate (MTSSL; Toronto Research Chemicals Inc., North York, Ontario) at room temperature for 4 hours. Excess label was eliminated during ion exchange chromatography. As mentioned above, in some cases TonB_{ΔTMD} was reacted with 1 mM DTT at room temperature for 30 min. to reduce any disulfide bonds prior to spin-labeling. Continuous-wave EPR spectroscopy was performed on a Bruker EMX spectrometer fitted with an ER4123D dielectric resonator (Bruker Biospin, Billerica, MA). All X-band spectra were taken using 2 mW incident microwave power, 1 G field modulation, and a sweep width of 100 G. Samples were adjusted to approximately 50-

100 μM , and volumes of 5 μL were loaded into capillaries (0.60 mm i.d. x 0.84 mm o.d.; Vitrocom, Mountain Lakes, NJ). Spectra were baseline corrected and normalized using LabVIEW software provided by Christian Altenbach (UCLA).

For pulsed EPR measurements, 25 μL of $\sim 125\text{-}185$ μM TonB $_{\Delta\text{TMD}}$ diluted in 10 mM Hepes pH 6.5, 128 mM NaCl, 25% glycerol was loaded into quartz capillaries (1.5 mm i.d. x 1.8 mm o.d. Vitrocom, Mountain Lakes, NJ). For measurements with transporter, $\sim 100\text{-}150$ μM BtuB, FhuA, or FecA was added at the expense of Hepes buffer for a ~ 0.85 molar ratio with respect to TonB. For samples with substrate, $\sim 350\text{-}550$ μM ferric citrate, Fe $^{3+}$ -ferrichrome, or vitamin B $_{12}$ with 1.5 mM CaCl $_2$ were also added at the expense of Hepes buffer. Samples for double electron-electron resonance (DEER) were flash-frozen in isopropanol cooled with dry ice, and the data were recorded at 80 K on a Bruker Elexsys E580 spectrometer fitted with an ER4118X-MS3 split-ring resonator. Data were acquired using the four-pulse DEER sequence⁴³ with a 16 ns $\pi/2$ and two 32 ns π observe pulses separated by a π pump pulse that was optimized at 28 ns. The dipolar evolution times were typically 0.7-2.0 μs , and were limited by the measured phase memory time of each sample. The pump frequency was set to the center maximum of the nitroxide spectrum, and the observe frequency was set to the low-field maximum. The phase-corrected dipolar evolution data were processed assuming a three-dimensional background and Fourier transformed, and the distance distributions were obtained using Tikhonov regularization with DeerAnalysis2009 software.⁶³

6.5 References

1. Jana, B., Manning, M. & Postle, K. Mutations in the ExbB Cytoplasmic Carboxy Terminus Prevent Energy-Dependent Interaction between the TonB and ExbD Periplasmic Domains. *Journal of Bacteriology* **193**, 5649-5657 (2011).
2. Ollis, A.A., Manning, M., Held, K.G. & Postle, K. Cytoplasmic membrane protonmotive force energizes periplasmic interactions between ExbD and TonB. *Molecular Microbiology* **73**, 466-481 (2009).
3. Ghosh, J. & Postle, K. Disulphide trapping of an in vivo energy-dependent conformation of Escherichia coli TonB protein. *Molecular Microbiology* **55**, 276-288 (2005).
4. Ghosh, J. & Postle, K. Evidence for dynamic clustering of carboxy-terminal aromatic amino acids in TonB-dependent energy transduction. *Molecular Microbiology* **51**, 203-213 (2004).
5. Larsen, R.A., Thomas, M.G. & Postle, K. Protonmotive force, ExbB and ligand-bound FepA drive conformational changes in TonB. *Molecular Microbiology* **31**, 1809-1824 (1999).
6. Kohler, S.D., Weber, A., Howard, S.P., Welte, W. & Drescher, M. The proline-rich domain of TonB possesses an extended polyproline II-like conformation of sufficient length to span the periplasm of Gram-negative bacteria. *Protein Science* **19**, 625-630 (2010).
7. Shultis, D.D., Purdy, M.D., Banchs, C.N. & Wiener, M.C. Outer membrane active transport: structure of the BtuB:TonB complex. *Science* **312**, 1396-9 (2006).

8. Pawelek, P.D. et al. Structure of TonB in complex with FhuA, E-coli outer membrane receptor. *Science* **312**, 1399-1402 (2006).
9. Postle, K. & Kadner, R.J. Touch and go: tying TonB to transport. *Molecular Microbiology* **49**, 869-882 (2003).
10. Ferguson, A.D. et al. Structural basis of gating by the outer membrane transporter FecA. *Science* **295**, 1715-1719 (2002).
11. Ferguson, A.D., Hofmann, E., Coulton, J.W., Diederichs, K. & Welte, W. Siderophore-mediated iron transport: Crystal structure of FhuA with bound lipopolysaccharide. *Science* **282**, 2215-2220 (1998).
12. Chimento, D.P., Mohanty, A.K., Kadner, R.J. & Wiener, M.C. Substrate-induced transmembrane signaling in the cobalamin transporter BtuB. *Nature structural biology* **10**, 394-401 (2003).
13. Chimento, D.P., Kadner, R.J. & Wiener, M.C. Comparative structural analysis of TonB-dependent outer membrane transporters: implications for the transport cycle. *Proteins* **59**, 240-51 (2005).
14. Kim, M., Fanucci, G.E. & Cafiso, D.S. Substrate-dependent transmembrane signaling in TonB-dependent transporters is not conserved. *Proceedings of the National Academy of Sciences of the United States of America* **104**, 11975-80 (2007).
15. Xu, Q., Ellena, J.F., Kim, M. & Cafiso, D.S. Substrate-dependent unfolding of the energy coupling motif of a membrane transport protein determined by double electron-electron resonance. *Biochemistry* **45**, 10847-54 (2006).

16. Fanucci, G.E. et al. Substrate-induced conformational changes of the periplasmic N-terminus of an outer-membrane transporter by site-directed spin labeling. *Biochemistry* **42**, 1391-400 (2003).
17. Merianos, H.J., Cadieux, N., Lin, C.H., Kadner, R.J. & Cafiso, D.S. Substrate-induced exposure of an energy-coupling motif of a membrane transporter. *Nature structural biology* **7**, 205-9 (2000).
18. Cadieux, N. & Kadner, R.J. Site-directed disulfide bonding reveals an interaction site between energy-coupling protein TonB and BtuB, the outer membrane cobalamin transporter. *Proceedings of the National Academy of Sciences of the United States of America* **96**, 10673-8 (1999).
19. Ogierman, M. & Braun, V. Interactions between the outer membrane ferric citrate transporter FecA and TonB: Studies of the FecA TonB box. *Journal of Bacteriology* **185**, 1870-1885 (2003).
20. Moeck, G.S., Coulton, J.W. & Postle, K. Cell envelope signaling in *Escherichia coli*. Ligand binding to the ferrichrome-iron receptor fhua promotes interaction with the energy-transducing protein TonB. *The Journal of biological chemistry* **272**, 28391-7 (1997).
21. Gudmundsdottir, A., Bell, P.E., Lundrigan, M.D., Bradbeer, C. & Kadner, R.J. Point Mutations in a Conserved Region (Tonb Box) of *Escherichia-Coli* Outer-Membrane Protein Btub Affect Vitamin-B12 Transport. *Journal of Bacteriology* **171**, 6526-6533 (1989).

22. Coggshall, K.A., Cadieux, N., Piedmont, C., Kadner, R.J. & Cafiso, D.S. Transport-defective mutations alter the conformation of the energy-coupling motif of an outer membrane transporter. *Biochemistry* **40**, 13964-71 (2001).
23. Cadieux, N., Bradbeer, C. & Kadner, R.J. Sequence changes in the Ton box region of BtuB affect its transport activities and interaction with TonB protein. *Journal of Bacteriology* **182**, 5954-5961 (2000).
24. Cascales, E. et al. Colicin biology. *Microbiology and Molecular Biology Reviews* **71**, 158-229 (2007).
25. Fanucci, G.E., Cadieux, N., Kadner, R.J. & Cafiso, D.S. Competing ligands stabilize alternate conformations of the energy coupling motif of a TonB-dependent outer membrane transporter. *Proceedings of the National Academy of Sciences of the United States of America* **100**, 11382-7 (2003).
26. Adams, H., Zeder-Lutz, G., Schalk, I., Pattus, F. & Celia, H. Interaction of TonB with the outer membrane receptor FpvA of *Pseudomonas aeruginosa*. *Journal of Bacteriology* **188**, 5752-5761 (2006).
27. Lefevre, J., Delepelaire, P., Delepierre, M. & Izadi-Pruneyre, N. Modulation by substrates of the interaction between the HasR outer membrane receptor and its specific TonB-like protein, HasB. *Journal of molecular biology* **378**, 840-851 (2008).
28. Khursigara, C.M., De Crescenzo, G., Pawelek, P.D. & Coulton, J.W. Enhanced binding of TonB to a ligand-loaded outer membrane receptor - Role of the oligomeric state of TonB in formation of a functional FhuA center dot TonB complex. *Journal of Biological Chemistry* **279**, 7405-7412 (2004).

29. Khursigara, C.M., De Crescenzo, G., Pawelek, P.D. & Coulton, J.W. Kinetic analyses reveal multiple steps in forming TonB-FhuA complexes from *Escherichia coli*. *Biochemistry* **44**, 3441-3453 (2005).
30. Khursigara, C.M., De Crescenzo, G., Pawelek, P.D. & Coulton, J.W. Deletion of the proline-rich region of TonB disrupts formation of a 2 : 1 complex with FhuA, an outer membrane receptor of *Escherichia coli*. *Protein Science* **14**, 1266-1273 (2005).
31. Fanucci, G.E., Lee, J.Y. & Cafiso, D.S. Membrane mimetic environments alter the conformation of the outer membrane protein BtuB. *Journal of the American Chemical Society* **125**, 13932-3 (2003).
32. Peacock, R.S., Weljie, A.M., Howard, S.P., Price, F.D. & Vogel, H.J. The solution structure of the C-terminal domain of TonB and interaction studies with TonB box peptides. *Journal of molecular biology* **345**, 1185-1197 (2005).
33. Chang, C.S., Mooser, A., Pluckthun, A. & Wlodawer, A. Crystal structure of the dimeric C-terminal domain of TonB reveals a novel fold. *Journal of Biological Chemistry* **276**, 27535-27540 (2001).
34. Koding, J. et al. Crystal structure of a 92-residue C-terminal fragment of TonB from *Escherichia coli* reveals significant conformational changes compared to structures of smaller TonB fragments. *Journal of Biological Chemistry* **280**, 3022-3028 (2005).
35. Koedding, J. et al. Dimerization of TonB is not essential for its binding to the outer membrane siderophore receptor FhuA of *Escherichia coli*. *Journal of Biological Chemistry* **279**, 9978-9986 (2004).

36. Ollis, A.A. & Postle, K. ExbD Mutants Define Initial Stages in TonB Energization. *Journal of molecular biology* (2011).
37. Sauter, A., Howard, S.P. & Braun, V. In vivo evidence for TonB dimerization. *Journal of Bacteriology* **185**, 5747-5754 (2003).
38. Locher, K.P. et al. Transmembrane signaling across the ligand-gated FhuA receptor: crystal structures of free and ferrichrome-bound states reveal allosteric changes. *Cell* **95**, 771-8 (1998).
39. Brilllet, K. et al. A beta strand lock exchange for signal transduction in TonB-dependent transducers on the basis of a common structural motif. *Structure* **15**, 1383-1391 (2007).
40. Enz, S., Mahren, S., Stroecher, U.H. & Braun, V. Surface signaling in ferric citrate transport gene induction: Interaction of the FecA, FecR, and FecI regulatory proteins. *Journal of Bacteriology* **182**, 637-646 (2000).
41. Welz, D. & Braun, V. Ferric citrate transport of Escherichia coli: Functional regions of the FecR transmembrane regulatory protein. *Journal of Bacteriology* **180**, 2387-2394 (1998).
42. Moeck, G.S. & Letellier, L. Characterization of in vitro interactions between a truncated TonB protein from Escherichia coli and the outer membrane receptors FhuA and FepA. *Journal of Bacteriology* **183**, 2755-2764 (2001).
43. Pannier, M., Veit, S., Godt, A., Jeschke, G. & Spiess, H.W. Dead-time free measurement of dipole-dipole interactions between electron spins. *Journal of magnetic resonance* **142**, 331-340 (2000).

44. Jeschke, G. & Polyhach, Y. Distance measurements on spin-labelled biomacromolecules by pulsed electron paramagnetic resonance. *Physical chemistry chemical physics : PCCP* **9**, 1895-910 (2007).
45. Higgs, P.I., Larsen, R.A. & Postle, K. Quantification of known components of the Escherichia coli TonB energy transduction system: TonB, ExbB, ExbD and FepA. *Molecular Microbiology* **44**, 271-281 (2002).
46. Gumbart, J., Wiener, M.C. & Tajkhorshid, E. Coupling of calcium and substrate binding through loop alignment in the outer-membrane transporter BtuB. *Journal of molecular biology* **393**, 1129-42 (2009).
47. Peacock, R.S. et al. Characterization of TonB interactions with the FepA cork domain and FecA N-terminal signaling domain. *Biometals* **19**, 127-142 (2006).
48. Larsen, R.A., Wood, G.E. & Postle, K. The conserved proline-rich motif is not essential for energy transduction by Escherichia coli TonB protein. *Molecular Microbiology* **10**, 943-53 (1993).
49. Arndt, K.M., Muller, K.M. & Pluckthun, A. Factors influencing the dimer to monomer transition of an antibody single-chain Fv fragment. *Biochemistry* **37**, 12918-26 (1998).
50. Higgs, P.I. et al. TonB interacts with nonreceptor proteins in the outer membrane of Escherichia coli. *Journal of Bacteriology* **184**, 1640-1648 (2002).
51. Postle, K., Kastead, K.A., Gresock, M.G., Ghosh, J. & Swayne, C.D. The TonB Dimeric Crystal Structures Do Not Exist In Vivo. *Mbio* **1**(2010).

52. Kaserer, W.A. et al. Insight from TonB hybrid proteins into the mechanism of iron transport through the outer membrane. *Journal of Bacteriology* **190**, 4001-4016 (2008).
53. Vakharia-Rao, H., Kastead, K.A., Savenkova, M.I., Bulathsinghala, C.M. & Postle, K. Deletion and substitution analysis of the Escherichia coli TonB q160 region. *Journal of Bacteriology* **189**, 4662-4670 (2007).
54. Larsen, R.A. et al. His(20) provides the sole functionally significant side chain in the essential TonB transmembrane domain. *Journal of Bacteriology* **189**, 2825-33 (2007).
55. Fischer, E., Gunter, K. & Braun, V. Involvement of ExbB and TonB in transport across the outer membrane of Escherichia coli: phenotypic complementation of exb mutants by overexpressed tonB and physical stabilization of TonB by ExbB. *Journal of Bacteriology* **171**, 5127-34 (1989).
56. Meroueh, S.O. et al. Three-dimensional structure of the bacterial cell wall peptidoglycan. *Proceedings of the National Academy of Sciences of the United States of America* **103**, 4404-9 (2006).
57. Matias, V.R., Al-Amoudi, A., Dubochet, J. & Beveridge, T.J. Cryo-transmission electron microscopy of frozen-hydrated sections of Escherichia coli and Pseudomonas aeruginosa. *Journal of Bacteriology* **185**, 6112-8 (2003).
58. Sheffield, P., Garrard, S. & Derewenda, Z. Overcoming expression and purification problems of RhoGDI using a family of "parallel" expression vectors. *Protein Expression and Purification* **15**, 34-39 (1999).

59. Cadieux, N., Phan, P.G., Cafiso, D.S. & Kadner, R.J. Differential substrate-induced signaling through the TonB-dependent transporter BtuB. *Proceedings of the National Academy of Sciences of the United States of America* **100**, 10688-93 (2003).
60. Fanucci, G.E., Cadieux, N., Piedmont, C.A., Kadner, R.J. & Cafiso, D.S. Structure and dynamics of the beta-barrel of the membrane transporter BtuB by site-directed spin labeling. *Biochemistry* **41**, 11543-51 (2002).
61. Kaplan, R.S. & Pedersen, P.L. Determination of Microgram Quantities of Protein in the Presence of Milligram Levels of Lipid with Amido Black B-10. *Analytical Biochemistry* **150**, 97-104 (1985).
62. Cadieux, N., Barekzi, N. & Bradbeer, C. Observations on the calcium dependence and reversibility of cobalamin transport across the outer membrane Escherichia coli. *Journal of Biological Chemistry* **282**, 34921-34928 (2007).
63. Jeschke, G. et al. DeerAnalysis2006 - a comprehensive software package for analyzing pulsed ELDOR data. *Applied magnetic resonance* **30**, 473-498 (2006).

CHAPTER 7

Concluding Thoughts and Future Directions

In 1965, Professor Harden McConnell introduced spin labels as unique environmentally-sensitive probes that could be used for biomolecular EPR spectroscopy.¹ The applicability and potential utility of spin-labeling was appreciably magnified in 1989 when Professor Wayne Hubbell described the use of site-directed mutagenesis to facilitate the selective attachment of spin labels to proteins for EPR spectroscopy.^{2,3} Since then, SDSL-EPR has continued to grow and develop into a powerful tool for studying membrane protein structure and dynamics, providing many advantages over more traditionally used techniques such as NMR and X-ray crystallography. The work presented here regarding the use of SDSL-EPR in studying protein structure, interactions and signaling is a testament to that notion. However, in order to reach its maximum potential, we must continue to learn more about spin label behavior, so that we can account for its role and extract useful structural and dynamical data from spin-labeled proteins.

The first part of this dissertation (Chapter 3) exemplifies the advantageous use of SDSL-EPR for studying structural dynamics in a membrane transport protein, BtuB, under more physiologically relevant conditions compared to the requisite environment utilized in X-ray crystallographic endeavors. The effects on protein structure of stabilizing osmolytes that are commonly used in crystallization have been reasonably well studied. However, outside of the direct modulation of protein structure by inter-

protein crystal contacts (which does not appear to be the case for the BtuB Ton box), consequences arising from the constraints imposed by the crystal lattice are poorly understood.

As discussed in Chapter 3.3, the source of Ton box stabilization energy attributed to the crystal lattice may have several origins. The obvious next direction for future studies will be to attempt the crystallization of BtuB V10R1 in different space groups, which will produce different crystal contacts and variations in both the unit cell dimensions and overall crystal dimensions. For example, the crystallization procedures for BtuB *in meso* have already been determined, and the packing of BtuB in these crystals is different than *in surfo*.⁴ Hopefully, such efforts will allow for extraction of the lattice parameters that are important for imparting stabilization energy to the Ton box. Moreover, analysis of a broad range of proteins that undergo well-characterized conformational exchange, comparing data from the crystal and in solution, would be useful to determine whether the crystal lattice is a general modulator of protein conformational equilibria.

In Chapter 4, data was presented that advances our understanding of spin label configurations and dynamics from hydrocarbon-exposed sites on β -barrel membrane proteins. Combined with two other studies published around the same time,^{5,6} the data provide compelling evidence that spin label rotamers in hydrophobic environments tend to be different from those found at aqueous solvent-exposed sites. Specifically, the configuration of spin labels at sites in the membrane hydrocarbon will be influenced by the solvation environment and the availability of hydrophobic pockets on the protein

surface with which it can interact. In the case of BtuB, the structures of R1 presented in Chapter 4 represent the only two known rotamers at hydrocarbon-exposed sites on β -barrel membrane proteins. But the {p,p} and {t,m} rotamers observed crystallographically are only two examples, and the alternate {t,t} rotamer responsible for the slow component in the 156R1 spectrum represents nothing more than an educated guess. More work is certainly needed to create a rotamer library and to clarify the dependence of R1 motion on neighboring side-chains at sites near the aqueous interface.

Towards this end, some groups have pursued multifrequency⁷⁻⁹ or computational¹⁰⁻¹³ efforts. Due to the frequency dependence of dynamics that average the spectral anisotropy, the continued commercial development of instrumentation for multifrequency EPR experiments should be valuable for the identification and characterization of internal spin label dynamics, and the separation of this contribution from protein dynamics. Furthermore, concerns over the uniqueness of spectral fits (e.g. with the MOMD model) due to overparameterization should be addressed by fitting EPR spectra at multiple frequencies, which should reduce the inherent ambiguity.

Quantum mechanical computations^{10,11} on model spin-labeled α -helical peptides have predicted spin label conformations and interactions in good agreement with experimental data, and revealed comprehensive torsional profiles for R1. Molecular dynamics simulations have been applied to more thoroughly study the internal motions of R1 and its interactions.^{12,13} In principle, with sufficiently long trajectories (allowing for the proper sampling of conformational space in an explicit solvent system) and the implementation of accurate force fields (such as a classical Drude oscillator that accounts

for electronic polarizability), molecular dynamics simulations could provide a considerably detailed representation of spin label behavior. Despite recent improvements in these areas, such endeavors remain challenging in practice. However, some simulations reveal an unexpected complexity in the interconversion between multiple spin label configurations, rendering a wide range of microscopic spin label dynamics capable of yielding nearly identical spectra.¹³ Furthermore, the intricate motional models from these simulations were able to produce theoretical EPR spectra in excellent agreement with the experimental spectra at multiple frequencies. This finding is not consistent with inferences from experimental data and quantum mechanical calculations, and presents the concerning possibility that the interpretation of spin label structure and dynamics may be more nebulous than previously thought. More accurate computational simulations, combined with experimental work and multifrequency spectral fitting, will be necessary in future ventures.

Chapters 5 and 6 described the use of SDSL-EPR for studying signaling mechanisms and important protein-protein interactions in TonB-dependent transport. In Chapter 5, a two mutant cycle analysis combined with SDSL indicated that the R14 and D316 side-chains are not used by ColE3R to refold the Ton box, in contrast to their apparent role in undocking the Ton box when CNCbl binds BtuB. This supports the existence of multiple signaling pathways through a β -barrel membrane protein. However, it is not known whether the pathways are entirely exclusive or if a subset of similar components are involved. Future studies, using the structure-based sequence alignments as a guide,¹⁴ should focus on identifying additional components of these

unique signaling pathways in BtuB and other transporters using the spin-labeled Ton box as a proxy for interactions between residues.

In Chapter 6 a multidisciplinary approach was utilized to study the interaction between TonB and three of its cognate transporters; although in principle SDSL-EPR may be used to determine weak (minimum $K_D \approx 10^{-5}$ M) protein-protein binding affinities,¹⁵ the nanomolar affinities between these proteins required a more sensitive technique such as fluorescence. The data suggest that when overexpressed and purified according to the given procedures, TonB is structurally heterogeneous and the conformations are in very slow exchange. The TonB conformational population that gives rise to the low-affinity mode of binding is of unknown structure and unknown physiological relevance. Although it could represent stably misfolded TonB, the protein was well-tolerated after overexpression in the cytoplasm, appears to be intact and well solvated following purification, and possesses low μ M affinity for the TBDTs. Thus, it may represent the conformation of newly synthesized TonB *in vivo* that has not yet assembled into a functional complex with ExbB and ExbD. Isolation and structural characterization of this conformation may provide useful information on the mechanism of conformational cycling mediated by ExbB and ExbD.

DEER spectroscopy suggests that the high-affinity population of TonB is structurally similar to the strand-exchanged, PG-binding dimer that has only been observed for the shortest TonB fragments characterized structurally. Moreover, opposite to what has been published previously,^{16,17} the DEER data suggest that the TonB dimer dissociates upon binding to the TBDTs. Considering the limiting amount of TonB in the

cell and the finding that the TBDTs can associate with PG-binding proteins, the previously proposed situation where monomeric TonB recruits a second TonB protein to initiate transport seems less efficient and unlikely. However, a more thorough and quantitative treatment of the experiments presented here will be required to better characterize the recognition mechanism and structural rearrangements involved in dimer dissociation. Furthermore, it is not known whether the polyproline segment participates in TonB dimerization contacts. If this is the case, it would be interesting to determine the affinity of the ExbD periplasmic domain for TonB in the dimeric versus monomeric (i.e. TBDT-bound) form; it is tempting to imagine that dissociation of the TonB dimer upon recognition of a TBDT might also serve as a signal to the CM that initiates the next steps required for transport.

Chapter 7 References

1. Stone, T.J., Buckman, T., Nordio, P.L. & McConnell, H.M. Spin-labeled biomolecules. *Proceedings of the National Academy of Sciences of the United States of America* **54**, 1010-7 (1965).
2. Altenbach, C., Flitsch, S.L., Khorana, H.G. & Hubbell, W.L. Structural Studies on Transmembrane Proteins .2. Spin Labeling of Bacteriorhodopsin Mutants at Unique Cysteines. *Biochemistry* **28**, 7806-7812 (1989).
3. Todd, A.P., Cong, J.P., Levinthal, F., Levinthal, C. & Hubbell, W.L. Site-Directed Mutagenesis of Colicin-E1 Provides Specific Attachment Sites for Spin

- Labels Whose Spectra Are Sensitive to Local Conformation. *Proteins-Structure Function and Genetics* **6**, 294-305 (1989).
4. Cherezov, V. et al. In meso structure of the cobalamin transporter, BtuB, at 1.95 Å resolution. *Journal of molecular biology* **364**, 716-34 (2006).
 5. Kroncke, B.M., Horanyi, P.S. & Columbus, L. Structural Origins of Nitroxide Side Chain Dynamics on Membrane Protein alpha-Helical Sites. *Biochemistry* **49**, 10045-10060 (2010).
 6. Jimenez, R.H., Freed, D.M. & Cafiso, D.S. Lipid and membrane mimetic environments modulate spin label side chain configuration in the outer membrane protein A. *The journal of physical chemistry. B* **115**, 14822-30 (2011).
 7. Zhang, Z. et al. Multifrequency electron spin resonance study of the dynamics of spin labeled T4 lysozyme. *The journal of physical chemistry. B* **114**, 5503-21 (2010).
 8. Liang, Z.C., Lou, Y., Freed, J.H., Columbus, L. & Hubbell, W.L. A multifrequency electron spin resonance study of T4 lysozyme dynamics using the slowly relaxing local structure model. *Journal of Physical Chemistry B* **108**, 17649-17659 (2004).
 9. Nsmelov, Y.E., Karim, C.B., Song, L., Fajer, P.G. & Thomas, D.D. Rotational dynamics of phospholamban determined by multifrequency electron paramagnetic resonance. *Biophysical journal* **93**, 2805-12 (2007).
 10. Tombolato, F., Ferrarini, A. & Freed, J.H. Dynamics of the nitroxide side chain in spin-labeled proteins. *The journal of physical chemistry. B* **110**, 26248-59 (2006).

11. Warshaviak, D.T., Serbulea, L., Houk, K.N. & Hubbell, W.L. Conformational analysis of a nitroxide side chain in an alpha-helix with density functional theory. *The journal of physical chemistry. B* **115**, 397-405 (2011).
12. LaConte, L.E., Voelz, V., Nelson, W., Enz, M. & Thomas, D.D. Molecular dynamics simulation of site-directed spin labeling: experimental validation in muscle fibers. *Biophysical journal* **83**, 1854-66 (2002).
13. Sezer, D., Freed, J.H. & Roux, B. Multifrequency electron spin resonance spectra of a spin-labeled protein calculated from molecular dynamics simulations. *Journal of the American Chemical Society* **131**, 2597-605 (2009).
14. Chimento, D.P., Kadner, R.J. & Wiener, M.C. Comparative structural analysis of TonB-dependent outer membrane transporters: implications for the transport cycle. *Proteins* **59**, 240-51 (2005).
15. Sarewicz, M., Szytula, S., Dutka, M., Osyczka, A. & Froncisz, W. Estimation of binding parameters for the protein-protein interaction using a site-directed spin labeling and EPR spectroscopy. *European biophysics journal : EBJ* **37**, 483-93 (2008).
16. Khursigara, C.M., De Crescenzo, G., Pawelek, P.D. & Coulton, J.W. Deletion of the proline-rich region of TonB disrupts formation of a 2 : 1 complex with FhuA, an outer membrane receptor of Escherichia coli. *Protein Science* **14**, 1266-1273 (2005).
17. Khursigara, C.M., De Crescenzo, G., Pawelek, P.D. & Coulton, J.W. Kinetic analyses reveal multiple steps in forming TonB-FhuA complexes from Escherichia coli. *Biochemistry* **44**, 3441-3453 (2005).